Nonlinear Dynamics of Wind Turbine Wings

Larsen, Jesper Winther

Publication date:
2005

Document Version
Publisher's PDF, also known as Version of record

Aalborg University

Nonlinear Dynamics of Wind Turbine Wings

by

Jesper Winther Larsen

Submitted for the degree of
Doctor of Philosophy

Department of Civil Engineering
Faculty of Engineering and Science
July 2005

Preface

The present thesis “Nonlinear Dynamics of Wind Turbine Wings” has been prepared in connection with a Ph.D. study carried out in the period August 2002 to July 2005 at the Department of Civil Engineering, Aalborg University, Denmark. The study was financial supported by the Danish Technical Research Council (STVF) within the programme “Damping Mechanisms in Dynamics of Structures and Materials”. The support is duely acknowledged.

First of all, I wish to thank my supervisor, Prof. Dr. Techn. Søren R.K. Nielsen, for his great interest in the project and persistent guidance throughout my study.

During a 4 months stay at the DUWIND group, Delft University, the Netherlands, I was introduced to the fields of computational fluid dynamics with emphasis on fluid structure interaction of wind turbine wings. Special thanks should be directed to Prof. Dr. Gijs Van Kuik from the DUWIND group and Dr. Hester Bijl from the Aerodynamics group, who made my stay possible and supervised my work. I am also grateful to the entire staff within the DUWIND group for their succeeding efforts to make my stay both very pleasant and fruitful.

I would like to thank my colleagues in the Department of Civil Engineering, friends and family for their support and assistance. Finally, special thanks to my fiancée for her everlasting patience and encouragement during the project.

Aalborg, July 1, 2005 Jesper Winther Larsen

Summary in English

Wind turbines with a nominal effect of 5MW with a rotor diameter of up to 126m are produced today. With the increasing size wind turbines also become more and more optimized with respect to structural dimensions and material usage, without increasing the stiffness proportionally. Consequently, large wind turbines become increasingly flexible and dynamically sensitive. This project focuses on the structural analysis of highly flexible wind turbine wings, and the aerodynamic loading of wind turbine wings under large changes in flow field due to elastic deformations and changing wind conditions.

The nonlinear equations of motion of a rotating wing are derived using the Bernoulli-Euler beam theory within a blade fixed rotating coordinate system. By applying forced support point motion, the tower-nacelle system is decoupled from the wing. The model introduces contributions from a nonlinear description of the curvature, rotation of the aerodynamic loading due to deflection, displacement of the mass due to deflection, and contributions from the support point motion and rotation of the beam. Nonlinearities up to third order are retained in the final formulation of the equations of motion. A two-degrees-of-freedom reduced modal model is derived using the fundamental blade and edgewise eigenmodes, and the important nonlinear coupling terms are found and kept for further analysis. 4 characteristic frequencies are considered with respect to stability and resonance behaviour, which are the rotational frequency of the rotor, the support point frequency and the eigenfrequencies of the blade and edgewise modes, respectively. Stability of the nonlinear wing is evaluated by the use of Lyapunov exponents. Stability boundaries are found with respect to the mentioned frequencies, modal damping and support point amplitude during harmonic support point motion and constant lift and drag coefficients.

Wind turbine wings experience significant changes in both flow velocity and direction due to tower passage, rotation in a shear wind field, turbulence components, active control of the wing and elastic deformations. A so-called semi-empirical dynamic stall model of a two-dimensional wing section is devised. The model includes 4 state variables describing important contributions as regards the aerodynamics of wind turbine wings. The model uses two state variables to describe the dynamic lift under attached flow conditions, one state variable to account for the dynamic effects of trailing edge separation, and finally, one state variable to introduce contributions from leading edge separation. Five other dynamic stall models are described and they are validated against experimental data. The devised model is shown to perform as well as any other and more complicated models.

Next, the nonlinear structural model and the dynamic stall model are combined, and numerical simulations illustrate the performance of the combined model. The numerical simulations include: variation of pitch setting with no support point motion, harmonic variation of support point motion at various constant pitch settings, simulation in a shear wind field including tower passage, and the performance of a linear control algorithm using the pitch system as actuator.

Finally, a stability analysis is performed of the wing undergoing stochastically varying support point motion. The structural dynamics of the wing is relatively complicated. To understand the behaviour of the nonlinear stochastically parametrically excited system, two simpler systems are initially analysed. Firstly, a stability analysis is carried out by use of Lyapunov exponents of a mechanical system parametrically excited by a stochastic renewal jump process. Secondly, the stability of a support point excited cable with a small sag is analysed by use of the Floquet theory. The stability of the nonlinear wing is shown to be related to a one-dimensional outcrossing problem of the excitation envelope process, as is the case for the support point excited cable.

Summary in Danish

Vindmøller med en effect på 5 MW og rotordiameter på 126 m bliver produceret i dag. Møllerne bliver optimeret mere og mere både hvad angår dimensionering og materialer uden tilsvarende øgning af stivhederne. Dette introducerer øget fleksibilitet og derved en mere dynamisk følsom konstruktion. Projektet fokuserer på den strukturelle analyse af fleksible vindmøllevinger samt den aerodynamiske belastning ved store variationer i strømningsfeltet pga. elastiske deformationer og ændringer i vindforholdene.

Først er ikke-lineære bevægelsesligninger for en roterende vinge udledt ved brug af Bernoulli-Euler bjælketeori, hvor der benyttes et roterende koordinatsystem, der følger vingen. Ved at påføre tvungne understøtningsflytninger er tårn-nacelle systemet dekoblet fra vingen. Modellen introducerer bidrag fra en ikke-lineær beskrivelse af krumningen, rotation af de aerodynamiske laster samt forskydning af masse pga. udbøjning af vingen. Desuden indføres bidrag fra understøtningsflytningerne. Ikke-lineariteter op til tredje orden bibeholdes i modellen. En to-frihedsgrads modaludvikling foretages, hvor første blad- og kant-egensvingningsform benyttes, uvæsentlige led identificeres og ignoreres i følgende analyser. 4 karakteristiske frekvenser er af betydning, rotationsfrekvensen af rotoren, understøtningsfrekvensen og de to egenfrekvenser. Stabiliteten af det ikke-lineære vingesystem analyseres ved Lyapunov eksponenten for de nævnte frekvenser. Desuden er stabilitetsgrænser bestemt for variation af modal dæmpning samt understøtningsamplitude.

Vindmøllervinger oplever betydelige ændringer i både stømningshastighed og -retning, hvilket skyldes virkninger fra tårnpassage, rotation i en grænselagsstrømning, turbulenskomponenter, aktiv kontrol samt elastiske deformationer af vingerne. En såkaldt semi-empirisk dynamisk stall last model for et todimensionalt vingeprofil er udviklet. Modellen inkluderer 4 tilstandsvariable, der beskriver betydningsfulde bidrag i forbindelse med vindmøllevingeprofiler. Der benyttes to tilstandsvariable til at beskrive det dynamiske løft under fuldt vedhæftet strømning, én tilstandsvaribel til at beskrive den dynamiske bevægelse af bagkantsseperationspunktet samt én tilstandsvariabel, der beskriver effekten af ledende kant seperation. 5 andre dynamisk stall modeller er beskrevet, og de er alle benyttet til at simulere forsøgsdata. Den opstillede model beskriver forsøgsdataene i ligeså tilstrækkelig grad som mere komplicerede modeller.

Herefter kobles den ikke-lineære strukturmodel med den dynamiske stall model. Numeriske eksempler illustrerer, hvorledes modellen virker. De numeriske simuleringer inkluderer: variation af pitchindstillingen uden påvirkning fra understøtningsbevægelsen, harmonisk variation af understøtningsbevægelsen ved forskellige pitchindstillinger, simulering af vingen i en grænselagsstrømning med bidrag fra tårnpassage, samt effekten af at indfører en lineær kontrol af vingen, hvor pitchsystemet benyttes som aktuator.

Til slut analyseres stabiliteten af vingen ved stokastisk variation af understøtningsbevægelsen. Den dynamiske beskrivelse af vingen er relativ kompliceret, hvorfor to simplere systemer først analyseres, for at forstå opførelsen af ikke-lineær systemer, der påvirkes stokastisk parametrisk. Først analyseres stabiliteten af et mekanisk system der påvirkes af en renewal jump proces vha. Lyapunov eksponenten. Herefter benyttes Floquet teori til at analysere stabiliteten af et kable med et lille nedhæng, der påvirkes af understøtningsflytninger. Den stokastiske stabilitet af den ikke-lineære vinge viser sig at afhænge af den stokastiske påvirknings indhyldningskurve, hvilket også er tilfældet for kablet.

Contents

1 Introduction **1**

1.1 Background . . . 1
1.2 Wind Turbine Dynamics . . . 4
1.2.1 Wind field description . . . 4
1.2.2 Aerodynamics . . . 5
1.2.3 Structural modelling . . . 6
1.3 Aeroelastic Codes used in the Wind Industry . . . 7
1.3.1 FLEX5 . . . 8
1.3.2 HAWC . . . 8
1.4 Presentation of the Problem . . . 8
1.4.1 Nonlinear considerations . . . 9
1.5 Overview of the Thesis . . . 10

2 Nonlinear Structural Dynamics of Wind Turbine Wings **13**

2.1 Nonlinear Structural Model of Wind Turbine Wings . . . 13
2.1.1 Geometrical description . . . 15
2.1.2 Nonlinear Bernoulli-Euler beam theory . . . 19
2.1.3 External load and normal force . . . 26
2.1.4 Related linear eigenvalue problem . . . 28
2.1.5 Modal equations of motion . . . 29
2.1.6 Reduction to a two-degrees-of-freedom system . . . 30
2.1.7 Numerical example . . . 33
2.1.8 Concluding remarks . . . 40
2.2 Parametric Stability of Wind Turbine Wings . . . 41
2.2.1 Harmonic response analysis . . . 42
2.2.2 Variational equations . . . 44
2.2.3 Parametric stability analysis . . . 48
2.2.4 Concluding remarks . . . 50

3 Dynamic Stall Models of Wind Turbine Airfoils 55
3.1 Introduction . . . 55
3.2 A Dynamic Stall Model for Wind Turbines . . . 60
3.2.1 Stationary lift and separation . . . 60
3.2.2 Dynamic lift and separation . . . 61
3.2.3 Leading edge separation . . . 63
3.2.4 State formulation . . . 64
3.3 Other Dynamic Stall Models . . . 66
3.3.1 Beddoes-Leishman model . . . 66
3.3.2 ONERA model . . . 67
3.3.3 Øye model . . . 69
3.3.4 Risø model . . . 70
3.3.5 Boeing-Vertol model . . . 72
3.4 Comparison of Models . . . 73
3.5 Other aspects of dynamic stall models . . . 78
3.5.1 Aeroelastic Modelling . . . 78
3.5.2 3-D effects . . . 79
3.6 Concluding Remarks . . . 80

4 Coupling of Two-Degrees-of-Freedom Structural Model and Dynamic Stall Model 81
4.1 Formulation of the Combined Problem . . . 81
4.1.1 Wind profile . . . 81
4.1.2 Aeroelastic forces . . . 83
4.1.3 Structural system . . . 83
4.2 Numerical Examples . . . 84
4.2.1 Data used in numerical simulations . . . 84
4.2.2 Pitch of wing in constant wind field . . . 85
4.2.3 Support point motion in constant wind field . . . 87
4.2.4 Rotation of wing in boundary layer flow with tower passage . . . 88
4.2.5 Active Vibration Control of Wind Turbine Wings under Dynamic Stall . . 89
4.3 Concluding Remarks . . . 91

5 Stochastic Stability of Linear and Nonlinear Parametrically Excited Systems 99
5.1 Stochastic Stability of Mechanical Systems Under Renewal Jump Process Parametric Excitation using Lyapunov Exponents . . . 99
5.1.1 Statement of the problem . . . 100
5.1.2 Moment stability . . . 103
5.1.3 Transformation to hyperspherical coordinates . . . 104
5.1.4 Lyapunov exponents and stability with probability 1 . . . 107
5.1.5 Numerical results . . . 110
5.1.6 Concluding remarks . . . 115
5.2 Stochastic Stability of Whirling Motion of a Shallow Cable Using Floquet Theory 116
5.2.1 Modal equations of motion . . . 118
5.2.2 Harmonic analysis . . . 123
5.2.3 Stability analysis of harmonic solutions . . . 126
5.2.4 Narrow-banded excitation . . . 127

5.2.5 Homogeneous continuous time Markov chain . . . 129
5.2.6 Triggering mechanisms for transition between states . . . 131
5.2.7 Numerical example . . . 133
5.2.8 Concluding remarks . . . 136
5.3 Stochastic Stability of a Nonlinear Parametrically Excited Wind Turbine Wing . . 137
5.3.1 Narrow-banded support point motion . . . 137
5.3.2 Numerical analysis . . . 139
5.3.3 Concluding remarks . . . 142

6 Conclusion **145**
6.1 Overall Conclusions . . . 145

References **150**

A Analytical Solution of Cable Equations Using a Truncated Fourier Expansion **157**

B Stability Analysis Using Lyapunov Exponents and Floquet Theory **161**
B.1 Lyapunov Exponents . . . 161
B.2 Floquet Theory . . . 163

CHAPTER 1
Introduction

For many years numerical analyses of wind turbines have been done by linear structural models combined with various nonlinear unsteady load models. As wind turbines increase in size without corresponding increase in stiffness, considerable deformations arise, and geometrical and inertial nonlinearities need to be considered. In this introduction a brief overview is made of the aspects to consider when working with wind turbine dynamics including aerodynamics, structural modelling and wind field description. Further, a description is given of the features of two main programs used for calculating wind turbine performance and loading. Finally, nonlinear considerations for this project are outlined. The introduction is concluded with an overview of the different chapters included in the present thesis.

1.1 Background

Within the last 30 years wind turbines have grown from less than 100 kW machines produced mainly to relive an environmental concern of limited fossil fuel sources, to 5 MW impressive high tech machines, starting to play an increasingly important role on the electricity market. Figure 1.1a shows a small Bonus 30 kW wind turbine from 1980 (Danish Wind Industry Association 2005), and Figure 1.1b illustrates a row of 2.3 MW Bonus wind turbines placed at Rødsand wind farm (Offshore Center Denmark 2005).

From initially being isolated grid connected machines, wind turbines are now a days mostly organised in wind farms of several MW sized turbines. Large wind turbines have a massive effect on the surrounding flow field. Especially, turbulence phenomena are introduce within the wake due to vortex shedding of the blades. Also, a considerable rotation of the entire wake is initiated. These effects are undesirable interaction effects, which are sought minimised mainly through increasing the distances between the turbines. Furthermore, the increase in wing size have made transportation of wings over land a considerable problem. Favourable turbulence intensity and higher wind velocities over sea launched the development of offshore wind turbine farms approximately 15 years ago.

Eight offshore wind farms have so far been constructed within Danish waters. A map of their locations is given in Figure 1.2, and the specific data for the eight wind farms are listed in Table 1.1, (Offshore Center Denmark 2005). The area spanning Horns Rev wind farm is 20 km ^{2}, making a corresponding land wind farm virtual impossible within Danish borders. Thus, growth of wind turbines are no longer limited by transportation issues or finding sufficiently large areas.

It is a well known fact that wind turbines grow in size both with regards to power output and physical magnitude. Figure 1.3 illustrates the increase in rotor diameter and relative size over the last 20 years, (Danish Energy Authority 2005). It should be mentioned that the Tvind wind

a) b)

Figure 1.1 a) Bonus Energy 30 kW. b) Row of Bonus Energy 2.3 MW placed at Rødsand.

Figure 1.2 Position of the eight offshore wind farms.

Position	Year	Number of turbines	Power pr. Turbine [MW]	Total power [MW]
Vindeby (1)	1991	11	0.45	4.95
Tunø Knob (2)	1995	10	0.50	5.0
Middelgrunden (3)	2000	20	2.0	40.0
Horns Rev (4)	2002	80	2.0	160.0
Rønland (5)	2003	8	4×2.0 4×2.3	17.2
Rødsand (6)	2003	72	2.3	165.6
Samsø (7)	2003	10	2.3	23.0
Frederikshavn (8)	2003	3	1×3.0 2×2.3	7.6
Total		214	1.978	423.35

Table 1.1 Data for the 8 Danish offshore wind farms.

turbine, erected in the late 70's, had a rotor diameter of 54 m producing 2 MW. More than 15 years later, this was still the largest turbine created.

Danish wind energy is beginning to make a considerable contribution to the total Danish electricity production. The yearly wind produced electricity since 1983 is illustrated in Figure 1.4, (Danish Wind Industry Association 2005). The electricity consumption in 2003 was 35

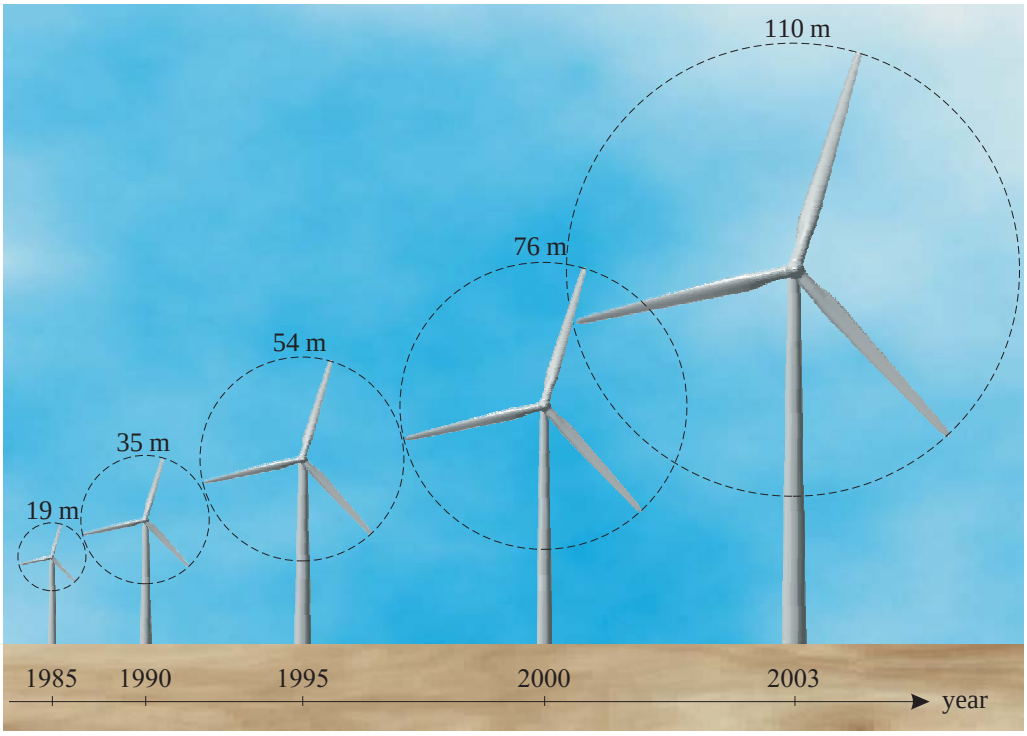

Figure 1.3 Rotor diameter and relative size of installed wind turbines in Denmark.

GWh and the wind produced electricity was 16%. Normalizing with the average wind energy from 1979 to 2002, the total share of wind produced electricity was 19.4% with an increase of 3.7% compared to 2002.

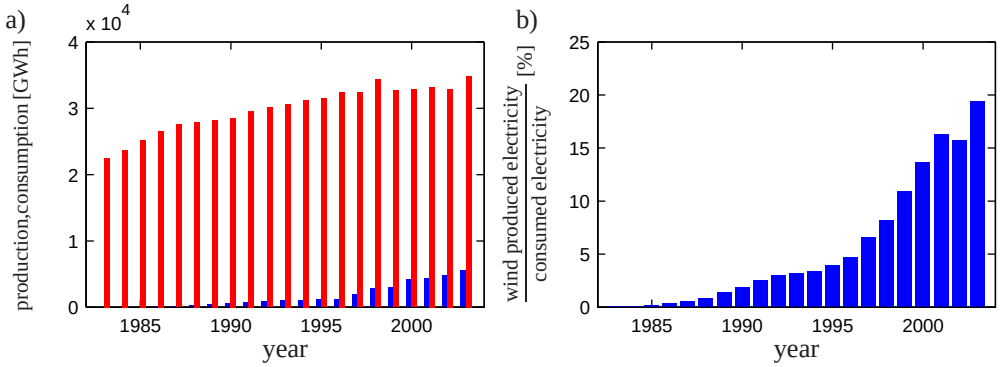

Figure 1.4 a) (■) Consumed electricity in Denmark. (■) Wind turbine produced electricity. b) Share of consumed electricity produced by wind turbines, normalized with respect to wind energy.

The political goal since 1996 has been to install a total of 1500 MW before 2005 and further introduce installations of 5500 MW before 2030 with 4000 MW produced by offshore wind turbines, (Danish Energy Authority 1996). The total wind energy capacity since 1983 is illustrated in Figure 1.5a, (Danish Wind Industry Association 2005). The increase since 1996 is significant, and the political goal of 1500 MW was already achieved in 1998. As a direct consequence of the increase of the rotor diameter, illustrated in Figure 1.3, and the introduction of large offshore wind farms, the average power output per turbine has increased from 500 kW in 1995 to 2 MW in 2003.

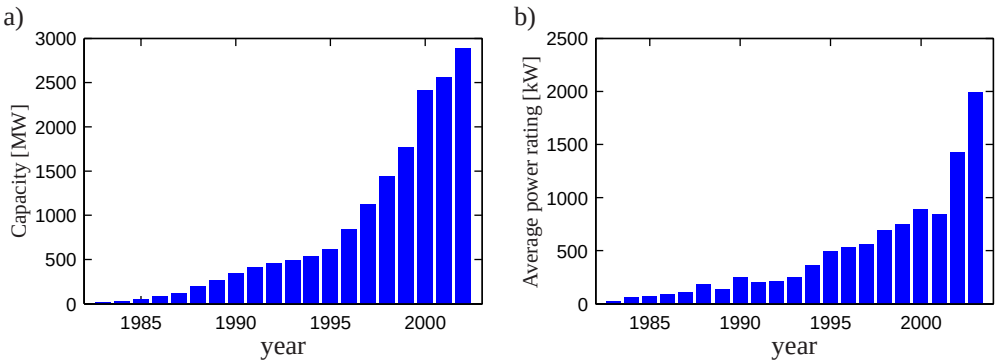

Figure 1.5 a) Total installed wind power capacity in Denmark. b) Averaged power rating of installed wind turbines in Denmark.

1.2 Wind Turbine Dynamics

Obviously, the wind makes wind turbine rotors rotate. However, many engineering disciplines are involved when trying to understand the behaviour of a wind turbine. The incoming flow field, the aerodynamics of the rotor blades, the structural dynamics of wings, drive train and tower, control issues, the energy transformation in the generator and the modelling of the tower support are just a few of the engineering tasks used within the field of wind turbines. Several practical issues, such as wing production, logistic and assembling should also be addressed, together with the impact on society, environment and economy. Many other issues may be mentioned, but a few of them will be given some special attention.

1.2.1 Wind field description

The incoming flow field is usually described as a constant or slowly varying mean wind component with a stochastic varying perturbation on top, named the turbulence component. The modelling of the mean wind may be divided into two subproblems. Firstly, the undisturbed flow field is determined as a variation with height depending on the roughness of the surrounding area. This is the so-called shear field. If the wind turbine is located at the top of a hill certain modifications can be introduced to account for induced flow velocities. Often standard mean wind flow fields are use, see e.g. (Danish Standard 1998). Secondly, changes are made to the undisturbed mean flow as a consequence of placing the wind turbine. The flow field approaching

the turbine contains a stagnation point upwind of the tower. As a rotor blade moves through this rapidly changing flow field wing vibrations are introduced. However, as long as the boundary layers over the profile of the blade are attached, these vibrations are rapidly dissipated due to aerodynamic damping. The effect of tower passage on rotor dynamics is described in Chapter 4.

Consider a section of the wing placed a certain distance from the rotor axle. Then, the incoming wind component mentioned above, and a meeting wind component are felt depending on the distance to the rotor axle and the rotational speed. Most three bladed wind turbines rotate clockwise looking from the upwind side, which induces a counterclockwise rotation of the surrounding flow field. Also, a complicated series of tip and root vortices are induced by the rotating blades, creating considerable changes in the incoming flow field. These effects can be taken into consideration through the Blade-Element-Momentum methods (BEM), see e.g. (Hansen 2000), where induction factors reducing the incoming mean wind and increasing the meeting wind component are introduced. This is a consequence of extracting energy from the wind and the counter-rotating wake.

The turbulence component is introduced as a perturbation to the mean flow field. The time variation of the turbulence components felt at a given spatial point, can be seen as the result of a constant spatial turbulence field translated with the mean flow velocity through the point as presumed by Taylor's hypothesis of frozen turbulence. Hence, a turbulence fluctuation is convected downstream with a convection velocity equal to the mean velocity. To generate a spatial field of turbulence components two methods are mainly used. One is devised by Mann and Krenk (1993), and the other is by P. S. Veers (1988) also named the SANDIA method. The method of Mann and Krenk introduces correlation between the different turbulence components together with the spatial correlation, whereas the SANDIA method disregards correlation between components.

1.2.2 Aerodynamics

The instantaneous wind velocity and direction is known for any spatial point in the field. Normally, wind components are known at discrete points and some sort of interpolation is carried out to find the wind components at various wing sections located at given coordinates in space and time. A horizontal axis wind turbine wing works in principle as an aircraft wing. The main force is the lift component working perpendicular to the incoming wind direction. At high angles of attack separation may occur, resulting in a loss of lift. This phenomena is named stall. A more thorough description of the various aerodynamic effects are given in chapter 3. The principle of a lifting surface for a wind turbine profile is illustrated in Figure 1.6. The rotation is assumed from left to right as indicated, which induces a meeting wind component illustrated by a red arrow, and the incoming wind is indicated by a green arrow from the bottom up. The tower is located at the top of the figure on the so-called suction side of the profile. The resultant wind component has a given angle of attack relative to a defined axis through the profile. The flow generates a pressure and a suction on the different sides of the profiles as indicated in Figure 1.6, which initiate a lift and drag force dependent on the angle of attack and unsteady flow conditions. The lift and drag components are projections of the resulting force onto the directions perpendicular and parallel to the resulting flow direction, respectively. Assuming that the lift and drag is known the components may be projected onto the tangential and normal directions of the rotor plane as illustrated in Figure 1.6. As long as the tangential component is in the rotational direction, a positive torque is produced on the rotor axle for generating electricity. The normal force introduces a bending deformation in the so-called blade direction, while the tangential force causes bend-

ing deformation in the edgewise direction. The lift is the primary component when considering wind turbine wings, however, the drag may be significant at high angles of attack. In chapter 3 a so-called semi-empirical model is devised for calculating the lift under dynamic variation of the surrounding flow field. Especially, the dynamic variation of lift under stall conditions are of great importance, since a significant increase in lift compared to the quasi static case can occur as well as loss of aerodynamic damping. The term semi-empirical is used because the dynamic stall model assume knowledge of the quasi-static lift force as a function of the angle of attack. Ordinarily, the quasi-static lift curve is determined from experimental data.

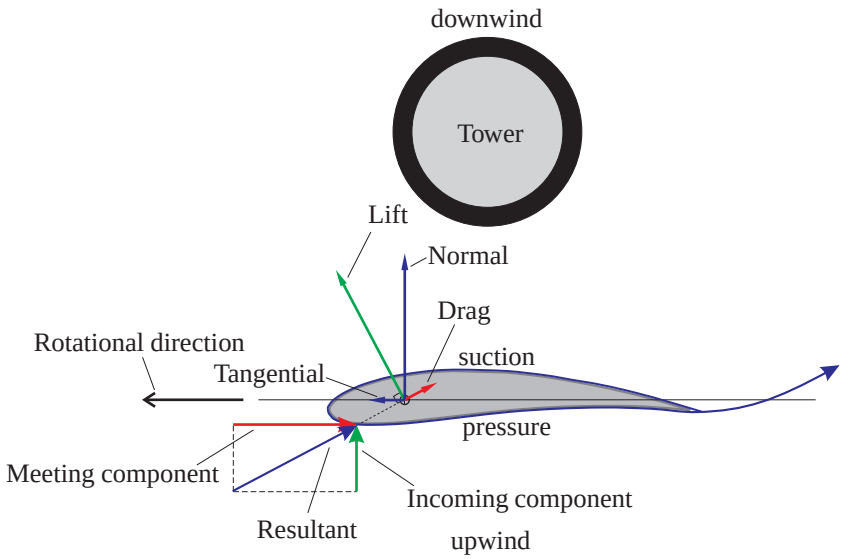

Figure 1.6 Lifting principal of a wind turbine wing.

1.2.3 Structural modelling

The normal and tangential forces illustrated in Figure 1.6 introduces deformation of the wing section in blade and edgewise directions, respectively. Since, the flow field is unsteady, the forces become unsteady, resulting in unsteady deformations of the wing. The unsteady deformations of the wing creates changing flow condition, which, all combined, generates a highly dynamic sensitive system. As illustrated in Figure 1.3, the wings of new wind turbines span more than 55 m. In written hour, the longest wing produced is a 62.5 m LM wing constructed for a 5 MW wind turbine manufactured by REpower (REpower systems 2005). Erection of the turbine is depicted in Figure 1.7a. Static testing of the wing at the test bed in Lunderskov, Denmark, is illustrated in Figure 1.7b. With a maximum chord of 4.6 m and a weight of approximately 17.7 t the wing is still highly flexible in the blade direction (LM 2005), making large deformations out of the rotor plane possible.

To create a numerical model of a wind turbine, the finite element approach or modal approach are commonly used to discretize the continues system. Considering the length to chord and length to thickness ratios, the Bernoulli-Euler beam theory may be applied with sufficient ac-

a) b)

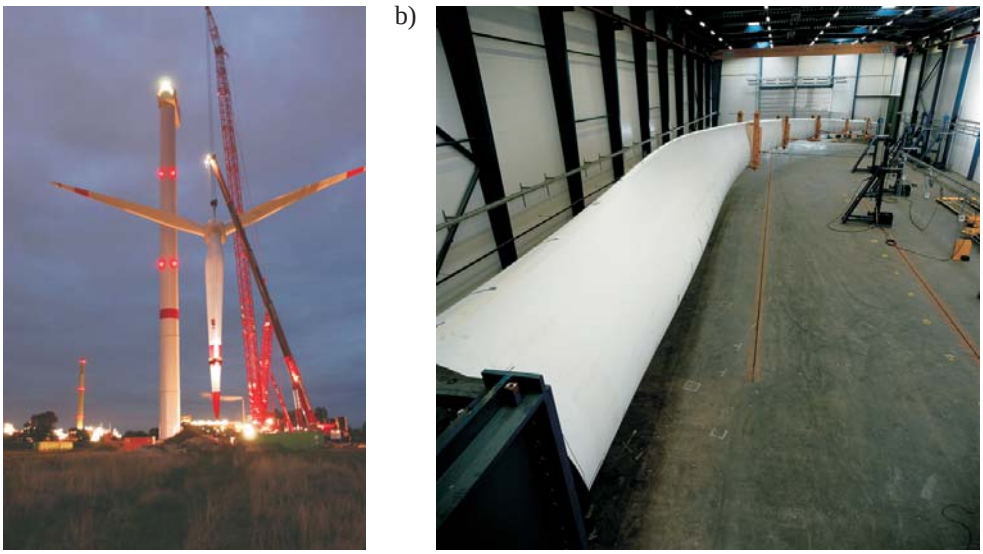

Figure 1.7 a) Erection of the REpower 5 MW turbine in Brunsbüttel, Germany. b) Static testing of the LM62.5 wing used for the REpower 5 MW turbine.

curacy. The size of the structural system is usually between 100 and 1000 degrees of freedom for the finite element model. The modal approach introduces modal modes, damping and frequencies, where the modes and frequencies are determined from eigenvalue and eigenvector analyses of a finite element model. The advantage of the modal approach is a significant reduction of the degrees of freedom. However, the behaviour of the reduced model may be faulty if excitation of disregarded modes occur.

Normally, the equation of motion of the wings are formulated in a wing fixed coordinate system, in which various centrifugal and Coriolis terms appear due to the rotational component. The tower displacements are often introduced as rigid body motion of the wing, which consequently brings forward some inertial terms together with extra contributions to the centrifugal and Coriolis terms. Within the modal approach the centrifugal terms can be decoupled by a proper choice of eigenmodes, or they may be applied as external loading. The centrifugal forces tend to increase the stiffness and consequently the eigenfrequencies.

1.3 Aeroelastic Codes used in the Wind Industry

Manufactures of wind turbines use various numerical codes when determining the dimensioning criteria of e.g. the wings or tower. The ones used in the Danish wind industry are FLEX5 and HAWC. Parts of these systems are described in short below, including the wind field modelling, the structural system and the aerodynamic loading.

1.3.1 FLEX5

The aeroelastic design code FLEX5 is originally developed at the Fluid Mechanics Department at the Technical University of Denmark by Øye. The code is mainly used by Vestas Wind Systems A/S, where the original FLEX core is being further developed, (Svendsen 2005). The equations of motions are based on a linear modal treatment, where coupling effects between the tower deformation and wing system are included. For rotating systems the system matrices cannot normally be assumed to be symmetric. However, in FLEX5 the equations of motion are based on a series-system approach for which the mass matrix becomes symmetric and the damping and stiffness matrices become diagonal. The Coriolis and other gyroscopic terms, which will give rise to cross terms and asymmetry in the damping and stiffness matrices, are in FLEX5 treated as external loading, which yields symmetric and time-invariant system matrices. The modal modes used for the wings are the first two in-plane and the first two out-of-plane modes, and for the tower, forward and sideward bending together with a torsional mode.

The Øye model for dynamic stall, described in Chapter 3, is used for modelling the dynamic variation of lift throughout the wing. The incoming mean wind field is corrected for tower passage using a potential flow with a dipole simulating the tower, and the effects of induced velocities are included by the BEM method. The turbulence field is loaded as a spatial field translated through the turbine with the mean wind velocity, hence, the generated turbulence field may be created by any method of choice.

1.3.2 HAWC

HAWC was originally developed by Petersen (1990) at Risø National Laboratory, Denmark. The model is used by Siemens Wind Power. The structural system is modelled as a full finite element model of both the wings and tower. The original release of the model was essential linear assuming small deformations. Deformations of the tower are included in the mass, damping and stiffness matrices making these time dependent. Coriolis effects are introduced in addition to contributions from the rotational speed, and inertial loads from rigid body motions of the wings. The dynamic stall model is a modified version of the Beddoes-Leishman model developed at Risø National Laboratory. Both models are described in Chapter 3. The aerodynamic loads are introduced in the direction orthogonal to the deformed wing. Furthermore, an inertial contribution to the pitching moment is included from the displacement of the centre of gravity due to deformation of the wing. The Risø National Laboratory has developed further on the original code, whereas, Siemens Wind Power have started to develop and use a completely new version of the code using co-rotational beam elements, capable of modelling large deformations. An example of a co-rotational formulation can be found in Krenk (2004b). The wind field is modelled in the same manner as FLEX5 including tower passage, induced velocities and a Taylor type hypothesis of a convected frozen turbulence field.

1.4 Presentation of the Problem

Based on the previous introduction it is clear that wind turbines have increased immensely in size since the first commercial wind turbines were introduced, and so far no indications of stagnation of this tendency is noted. Also, with a desire to lower weight of the wings in order to decrease the total cost of the turbine, the wings become more and more flexible. As computer power

increases it is now possible to simulate several load conditions including failure situations and fatigue loads for dimensioning and verification of prototypes. However, test machines are still erected to calibrate the numerical simulations. The demand for nonlinear considerations seems inevitable if realistic behaviour should be modelled numerically, making expensive prototype machines obsolete. Within this project emphasis is upon nonlinearities of the structural dynamics of wind turbine wings and the aerodynamic loading during stall conditions.

1.4.1 Nonlinear considerations

At first, the nonlinear structural dynamics of a wind turbine wing is considered. within the analysis the tower deformations are decoupled from the wing system, applying a forced support point motion on the wing. This introduces a rigid body translation and rotation of the entire wing. The low frequency behaviour of the wing is fairly accurate described by a Bernoulli-Euler beam structure. Assuming large displacements of the wing in both edgewise and blade directions the curvature of the wing can no longer be determined as the second derivative of the elastic displacement field. Hence, a nonlinear description of the curvature should be introduced. Ordinarily, the aerodynamic loads are applied to the blade and edgewise directions of the undeformed beam. However, large displacement causes large rotations of the wing sections, and consequently a significant rotation of the aerodynamic loads. The axial component of the rotated load influences the normal force, and hence the geometrical stiffness of the wing. The nonlinear description of curvature and rotation of the aerodynamic loading are classified as geometrical nonlinearities. Inertial nonlinearities are mainly introduced via the support point motion. However, a considerable mass is translated in the negative axial direction due to large bending deformations, which adds to the inertial terms. In both cases the axial components of the induced inertial loads influences the geometrical stiffness through a modification of the normal force.

Due to large changes in the flow conditions during tower passages and turbulence components, the aerodynamic loading changes considerably even during normal operating conditions. Large deformation velocities will also contribute significantly to the time varying flow conditions. All aeroelastic codes apply more or less complex numerical models for including stall effects, which in essence are highly nonlinear. The angle of attack for a horizontal axis wind turbine will, even when considering the twist, vary from within the deep stall region at the root to the attached flow regime at the tip, or the entire wing may be within the stall region during active control or failure situations. When aeroelastic contributions are included the variation of the effective angle of attack is relatively high, introducing significant nonlinear effects on the aeroelastic loading components.

The qualitatively and quantitatively behaviour and relative importance of all these nonlinearities may be highly complex and virtual impossible to analyse by analytical methods. For this reason numerical simulation is used as a tool to analyse the nonlinear systems. Through this project a structural nonlinear model of a wind turbine wing is devised including the abovementioned nonlinear effects. Furthermore, a dynamic stall model is developed only adding contribution which are estimated to be of importance when considering the aerodynamics of wind turbine wings. The nonlinear systems are investigating both separately and in combination. The behaviour of the structural system is analysed during constant aerodynamic loading, and the aeroelastic dynamic stall model is analysed during forced variation of the angle of attack.

1.5 Overview of the Thesis

- Chapter 2 describes the derivation of the nonlinear structural equations of motion of a wind turbine wing subjected to support point rotation and translation. The model is devised using Newton's second law of motion and the beam theory of Bernoulli-Euler. As wind turbines become larger and more flexible the necessity of active control increases. In practise, the instrumentation of a wind turbine only allow to identify the fundamental blade and edgewise eigenmodes. With this in mind, the equations of motions are reduced using the modal approach with two degrees of freedom including the fundamental blade and edgewise modes. The nonlinear system retains contributions of up to third order and insignificant contributions are disregarded. The reduced order model are then analysed with respect to harmonic support point motion, rotational frequency of the rotor and eigenfrequency ratio between the eigenfrequencies of the fundamental modes.

- In Chapter 3 a dynamic stall model of the lift component is formulated. The model includes 4 state variables, using two state variables to describe the dynamic variation of lift under fully attached flow condition, one state variable to describe the dynamic variation of the trailing edge separation point, and one state variable describing effects of leading edge separation. 5 other dynamic stall models are describe and the various models are compared with experimental data.

- Chapter 4 explains how the structural and dynamic stall model are combined and various numerical examples are given. The numerical examples include: forced pitch variation of the wing, harmonic support point motion in constant and shear wind field including tower passage effects, and simulations including an active control algorithm.

- The previous analyses are performed with harmonic variation of the support point motion. In reality the excitation will be stochastic narrow banded, perhaps even broad banded. The nonlinear structural model of the wing includes both linear and nonlinear parametric excitation in addition to additive load terms from the support point motion. In Chapter 5 the stochastic stability of various nonlinear parametrically excited systems are analysed. Due to the complexity of the wing model, the stochastic stability of two different systems including parametric and nonlinear terms are analysed, to illustrated classical approaches and behaviour of nonlinear stochastically parametrically excited systems. First, the stochastic stability of a mechanical system is analysed when the system is excited parametrically by a renewal jump process. This analysis is relevant since parametric excitation plays an important role for the wing. Then, the behaviour of a cable with moderate sag is analysed when excited harmonically and stochastically by support point motion. The analysis is performed for a reduced two-degrees-of-freedom system similar to the one applied for the wing. Again parametric excitation plays an important role for the behaviour of the system. Finally, a numerical analysis is carried out, when the nonlinear wing is excited by stochastic support point motion.

- Finally, Chapter 6 summarize the main conclusion of the project.

The thesis is based on a series of journal papers written within the Ph.D. project. The formulation and parametric analyses of a nonlinear wind turbine wing, given in Chapter 2, are based on Larsen and Nielsen (2004a, 2005b). The contents of Chapter 3 is based on Larsen *et*

al. (2005). In section 5.1 is the stability analysis of a stochastic parametric mechanical system given. The results are also presented by Iwankiewicz *et al.* (2005). The analyses and results from section 5.2, describing the behaviour of a support point excited cable, are also published by Larsen and Nielsen(2004b). Furthermore, four papers are under preparation, which have only partially been incorporated in this thesis. Firstly, the stochastic stability of the nonlinear wind turbine wing, analysed in section 5.3, will be published by Larsen *et al.* (2005). Under certain conditions the nonlinear wind model exhibits chaotic response. The idea of the paper is to analyse the behaviour of the strange attractor under stochastic support point excitation. A nonlinear finite element model using co-rotating beam elements is under preparation (Holm-Jørgensen *et al.* 2005), based on the formulation described in Chapter 2. The idea is to study possible energy transfers from the two lowest modes to higher modes via nonlinear couplings, and the influence of these couplings on the stability and chaotic behaviour. Finally, the formulation of an active control law during dynamic stall conditions applied to the nonlinear wing is under preparation by Larsen and Nielsen (2005a)

CHAPTER 2
Nonlinear Structural Dynamics of Wind Turbine Wings

This chapter deals with the formulation and analysis of nonlinear vibrations of a wind turbine wing described in a wing fixed moving coordinate system. The considered structural model is a Bernoulli-Euler beam with due consideration to axial twist, and is excited by aerodynamic loads and support point displacements. The model includes geometrical nonlinearities induced by the rotation of the aerodynamic load and the curvature, as well as inertial induced nonlinearities caused by the support point motion. The nonlinear partial differential equations of motion in the moving frame of reference are discretized, using the fixed base eigenmodes as a functional basis and a reduced two-degrees-of-freedom system in blade and edgewise directions are formulated. Important nonlinear couplings between the fundamental blade mode and edgewise mode are identified and only these are retained for further analysis. Assuming harmonic displacement of the tower-nacelle system dominated by the first fundamental tower mode, the frequency response of the system is analysed with respect to eigenfrequency ratio and excitation frequency ratio between the rotational frequency and the frequency of the support point motion.

2.1 Nonlinear Structural Model of Wind Turbine Wings

In recent years wind turbines have been growing in size. Offshore wind turbines with a nominal power of up to 10 MW and a rotor diameter of 175 metres, placed on water depths as deep as 20 metres are under serious consideration. Since the stiffness is not increasing proportionally, structures of that magnitude are severely dynamical sensitive. Moreover, very large displacements of the wing may occur, for which reason nonlinear effects cannot be ignored. Most of the available commercial programs for numerical analysis of wind turbines use rather simplified linear structural models which cannot be applied on structures with considerable deformations. The response of a nonlinear system may differ qualitatively from that of a corresponding linear system in a number of ways. Hence, before numerical based nonlinear algorithms can be devised it is necessary to understand the various nonlinear interactions thoroughly. This deeper insight is best achieved by the analysis of simplified nonlinear reduced degrees-of-freedom models, which are believed to provide a qualitatively correct description of the structure.

Krenk (1983a) developed a linear theory for pretwisted elastic beams under general loads assuming the cross sections are only deformed in the longitudinal direction. The theory was further developed in Krenk (1983b), where an explicit asymptotic formula for the torsion-extension coupling for pretwisted elastic beams with arbitrary homogeneous cross section was indicated.

Yang, Jiang and Chen (2004) derived a set of fully coupled nonlinear integro-differential equations for the description of axial, transverse and rotational motions of a rotating Bernoulli-Euler beam. The centrifugal stiffening effect is included without any restriction concerning angular speed. Based on an FE discretization the model is used to study suppression of transverse vibrations by controlling the angular speed. Oh and Librescu (2003) presented a linear dynamic theory of rotating blades with constant rotational speed modelled as anisotropic thin walled beams. The structural model encompasses directionality of fibrous composite materials, transverse shear, pretwist, a rigid hub and rotary inertia. Validation of the natural frequencies for sheareable beams of the presented model is made against various comparable FE models. Esmailzadeh and Jalili (1998) developed a linear structural model for a non-rotating cantilever Timoshenko beam with a tip mass excited by support motion causing parametric excitation. The idea was to study the influence of the ratio between the beam mass and the tip mass on the mode shapes, natural frequencies and the stability regions under harmonic excitation. They showed that increasing the tip mass would reduce the stability region, and using a Bernoulli-Euler model leads to incorrect stable regions compared to those found from the Timoshenko model. Krenk and Gunneskov (1986) developed a triangulation procedure for the determination of elastic cross sections with moderate wall thickness for finding cross sectional parameters like area, moments of inertia, shear stress distributions in torsion and shear, the torsional stiffness and the shear flexibility tensor. The procedure was used on different turbine blades including various NACA profiles. In a series of papers Dwivedy and Kar (1999a, 1999b) investigated the parametric stability of a base excited cantilever beam with an attached mass retaining up to cubic nonlinearities. They analysed the steady state, periodic and chaotic response under parametric and internal resonances by the methods of multiple scales and normal forms. Kane et al. (1987) obtained a comprehensive theory for dealing with vibrations of a beam attached to a moving base. They included the stretch, bending in two principal directions, shear deformations and warping of the beam. Hanagud and Sarkar (1989) formulated the problem of a cantilever beam attached to a moving support. They redefined the stretch term given by Kane et al. (1987). The formulation is valid for large displacements, and the stability characteristics of a beam under spin-up manoeuver was studied. It was demonstrated that structural nonlinearities play a major role in the response characteristics.

In this section the nonlinear dynamic response of rotating wind turbine wings are developed with emphasis on modal interactions due to parametric and additive excitation from the support point motions. The interaction between the nacelle and the wings is introduced as a support point motion of the wings, caused by the stationary motion of the turbine in the non-homogeneous mean wind field. The displacement and rotation of the support point introduce nonlinear inertia loads on the wing in addition to the parametric and additive excitation. Additionally, nonlinearities are introduced via the curvature of the wing and the rotation of the aerodynamic load. The aim is to analyse various nonlinear phenomena by a Galerkin reduced degrees-of-freedom model using the undamped fixed base eigenmodes as shape functions. Especially, the important nonlinear couplings between the fundamental blade mode and the fundamental edgewise mode are identified by reducing the model to a two-degrees-of-freedom system. The accuracy of the reduced model is to be investigated by Holm-Jørgensen (2005), however, in contrast to the similar truncation of the shallow cable described in section 5.2, the reduced nonlinear wing model has not yet been verified numerically. Wind turbines are usually equipped with sensors at the root as illustrated with the strain gages s_1 and s_2 in Figure 2.1.

In principle, if an exact mathematical model for the structural system is available, if the external loading is exactly known in space and time, and if no measurement noise is present,

Figure 2.1 Sensor position for an ordinary wind turbine wing indicated by s_1 and s_2.

then the complete state vector describing the dynamics of the system can be reconstructed from a reduced number of observed state variables, a so-called full state observer or a Luenberger observer, see e.g. Preumont (2002). In practice, the assumptions of a full state observer cannot be met. Firstly, the loading is non-observable, e.g. turbulence components may vary the loading significantly. Secondly, the sensors are usually calibrated to a given current via static loading, see Figure 1.7. Hence, the static displacement of the wing tip may be observed, but not necessarily the dynamic deformation. Consequently, any dynamic state observation through the sensors introduces noise. This means that the estimation of higher order modes becomes increasingly uncertain. The above arguments are incentives to formulate the mentioned two-degrees-of-freedom problem. Higher modes may be included in the model, however, the complexity of the system increases substantial with the numbers of degrees-of-freedom.

As long as the boundary layer is attached to the profile the blade mode is strongly dampened due to aerodynamic damping. The damping in the edgewise mode is much smaller. However, during dynamic stall the damping in the blade mode is reduced significantly. Accordingly, in this study the damping in the edgewise mode is kept at a constant low value, whereas the damping in the blade mode is varied to simulate various degrees of aerodynamic damping.

In practice, a frequency ratio between the fundamental edgewise and blade frequencies of $\omega_2/\omega_1 \simeq 2$ is often met. For this reason, the analysis of this section concentrates on nonlinear interactions for wings with the indicated eigenfrequency ratio.

2.1.1 Geometrical description

A global (x_1, x_2, x_3)-coordinate system is placed at the bottom of the tower with the x_1-axis oriented parallel to the rotor axes as shown in Figure 2.2. To simplify matters the tilt angle and the cone angle of the wind turbine are assumed to be zero. As the tower-nacelle system deforms a rotation and displacement of the hub occurs, which introduce a rotation of the rotor plane. Additionally, a blade fixed (x_1', x_2', x_3')-coordinate system with origo at the hub and with the (x_2', x_3')-plane parallel to the global (x_2, x_3)-plane is introduced. The position of the x_2'-axis is determined by the phase angle $\Phi(t)$ from the global x_2-axis to the local x_2'-axis with the sign definition shown in Figure 2.2. The x_3'-axis is oriented from the hub towards the free end. Then, the x_1' and x_2'-axes define the blade and edgewise directions, respectively. The shear centres of the cross-sections along the beam are assumed to be positioned on the x_3'-axis.

The wing is decoupled from the nacelle and the tower by introducing prescribed linear translation and rotation vectors $\mathbf{u}_0(t)$ and $\boldsymbol{\theta}_0(t)$ with the global and local coordinates $u_{i,0}(t)$, $\theta_{i,0}(t)$ and $u_{i,0}'(t)$, $\theta_{i,0}'(t)$. To simplify matters further only the deformation components $u_{1,0}(t)$ and $\theta_{2,0}(t)$ are considered, as shown in Figure 2.3a. Additionally, these components, which are causing quasi-static displacements merely in the blade direction, are assumed to be related through the fundamental eigenmode of the tower. Hence, the following support point motions

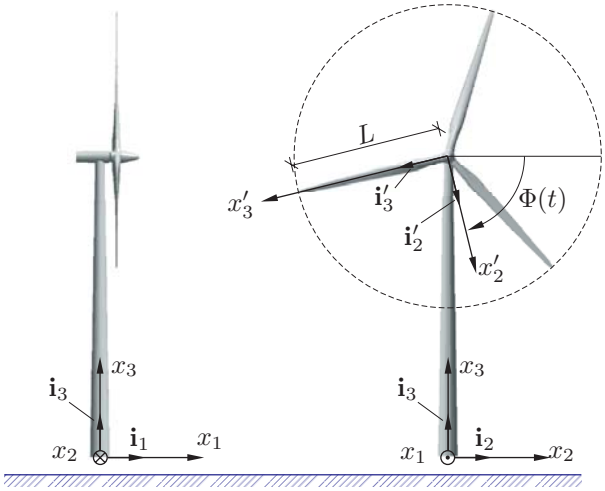

Figure 2.2 Definitions of coordinate systems.

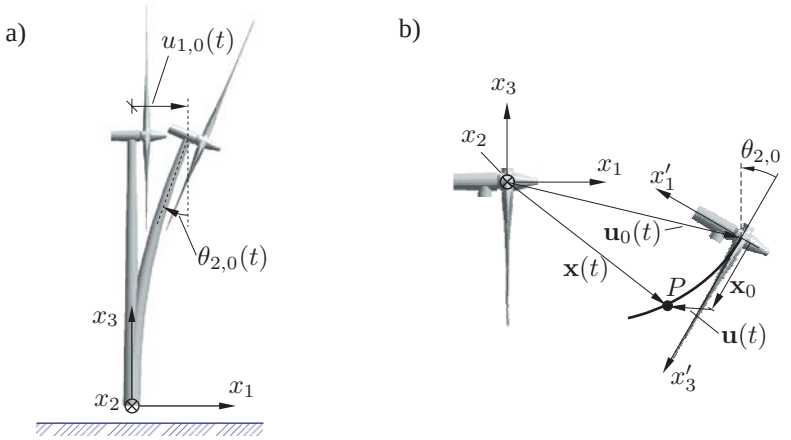

Figure 2.3 Definition of material point deformation.

are assumed

$$u_{1,0}(t) = U_{1,0}u(t), \quad \theta_{2,0}(t) = \Theta_{2,0}u(t), \quad u_{2,0}(t) = u_{3,0}(t) = \theta_{1,0}(t) = \theta_{3,0}(t) = 0. \quad (2.1)$$

The eigenmode component $U_{1,0}$ may be chosen as 1. Then, the modal coordinate of the tower $u(t)$ may be interpreted as the physical horizontal displacement of the nacelle.

The base unit vectors of the fixed (x_1, x_2, x_3) and the movable (x_1', x_2', x_3')-coordinate system are denoted as $\mathbf{i}_j$ and $\mathbf{i}_j'(t)$, $j = 1, 2, 3$, respectively. The transformation between the said base vectors and the local and global components v_i' and v_j of a vector $\mathbf{v}$ is given as

$$\mathbf{i}_i'(t) = A_{ij}(t)\mathbf{i}_j, \quad v_i' = A_{ij}(t)v_j. \tag{2.2}$$

In (2.2) and below the summation convention over dummy indices has been applied. Dummy Latin indices range over 1, 2 and 3, and dummy Greek indices over 1 and 2. The following notation will be used. A vector is represented by bold signature, e.g. $\mathbf{v}$, while the components of $\mathbf{v}$ in a given coordinate system are represented as a column matrix by a single underline, e.g. $\underline{v}$. Finally, a two dimensional matrix is represented by a double underline, e.g. $\underline{\underline{A}}$.

The coordinate transformation matrix $\underline{\underline{A}}(t)$ is found as a rotation $\theta_{2,0}$ of the rotor plane followed by a wing rotation $\Phi(t)$ around the x_2'-axis of the wing fixed (x_1', x_2', x_3')-coordinate system. This gives the following transformation matrix between the global (x_1, x_2, x_3)-coordinate system and the local (x_1', x_2', x_3')-coordinate system

$$\underline{\underline{A}}(t) = \begin{bmatrix} -1 & 0 & 0 \\ 0 & \cos\Phi & -\sin\Phi \\ 0 & -\sin\Phi & -\cos\Phi \end{bmatrix} \begin{bmatrix} \cos\theta_{2,0} & 0 & -\sin\theta_{2,0} \\ 0 & 1 & 0 \\ \sin\theta_{2,0} & 0 & \cos\theta_{2,0} \end{bmatrix}. \tag{2.3}$$

The time-derivative of $\Phi(t)$ specifies the rotational speed of the rotor

$$\Omega(t) = \dot{\Phi}(t). \tag{2.4}$$

Then the local components of the support point motion become $u_{i,0}'(t) = A_{i1}(t)u(t)$ and $\theta_{i,0}'(t) = A_{i2}\Theta_{2,0}u(t)$. Hence, the local components become

$$\underline{u}_0'(t) = \begin{bmatrix} -u(t)\cos\theta_{2,0} \\ -u(t)\sin\Phi\sin\theta_{2,0} \\ -u(t)\cos\Phi\sin\theta_{2,0} \end{bmatrix}, \quad \underline{\theta}_0'(t) = \begin{bmatrix} 0 \\ \Theta_{2,0}u(t)\cos\Phi \\ -\Theta_{2,0}u(t)\sin\Phi \end{bmatrix} \tag{2.5}$$

To simplify matters, the effects on the hub displacement from the rotation $\theta_{2,0}$ are disregarded. Hence, $u_{1,0}'(t) \simeq -u(t)$, $u_{2,0}'(t) = u_{3,0}'(t) \simeq 0$.

Figure 2.3b shows a wing with prescribed support point motions. A material point P defined by the position vector $\mathbf{x}_0(x_3', t)$ from the origo of the local moving coordinate system is considered, which is assumed to undergo the elastic deformation $\mathbf{u}(x_3', t)$ with local components $u_j'(x_3', t)$ and a support point translation $\mathbf{u}_0(t)$ with global components $u_{j,0}(t)$. The position vector of P relative to the hub in the referential position is denoted as $\mathbf{x}(x_3', t)$. The local coordinates of $\mathbf{x}_0$ are time-invariant and given as

$$\underline{x}_0' = \begin{bmatrix} 0 \\ 0 \\ x_3' \end{bmatrix}. \tag{2.6}$$

The indicated vectors are related as, see Figure 2.3b

$$\mathbf{x}(t) = \mathbf{u}_0(t) + \mathbf{x}_1(t), \tag{2.7}$$

where $\mathbf{x}_1(t) = \mathbf{x}_0 + \mathbf{u}(t)$. The global components of the position vector $\mathbf{x}(t)$, the velocity vector $\mathbf{v}(t)$ and the acceleration vector $\mathbf{a}(t)$ of point P, are given by the following column matrices

$$\begin{aligned}
\underline{x}(t) &= \underline{u}_0(t) + \underline{\underline{A}}^T(t)\underline{x}_1(t),\\
\underline{v}(t) &= \dot{\underline{u}}_0(t) + \dot{\underline{\underline{A}}}^T(t)\underline{x}_1(t) + \underline{\underline{A}}^T(t)\dot{\underline{x}}_1(t),\\
\underline{a}(t) &= \ddot{\underline{u}}_0(t) + \ddot{\underline{\underline{A}}}^T(t)\underline{x}_1(t) + 2\,\dot{\underline{\underline{A}}}^T(t)\dot{\underline{x}}_1(t) + \underline{\underline{A}}^T(t)\ddot{\underline{x}}_1(t).
\end{aligned} \tag{2.8}$$

where the local coordinates of $\mathbf{x}_1(t)$ are given as

$$\underline{x}_1'(t) = \begin{bmatrix} u_1' \\ u_2' \\ u_3' + x_3' \end{bmatrix}. \tag{2.9}$$

By premultiplication of $\underline{\underline{A}}(t)$ the local components of the velocity and acceleration vectors are obtained

$$\underline{v}'(t) = \dot{\underline{u}}_0'(t) + \dot{\underline{x}}_1(t) + \underline{\underline{A}}(t)\dot{\underline{\underline{A}}}^T(t)\underline{x}_1(t), \tag{2.10}$$

$$\underline{a}'(t) = \ddot{\underline{u}}_0'(t) + \ddot{\underline{x}}_1(t) + \underline{\underline{A}}(t)\ddot{\underline{\underline{A}}}^T(t)\underline{x}_1(t) + 2\underline{\underline{A}}(t)\dot{\underline{\underline{A}}}^T(t)\dot{\underline{x}}_1(t), \tag{2.11}$$

where it has been used that $\underline{\underline{A}}(t)$ is orthonormal, hence

$$\underline{\underline{A}}(t)\underline{\underline{A}}^T(t) = \underline{\underline{I}}, \tag{2.12}$$

Differentiation of (2.12) provides the relation $\underline{\underline{A}}(t)\,\dot{\underline{\underline{A}}}^T(t) = -\dot{\underline{\underline{A}}}(t)\underline{\underline{A}}^T(t)$, which shows that the matrix $\underline{\underline{A}}(t)\dot{\underline{\underline{A}}}^T(t)$ is skew symmetric, and at most contains three non-trivial components.

Let $\boldsymbol{\omega}(t)$ be the angular velocity vector of the support point. This rotation induces a velocity vector of the point P of magnitude

$$\mathbf{v}(t) = \boldsymbol{\omega}(t) \times \mathbf{x}_1(t). \tag{2.13}$$

The local components of $\mathbf{v}(t)$ may be written as

$$\underline{v}'(t) = \underline{\underline{\tilde{\omega}}}'(t)\underline{x}'(t), \quad \underline{\underline{\tilde{\omega}}}'(t) = \mathrm{spin}\Big(\underline{\omega}'(t)\Big) = \begin{bmatrix} 0 & -\omega_3' & \omega_2' \\ \omega_3' & 0 & -\omega_1' \\ -\omega_2' & \omega_1' & 0 \end{bmatrix}, \tag{2.14}$$

where the column matrix $\underline{\omega}'(t)$ stores the local components of the angular velocity vector, and $\underline{\underline{\tilde{\omega}}}$ denotes the so-called spin matrix related to $\boldsymbol{\omega}$. This is related to the transformation matrix as

$$\underline{\underline{\tilde{\omega}}}'(t) = \underline{\underline{A}}(t)\dot{\underline{\underline{A}}}^T(t), \tag{2.15}$$

The following relation may be derived

$$\underline{\underline{A}}(t)\ddot{\underline{\underline{A}}}^T(t) = \frac{d}{dt}\left(\underline{\underline{A}}(t)\dot{\underline{\underline{A}}}^T(t)\right) - \dot{\underline{\underline{A}}}(t)\dot{\underline{\underline{A}}}^T(t) = \frac{d}{dt}\left(\underline{\underline{A}}(t)\dot{\underline{\underline{A}}}^T(t)\right) - \dot{\underline{\underline{A}}}(t)\underline{\underline{A}}^T(t)\underline{\underline{A}}(t)\dot{\underline{\underline{A}}}^T(t)$$
$$= \dot{\tilde{\underline{\underline{\omega}}}}'(t) - \tilde{\underline{\underline{\omega}}}'^T(t)\tilde{\underline{\underline{\omega}}}'(t). \tag{2.16}$$

By use of (2.15) and (2.16), (2.11) may then be written as

$$\underline{a}'(t) = \underline{\ddot{u}}_0'(t) + \underline{\ddot{x}}_1(t) + \underline{\underline{D}}(t)\underline{x}_1(t) + \underline{\underline{E}}(t)\underline{\dot{x}}_1(t), \quad \underline{\underline{E}}(t) = 2\tilde{\underline{\underline{\omega}}}'(t), \quad \underline{\underline{D}}(t) = \dot{\tilde{\underline{\underline{\omega}}}}'(t) - \tilde{\underline{\underline{\omega}}}'^T(t)\tilde{\underline{\underline{\omega}}}'(t). \tag{2.17}$$

It should be noted that (2.17) applies to any form of rotation specified by the local components ω_i' of the angular velocity vector. In this particular case the local components of $\boldsymbol{\omega}(t)$ are defined by the rotational speed and the time derivative of the support point rotations. Hence,

$$\underline{\omega}'(t) = \begin{bmatrix} \Omega(t) \\ \dot{\theta}_{2,0}'(t) \\ \dot{\theta}_{3,0}'(t) \end{bmatrix}, \tag{2.18}$$

where $\dot{\theta}_{2,0}'(t)$ and $\dot{\theta}_{3,0}'(t)$ are the local components of $\dot{\boldsymbol{\theta}}_0(t)$. Hence, $\dot{\theta}_{2,0}'(t) = \dot{\theta}_{2,0}\cos(\Omega t)$ and $\dot{\theta}_{3,0}'(t) = -\dot{\theta}_{2,0}\sin(\Omega t)$. Now, the components of $\underline{\underline{E}}(t)$ and $\underline{\underline{D}}(t)$ become

$$\underline{\underline{E}}(t) = 2\begin{bmatrix} 0 & -\dot{\theta}_{3,0}' & \dot{\theta}_{2,0}' \\ \dot{\theta}_{3,0}' & 0 & -\Omega \\ -\dot{\theta}_{2,0}' & \Omega & 0 \end{bmatrix},$$
$$\underline{\underline{D}}(t) = \begin{bmatrix} 0 & -\ddot{\theta}_{3,0}' & \ddot{\theta}_{2,0}' \\ \ddot{\theta}_{3,0}' & 0 & -\dot{\Omega} \\ -\ddot{\theta}_{2,0}' & \dot{\Omega} & 0 \end{bmatrix} - \begin{bmatrix} \dot{\theta}_{3,0}'^2 + \dot{\theta}_{2,0}'^2 & -\dot{\theta}_{2,0}'\Omega & -\dot{\theta}_{3,0}'\Omega \\ -\dot{\theta}_{2,0}'\Omega & \dot{\theta}_{3,0}'^2 + \Omega^2 & -\dot{\theta}_{3,0}'\dot{\theta}_{2,0}' \\ -\dot{\theta}_{3,0}'\Omega & -\dot{\theta}_{3,0}'\dot{\theta}_{2,0}' & \dot{\theta}_{2,0}'^2 + \Omega^2 \end{bmatrix}. \tag{2.19}$$

Terms entering via the matrix $\underline{\underline{D}}(t)$ specify centrifugal accelerations, whereas $\underline{\underline{E}}(t)$ determines various Coriolis acceleration terms.

2.1.2 Nonlinear Bernoulli-Euler beam theory

Consider a differential beam element of the length $ds_0 = dx_3'$ placed along the beam axis at x_3' in the referential state. The length of the beam element in the deformed state is ds, and the displacement vector is $\mathbf{u}(x_3', t)$. As a result of the rotation of the element the material fixed basis is rotated into a new $(\mathbf{i}_1'', \mathbf{i}_2'', \mathbf{i}_3'')$ basis, defining a local (x_1'', x_2'', x_3'')-coordinate system, see Figure 2.4. The transformation between the global and the rotated basis is given by the tensor relations, see (Krenk 2004b)

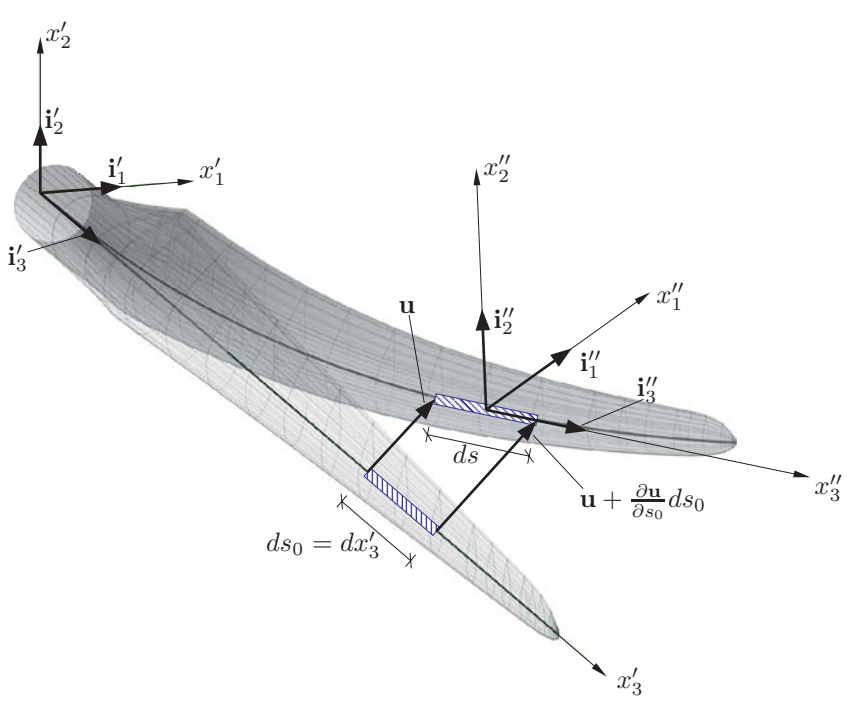

Figure 2.4 Definition of local (x_1', x_2', x_3')-coordinate system and the deformed (x_1'', x_2'', x_3'')-coordinate system.

$$\mathbf{i}_j'' = \big(\mathbf{I} + 2\mathbf{i}_j''\mathbf{i}_j' - 2\mathbf{nn}\big) \cdot \mathbf{i}_j'. \tag{2.20}$$

where $\cdot$ denotes a scalar product, $\mathbf{I}$ is the identity tensor, and $\mathbf{nn}$ indicates a dyadic product of the unit vector $\mathbf{n}$ given as

$$\mathbf{n} = \frac{\mathbf{i}_3' + \mathbf{i}_3''}{|\mathbf{i}_3' + \mathbf{i}_3''|}. \tag{2.21}$$

It is easily shown that $\mathbf{i}_3'' = -\mathbf{i}_3' + 2\mathbf{n}(\mathbf{n} \cdot \mathbf{i}_3')$. Hence, (2.20) reduces to

$$[\mathbf{i}_1'' \ \mathbf{i}_2'' \ \mathbf{i}_3''] = [\mathbf{I} - 2\mathbf{nn}] \cdot [\mathbf{i}_1' \ \mathbf{i}_2' \ -\mathbf{i}_3'], \tag{2.22}$$

further that (2.22), (2.21) provide $\mathbf{i}_j'' \cdot \mathbf{i}_k'' = \delta_{jk}$.

Let $\varepsilon_3'' = \frac{ds}{ds_0} - 1$ be the axial strain in the rotated frame of reference, where ds indicates the deformed length of the element. Then, the basis unit vectors $\mathbf{i}_3''$ and $\mathbf{i}_3'$ are related to the displacement gradients as

$$\big(1 + \varepsilon_3''\big)\mathbf{i}_3'' = \mathbf{i}_3' + \frac{\partial \mathbf{u}}{\partial x_3'}. \tag{2.23}$$

The axial strain becomes

$$\varepsilon_3'' + \frac{1}{2}\left(\varepsilon_3''\right)^2 = \mathbf{i}_3' \cdot \frac{\partial \mathbf{u}}{\partial x_3'} + \frac{1}{2}\frac{\partial \mathbf{u}}{\partial x_3'} \cdot \frac{\partial \mathbf{u}}{\partial x_3'} = \frac{\partial u_3'}{\partial x_3'} + \frac{1}{2}\frac{\partial u_j'}{\partial x_3'}\frac{\partial u_j'}{\partial x_3'}. \tag{2.24}$$

The right-hand side of (2.24) represents the axial Green strain evaluated in the referential frame of reference. In what follows the beam is assumed to be inextensible, which means that $\varepsilon_3'' = 0$. Hence, (2.24) implies

$$\frac{\partial u_3'}{\partial x_3'} = -\frac{1}{2}\frac{\partial u_j'}{\partial x_3'}\frac{\partial u_j'}{\partial x_3'} = -\frac{1}{2}\frac{\partial u_\alpha'}{\partial x_3'}\frac{\partial u_\alpha'}{\partial x_3'} + O(\varepsilon^2). \tag{2.25}$$

where

$$\varepsilon = \left|\frac{\partial u_3'}{\partial x_3'}\right|. \tag{2.26}$$

has been introduced as a characteristic error measure in the following derivations. It follows that the remainder in (2.25) is of the 4th order in the deformation gradient $\frac{\partial u_\alpha'}{\partial x_3'}$. Then, from (2.21), (2.23) and (2.25)

$$\mathbf{i}_3'' \simeq \mathbf{i}_3' + \frac{\partial \mathbf{u}}{\partial x_3'} \quad \Rightarrow$$

$$\mathbf{n} = \frac{2\mathbf{i}_3' + \dfrac{\partial \mathbf{u}}{\partial x_3'}}{\sqrt{4 - \dfrac{\partial u_\alpha'}{\partial x_3'}\dfrac{\partial u_\alpha'}{\partial x_3'} + O(\varepsilon^2)}} = \left(\mathbf{i}_3' + \frac{1}{2}\frac{\partial \mathbf{u}}{\partial x_3'}\right)\left(1 + \frac{1}{8}\frac{\partial u_\alpha'}{\partial x_3'}\frac{\partial u_\alpha'}{\partial x_3'} + O(\varepsilon^2)\right). \tag{2.27}$$

Hence, within an error of the order $O(\varepsilon^2)$ the components of $\mathbf{n}$ in the referential frame of reference may be written as

$$\begin{bmatrix} n_1' \\ n_2' \\ n_3' \end{bmatrix} \simeq \begin{bmatrix} a\dfrac{\partial u_1'}{\partial x_3'} \\ a\dfrac{\partial u_2'}{\partial x_3'} \\ b \end{bmatrix}, \quad a = \frac{1}{2} + \frac{1}{16}\frac{\partial u_\alpha'}{\partial x_3'}\frac{\partial u_\alpha'}{\partial x_3'}, \quad b = 1 - \frac{1}{8}\frac{\partial u_\alpha'}{\partial x_3'}\frac{\partial u_\alpha'}{\partial x_3'}. \tag{2.28}$$

The rotation tensor between the referential and the deformed system has the following dyadic expansions

$$\mathbf{B} = B_{kl}'\,\mathbf{i}_k'\mathbf{i}_l' = B_{kl}''\,\mathbf{i}_k''\mathbf{i}_l''. \tag{2.29}$$

Further,

$$\mathbf{i}''_j = \mathbf{B}\cdot\mathbf{i}'_j = B''_{kl}\big(\mathbf{i}''_l\cdot\mathbf{i}'_j\big)\mathbf{i}''_k \quad \Rightarrow \quad B''_{kl}\big(\mathbf{i}''_l\cdot\mathbf{i}'_j\big)=\delta_{jk} \quad \Rightarrow$$
$$B''_{jl} = \mathbf{i}'_j\cdot\mathbf{i}''_l. \tag{2.30}$$

Let $\underline{\underline{B}} = [B''_{jl}]$ be the matrix components of the rotation tensor in the rotated frame of reference. Then, the transformation between the referential and deformed components v'_j and v''_k of a vector $\mathbf{v}$ is

$$v'_j = B''_{jk}v''_k. \tag{2.31}$$

Within an error of the magnitude $O(\varepsilon^2)$ these components may be obtained from insertion of (2.28) into (2.22) as follows

$$\begin{aligned}\underline{\underline{B}} &\simeq \begin{bmatrix} 1-2a^2\Big(\dfrac{\partial u'_1}{\partial x'_3}\Big)^2 & -2a^2\dfrac{\partial u'_1}{\partial x'_3}\dfrac{\partial u'_2}{\partial x'_3} & 2ab\dfrac{\partial u'_1}{\partial x'_3} \\ -2a^2\dfrac{\partial u'_1}{\partial x'_3}\dfrac{\partial u'_2}{\partial x'_3} & 1-2a^2\Big(\dfrac{\partial u'_2}{\partial x'_3}\Big)^2 & 2ab\dfrac{\partial u'_2}{\partial x'_3} \\ -2ab\dfrac{\partial u'_1}{\partial x'_3} & -2ab\dfrac{\partial u'_2}{\partial x'_3} & -1+2b^2 \end{bmatrix} \\ &\simeq \begin{bmatrix} 1-\dfrac{1}{2}\Big(\dfrac{\partial u'_1}{\partial x'_3}\Big)^2 & -\dfrac{1}{2}\dfrac{\partial u'_1}{\partial x'_3}\dfrac{\partial u'_2}{\partial x'_3} & \dfrac{\partial u'_1}{\partial x'_3} \\ -\dfrac{1}{2}\dfrac{\partial u'_1}{\partial x'_3}\dfrac{\partial u'_2}{\partial x'_3} & 1-\dfrac{1}{2}\Big(\dfrac{\partial u'_2}{\partial x'_3}\Big)^2 & \dfrac{\partial u'_2}{\partial x'_3} \\ -\dfrac{\partial u'_1}{\partial x'_3} & -\dfrac{\partial u'_2}{\partial x'_3} & 1-\dfrac{1}{2}\dfrac{\partial u'_\alpha}{\partial x'_3}\dfrac{\partial u'_\alpha}{\partial x'_3} \end{bmatrix},\end{aligned} \tag{2.32}$$

where the order of magnitude relations $\big(\frac{\partial u'_1}{\partial x'_3}\big)^2 = O(\varepsilon)$, $\big(\frac{\partial u'_2}{\partial x'_3}\big)^2 = O(\varepsilon)$, $\frac{\partial u'_1}{\partial x'_3}\frac{\partial u'_2}{\partial x'_3} = O(\varepsilon)$ have been used. The orthonormal properties of $\underline{\underline{B}}$ in the final result are easily verified to be accurate to the third order in $\frac{\partial u'_\alpha}{\partial x'_3}$. Hodges (1974, p.49) arrived at approximately the same result. However, the cross terms $B''_{12} = 0$ and $B''_{21} = -\frac{\partial u'_1}{\partial x'_3}\frac{\partial u'_2}{\partial x'_3}$, differ from the present result. Since these terms do not influence the orthonormality to the considered accuracy, both formulations may be considered valid approximations.

Figure 2.5 shows the beam element in the deformed state. $\mathbf{x}$ denotes a position vector from the origo of the referential coordinate system to the deformed left-end section of the beam element. $-\mathbf{N}$ and $-\mathbf{M}$ denote the section force and section moment at the left-end section. The corresponding quantities at the right-end section become $\mathbf{N}+\frac{\partial\mathbf{N}}{\partial x'_3}dx'_3$ and $\mathbf{M}+\frac{\partial\mathbf{M}}{\partial x'_3}dx'_3$. The external load per unit length of the referential state is denoted $\mathbf{p}$, so the external load on the beam element becomes $\mathbf{p}dx'_3$. Force and moment equilibrium of the beam element are expressed by the equilibrium equations

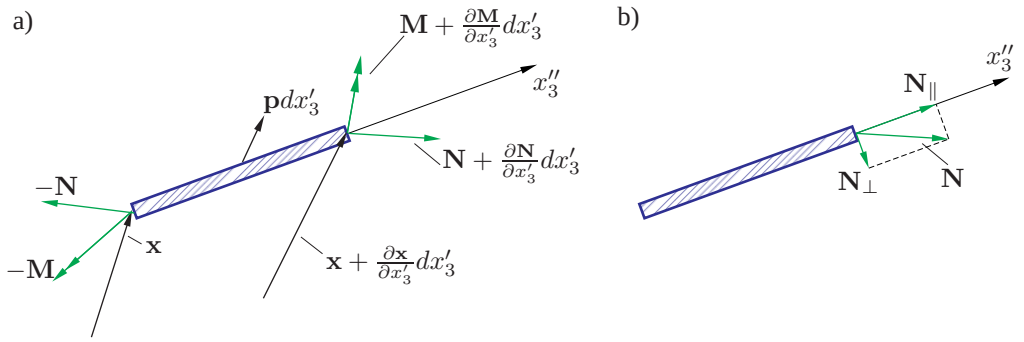

Figure 2.5 Beam element with section forces, displacement components and applied force.

$$\frac{\partial \mathbf{N}}{\partial x_3'} + \mathbf{p} = \mathbf{0}, \tag{2.33}$$

$$\frac{\partial \mathbf{M}}{\partial x_3'} + \frac{\partial \mathbf{x}}{\partial x_3'} \times \mathbf{N} = \mathbf{0}, \tag{2.34}$$

where $\times$ denotes a vectorial product. As illustrated in Figure 2.5b the section force vector $\mathbf{N}$ is resolved into a normal force vector $\mathbf{N}_\parallel$ tangential to the deformed beam axis and a vector $\mathbf{N}_\perp$ in the orthogonal direction. Hence, $\mathbf{N}_\parallel$ is perpendicular to $\frac{\partial \mathbf{x}}{\partial x_3'}$ and does not contribute to the moment equilibrium. Then (2.33) and (2.34) may be reformulated as

$$\frac{\partial \mathbf{N}_\parallel}{\partial x_3'} + \frac{\partial \mathbf{N}_\perp}{\partial x_3'} + \mathbf{p} = \mathbf{0}, \tag{2.35}$$

$$\frac{\partial \mathbf{M}}{\partial x_3'} + \frac{\partial \mathbf{x}}{\partial x_3'} \times \mathbf{N}_\perp = \mathbf{0}. \tag{2.36}$$

Let $\delta\mathbf{u}$ and $\delta\boldsymbol{\varphi}$ denote a virtual displacement and rotation vectors of the beam element. Then the equivalent weak form of (2.35) and (2.36) reads

$$\begin{aligned}
&\int_0^L \left(\delta\mathbf{u} \cdot \left(\frac{\partial \mathbf{N}_\parallel}{\partial x_3'} + \frac{\partial \mathbf{N}_\perp}{\partial x_3'} + \mathbf{p} \right) + \delta\boldsymbol{\varphi} \cdot \left(\frac{\partial \mathbf{M}}{\partial x_3'} + \frac{\partial \mathbf{x}}{\partial x_3'} \times \mathbf{N}_\perp \right) \right) dx_3' \\
&\quad = -\int_0^L \left[\delta \left(\frac{\partial \mathbf{u}}{\partial x_3'} \right) \cdot \mathbf{N}_\parallel + \left(\frac{\partial (\delta\mathbf{u})}{\partial x_3'} - \delta\boldsymbol{\varphi} \times \frac{\partial \mathbf{x}}{\partial x_3'} \right) \cdot \mathbf{N}_\perp + \frac{\partial (\delta\boldsymbol{\varphi})}{\partial x_3'} \cdot \mathbf{M} \right] dx_3' \\
&\qquad + \int_0^L \delta\mathbf{u} \cdot \mathbf{p} \, dx_3' + \left[\delta\mathbf{u} \cdot \left(\mathbf{N}_\parallel + \mathbf{N}_\perp \right) + \delta\boldsymbol{\varphi} \cdot \mathbf{M} \right]_0^L = 0.
\end{aligned} \tag{2.37}$$

The last formulation follows from integration by parts, and use of the identity $\delta\boldsymbol{\varphi} \cdot \left(\frac{\partial \mathbf{x}}{\partial x_3'} \times \mathbf{N}_\perp \right) = \left(\delta\boldsymbol{\varphi} \times \frac{\partial \mathbf{x}}{\partial x_3'} \right) \cdot \mathbf{N}_\perp$. The boundary term in (2.37) vanishes at the boundaries, where $\delta\mathbf{u}(0) = \delta\boldsymbol{\varphi}(0) = \mathbf{N}_\parallel(L) = \mathbf{N}_\perp(L) = \mathbf{M}(L) = \mathbf{0}$. Then, (2.37) may be written as

$$\int_0^L \left(\delta\left(\frac{\partial \mathbf{u}}{\partial x_3'}\right)\cdot \mathbf{N}_{\parallel} + \delta\boldsymbol{\varepsilon}\cdot\mathbf{N}_{\perp} + \delta\boldsymbol{\kappa}\cdot\mathbf{M}\right)dx_3' = \int_0^L \delta\mathbf{u}\cdot\mathbf{p}\; dx_3', \tag{2.38}$$

$\delta\boldsymbol{\varepsilon}$ and $\delta\boldsymbol{\kappa}$ denote the variation of the strain $\boldsymbol{\varepsilon}$ and curvature $\boldsymbol{\kappa}$ vectors, which are work conjugated to the section force vector $\mathbf{N}$ and the moment vector $\mathbf{M}$, given as

$$\delta\boldsymbol{\varepsilon} = \delta\left(\frac{\partial \mathbf{u}}{\partial x_3'}\right) - \delta\boldsymbol{\varphi}\times\frac{\partial \mathbf{x}}{\partial x_3'}, \quad \delta\boldsymbol{\kappa} = \delta\left(\frac{\partial \boldsymbol{\varphi}}{\partial x_3'}\right). \tag{2.39}$$

In Bernoulli-Euler beam theory shear deformations are neglected. When the virtual work is evaluated in the rotated coordinate system this means that $\delta\varepsilon_1'' = \delta\varepsilon_2'' = 0$. The aeroelastic load and the inertia load act in the aerodynamic and mass centre of gravity, respectively. These usually do not coincide with the shear centre of the section generating a twisting moment. However, due to the relative large rotational stiffness of wind turbine wing sections the effects of twisting moment M_3'' are disregarded in the following. Hence, the virtual work from the torsional moment M_3'' and the shear force components N_1'' and N_2'' is neglected. $\mathbf{N}_{\parallel}$ is tangential to the deformed beam, i.e. the following expansion prevails in the referential and deformed frame of reference

$$\mathbf{N}_{\parallel} = N_3''\mathbf{i}_3'' = N_{\alpha\parallel}'\mathbf{i}_\alpha' + N_{3\parallel}'\mathbf{i}_3'. \tag{2.40}$$

It follows that

$$N_{\alpha\parallel}' = N_3''\mathbf{i}_\alpha'\cdot\mathbf{i}_3'' = N_3''B_{\alpha 3}'' = N_3''\frac{\partial u_\alpha'}{\partial x_3'}. \tag{2.41}$$

Then the virtual work affecting the normal force in (2.38) may be written as

$$\begin{aligned}\int_0^L \delta\left(\frac{\partial \mathbf{u}}{\partial x_3'}\right)\cdot\mathbf{N}_{\parallel}\,dx_3' &= \int_0^L \left[\delta\left(\frac{\partial u_\alpha'}{\partial x_3'}\right)N_3''\frac{\partial u_\alpha'}{\partial x_3'} + \delta\left(\frac{\partial u_3'}{\partial x_3'}\right)N_{3\parallel}'\right]dx_3' \\ &= \int_0^L \left[\delta\left(\frac{\partial u_\alpha'}{\partial x_3'}\right)N_3''\frac{\partial u_\alpha'}{\partial x_3'} - \delta u_3'\left(\frac{\partial N_{3\parallel}'}{\partial x_3'}\right)\right]dx_3' + \left[\delta u_3' N_{3\parallel}'\right]_0^L.\end{aligned} \tag{2.42}$$

The last term in (2.42) vanishes due to boundary conditions. Then, (2.38) reduces to

$$\int_0^L \left[\delta\left(\frac{\partial u_\alpha'}{\partial x_3'}\right)N_3''\frac{\partial u_\alpha'}{\partial x_3'} + \delta\kappa_\alpha'' M_\alpha''\right]dx_3' = \int_0^L \left[\delta u_\alpha' p_\alpha' + \delta u_3'\left(p_3' + \frac{\partial N_{3\parallel}'}{\partial x_3'}\right)\right]dx_3'. \tag{2.43}$$

The last term in the integrand on the right-hand side provides the following equilibrium equation in the axial direction

$$\frac{\partial N_3'}{\partial x_3'} + p_3' = 0. \tag{2.44}$$

for ease in notation N_3' has been introduced for $N_{3\|}$. $\boldsymbol{\kappa}$ is defined from the rotation tensor $\mathbf{B}$ as follows, see (Krenk 2004b).

$$\boldsymbol{\kappa} \times \mathbf{I} = \frac{\partial \mathbf{B}}{\partial x_3'} \cdot \mathbf{B}^T, \tag{2.45}$$

where $\mathbf{I}$ is the identity tensor and $\mathbf{B}^T$ is the inverse rotation tensor. Then, the components κ_i'' in the rotated frame of reference are given as

$$\underline{\underline{\tilde{\kappa}}}'' = \frac{\partial \underline{\underline{B}}}{\partial x_3'} \underline{\underline{B}}^T. \tag{2.46}$$

Preserving terms up to cubic order the following results may be derived after some algebra.

$$\begin{aligned}
\kappa_\alpha'' &= -e_{\alpha\beta}\frac{\partial^2 u_\beta'}{\partial x_3'^2} - \frac{1}{2}e_{\alpha\beta}\frac{\partial u_\beta'}{\partial x_3'}\frac{\partial u_\gamma'}{\partial x_3'}\frac{\partial^2 u_\gamma'}{\partial x_3'^2}, \\
\kappa_3'' &= -\frac{1}{2}e_{\alpha\beta}\frac{\partial^2 u_\alpha'}{\partial x_3'^2}\frac{\partial u_\beta'}{\partial x_3'}.
\end{aligned} \tag{2.47}$$

Since it has been assumed that $M_3'' = 0$ we would expect $\kappa_3'' \neq 0$. Hence, the fact that (2.47) provides $\kappa_3'' \neq 0$ may be considered a minor inconsistency in the theory. One of the basic assumptions is that the no rotation occur over a differential beam element. It seems that the rotation through the smallest angle given by (2.32) introduce a change in the axial curvature and hence a change in rotation over a beam element. From (2.47) follows the corresponding components of $\delta\kappa_\alpha$

$$\delta\kappa_\alpha'' = -e_{\alpha\beta}\delta\left(\frac{\partial^2 u_\beta'}{\partial x_3'^2}\right) - \frac{1}{2}e_{\alpha\beta}\left(\delta\left(\frac{\partial u_\beta'}{\partial x_3'}\right)\frac{\partial u_\gamma'}{\partial x_3'}\frac{\partial^2 u_\gamma'}{\partial x_3'^2} + \frac{\partial u_\beta'}{\partial x_3'}\delta\left(\frac{\partial u_\gamma'}{\partial x_3'}\right)\frac{\partial^2 u_\gamma'}{\partial x_3'^2} + \frac{\partial u_\beta'}{\partial x_3'}\frac{\partial u_\gamma'}{\partial x_3'}\delta\left(\frac{\partial^2 u_\gamma'}{\partial x_3'^2}\right)\right). \tag{2.48}$$

The constitutive relations of Bernoulli-Euler beams postulate a linear relationship between moment components M_α'' and curvature components κ_α'' as follows

$$M_\alpha'' = EI_{\alpha\beta}''\kappa_\beta''. \tag{2.49}$$

In (2.49) E is the elasticity modulus, and $I_{\alpha\beta}''$ is the inertia tensor.

Let (x_1''', x_2''', x_3''') denote a principle axes coordinate system rotated the twist angle $\varphi(x_3'')$ around the x_3''-axis with the sign defined in Figure 2.6. Then,

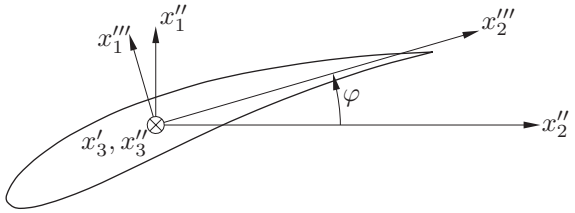

Figure 2.6 Principal coordinate system.

$$I''_{\alpha\beta} = I'''_{\gamma\delta} C_{\alpha\gamma} C_{\beta\delta}, \tag{2.50}$$

where $I'''_{\alpha\beta}$ denotes the components of the inertia tensor in the (x_1''', x_2''', x_3''')-system. These may be stored as the diagonal matrix

$$\underline{\underline{I}}''' = \begin{bmatrix} I'''_{11} & 0 \\ 0 & I'''_{22} \end{bmatrix}, \tag{2.51}$$

$C_{\alpha\beta}$ describes the components of the transformation matrix between the principal (x_1''', x_2''')-coordinate system and the local (x_1'', x_2'')-coordinate system as represented by the matrix

$$\underline{\underline{C}} = \begin{bmatrix} \cos\varphi & \sin\varphi \\ -\sin\varphi & \cos\varphi \end{bmatrix}. \tag{2.52}$$

2.1.3 External load and normal force

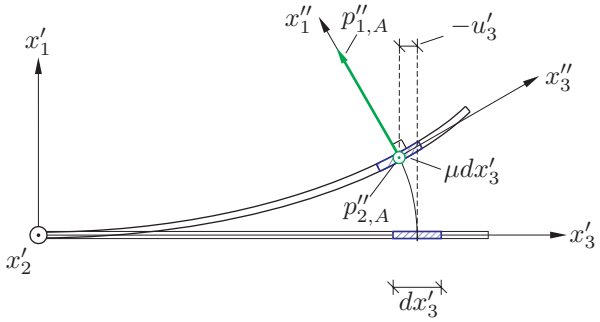

Figure 2.7 Geometrical nonlinear effects due to beam deformation.

Left is to determine the external load p'_α in the referential frame of reference and the normal force N_3'' in the rotated frame of reference. The external load originates from the aerodynamic loading and support point motion. Usually, the aerodynamic loads are determined for 2D sections throughout the wing perpendicular to the deformed beam axis x_3''. This is illustrated in Figure 2.7,

for the (x_1', x_3')-plane. To determine the aerodynamic loads in the referential frame of reference entering the right-hand side of (2.43), the vector component relation in (2.31) is used

$$p'_{i,A} = B''_{i\beta}\, p''_{\beta,A} = \begin{bmatrix} \left(1 - \frac{1}{2}\left(\frac{\partial u_1'}{\partial x_3'}\right)^2\right) p''_{1,A} - \frac{1}{2}\frac{\partial u_1'}{\partial x_3'}\frac{\partial u_2'}{\partial x_3'} p''_{2,A} \\ -\frac{1}{2}\frac{\partial u_1'}{\partial x_3'}\frac{\partial u_2'}{\partial x_3'} p''_{1,A} + \left(1 - \frac{1}{2}\left(\frac{\partial u_2'}{\partial x_3'}\right)^2\right) p''_{2,A} \\ -\left(\frac{\partial u_1'}{\partial x_3'} p''_{1,A} + \frac{\partial u_2'}{\partial x_3'} p''_{2,A}\right) \end{bmatrix}. \tag{2.53}$$

Then, the total external force components orthogonal to the beam axis become

$$p'_\alpha = p'_{\alpha,A} - \mu a'_\alpha. \tag{2.54}$$

where D'Alambert's principle is used and the acceleration components a'_α are obtained from (2.17).

The normal force N_3' is made up of a quasi-static referential contribution $N'_{3,s}$ due to the centrifugal axial force at the rotational speed $\Omega(t)$, and a dynamic contribution $N'_{3,d}$, caused by the axial inertial load $p'_{3,G}$ and the axial component $p'_{3,A}$ of the aerodynamic load. Then, N_3' is given as, cf. (2.44)

$$N_3' = N'_{3,s} + \int_{x_3'}^{L} \left(p'_{3,G} + p'_{3,A}\right) dx_3'. \tag{2.55}$$

In the present case elastic elongation of the beam is disregarded, and the geometric nonlinear effect is entirely caused by the rotation of the normal force, Hence, $N_3'' = N_3'$. $N'_{3,s}$ in (2.55) originates from the term $D_{33}(t)x_3'$ in (2.17) and is given as

$$N'_{3,s}(x_3', t) = \Omega^2(t) \int_{x_3'}^{L} \mu(x_3') x_3' dx_3'. \tag{2.56}$$

In (2.55) $p'_{3,G} = -\mu\left(a_3' + \ddot{u}_3'\right)$, where a_3' denotes the component along the x_3'-axis of the acceleration vector (2.17). Notice, that the centrifugal acceleration term $-\Omega^2(t)x_3'$ in (2.17) has already been accounted for via $N'_{3,s}$. As seen in Figure 2.7 the displacement of the beam causes an axial displacement u_3', which will introduce an axial inertial load $-\mu\ddot{u}_3'$. This load causes a nonlinear term of the 3rd order, when included into N_3'. With a consistent approximation u_3' may be calculated from

$$u_3'(x_3', t) = -\int_0^{x_3'} \left(1 - \sqrt{1 - \left(\frac{\partial u_1'}{\partial x_3'}\right)^2 - \left(\frac{\partial u_2'}{\partial x_3'}\right)^2}\right) dx_3' \simeq -\frac{1}{2}\int_0^{x_3'} \left(\frac{\partial u_\alpha'}{\partial x_3'}\frac{\partial u_\alpha'}{\partial x_3'}\right) dx_3' \quad \Rightarrow$$

$$\ddot{u}_3'(x_3', t) = -\int_0^{x_3'} \left(\frac{\partial \dot{u}_\alpha'}{\partial x_3'}\frac{\partial \dot{u}_\alpha'}{\partial x_3'} + \frac{\partial u_\alpha'}{\partial x_3'}\frac{\partial \ddot{u}_\alpha'}{\partial x_3'}\right) dx_3'. \tag{2.57}$$

Combining (2.17), (2.54) and (2.55) the following expressions are obtained for the dynamic loads per unit length and the axial force

$$
\begin{aligned}
p_1' &= p_{1,A}' - \mu\Big(\ddot{u}_{1,0}' + \ddot{u}_1' - \big(\dot{\theta}_{3,0}'^2 + \dot{\theta}_{2,0}'^2\big)u_1' - \big(\ddot{\theta}_{3,0}' - \dot{\theta}_{2,0}'\Omega\big)u_2' + \big(\ddot{\theta}_{2,0}' + \dot{\theta}_{3,0}'\Omega\big)x_3' - 2\dot{\theta}_{3,0}'\dot{u}_2'\Big),\\
p_2' &= p_{2,A}' - \mu\Big(\ddot{u}_2' + \big(\ddot{\theta}_{3,0}' + \dot{\theta}_{2,0}'\Omega\big)u_1' - \big(\dot{\theta}_{3,0}'^2 + \Omega^2\big)u_2' - \big(\dot{\Omega} - \dot{\theta}_{3,0}'\dot{\theta}_{2,0}'\big)x_3' + 2\dot{\theta}_{3,0}'\dot{u}_1'\Big),\\
N_3' &= N_{3,s}' + \int_{x_3'}^{L}\Big[p_{3,A}' - \mu\Big(-\big(\ddot{\theta}_{2,0}' - \dot{\theta}_{3,0}'\Omega\big)u_1' + \big(\dot{\Omega} + \dot{\theta}_{3,0}'\dot{\theta}_{2,0}'\big)u_2' - \dot{\theta}_{2,0}'^2 x_3' - 2\dot{\theta}_{2,0}'\dot{u}_1' + 2\Omega\dot{u}_2' + \ddot{u}_3'\Big)\Big]dx_3',
\end{aligned}
\tag{2.58}
$$

where $p_{i,A}'$ is given in (2.53), and $\ddot{u}_3'$ is determined from (2.57).

2.1.4 Related linear eigenvalue problem

In order to discretize the variational equation (2.43) the displacement components $u_\alpha'(x_3', t)$ are represented by the following modal expansion

$$
u_\alpha'(x_3', t) = \sum_{j=1}^{\infty} \Phi_\alpha^{(j)}(x_3')q_j(t). \tag{2.59}
$$

$q_j(t)$ denotes the modal coordinates and $\Phi_\alpha^{(j)}(x_3')$ represents the undamped eigenmodes, which are determined from the following linear self-adjoint eigenvalue problem

$$
\begin{aligned}
&\frac{d^2}{dx_3'^2}\left(e_{\alpha\gamma}EI_{\gamma\delta}''e_{\delta\beta}\frac{d^2\Phi_\beta^{(j)}}{dx_3'^2}\right) + \frac{d}{dx_3'}\left(N_{3,s}''\frac{d\Phi_\alpha^{(j)}}{dx_3'}\right) + \omega_j^2\mu(x_3')\Phi_\alpha^{(j)}(x_3') = 0,\\
&\Phi_\alpha^{(j)}(0) = \frac{d\Phi_\alpha^{(j)}(0)}{dx_3'} = 0, \quad EI_{\alpha\delta}''(L)e_{\delta\beta}\frac{d^2\Phi_\beta^{(j)}(L)}{dx_3'^2} = \frac{d}{dx_3'}\left(EI_{\alpha\delta}''(L)e_{\delta\beta}\frac{d^2\Phi_\beta^{(j)}(L)}{dx_3'^2}\right) = 0.
\end{aligned}
\tag{2.60}
$$

$N_{3,s}''(x_3') = N_{3,s}'(x_3')$ as given by (2.56) has been taken at a constant referential value Ω_0 of the rotational speed. At the formulation of the mechanical boundary condition at $x_3' = L$ for the shear force it has been utilized that $N_{3,s}''(L) = 0$. ω_j denotes the circular eigenfrequencies of the wing, under the rotational speed Ω_0 and fixed at the hub. The eigenmodes $\Phi_\alpha^{(j)}(x_3')$ fulfil the orthogonality conditions

$$
\int_0^L \left[\frac{d^2\Phi_\alpha^{(j)}}{dx_3'^2}e_{\alpha\gamma}EI_{\gamma\delta}''e_{\beta\delta}\frac{d^2\Phi_\beta^{(k)}}{dx_3'^2} + \frac{d\Phi_\alpha^{(j)}}{dx_3'}N_{3,s}''\frac{d\Phi_\alpha^{(k)}}{dx_3'}\right]dx_3' = \begin{cases} 0 & , \quad j \neq k, \\ \omega_j^2 M_j & , \quad j = k, \end{cases} \tag{2.61}
$$

$$\int_0^L \mu(x_3')\Phi_\alpha^{(j)}(x_3')\Phi_\alpha^{(k)}(x_3')dx_3' = \begin{cases} 0 & , \quad j \neq k, \\ M_j & , \quad j = k, \end{cases} \tag{2.62}$$

where M_j denotes the modal mass related to the jth mode. The eigenvalue problem has been solved numerically by means of an FE method, which additionally provides all necessary derivatives of the eigenmodes. Then, based on these solutions all quadratures involving the eigenmodes and their derivatives are evaluated by means of the trapezoidal rule.

Additionally, we shall assume that the variational field $\delta u_\alpha'(x_3')$ is expanded in the same functional modal basis as the displacement field, corresponding to the following Galerkin type of variation

$$\delta u_\alpha'(x_3', t) = \sum_{j=1}^{\infty} \Phi_\alpha^{(j)}(x_3')\delta q_j(t). \tag{2.63}$$

2.1.5 Modal equations of motion

The idea is to use (2.59) and (2.63) in the variational equation (2.43). This is acceptable since all kinematical requirements are fulfilled by the mode shapes $\Phi_\alpha^{(j)}(x_3')$. Assuming that the rotational speed is constant, i.e. $\Omega(t) = \Omega_0$, then the mode shapes derived from (2.60) will decouple the non-gyroscopic linear terms in (2.43). The resulting ordinary differential equations for the modal coordinates become

$$\begin{aligned} &\sum_{j=1}^{\infty}\Big(m_{ij}\ddot{q}_j + c_{ij}(t)\dot{q}_j + k_{ij}(t)q_j\Big) + \sum_{j=1}^{\infty}\sum_{k=1}^{\infty}\Big(a_{ijk}(t)q_jq_k + b_{ijk}(t)q_j\dot{q}_k\Big) \\ &\quad + \sum_{j=1}^{\infty}\sum_{k=1}^{\infty}\sum_{l=1}^{\infty}\Big(d_{ijkl}q_jq_kq_l + g_{ijkl}\Big(q_j\dot{q}_k\dot{q}_l + q_jq_k\ddot{q}_l\Big)\Big) = f_i(t), \end{aligned} \tag{2.64}$$

where

$$\begin{aligned} m_{ij} &= M_i\delta_{ij}, \\ c_{ij}(t) &= 2\zeta_i\omega_iM_i\delta_{ij} + \int_0^L \mu\Phi_\alpha^{(i)}E_{\alpha\beta}\Phi_\beta^{(j)}\,dx_3', \\ k_{ij}(t) &= M_i\omega_i^2\delta_{ij} + \int_0^L\Big[\mu\Phi_\alpha^{(i)}D_{\alpha\beta}\Phi_\beta^{(j)} - \frac{\partial\Phi_\alpha^{(i)}}{\partial x_3'}\frac{\partial\Phi_\alpha^{(j)}}{\partial x_3'}\int_{x_3'}^L \mu D_{33}x_3'\,dx_3'\Big]dx_3'. \end{aligned} \tag{2.65}$$

In (2.65) and below the summation convention has been abandoned over the modal coordinate indices. Further, in $c_{ij}(t)$ a damping term has been introduced via the modal damping ratio ζ_i accounting for structural and aerodynamic damping. As seen, the support point rotations $\theta_{2,0}'(t)$ and $\theta_{3,0}'(t)$ cause parametric excitation in the linear terms. The nonlinear coupling coefficients in (2.64) are defined as follows

$$
\begin{aligned}
a_{ijk}(t) &= \int_0^L \left[\frac{\partial \Phi_\alpha^{(i)}}{\partial x_3'} \frac{\partial \Phi_\alpha^{(j)}}{\partial x_3'} \int_{x_3'}^L \left[- p''_{\beta,A} \frac{\partial \Phi_\beta^{(k)}}{\partial x_3'} - \mu D_{3\beta} \Phi_\beta^{(k)} \right] dx_3' \right. \\
&\quad \left. + \frac{1}{2} \Phi_\alpha^{(i)} p''_{\beta,A} \frac{\partial \Phi_\alpha^{(j)}}{\partial x_3'} \frac{\partial \Phi_\beta^{(k)}}{\partial x_3'} \right] dx_3', \\
b_{ijk}(t) &= \int_0^L \left[\frac{\partial \Phi_\alpha^{(i)}}{\partial x_3'} \frac{\partial \Phi_\alpha^{(j)}}{\partial x_3'} \int_{x_3'}^L -\mu E_{3\beta} \Phi_\beta^{(k)} \, dx_3' \right] dx_3', \\
d_{ijkl} &= \int_0^L \frac{1}{2} e_{\alpha\eta} EI''_{\alpha\beta} e_{\beta\xi} \left[\frac{\partial^2 \Phi_\eta^{(i)}}{\partial x_3'^2} \frac{\partial \Phi_\xi^{(j)}}{\partial x_3'} \frac{\partial \Phi_\gamma^{(k)}}{\partial x_3'} \frac{\partial^2 \Phi_\gamma^{(l)}}{\partial x_3'^2} + \frac{\partial^2 \Phi_\xi^{(l)}}{\partial x_3'^2} \frac{\partial \Phi_\eta^{(i)}}{\partial x_3'} \frac{\partial \Phi_\gamma^{(j)}}{\partial x_3'} \frac{\partial^2 \Phi_\gamma^{(k)}}{\partial x_3'^2} \right. \\
&\quad \left. + \frac{\partial^2 \Phi_\xi^{(l)}}{\partial x_3'^2} \frac{\partial \Phi_\eta^{(j)}}{\partial x_3'} \frac{\partial \Phi_\gamma^{(i)}}{\partial x_3'} \frac{\partial^2 \Phi_\gamma^{(k)}}{\partial x_3'^2} + \frac{\partial^2 \Phi_\xi^{(l)}}{\partial x_3'^2} \frac{\partial \Phi_\eta^{(j)}}{\partial x_3'} \frac{\partial \Phi_\gamma^{(k)}}{\partial x_3'} \frac{\partial^2 \Phi_\gamma^{(i)}}{\partial x_3'^2} \right] dx_3', \\
g_{ijkl} &= \int_0^L \left[\frac{\partial \Phi_\alpha^{(i)}}{\partial x_3'} \frac{\partial \Phi_\alpha^{(j)}}{\partial x_3'} \int_{x_3'}^L \left[\mu \int_0^{x_3'} \frac{\partial \Phi_\beta^{(k)}}{\partial x_3'} \frac{\partial \Phi_\beta^{(l)}}{\partial x_3'} dx_3' \right] dx_3' \right] dx_3', , \\
f_i(t) &= \int_0^L \Phi_\alpha^{(i)} \left(p''_{\alpha,A} - \mu \left(\ddot{u}'_{\alpha,0} + D_{\alpha 3} x_3' \right) \right) dx_3'.
\end{aligned}
\tag{2.66}
$$

As seen, the parametric excitation from $\theta'_{2,0}(t)$ and $\theta'_{3,0}(t)$ is also present in the quadratic nonlinear coupling terms $b_{ijk}(t)$ and a_{ijk}. By contrast, the support point displacement $u'_{1,0}(t)$ only enters the equations as an additive load term via the modal loads $f_i(t)$. $b_{ijk}(t)$ and g_{ijkl} are quadratic and cubic nonlinear coupling coefficients originating from inertial nonlinearities, whereas d_{ijkl} is a purely geometrical nonlinear term from the nonlinear description of the curvature. The quadratic nonlinear coupling coefficients $a_{ijk}(t)$ include both contributions from the rotation of the aeroelastic loads and from the support point rotations.

2.1.6 Reduction to a two-degrees-of-freedom system

In what follows it is assumed that merely the fundamental blade and edgewise modal coordinates are performing large vibrations due to resonance, whereas all other modal coordinates remain small, and may be described by a linear theory. Moreover, these degrees of freedom are completely decoupled from the fundamental blade and edgewise modal coordinates. Accordingly, the influence of the linear degrees of freedom on the qualitatively behaviour of the nonlinear modal coordinates may be considered weak. Hence, (2.64) reduces to

$$
\begin{aligned}
&M_1\big(\ddot{q}_1 + 2\zeta_1\omega_1\dot{q}_1 + \omega_1^2 q_1\big) + c_{12}\dot{q}_2 + k_{11}q_1 + k_{12}q_2 \\
&\quad + a_{111}q_1^2 + \big(a_{112} + a_{121}\big)q_1q_2 + a_{122}q_2^2 + b_{111}q_1\dot{q}_1 + b_{112}q_1\dot{q}_2 + b_{121}q_2\dot{q}_1 + b_{122}q_2\dot{q}_2 \\
&\quad + d_{1111}q_1^3 + \big(d_{1112} + d_{1121} + d_{1211}\big)q_1^2q_2 + \big(d_{1122} + d_{1212} + d_{1221}\big)q_1q_2^2 + d_{1222}q_2^3 \\
&\quad + g_{1111}\big(q_1\dot{q}_1^2 + q_1^2\ddot{q}_1\big) + g_{1112}\big(q_1\dot{q}_1\dot{q}_2 + q_1^2\ddot{q}_2\big) + g_{1121}\big(q_1\dot{q}_1\dot{q}_2 + q_1q_2\ddot{q}_1\big) \\
&\quad + g_{1211}\big(q_2\dot{q}_1^2 + q_1q_2\ddot{q}_1\big) + g_{1122}\big(q_1\dot{q}_2^2 + q_1q_2\ddot{q}_2\big) + g_{1212}\big(q_2\dot{q}_1\dot{q}_2 + q_1q_2\ddot{q}_2\big) \\
&\quad + g_{1221}\big(q_2\dot{q}_1\dot{q}_2 + q_2^2\ddot{q}_1\big) + g_{1222}\big(q_2\dot{q}_2^2 + q_2^2\ddot{q}_2\big) = f_1(t),
\end{aligned}
\tag{2.67}
$$

$$
\begin{aligned}
&M_2\big(\ddot{q}_2 + 2\zeta_2\omega_2\dot{q}_2 + \omega_2^2 q_2\big) + c_{21}\dot{q}_1 + k_{22}q_2 + k_{21}q_1 \\
&\quad + a_{211}q_1^2 + \big(a_{212} + a_{221}\big)q_1q_2 + a_{222}q_2^2 + b_{211}q_1\dot{q}_1 + b_{212}q_1\dot{q}_2 + b_{221}q_2\dot{q}_1 + b_{222}q_2\dot{q}_2 \\
&\quad + d_{2111}q_1^3 + \big(d_{2112} + d_{2121} + d_{2211}\big)q_1^2q_2 + \big(d_{2122} + d_{2212} + d_{2221}\big)q_1q_2^2 + d_{2222}q_2^3 \\
&\quad + g_{2111}\big(q_1\dot{q}_1^2 + q_1^2\ddot{q}_1\big) + g_{2112}\big(q_1\dot{q}_1\dot{q}_2 + q_1^2\ddot{q}_2\big) + g_{2121}\big(q_1\dot{q}_1\dot{q}_2 + q_1q_2\ddot{q}_1\big) \\
&\quad + g_{2211}\big(q_2\dot{q}_1^2 + q_1q_2\ddot{q}_1\big) + g_{2122}\big(q_1\dot{q}_2^2 + q_1q_2\ddot{q}_2\big) + g_{2212}\big(q_2\dot{q}_1\dot{q}_2 + q_1q_2\ddot{q}_2\big) \\
&\quad + g_{2221}\big(q_2\dot{q}_1\dot{q}_2 + q_2^2\ddot{q}_1\big) + g_{2222}\big(q_2\dot{q}_2^2 + q_2^2\ddot{q}_2\big) = f_2(t).
\end{aligned}
\tag{2.68}
$$

With the local components of the support point motions given by (2.1), the time dependent coefficients (2.65) and (2.66) may be written in the following way

$$
\begin{aligned}
k_{ij}(t) &= -k_{ij,11}\Theta_{2,0}^2\dot{u}^2(t) + k_{ij,12}\Theta_{2,0}\Big(\ddot{u}(t)\sin\Omega_0 t + \dot{u}(t)\Omega_0\cos\Omega_0 t\Big) + k_{ij,21}\Theta_{2,0}\Big(-\ddot{u}(t)\sin\Omega_0 t + \dot{u}(t)\Omega_0\cos\Omega_0 t\Big) \\
&\quad + k_{ij,22}\Big(-\Theta_{2,0}^2\dot{u}^2(t)\sin^2\Omega_0 t - \Omega_0^2\Big) + k_{ij,33}\Theta_{2,0}^2\dot{u}^2(t)\cos^2\Omega_0 t, \\
c_{ij}(t) &= -c_{ij,1}\dot{u}(t)\Theta_{2,0}\sin\Omega_0 t, \\
a_{ijk}(t) &= a_{ijk,0}(t) - a_{ijk,1}\Theta_{2,0}\Big(\ddot{u}(t)\cos\Omega_0 t + \dot{u}(t)\Omega_0\sin\Omega_0 t\Big) - a_{ijk,2}\Theta_{2,0}^2\dot{u}^2(t)\sin\Omega_0 t\cos\Omega_0 t, \\
b_{ijk}(t) &= -b_{ijk,1}\Theta_{2,0}\dot{u}(t)\cos\Omega_0 t + b_{ijk,2}\Omega_0, \\
f_i(t) &= f_{i,0}(t) + f_{i,1}\Theta_{2,0}\Big(\ddot{u}(t)\cos\Omega_0 t - \Omega_0\dot{u}(t)\sin\Omega_0 t\Big) - f_{i,2}\Theta_{2,0}^2\dot{u}^2(t)\sin\Omega_0 t\cos\Omega_0 t + f_{i,3}\ddot{u}(t),
\end{aligned}
\tag{2.69}
$$

where the time independent coefficients are found to be

$$c_{ij,1} = 2\int_0^L \mu\Big(-\Phi_1^{(i)}\Phi_2^{(j)} + \Phi_2^{(i)}\Phi_1^{(j)}\Big)dx_3',$$

$$k_{ij,\alpha\beta} = \int_0^L \mu\Phi_\alpha^{(i)}\Phi_\beta^{(j)}dx_3', \quad k_{ij,33} = \int_0^L \left[\frac{\partial\Phi_\alpha^{(i)}}{\partial x_3'}\frac{\partial\Phi_\alpha^{(j)}}{\partial x_3'}\int_{x_3'}^L \mu x_3'\,dx_3'\right]dx_3',$$

$$a_{ijk,0} = \int_0^L \left[\frac{\partial\Phi_\alpha^{(i)}}{\partial x_3'}\frac{\partial\Phi_\alpha^{(j)}}{\partial x_3'}\int_{x_3'}^L -p''_{\beta,A}\frac{\partial\Phi_\beta^{(k)}}{\partial x_3'}dx_3' + \frac{1}{2}\Phi_\alpha^{(i)}p''_{\beta,A}\frac{\partial\Phi_\alpha^{(j)}}{\partial x_3'}\frac{\partial\Phi_\beta^{(k)}}{\partial x_3'}\right]dx_3',$$

$$a_{ijk,\alpha} = \int_0^L \left[\frac{\partial\Phi_\beta^{(i)}}{\partial x_3'}\frac{\partial\Phi_\beta^{(j)}}{\partial x_3'}\int_{x_3'}^L -\mu\Phi_\alpha^{(k)}dx_3'\right]dx_3', \quad b_{ijk,\alpha} = 2a_{ijk,\alpha},$$

$$f_{i,0} = \int_0^L \Phi_\alpha^{(i)}p''_{\alpha,A}dx_3', \quad f_{i,\alpha} = -\int_0^L \Phi_\alpha^{(i)}\mu x_3'dx_3' \quad f_{i,3} = \int_0^L \Phi_1^{(i)}\mu dx_3'. \tag{2.70}$$

To investigate the relative importance of the nonlinear terms entering (2.67) and (2.68) the following time variations of the horizontal displacement of the nacelle are assumed to be

$$u(t) = u_0\cos\omega_0 t. \tag{2.71}$$

Typically, $\omega_0 \simeq 3\Omega_0$ for a three bladed rotor moving in a nonhomogeneous shear mean wind field.

The incoming wind velocity $V_1'(x_3',t)$ as seen from a considered cross section of the wing varies periodically with the rotational speed Ω_0. $V_1'(x_3',t)$ is assumed to vary logarithmic in the following way

$$V_1'(x_3',t) = V_0\frac{\ln x_3}{\ln h} = V_0\frac{\ln\left(h - x_3'\cos\Omega_0 t\right)}{\ln h}, \tag{2.72}$$

where V_0 is the undisturbed mean wind velocity and h is the height of the rotor axis. The rotational wind velocity is given as $V_2'(x_3') = x_3'\Omega_0$. Then, the resulting wind velocity $V(x_3',t)$ may be written as

$$V(x_3',t) = \sqrt{V_1'^2(x_3',t) + V_2'^2(x_3')}. \tag{2.73}$$

Based on (2.73) the following expression for the aerodynamic loads are derived

$$p''_{1,A}(x_3',t) = \frac{1}{2}\rho V^2(x_3',t)c(x_3')c_L \simeq p''_{1,A,0}(x_3') + \Delta p''_{1,A,1}(x_3')\cos\Omega_0 t,$$

$$p''_{2,A}(x_3',t) = \frac{1}{2}\rho V^2(x_3',t)c(x_3')c_D \simeq p''_{2,A,0}(x_3') + \Delta p''_{2,A,1}(x_3')\cos\Omega_0 t. \tag{2.74}$$

$p''_{\alpha,A,0}(x'_3)$ denotes the mean value of $p''_{\alpha,A}(x'_3,t)$, when the wing is at the top and bottom positions. Correspondingly, $\Delta p''_{\alpha,A,1}(x'_3)$ denotes half of the difference between these extreme values. c_L and c_D are the lift and drag coefficients. The coefficients $a_{ijk,0}(t)$ and $f_{i,0}(t)$ in (2.70) may then be written in the following way

$$a_{ijk,0}(t) = a_{ijk,00} + \Delta a_{ijk,01}\cos\Omega_0 t, \quad f_{i,0}(t) = f_{i,00} + \Delta f_{i,01}\cos\Omega_0 t \tag{2.75}$$

with

$$a_{ijk,00} = \int_0^L \left[\frac{\partial\Phi_\alpha^{(i)}}{\partial x'_3}\frac{\partial\Phi_\alpha^{(j)}}{\partial x'_3}\int_{x'_3}^L\left[-p''_{\beta,A,0}\frac{\partial\Phi_\beta^{(k)}}{\partial x'_3}\right]dx'_3 + \frac{1}{2}\Phi_\alpha^{(i)}p''_{\beta,A,0}\frac{\partial\Phi_\alpha^{(j)}}{\partial x'_3}\frac{\partial\Phi_\beta^{(k)}}{\partial x'_3}\right]dx'_3,$$

$$\Delta a_{ijk,01} = \int_0^L \left[\frac{\partial\Phi_\alpha^{(i)}}{\partial x'_3}\frac{\partial\Phi_\alpha^{(j)}}{\partial x'_3}\int_{x'_3}^L\left[-\Delta p''_{\beta,A,1}\frac{\partial\Phi_\beta^{(k)}}{\partial x'_3}\right]dx'_3 + \frac{1}{2}\Phi_\alpha^{(i)}\Delta p''_{\beta,A,1}\frac{\partial\Phi_\alpha^{(j)}}{\partial x'_3}\frac{\partial\Phi_\beta^{(k)}}{\partial x'_3}\right]dx'_3,$$

$$f_{i,00} = \int_0^L \Phi_\alpha^{(i)}p''_{\alpha,A,0}dx'_3, \quad \Delta f_{i,01} = \int_0^L \Phi_\alpha^{(i)}\Delta p''_{\alpha,A,1}dx'_3. \tag{2.76}$$

2.1.7 Numerical example

The theory will be demonstrated using a 46 m wing. The aerodynamic profiles are NACA 63-418 section profile as illustrated in Figure 2.10, scaled with chord and height values indicated in Figure 2.11d. The inner 2.0 metres of the wing has a circular cross section with 2.0 metres in diameter. The wing has a total weight of 10 t. The stiffness and mass distribution are chosen so the eigenfrequencies approximately match those given by the manufacture of a corresponding wing size. The twist throughout the wing is chosen so that the angle of attack of the resulting wind is approximately 6° at a constant rotational speed of 1.6 s^{-1}, and an incoming wind velocity of 12 m/s.

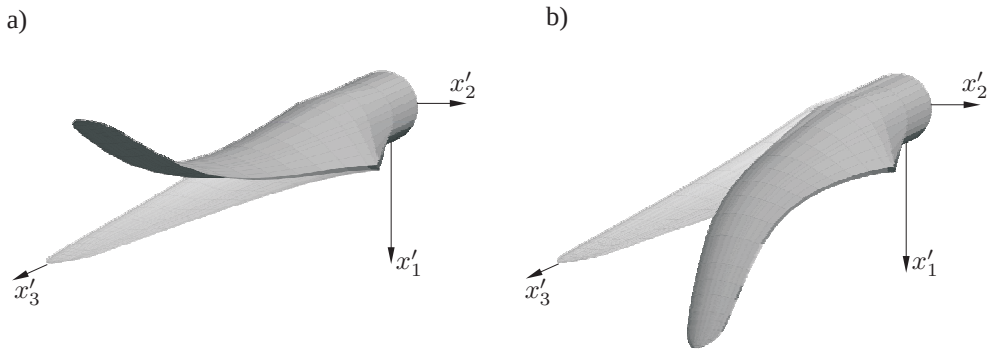

Figure 2.8 a) First eigenmode $\Phi^{(1)}$. b) Second eigenmode $\Phi^{(2)}$.

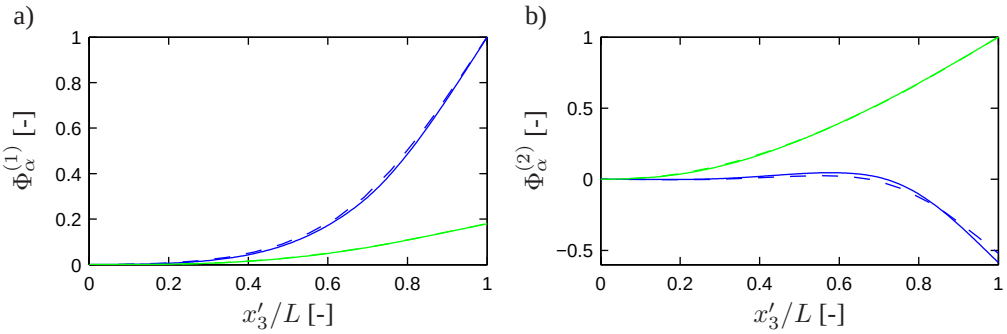

Figure 2.9 Components of eigenmodes. (——) Φ_1 Bernoulli-Euler beam. (– –) Φ_1 Mindlin-Reissner laminated shell theory. (——) Φ_2 Bernoulli-Euler beam. (– –) Φ_2 Mindlin-Reissner laminated shell theory. a) First eigenmode $\Phi^{(1)}$. b) Second eigenmode $\Phi^{(2)}$.

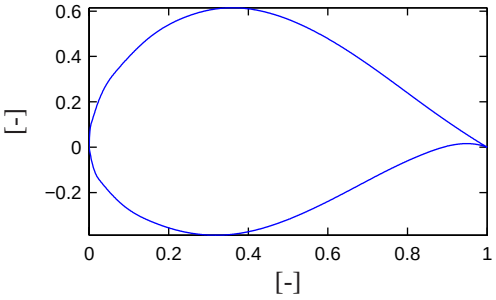

Figure 2.10 Normalized profile of a NACA 63-418 wing section.

Mode	1	2
ω_i [s^{-1}], $\Omega_0 = 0$ s^{-1}	4.61	9.39
ω_i [s^{-1}], $\Omega_0 = 1.6$ s^{-1}	5.14	9.49
M_i [kg]	427.9	852.1
ζ_i [-]	Variable	0.01

Table 2.1 Fixed base circular eigenfrequencies, modal masses and damping ratios.

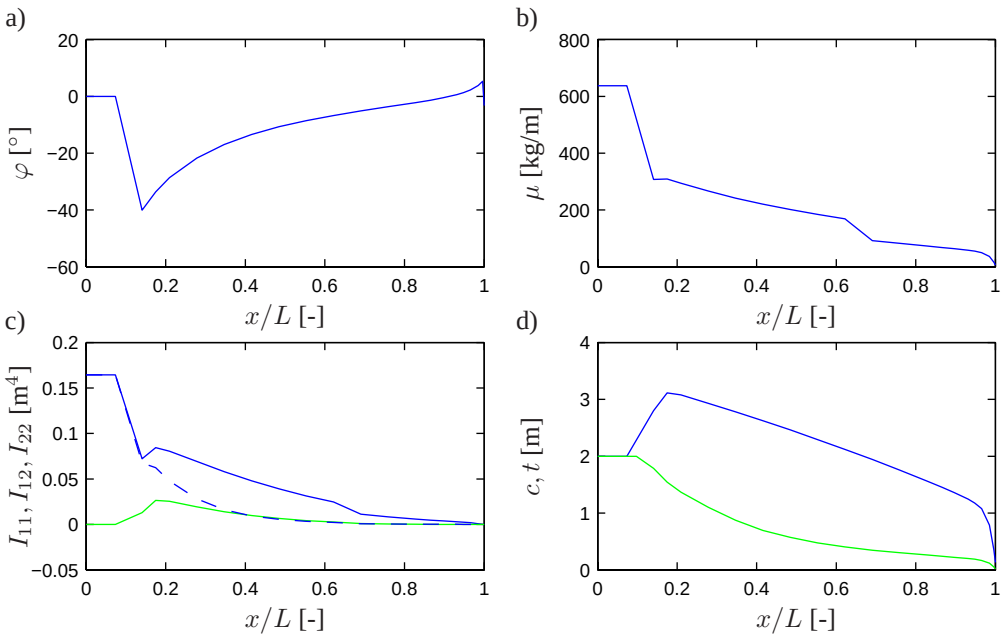

Figure 2.11 a) Twist angle throughout the beam. b) Mass per unit length. c) Distribution of local moment of inertia. (——) I_{11}. (——) I_{12}. (– –) I_{22}. d) (——) Chord length c. (——) Thickness t of cross sections.

The fundamental blade and edgewise eigenmodes are illustrated in Figure 2.8. The components in the x_1'- and x_2'-directions are shown in Figure 2.9 with the dominating components normalized to 1 at the wing tip. The components determined by Bernoulli-Euler beam theory are plotted as (——) and (——) for the inplane and out-of-plane components, respectively. For comparison the corresponding components obtained by an equivalent Mindlin-Reissner laminated shell theory are indicated by (– –) and (– –). Very small deviations are registered, indicating that the beam theory is sufficiently adequate in determining the lower order mode shapes. As seen, a considerable edgewise component is present in the blade mode $\Phi^{(1)}$ and an even more dominating blade component is present in the edgewise mode $\Phi^{(2)}$. The wing has the twist angle, the mass, local moments of inertia, chord length and thickness distributions as indicated in Figure 2.11.

Modal parameters for the first two fixed base modes of the wing are listed in Table 2.1 for the rotational speeds $\Omega_0 = 0\ \mathrm{s}^{-1}$ and $\Omega_0 = 1.6\ \mathrm{s}^{-1}$. The structural and aerodynamic damping in the edgewise mode is kept constant at the modal damping ratio $\zeta_2 = 0.01$. In the blade mode the aerodynamic damping ratio may vary from about 0.2 in case of fully attached flow to negative values under deep stall. As a consequence ζ_1 is varied in steps between the values 0.01 to 0.20 in the following study. The lift and drag coefficients are assumed to be

$$c_L = 1.5 \quad , \quad c_D = 0.05. \tag{2.77}$$

With the described wing properties the coefficients in (2.69) and (2.70) become

$$c_{ij,1} = \begin{bmatrix} 0 & -1078.62 \\ 1078.62 & 0 \end{bmatrix} \text{kg}, \quad k_{ij,11} = \begin{bmatrix} 381.34 & -115.92 \\ -115.92 & 61.04 \end{bmatrix} \text{kg},$$

$$k_{ij,12} = \begin{bmatrix} 81.22 & 517.92 \\ -21.41 & -114.93 \end{bmatrix} \text{kg}, \quad k_{ij,21} = k_{ij,12}^T,$$

$$k_{ij,22} = \begin{bmatrix} 17.72 & 115.95 \\ 115.95 & 784.94 \end{bmatrix} \text{kg}, \quad k_{ij,33} = \begin{bmatrix} 806.29 & -206.29 \\ -206.29 & 1373.31 \end{bmatrix} \text{kg},$$

$$f_{i,00} = \begin{bmatrix} 48535.1 \\ -10426.40 \end{bmatrix} \text{N} \quad , \Delta f_{i,01} = \begin{bmatrix} 993.93 \\ -177.19 \end{bmatrix} \text{N} \quad , f_{i,1} = \begin{bmatrix} -28510.61 \\ 4681.19 \end{bmatrix} \text{kgm},$$

$$f_{i,2} = \begin{bmatrix} -6619,84 \\ -47391,25 \end{bmatrix} \text{kgm} \quad , f_{i,3} = \begin{bmatrix} -872.82 \\ 75.82 \end{bmatrix} \text{kg},$$

$$a_{1jk,00} = \begin{bmatrix} -17.50 & 15.79 \\ -14.52 & 11.17 \end{bmatrix} \text{N/m}^2, \quad a_{2jk,00} = \begin{bmatrix} 20.41 & -18.54 \\ -40.57 & 33.85 \end{bmatrix} \text{N/m}^2,$$

$$\Delta a_{1jk,01} = \begin{bmatrix} -0.33 & 0.30 \\ -0.29 & 0.22 \end{bmatrix} \text{N/m}^2, \quad \Delta a_{2jk,01} = \begin{bmatrix} 0.39 & -0.35 \\ -0.79 & 0.65 \end{bmatrix} \text{N/m}^2,$$

$$a_{1jk,1} = \begin{bmatrix} -12.76 & 4.82 \\ 4.79 & -2.56 \end{bmatrix} \text{kg/m}, \quad a_{2jk,1} = \begin{bmatrix} 4.79 & -2.56 \\ -18.70 & 6.02 \end{bmatrix} \text{kg/m},$$

$$a_{1jk,2} = \begin{bmatrix} -2.60 & -15.78 \\ 0.88 & 4.83 \end{bmatrix} \text{kg/m}, \quad a_{2jk,2} = \begin{bmatrix} 0.88 & 4.83 \\ -3.95 & -25.05 \end{bmatrix} \text{kg/m},$$

$$d_{11kl} = \begin{bmatrix} 15.65 & -13.28 \\ -11.54 & 15.37 \end{bmatrix} \text{N/m}^3, \quad d_{12kl} = \begin{bmatrix} -3.33 & 48.90 \\ 8.21 & -29.02 \end{bmatrix} \text{N/m}^3,$$

$$d_{21kl} = \begin{bmatrix} -9.38 & 33.76 \\ 12.12 & -31.91 \end{bmatrix} \text{N/m}^3, \quad d_{22kl} = \begin{bmatrix} 26.60 & -49.99 \\ -5.15 & 110.58 \end{bmatrix} \text{N/m}^3,$$

$$g_{11kl} = \begin{bmatrix} 0.46 & -0.20 \\ -0.20 & 0.64 \end{bmatrix} \text{kg/m}^2, \quad g_{12kl} = \begin{bmatrix} -0.20 & 0.11 \\ 0.11 & -0.25 \end{bmatrix} \text{kg/m}^2,$$

$$g_{21kl} = g_{12kl}, \quad g_{22kl} = \begin{bmatrix} 0.64 & -0.26 \\ -0.26 & 0.93 \end{bmatrix} \text{kg/m}^2. \tag{2.78}$$

The numerical results will be given in terms of the root-mean-square values of the modal coordinates q_1 and q_2 with the mean values subtracted. The resulting quantities are denoted as Q_1 and Q_2, respectively.

Figure 2.12 shows Q_1 and Q_2 as functions of the excitation frequency ω_0 found by numerical integration of the modal differential equations of motion with $\zeta_1 = \zeta_2 = 0.01$, $u_0 = 0.3$ m and $\Omega_0 = 1.6$ s^{-1}, using a Runge-Kutta fourth order algorithm with the time steps $\Delta t = 0.002\frac{2\pi}{\omega_0}$. The full line indicates results obtained by the total system given in (2.67) and (2.68). The dashed line is the corresponding result achieved when the cubic coupling coefficients d_{i122}, d_{i212}, d_{i221}, d_{i222}, g_{i112}, g_{i121}, g_{i122}, g_{i212}, g_{i221}, g_{i222} are set equal to zero together with the quadratic coupling coefficients a_{i22} and b_{i22}. The correspondingly reduced modal differential equations are given by (2.79). As seen, the response curve does not change significantly when

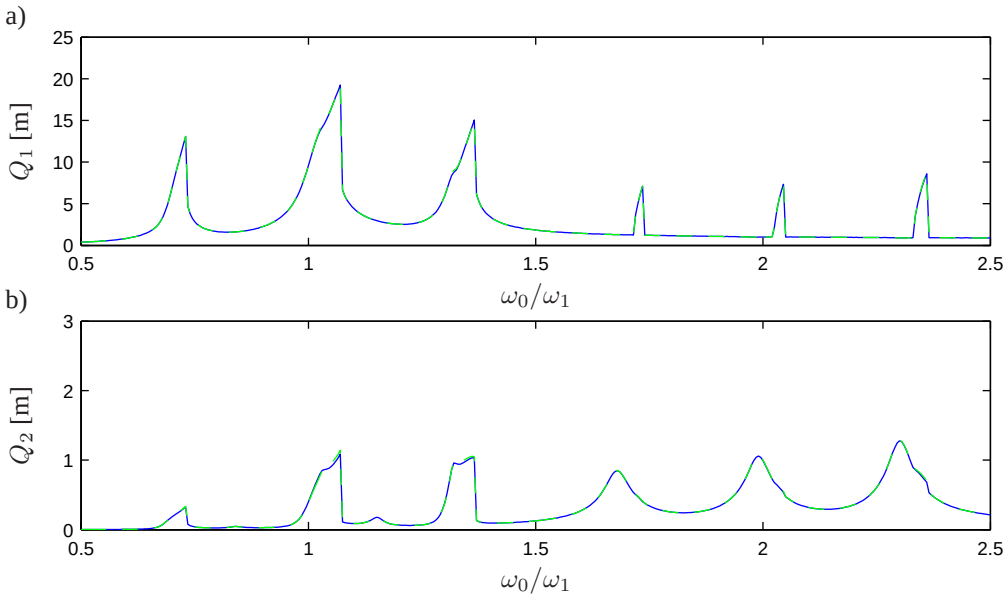

Figure 2.12 Comparison of modal coordinates determined from the full and reduced model. $\zeta_1 = \zeta_2 = 0.01$, $u_0 = 0.30$ m, $\Omega_0 = 1.6$ s^{-1}, $\omega_2/\omega_1 = 2$. (———) Full model (2.67), (2.68). (– – –) Reduced model (2.79). a) $Q_1(\omega_0)$. b) $Q_2(\omega_0)$.

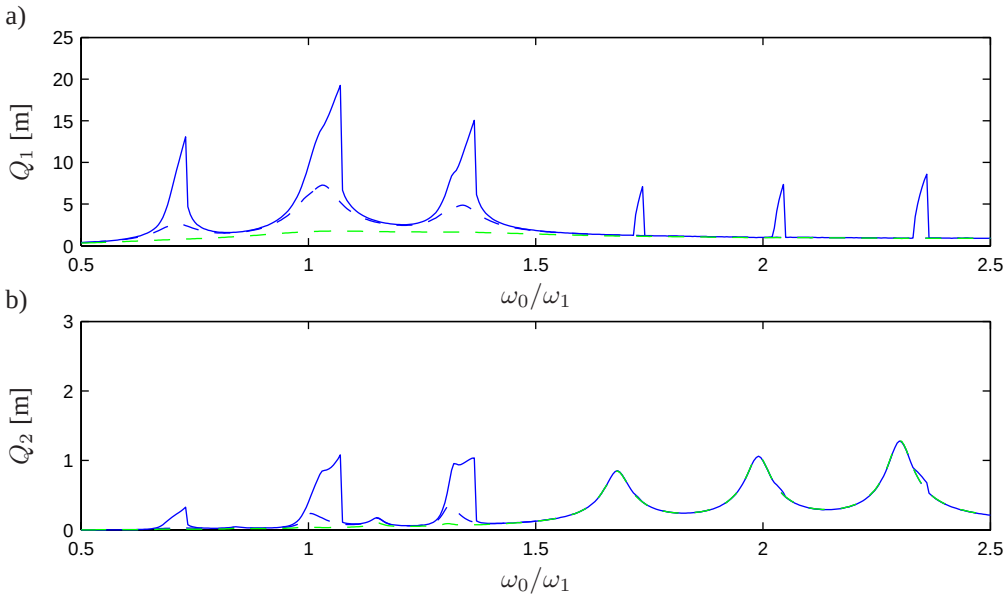

Figure 2.13 Modal coordinates at various values of ζ_1. $u_0 = 0.30$ m, $\Omega_0 = 1.6$ s^{-1}, $\omega_2/\omega_1 = 2$. (———) $\zeta_1 = 0.01$. (– – –) $\zeta_1 = 0.05$. (– – –) $\zeta_1 = 0.2$. a) $Q_1(\omega_0)$. b) $Q_2(\omega_0)$.

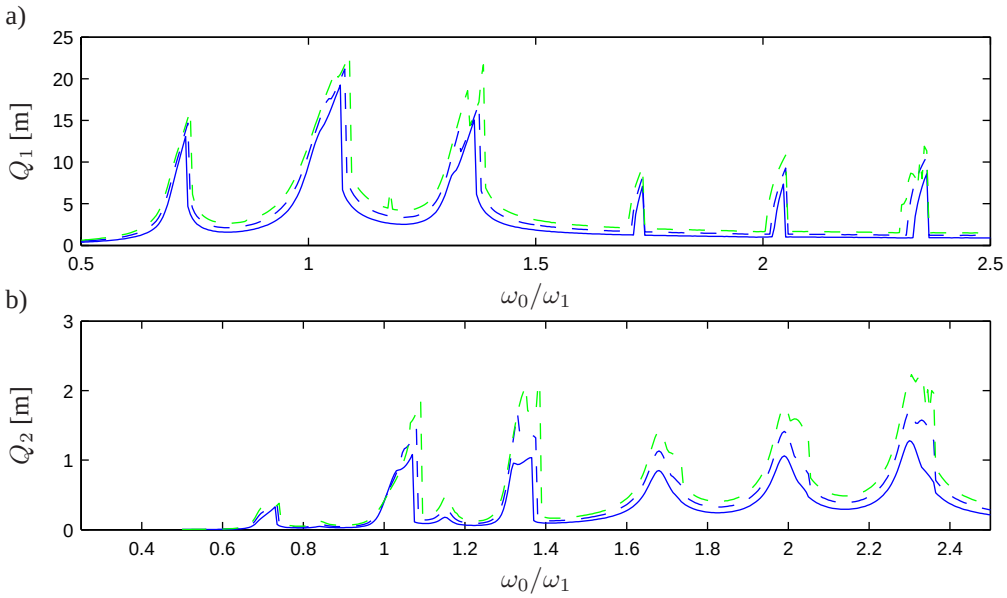

Figure 2.14 Modal coordinates at various values of u_0. $\zeta_1 = \zeta_2 = 0.01$, $\Omega_0 = 1.6$ s^{-1}, $\omega_2/\omega_1 = 2$. (——) $u_0 = 0.3$ m. (– –) $u_0 = 0.4$ m. (– –) $u_0 = 0.5$ m. a) $Q_1(\omega_0)$. b) $Q_2(\omega_0)$.

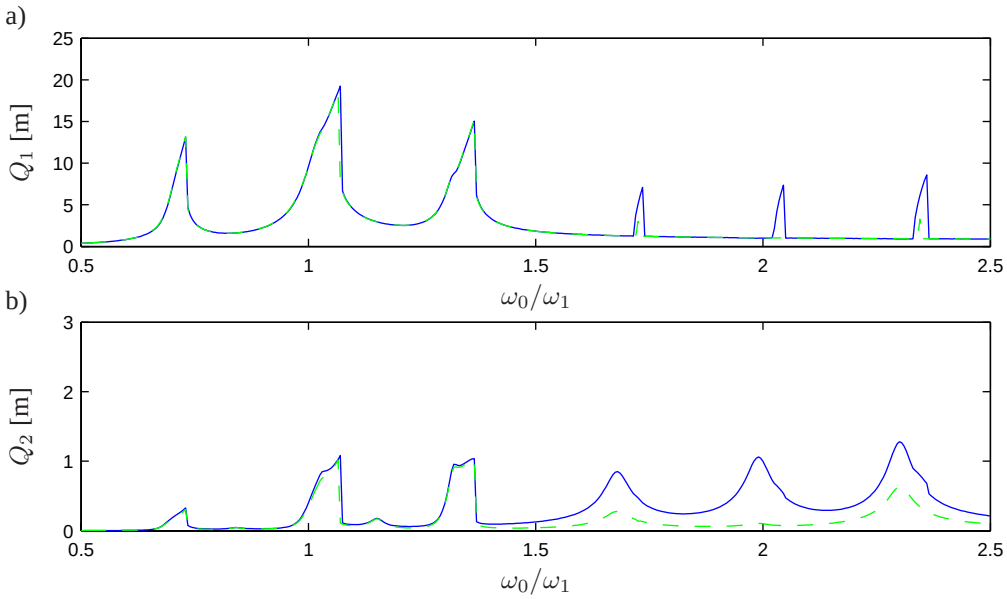

Figure 2.15 Comparison of modal coordinates determined from the reduced model with and without contribution from f_2. $u_0 = 0.30$ m, $\zeta_1 = \zeta_2 = 0.01$, $\Omega_0 = 1.6$ s^{-1}, $\omega_2/\omega_1 = 2$. (——) $f_2 \neq 0$. (– –) $f_2 = 0$. a) $Q_1(\omega_0)$. b) $Q_2(\omega_0)$.

the system is reduced as indicated. Keeping the terms in (2.67) and (2.68), which influence the frequency response curve and the stability region qualitatively and quantitatively, the reduced equations of motion become

$$
\begin{aligned}
&M_1\big(\ddot{q}_1+2\zeta_1\omega_1\dot{q}_1+\omega_1^2 q_1\big)+c_{12}(t)\dot{q}_2+k_{11}(t)q_1+k_{12}(t)q_2+a_{111}(t)q_1^2+\big(a_{112}(t)+a_{121}(t)\big)q_1q_2\\
&\quad+b_{111}(t)q_1\dot{q}_1+b_{112}(t)q_1\dot{q}_2+b_{121}(t)q_2\dot{q}_1+d_{1111}q_1^3+\big(d_{1112}+d_{1121}+d_{1211}\big)q_1^2q_2\\
&\quad+g_{1111}\big(q_1\dot{q}_1^2+q_1^2\ddot{q}_1\big)+g_{1211}\big(q_2\dot{q}_1^2+q_1q_2\ddot{q}_1\big)=f_1(t),\\
&M_2\big(\ddot{q}_2+2\zeta_2\omega_2\dot{q}_2+\omega_2^2 q_2\big)+c_{21}(t)\dot{q}_1+k_{21}(t)q_1+k_{22}(t)q_2+a_{211}(t)q_1^2+\big(a_{212}(t)+a_{221}(t)\big)q_1q_2\\
&\quad+b_{211}(t)q_1\dot{q}_1+b_{212}(t)q_1\dot{q}_2+b_{221}(t)q_2\dot{q}_1+d_{2111}q_1^3+\big(d_{2112}+d_{2121}+d_{2211}\big)q_1^2q_2\\
&\quad+g_{2111}\big(q_1\dot{q}_1^2+q_1^2\ddot{q}_1\big)+g_{2211}\big(q_2\dot{q}_1^2+q_1q_2\ddot{q}_1\big)=f_2(t).
\end{aligned}
\tag{2.79}
$$

Six main resonance peaks are present in the frequency response curve of both Q_1 and Q_2. They are located at $\omega_0/\omega_1 \simeq 0.66, 1.0, 1.33, 1.66, 2.0$ and 2.33. Further, two minor peaks appear in Q_2 at $\omega_0/\omega_1 = 0.83$ and 1.16. Especially, at high amplitude excitation the peaks become doubled peaked, see Figure 2.14.

Figure 2.13 shows the response for the reduced system for various values of ζ_1 modelling the variable aeroelastic damping in the blade direction. It is seen that for the edgewise component only resonance peaks at frequencies in the region $\omega_0/\omega_1 < 1.4$ is effected by changes in ζ_1. Hence, resonance in this region of the edgewise component is primarily due to coupling terms. In the blade component all resonance peaks are influenced by changes in ζ_1.

Figure 2.14 shows the corresponding frequency response curve at various values of the amplitude u_0 of the support point motion. For the blade component an increase of u_0 only introduces minor increases of the resonance peaks at $\omega_0/\omega_1 \simeq 0.66, 1.0$ and 1.66 and the increase in response of the remaining peaks are relatively small. The relative increase in the edgewise response is more significant for all peaks except for $\omega_0/\omega_1 \simeq 0.66$. Hence, the edgewise component is mainly excited by the support point motion, while the aerodynamic loading primarily excites the blade component.

Finally, the relative influence of the additive loading $f_2(t)$ and the nonlinear interactions from the blade mode on the response in the edgewise direction have been illustrated in Figure 2.15. As seen, the additive load term $f_2(t)$ does not change the resonance peaks in Q_2 for $\omega_0/\omega_1 < 1.4$. However, a significant decrease in the peaks at $\omega_0/\omega_1 > 1.4$ is observed. This supports the argument that the resonance peaks in Q_2 at low frequencies originate mainly from the coupling terms, while both the additive and parametric excitation contribute to the resonance peaks at $\omega_0/\omega_1 > 1.4$.

The additive load term $f_1(t)$ is partly responsible for the resonance peaks $\omega_0/\omega_1 = 0.66, 1.0$ and 1.33 in Q_1 while resonance in Q_1 at $\omega_0/\omega_1 > 1.4$ mainly is due to nonlinear coupling terms.

The parametric linear terms $c_{ij}(t)$ and $k_{ij}(t)$ introduce a decrease of resonance frequencies for the peaks at $\omega_0/\omega_1 = 1.66, 2.0$ and 2.33 in Q_2.

The parametric quadratic terms defined by $a_{i11}(t)$ and $b_{i11}(t)$ mainly stabilize the resonance peak at $\omega_0/\omega_1 \simeq 1.0$, but also a stabilizing influence at $\omega_0/\omega_1 = 1.66, 2.0$ and 2.33 is observed. Only minor changes are observed when disregarding the terms $a_{i12}(t), a_{i21}(t)$ and $b_{i21}(t)$, however, $b_{i12}(t)$ accounts for the coupling peaks in Q_1 at $\omega_0/\omega_1 = 1.66, 2.0$ and 2.33.

The cubic nonlinear terms have a significant stabilizing effect on all resonance peaks. If these terms are disregarded all resonance frequencies generate infinite response. However, when the cubic terms are included the peaks at $\omega_0/\omega_1 \simeq 0.66, 1.0$ and 1.33 curve a little to the right making the system stable. Furthermore, the cubic terms introduce an increase in the resonance frequency of Q_1 at $\omega_0/\omega_1 \simeq 1.66, 2.0$ and 2.33 so they do not coincide precisely with the corresponding resonance frequencies of Q_2. This shift in frequencies also makes the high frequency peaks stable.

The terms defined by coefficients d_{i111} and g_{i111} straighten the peaks for $\omega_0/\omega_1 < 1.4$. Looking at Figure 5.11 showing the frequency response of a shallow cable, several solution exists for a given excitation frequency. The same behaviour is observed if the terms involving d_{i111} and g_{i111} are disregarded. Also, a considerable damping is introduced via the mentioned cubic terms within the peaks at $\omega_0/\omega_1 > 1.4$. The cubic terms defined by d_{i112}, d_{i121} and d_{i211} have a significant stabilizing effect on the peaks at $\omega_0/\omega_1 = 1.0$ and 1.33. In case the cubic terms defined by d_{i112}, d_{i121} and d_{i211} are disregarded, instability occurs at $\omega_0/\omega_1 = 1.0, 1.33, 1.66,$ and 2.0 for $u_0 = 0.24$ m, 0.62 m, 0.98 m and 0.92 m, respectively. The remaining peaks stay stable at increasing u_0. When the mentioned cubic terms are included, all peaks become stable at increasing u_0. The cubic terms defined by g_{i211} only cause minor changes of the frequency response. If a wish exists to further reduce the equations of motion the parametric quadratic terms, defined by a_{i112}, a_{i121} and b_{i121}, together with the cubic terms g_{1211}, may be disregarded without major influence on the frequency response and stability.

2.1.8 Concluding remarks

A nonlinear two-degrees-of-freedom model modelling the nonlinear interactions between the fundamental blade and edgewise modes has been devised, retaining nonlinear terms up to cubic order. The model includes inertial nonlinearities from support point motions and geometrical nonlinearities from a nonlinear description of the curvature, and rotation of the aerodynamic loads caused by the deflection of the beam. Assuming a harmonic variation from the support point causing primarily quasi-static displacements in the blade direction, the important nonlinear couplings are identified, and a somewhat reduced system is indicated, retaining all terms of importance for the quantitative and qualitative behaviour of the system.

The numerical analysis focuses on the often met frequency ratio of $\omega_2/\omega_1 \simeq 2$, in which case 2:1 internal resonance may be induced in the edgewise mode by the blade mode via quadratic nonlinearities. It is demonstrated that significant resonances may occur at excitation frequencies fulfilling $\omega_0/\omega_1 \simeq 0.66, 1.33, 1.66$ and 2.33 in addition to the resonances at $\omega_0/\omega_1 \simeq 1.0$ and $\omega_0/\omega_2 \simeq 1.0$ partly caused by the additive loading.

At the resonance peaks $\omega_0/\omega_1 \simeq 1.0, 1.33, 1.66$ and 2.0 the system may render into parametric instability, dependent on the excitation amplitude u_0 and level of modal damping if the cubic terms are disregarded. If the cubic terms are included all resonance frequencies produce stable response.

It should be noticed that the dominating tower frequency in proportion to the blade frequency normally is placed in the interval $\omega_0/\omega_1 \in [0.5, 1.5]$.

2.2 Parametric Stability of Wind Turbine Wings

Nonlinear rotor dynamic is characterized by parametric excitation of both linear and nonlinear terms caused by centrifugal and Coriolis forces when formulated in a moving frame of reference in combination with the translational and rotational support point motions of the hub. Specific for wind turbine wings is that the parametric excitation is controlled by four different frequencies. Firstly, the wing is rotating with the circular frequency Ω_0, the so-called rotational speed, which causes both parametric and additive excitation of the wing. The tower is performing narrowbanded vibrations with a central circular frequency ω_0, which causes corresponding support point motions and rotations of the hub. For a three-bladed wind turbine ω_0 is close to $3\Omega_0$ due to the changes in wind load when the individual wings are in top and bottom position of the incoming shear wind field. Finally, nonlinear interactions and related parametric instability depends on the ratio between the fundamental fixed base circular eigenfrequencies ω_1 and ω_2 in the blade and edgewise directions. For larger wind turbine wings the frequency ratio $\omega_2/\omega_1 \simeq 2$ is often met.

Stability of motions may be studied by a variety of techniques. A quantitatively stability analysis of nonlinear systems may be performed by various perturbation methods, see e.g. (Nayfeh 2000). For nonlinear systems, which experience periodic response, the stability may be analysed by the Floquet theory (Nayfeh and Mook 1995). Nonlinear systems may experience almost periodic or even chaotic response. Under such conditions the Floquet theory is no longer applicable. To investigate the stability of such cases techniques based on a Lyapunov exponent may be used. Wolf *et al.* (1984) presented an algorithm for determining the entire spectrum of Lyapunov exponents from a time series of displacements components by means of the Gram-Schmidt reorthonormalization procedure. Also algorithms for finding only the largest Lyapunov exponent or the two largest Lyapunov exponents were devised. The procedures described by Wolf *et al.* are widely used in the literature.

Several extensive investigations on the onset of chaotic motions of the Duffing oscillator have been performed based on these algorithm, see e.g. (Moon 1987; Thomsen 1997). To and Liu (1996) investigated the chaotic behaviour of the Duffing oscillator both under deterministic, stochastic and combined deterministic and stochastic excitation by means of an averaged Lyapunov exponent and information dimension. Castanier and Pierre (1995) analysed wave propagation and localization phenomena in multi-coupled systems using both the algorithm by Wolf *et al.* and a perturbation technique for finding the first Lyapunov exponent. Comparison of the said methods and Monte Carlo analysis was made, and good agreement was demonstrated in several cases. Shin and Hammond (1998) showed that the conventional Lyapunov exponent is very useful for quantification of chaotic dynamics, but only represents the average long term behaviour. They introduced so-called instantaneous Lyapunov exponents for describing the local non-stationary behaviour of the system. Numerical examples were given for the Van der Pol and Duffing oscillators, where changes in damping were detected efficiently. The theory was also used to determine changes in damping properties of an experimental system.

Parametric excitation due to support point motion of nonlinear systems are also widely investigated in the literature. Ge and Tsen (2001) analysed the dynamic behaviour of a two-degrees-of-freedom rigid body with vibrating support. The Lyapunov direct method was used to determine the stability conditions, and various algorithms were used to effectively control the chaotic behaviour. In the same manner Ge and Shiue (2002) analysed the dynamic stability of a tachometer subjected to vertical harmonic support vibrations. In a series of papers Dwivedy and

Kar (1999a, 1999b, 1999c, 2001, 2003) investigated the parametric stability of a base excited cantilever beam with an attached mass retaining up to cubic nonlinearities. They analysed the steady state, periodic and chaotic response under parametric and internal resonances by the methods of multiple scales and normal forms. Nayfeh (1983b) analysed a two-degrees-of-freedom nonlinear system with quadratic nonlinearities subjected to parametric excitation, and a multi-degrees-of-freedom system under parametric excitation in (Nayfeh 1983a). Hanagud and Sarkar (1989) analysed a cantilever beam attached to a moving support. The formulation was shown to be valid for large displacements, and the stability characteristics of a beam under spin-up maneuver was studied. It was demonstrated that structural nonlinearities play a major role in the response characteristics.

This section deals with the onset of chaotic behaviour and parametric instability of nonlinear vibrations of wind turbine wings. The analyses are made for the reduced nonlinear system in (2.79), and the numerical examples presented in this section are carried out for a 46 m wing with properties as described in section 2.1.7. In the study the amplitude and frequency of the support point motion and the rotational speed are varied, along with the eigenfrequency ratio ω_2/ω_1 and the damping ratio ζ_1 of the blade mode. The damping ratio may vary significantly dependent on the boundary layer flow over the profile is attached or separated. The latter case occurs during large oscillations (dynamic stall), with the implication that the significant aerodynamic damping is lost. When the ratio between the tower frequency and rotational frequency is rational the response becomes periodic and stability of the solution at certain parameter values may be evaluated using Floquet theory. If the response becomes chaotic or almost periodic due to irrational excitation frequency ratios, this is no longer applicable. Instead the stability may be evaluated using the Lyapunov coefficient. Since the Floquet theory only is applicable in small regions of the investigated parameter space, the Lyapunov exponent approach, as given by Wolf *et al.* will be used to determine stability of the system throughout this study. The algorithm is given in Appendix B.

2.2.1 Harmonic response analysis

In the following the support point motion is assumed to vary harmonically with amplitude u_0 and circular frequency ω_0 as

$$u(t) = u_0 \cos \omega_0 t \tag{2.80}$$

Hence, the excitation period is $T_0 = 2\pi/\omega_0$. Initially, the eigenfrequency ratio $\omega_2/\omega_1 = 2$ is assumed, and the excitation frequency is specified as $\omega_0/\Omega_0 = 3$. Then, as seen from (2.69) the modal loads $f_1(t)$ and $f_2(t)$ contain harmonic components with the circular frequencies $m\Omega_0$, $m = 1, \ldots, 4$. At first, the equations (2.79) are considered when only the constant linear terms on the left-hand sides are retained, ignoring all linear parametric, quadratic parametric and cubic terms. The corresponding solution may be considered a 0th order solution in a perturbation approach, where the linear parametric terms, quadratic parametric terms and cubic terms represent various 1st order perturbations, which are independently investigated below. The circular frequencies $m\Omega_0 = m/3\omega_0$, $m = 1, \ldots, 4$, in the additive excitation terms will also be present in the 0th order solution. When any of these frequencies are equal to ω_1 or $\omega_2 = 2\omega_1$ resonance appear in the first and second modes. This happens for the excitation frequency ratios $\omega_0/\omega_1 = 3/m$ and $\omega_0/\omega_1 = 6/m$, respectively, as shown by the dashed curve on the frequency

response curve in Figure 2.16a. In the plots Q_1 and Q_2 signify the RMS value of $q_1(t)$ and $q_2(t)$ when averaged over one vibration period T.

The linear parametric coefficients $c_{ij}(t)$ and $k_{ij}(t)$ contain harmonic components with the circular frequencies $2\Omega_0$ and $4\Omega_0$. In combination with the harmonic components of the 0th order solution the linear parametric terms will contain harmonics at the circular frequencies $m\Omega_0 = m/3\Omega_0$, $m = 1, \ldots, 8$. When transferred to the right-hand side these terms may induce resonance at $\omega_0/\omega_1 = 3/m$ and $\omega_0/\omega_1 = 6/m$, $m = 1, \ldots, 8$ in the blade and edgewise modes, respectively. Hence, the resonance peaks for $m = 2, 3, 4$, present in the linear response, are influenced by the linear parametric excitation as well. However, as seen by the unbroken curve on Figure 2.16a the influence of the linear parametric terms is insignificant in the blade mode, whereas the effect in the edgewise mode merely is to reduce the resonance frequencies and introduces weak coupling between the considered modes.

The quadratic parametric coefficients $a_{ijk}(t)$ and $b_{ijk}(t)$ contain harmonic components with the frequencies $1\Omega_0$, $2\Omega_0$ and $4\Omega_0$. In combination with the harmonic components of the 0th order solution the quadratic nonlinear terms will contain harmonics at the frequencies $m\Omega_0 = m/3\omega_0$, $m = 1, \ldots, 12$. When transferred to the right hand side these terms may induce resonance at $\omega_0/\omega_1 = 3/m$ and $\omega_0/\omega_1 = 6/m$, $m = 1, \ldots, 12$. In Figure 2.16b it is seen that the resonance peaks for $m = 2, 3, 4$ become unstable in the blade mode when quadratic nonlinear terms are included, which means that these terms introduce parametric instability. In the edgewise mode resonance peaks are visible for $\omega_0/\omega_1 = 3/4$ and $\omega_0/\omega_1 = 1$ corresponding to $m = 4, 6$. Additionally, chaotic behaviour of the system occurs for $\omega_0/\omega_1 > 2$, corresponding to $\omega_0 > \omega_2$, which is not brought forward by the linear parametric terms.

The cubic 0th order solutions terms contain harmonics at the frequencies $m\Omega_0 = m/3\omega_0$, $m = 1, \ldots, 12$. When transferred to the right hand side these terms may induce resonance at $\omega_0/\omega_1 = 3/m$ and $\omega_0/\omega_1 = 6/m$, $m = 1, \ldots, 12$, as was the case for the quadratic parametric terms. In Figure 2.16c it is seen that the cubic terms influence the blade mode by curving the resonance peaks to the right. In the edgewise mode extra resonance peaks occur for $\omega_0/\omega_1 \simeq 3/4$ and $\omega_0/\omega_1 \simeq 1.0$ corresponding to $m = 4, 6$, as was the case for the quadratic parametric terms.

Finally, in Figure 2.16d the full model is compared with the linear response. Due to both the quadratic parametric terms and the cubic terms the response becomes chaotic for $\omega_0/\omega_1 > 1.5$. Comparison of Figure 2.16d, 2.16b and 2.16c indicates that the response in the region $\omega_0/\omega_1 > 1.5$ is mainly influenced by the quadratic parametric terms, while at $\omega_0/\omega_1 < 1.5$ the cubic terms are the main source for changes compared to the 0th order solution.

When $\omega_0/\Omega_0 \neq 3$ it turns out that the vibration period is determined from the interference of the response caused by the circular frequencies $\omega_0 + \Omega_0$ and $\omega_0 - \Omega_0$. The corresponding periods become

$$T^+ = \frac{2\pi}{\omega_0 + \Omega_0} = \frac{T_0}{1 + \frac{\Omega_0}{\omega_0}}, \quad T^- = \frac{2\pi}{\omega_0 - \Omega_0} = \frac{T_0}{1 - \frac{\Omega_0}{\omega_0}}. \tag{2.81}$$

In order to find the combined period of the response T the following ratios are evaluated

$$\frac{T}{T^+} = n\left(1 + \frac{m\Omega_0}{\omega_0}\right), \quad \frac{T}{T^-} = n\left(1 - \frac{m\Omega_0}{\omega_0}\right), \tag{2.82}$$

The factor n is found as the minimum value at which both T/T^+ and T/T^- attain integer values. Poincaré maps of 2000 excitation periods are plotted in Figure 2.17 for various ratios of

ω_0/Ω_0. The amplitude is $u_0 = 0.3$ m, the damping ratios $\zeta_1 = \zeta_2 = 0.01$ and the frequency ratio $\omega_0/\omega_1 = 0.8$. ($\circ$) indicates the phase value $(q_1, \dot{q}_1)$ for every excitation period T_0, and ($\times$) indicates the phase value at every response period T. As seen the period tends towards infinity as ω_0/Ω_0 becomes irrational. As an example $\omega_0/\Omega_0 = 3.14159$ results in $n = 314159$. For an irrational frequency ratio a so-called almost periodic response is achieved in which case a continuous closed curve is obtained in the phase plane for the Poincaré map. As seen from Figure 2.17 the amplitude of $q_1(t)$ increases as ω_0/Ω_0 is increased. The reason is that the fundamental blade circular eigenfrequency for the considered example is given as $\omega_1/\Omega_0 = 3.2125$. Hence, the simulations tends towards resonance in the fundamental eigenmode as ω_0/Ω_0 is increased.

2.2.2 Variational equations

In order to investigate the stability of a given motion $q_{i,0}(t)$, consider the following perturbed motion assumed to fulfill (2.79)

$$q_i(t) = q_{i,0}(t) + \Delta q_i(t). \tag{2.83}$$

where $\Delta q_i(t)$ is a small perturbation to the referential solution. Insertion of (2.83) in (2.79) and disregarding quadratic and cubic terms of $\Delta q_i(t)$ gives the following equations of motion for the perturbation $\Delta q_i(t)$

$$\begin{aligned}
&M_1\big(\Delta\ddot{q}_1 + 2\zeta_1\omega_1\Delta\dot{q}_1 + \omega_1^2\Delta q_1\big) + c_{12}(t)\Delta\dot{q}_2 + k_{11}(t)\Delta q_1 + k_{12}(t)\Delta q_2 \\
&\quad + 2a_{111}(t)q_{1,0}\Delta q_1 + \big(a_{112}(t) + a_{121}(t)\big)\big(q_{1,0}\Delta q_2 + q_{2,0}\Delta q_1\big) \\
&\quad + b_{111}(t)\big(q_{1,0}\Delta\dot{q}_1 + \dot{q}_{1,0}\Delta q_1\big) + b_{112}(t)\big(q_{1,0}\Delta\dot{q}_2 + \dot{q}_{2,0}\Delta q_1\big) \\
&\quad + b_{121}(t)\big(q_{2,0}\Delta\dot{q}_1 + \dot{q}_{1,0}\Delta q_2\big) + 3d_{1111}q_{1,0}^2\Delta q_1 \\
&\quad + \big(d_{1112} + d_{1121} + d_{1211}\big)\big(2q_{1,0}q_{2,0}\Delta q_1 + q_{1,0}^2\Delta q_2\big) \\
&\quad + g_{1111}\big(2\dot{q}_{1,0}q_{1,0}\Delta\dot{q}_1 + \dot{q}_{1,0}^2\Delta q_1 + 2\ddot{q}_{1,0}q_{1,0}\Delta q_1 + q_{1,0}^2\Delta\ddot{q}_1\big) \\
&\quad + g_{1211}\big(2\dot{q}_{1,0}q_{2,0}\Delta\dot{q}_1 + \dot{q}_{1,0}^2\Delta q_2 + \ddot{q}_{1,0}q_{2,0}\Delta q_1 + q_{1,0}\ddot{q}_{1,0}\Delta q_2 + q_{1,0}q_{2,0}\Delta\ddot{q}_1\big) = 0,
\end{aligned} \tag{2.84}$$

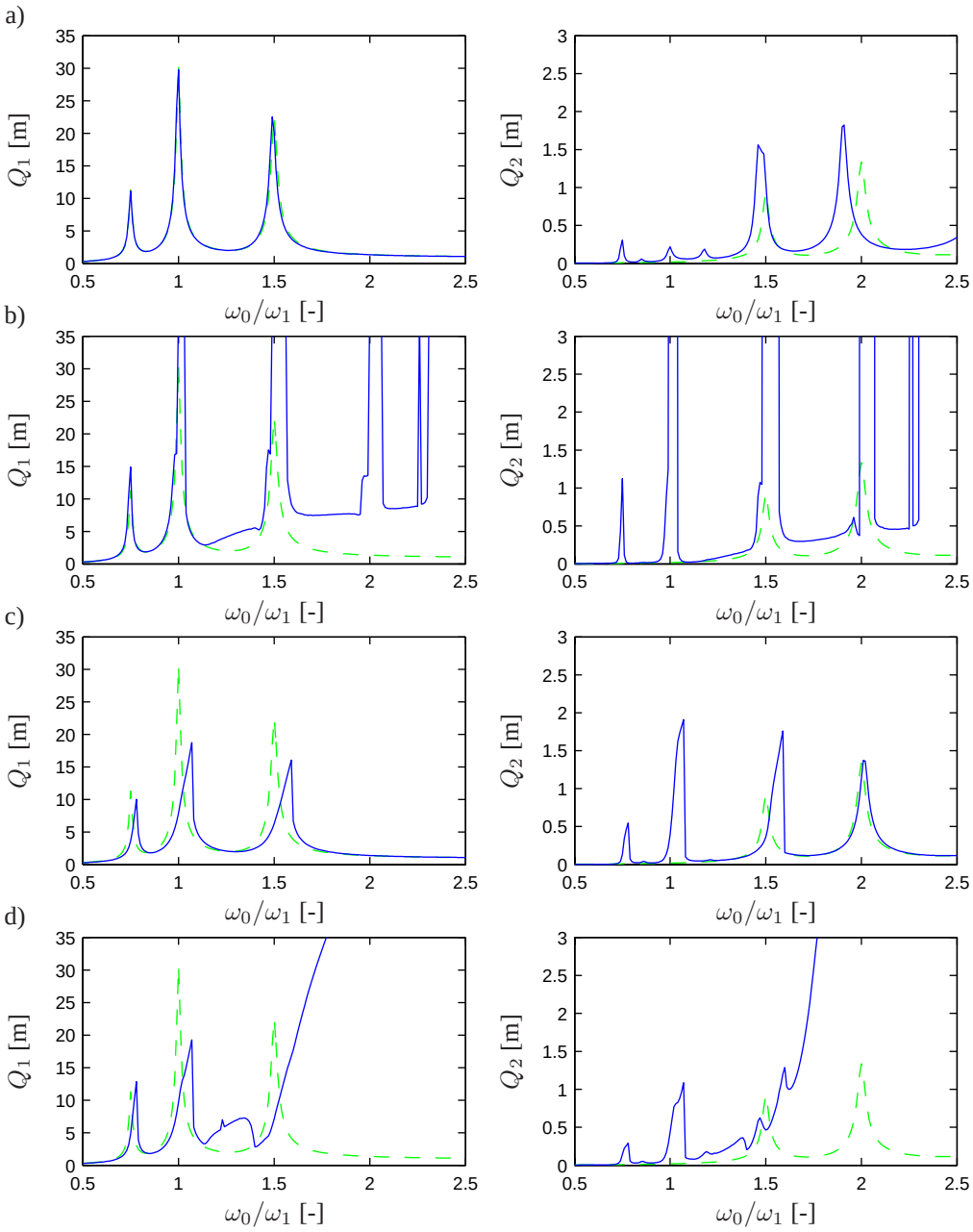

Figure 2.16 Influence of linear parametric, quadratic parametric and cubic terms, $v_0 = 0.3$ m, $\zeta_1 = \zeta_2 = 0.01$, $\omega_0/\Omega_0 = 3.0, \omega_2/\omega_1 = 2.0$. (– –) 0th order solution. a) (———) 0th order solution in combination with the linear parametric terms. b) (———) 0th order solution in combination with the quadratic parametric terms. c) (———) 0th order solution in combination with the cubic parametric terms. d) (———) the full model.

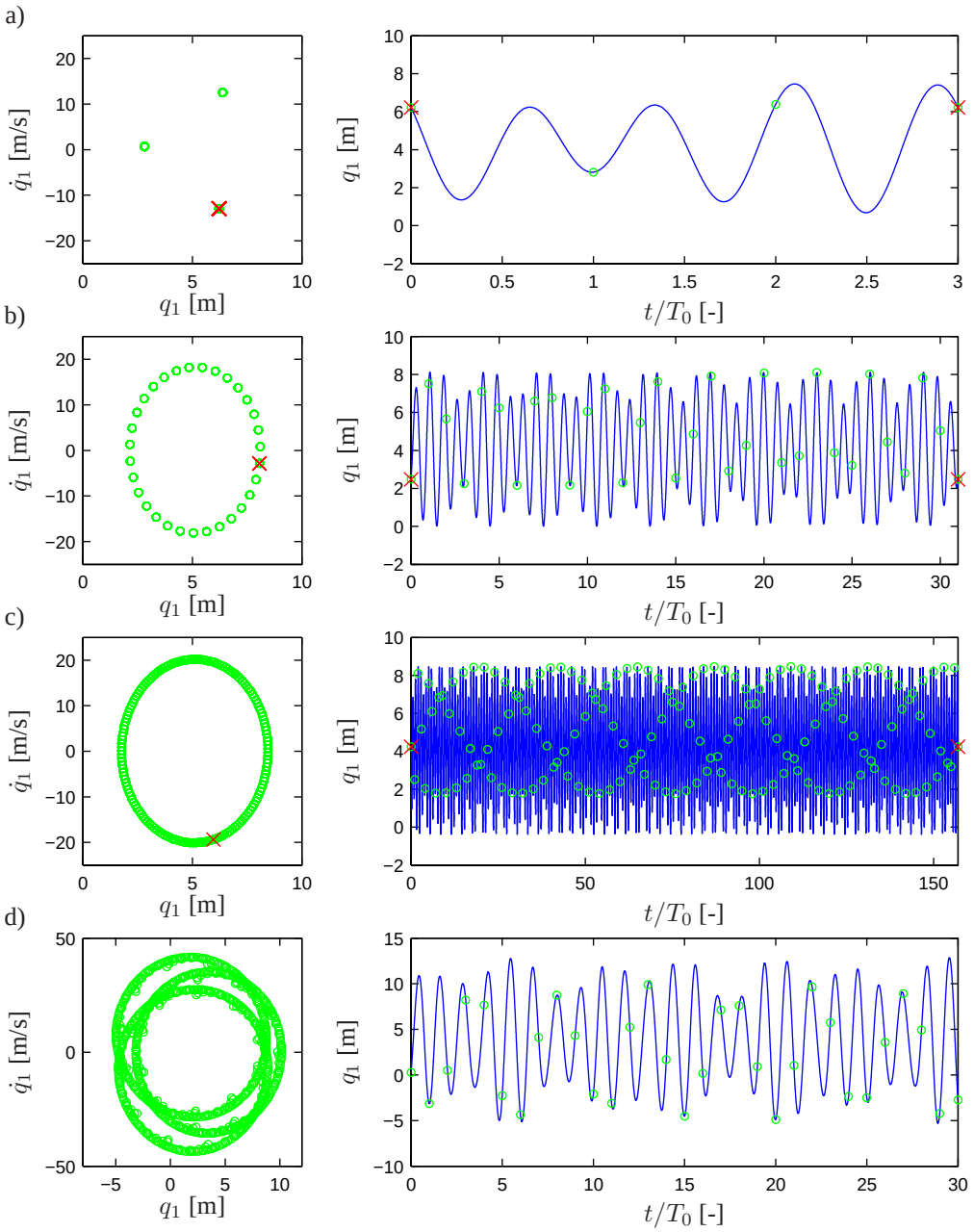

Figure 2.17 Poincaré map at various excitations frequency ratios and the corresponding time series of $q_1(t)$ shown for one response period T. $u_0 = 0.3$ m, $\zeta_1 = \zeta_2 = 0.01$, $\omega_2/\omega_1 = 2.0$, $\omega_0/\omega_1 = 0.8$. a) $\omega_0/\Omega_0 = 3$, $n = 3$. b) $\omega_0/\Omega_0 = 3.1$, $n = 31$. c) $\omega_0/\Omega_0 = 3.14$, $n = 157$. d) Chaotic response, $\omega_0/\Omega_0 = 3$, $\omega_0/\omega_1 = 2.3$.

$$
\begin{aligned}
&M_2\big(\Delta\ddot{q}_2 + 2\zeta_2\omega_2\Delta\dot{q}_2 + \omega_2^2\Delta q_2\big) + c_{21}(t)\Delta\dot{q}_1 + k_{21}(t)\Delta q_1 + k_{22}(t)\Delta q_2\\
&\quad + 2a_{211}(t)q_{1,0}\Delta q_1 + \big(a_{212}(t) + a_{221}(t)\big)\big(q_{1,0}\Delta q_2 + q_{2,0}\Delta q_1\big)\\
&\quad + b_{211}(t)\big(q_{1,0}\Delta\dot{q}_1 + \dot{q}_{1,0}\Delta q_1\big) + b_{212}(t)\big(q_{1,0}\Delta\dot{q}_2 + \dot{q}_{2,0}\Delta q_1\big)\\
&\quad + b_{221}(t)\big(q_{2,0}\Delta\dot{q}_1 + \dot{q}_{1,0}\Delta q_2\big) + 3d_{2111}q_{1,0}^2\Delta q_1\\
&\quad + \big(d_{2112} + d_{2121} + d_{2211}\big)\big(2q_{1,0}q_{2,0}\Delta q_1 + q_{1,0}^2\Delta q_2\big)\\
&\quad + g_{2111}\big(2\dot{q}_{1,0}q_{1,0}\Delta\dot{q}_1 + \dot{q}_{1,0}^2\Delta q_1 + 2\ddot{q}_{1,0}q_{1,0}\Delta q_1 + q_{1,0}^2\Delta\ddot{q}_1\big)\\
&\quad + g_{2211}\big(2\dot{q}_{1,0}q_{2,0}\Delta\dot{q}_1 + \dot{q}_{1,0}^2\Delta q_2 + \ddot{q}_{1,0}q_{2,0}\Delta q_1 + q_{1,0}\ddot{q}_{1,0}\Delta q_2 + q_{1,0}q_{2,0}\Delta\ddot{q}_1\big) = 0.
\end{aligned}
\tag{2.85}
$$

The variational equations (2.84) and (2.85) may be recast into the following state vector formulation

$$
\begin{aligned}
&\dot{\mathbf{v}}(t) = \mathbf{A}(t)\mathbf{v}(t),\\
&\mathbf{v}(t) = [\Delta q_1(t)\ \Delta q_2(t)\ \Delta\dot{q}_1(t)\ \Delta\dot{q}_2(t)]^T,\quad \mathbf{A}(t) = \begin{bmatrix}\mathbf{I} & \mathbf{0}\\ \mathbf{0} & \mathbf{M}(t)\end{bmatrix}^{-1}\begin{bmatrix}\mathbf{0} & \mathbf{I}\\ -\mathbf{K}(t) & -\mathbf{C}(t)\end{bmatrix},
\end{aligned}
\tag{2.86}
$$

where the components of $\mathbf{K}(t)$, $\mathbf{C}(t)$ and $\mathbf{M}(t)$ are given as

$$
\begin{aligned}
K_{11}(t) &= M_1\omega_1^2 + k_{11} + 2a_{111}q_{1,0} + \big(a_{112} + a_{121}\big)q_{2,0} + b_{111}\dot{q}_{1,0} + b_{112}\dot{q}_{2,0} + 3d_{1111}q_{1,0}^2\\
&\quad + 2\big(d_{1112} + d_{1121} + d_{1211}\big)q_{1,0}q_{2,0} + g_{1111}\big(\dot{q}_{1,0}^2 + 2\ddot{q}_{1,0}q_{1,0}\big) + g_{1211}\ddot{q}_{1,0}q_{2,0},\\
K_{12}(t) &= k_{12} + \big(a_{112} + a_{121}\big)q_{1,0} + b_{121}\dot{q}_{1,0}\\
&\quad + \big(d_{1112} + d_{1121} + d_{1211}\big)q_{1,0}^2 + g_{1211}\big(\dot{q}_{1,0}^2 + q_{1,0}\ddot{q}_{1,0}\big),\\
K_{21}(t) &= k_{21} + 2a_{211}q_{1,0} + \big(a_{212} + a_{221}\big)q_{2,0} + b_{211}\dot{q}_{1,0} + b_{212}\dot{q}_{2,0} + 3d_{2111}q_{1,0}^2\\
&\quad + 2\big(d_{2112} + d_{2121} + d_{2211}\big)q_{1,0}q_{2,0} + g_{2111}\big(\dot{q}_{1,0}^2 + 2\ddot{q}_{1,0}q_{1,0}\big) + g_{2211}\ddot{q}_{1,0}q_{2,0},\\
K_{22}(t) &= M_2\omega_2^2 + k_{22} + \big(a_{212} + a_{221}\big)q_{1,0} + b_{221}\dot{q}_{1,0}\\
&\quad + \big(d_{2112} + d_{2121} + d_{2211}\big)q_{1,0}^2 + g_{2211}\big(\dot{q}_{1,0}^2 + q_{1,0}\ddot{q}_{1,0}\big),
\end{aligned}
\tag{2.87}
$$

$$
\begin{aligned}
C_{11}(t) &= 2M_1\zeta_1\omega_1 + b_{111}q_{1,0} + b_{121}q_{2,0} + 2g_{1111}\dot{q}_{1,0}q_{1,0} + 2g_{1211}\dot{q}_{1,0}q_{2,0},\\
C_{12}(t) &= c_{12} + b_{112}q_{1,0},\\
C_{21}(t) &= c_{21} + b_{211}q_{1,0} + b_{221}q_{2,0} + 2g_{2111}\dot{q}_{1,0}q_{1,0} + 2g_{2211}\dot{q}_{1,0}q_{2,0},\\
C_{22}(t) &= 2M_2\zeta_2\omega_2 + b_{212}q_{1,0},
\end{aligned}
\tag{2.88}
$$

$$M_{11}(t) = M_1 + g_{1111}q_{1,0}^2 + g_{1211}q_{1,0}q_{2,0},$$
$$M_{12} = 0,$$
$$M_{21}(t) = g_{2111}q_{1,0}^2 + g_{2211}q_{1,0}q_{2,0},$$
$$M_{22} = M_2. \tag{2.89}$$

Solving (2.79) for $q_{1,0}(t)$ and $q_{2,0}(t)$, the time dependent components of $\mathbf{K}(t)$, $\mathbf{C}(t)$ and $\mathbf{M}(t)$ are found, and the linearized equations (2.84) and (2.85) may be solved. The stability of the system may then be evaluated by Floquet theory in case of periodic response (Nayfeh and Mook 1995) or by Lyapunov exponents as described by Wolf *et al.* (1984). Both methods are described in Appendix B.

2.2.3 Parametric stability analysis

In this section numerical analyses are carried out with independent variation of the frequency ratios ω_0/ω_1, ω_2/ω_1 and with ω_0/Ω_0 and $u_0 = 0.3$ m and 0.5 m. In light of the previous analysis showing the insufficiency of the Floquet theory, stability boundaries are found using Lyapunov exponents. In all the following analyses the circular eigenfrequency of the first mode is kept constant at $\omega_1 = 5.14$ rad/s. At the numerical integration (2.79) and (2.86) are solved simultaneously. The RMS values of the response Q_1 and Q_2 are determined using time series of 1000 excitation periods T_0. The numerical integration is performed by a 4th order Runge Kutta scheme with a time step $\Delta t = T_0/500$.

The first analysis is made with constant excitation ratio $\omega_0/\Omega_0 = 3.0$. The result is illustrated in Figure 2.18 in terms of contour curves of the various response quantities. Figure 2.18a-b show contour curves of Q_1 at 5, 10 and 20 m and Q_2 at 0.5, 2 and 4 m as functions of ω_0/ω_1 and ω_2/ω_1. In Figure 2.18c the contour curve at 0 is shown for the largest Lyapunov exponent, indicating areas where the solution is unstable. The blue regions indicate where chaotic response occur and red indicates regions with infinite response. Since ω_1 is kept constant and only ω_2 is varied in the fraction ω_2/ω_1, the positions of resonance peaks of the first mode are independent of ω_2/ω_1. Correspondingly, the positions of resonance peaks of the second mode vary linearly with ω_2/ω_1. In Figure 2.18a peaks are present at $\omega_0/\omega_1 \simeq 0.75$ and 1.0, which remain constant to variations in ω_2/ω_1, and hence represent resonance peaks of the first mode. At frequencies $\omega_0/\omega_1 > 1.1$ large regions of unstable response occur. The limit $\omega_0/\omega_1 = 1.1$ is relatively constant with variation of ω_2/ω_1. Within the region $\omega_0/\omega_1 > 1.1$ there exists two different areas divided by an almost constant line with respect to variation of ω_0/ω_1 located at $\omega_2/\omega_1 \simeq 2.2$. Below this limit the system produces infinite response in most part of the unstable region, while above the limit chaotic response exists in all unstable regions. Close to the boundary at $\omega_2/\omega_1 \simeq 2.2$ large regions of stable response exists even above $\omega_0/\omega_1 > 1.1$.

Figure 2.19a, 2.19b and 2.19c show contour curves for Q_1, Q_2 and λ with $u_0 = 0.3$ m, a constant eigenfrequency ratio $\omega_2/\omega_1 = 2.0$, and with variable excitation ratio ω_0/Ω_0. Looking at the figures from left to right it is seen that the primary resonance peaks located at $\omega_0/\omega_1 = 0.75$ and 1.0 are relatively unaffected by the excitation ratio. The combined peak at $\omega_0/\omega_1 = 1.5$ tends to divide into two peaks as ω_0/Ω_0 are varied from 3.0. Finally, the large unstable region to the far right is stabilized as the excitation ratio is increased, while the unstable region at $\omega_0/\omega_1 \simeq 1.25$ stablizes with increasing ω_0/Ω_0. It should be noted that all unstable regions produce chaotic response with $\omega_2/\omega_1 = 2.0$, except for a large region at the bottom right, which produces infinite

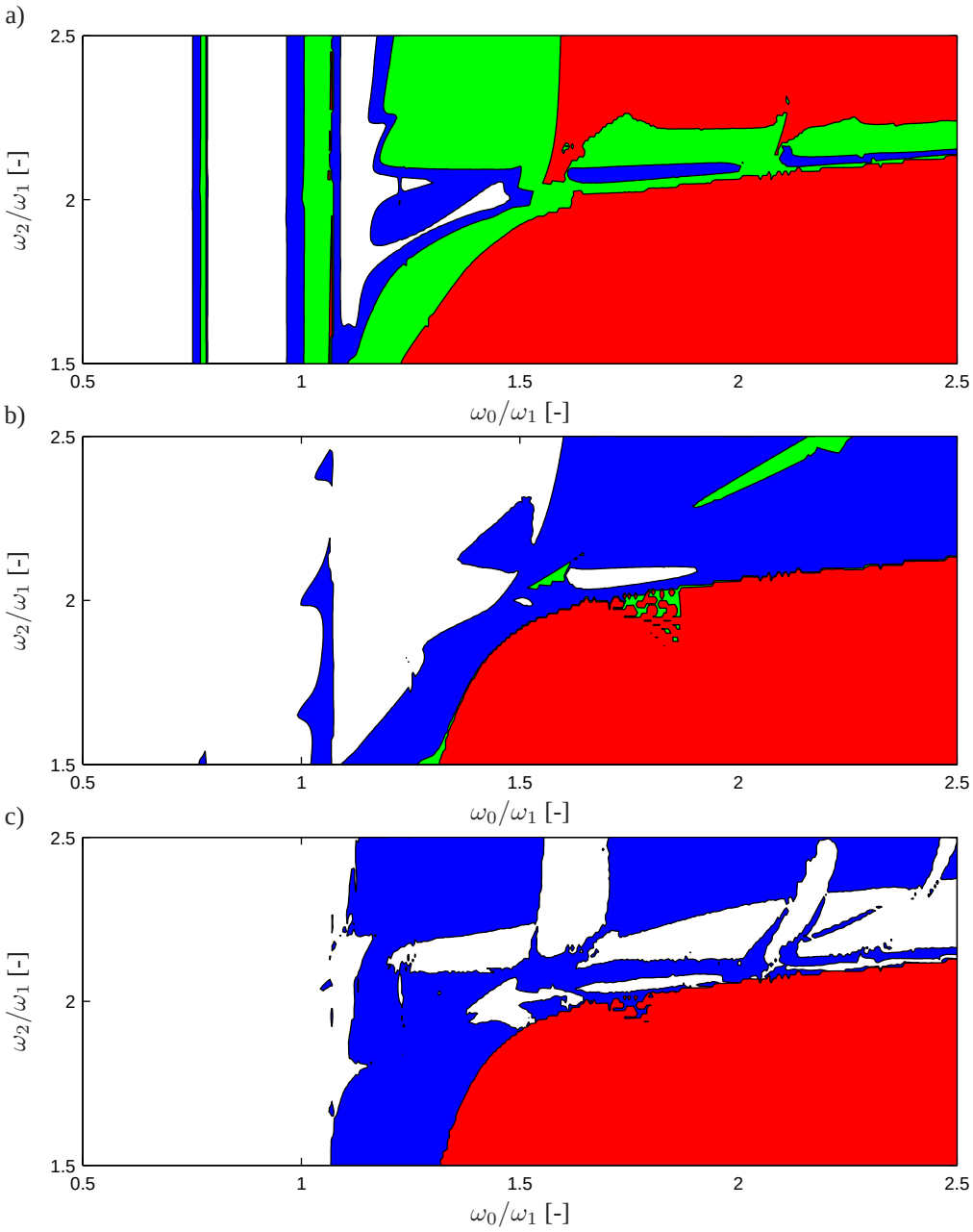

Figure 2.18 Contour curves for analysis made with constant excitation ratio $\omega_0/\Omega_0 = 3.0$. $u_0 = 0.3$ m.
a) Q_1 [m]. (■) $Q_1 > 5$ m. (■) $Q_1 > 10$ m. (■) $Q_1 > 20$ m.
b) Q_2 [m]. (■) $Q_2 > 0.5$ m. (■) $Q_2 > 2$ m. (■) $Q_2 > 4$ m.
c) Largest Lyapunov exponent λ [-]. (■) $\lambda > 0$. (■) Infinite response.

response. No instability occurs below $\omega_0/\omega_1 = 1.1$, except for a small region at $\omega_0/\omega_1 \simeq 0.9$ and $\omega_0/\Omega_0 \simeq 2.5$.

Figure 2.20a, 2.20b and 2.20c show Q_1, Q_2 and λ, respectively. Comparing with the results of Figure 2.19 it is seen that all unstable regions produce chaotic response. Also, the amplitude of the response are significantly reduced, especially $Q_2 < 2$ m in the considered parameter space. Also in this case the main regions at $\omega_0/\omega_1 > 1.1$ are unstable. However, regions around $\omega_0/\omega_1 = 1.5$ and 2.1 produce stable response. Within these stable regions relatively large response is produced compared with the surrounding chaotic regions.

Finally, the corresponding analysis as shown in Figs. 2.19 and 2.20 are carried out with $u_0 = 0.5$ m. Contour lines of λ are shown in Figure 2.21a and 2.21b with $\omega_2/\omega_1 = 2.0$ and $\omega_2/\omega_1 = 2.2$, respectively. Comparing Figure 2.21a with Figure 2.19c reveals that, no significant changes is seen on the stability regions at $\omega_0/\omega_1 < 1.5$. The regions with infinite response is slightly increased due to the influence of quadratic parametric terms.

Comparing Figure 2.21b with Figure 2.20c shows that for $\omega_2/\omega_1 = 2.2$ no significant changes of the stability regions occur when increasing u_0. It should be noted that no regions with infinite response occur.

To validate the stability determined by Lyapunov exponents, stability is determined as function of u_0 and ζ_1 with $\omega_0/\Omega_0 = 3.0$, $\omega_2/\omega_1 = 2.2$ and $\omega_0/\omega_1 = 1.7$. While simulating the response the periodicity of the response is investigated by a residual r given as

$$r = \left(\big(q_1(t) - q_1(t+T)\big)^2 + \big(q_2(t) - q_2(t+T)\big)^2 + \big(\dot{q}_1(t) - \dot{q}_1(t+T)\big)^2 + \big(\dot{q}_2(t) - \dot{q}_2(t+T)\big)^2 \right)^{1/2}, \tag{2.90}$$

where T is found from (2.82). A periodic response is assumed when $r < 0.001$ and when $r > 0.001$ either chaotic response or response going to infinity is assumed. The result is shown in Figure 2.22 where (——) indicate the contour line for $\lambda = 0$ and (——) is the contour line for $r = 0.001$. As seen, good agreement exists between the stability boundary determined by the residual and determined by the Lyapunov exponent.

2.2.4 Concluding remarks

The nonlinear parametric instability of a wind turbine wing model as a two-degrees-of-freedom system retaining up to cubic terms has been analysed at various excitation ratios between the support point excitation frequency and the rotational frequency of the rotor and at various eigenfrequency ratios.

For ordinary three bladed wind turbines, the dominating tower frequency in proportion to the rotational frequency is close to 3. For large wind turbines the eigenfrequency ratio of the fundamental modes may be close to 2. Since this may introduce internal 2:1 resonance, the numerical analysis is centred around these frequency ratios.

It is shown that the parametric instability mainly is influenced by quadratic parametric terms. These terms may produce large regions of chaotic response for fixed excitation ratios. Furthermore, it is shown that cubic nonlinear terms have a significant stabilizing effect at resonance frequencies.

At irrational excitation ratios the response is shown to be almost periodic. Hence, Floquet theory is not applicable for analysing the stability of the system. At rational excitation ratios

the response becomes periodic. However, the Floquet theory is only useful for finding stability boundaries in case of relatively short response periods. Instead, the theory of Lyapunov exponents is used for analysing the stability of the system.

Using numerical simulations it is shown that within a relatively small frequency band around $\omega_2/\omega_1 = 2.2$ large stable regions appear for $\omega_0/\omega_1 > 1.1$ in all other cases unstable response mainly occur in this region. With $\omega_2/\omega_1 > 2.2$ chaotic response is produced while the response becomes infinite at $\omega_2/\omega_1 < 2.2$. No significant changes of the stability regions appear when increasing u_0 except for smaller regions, which change character from chaotic to infinite response when $\omega_2/\omega_1 = 2.0$

The indicated results refers to a two-degrees-of-freedom reduced system including only the two lowest fundamental modes. The reduced model is convenient when working with control algorithms of wind turbines where only a few modes are observable. However, at resonance excitation frequencies, energy may transfer to higher modes via nonlinear couplings. The energy leakage from lower to higher modes may introduce qualitatively and quantitatively changes to the frequency response. This leakage can be investigated by two methods. Firstly, two extra modes may be included in the present formulation with an increase from 62 terms to 346 terms in the equations of motion. This approach will only include energy transfer from the first to the second modes, which may not provide a full picture of the energy transfer. Secondly, a nonlinear finite element approach can be used. The work of creating and analysing a nonlinear beam model using co-rotational beam elements formulated by Krenk (2004b) is in progress and will be presented within the paper Holm-Jørgensen *et al.* (2005).

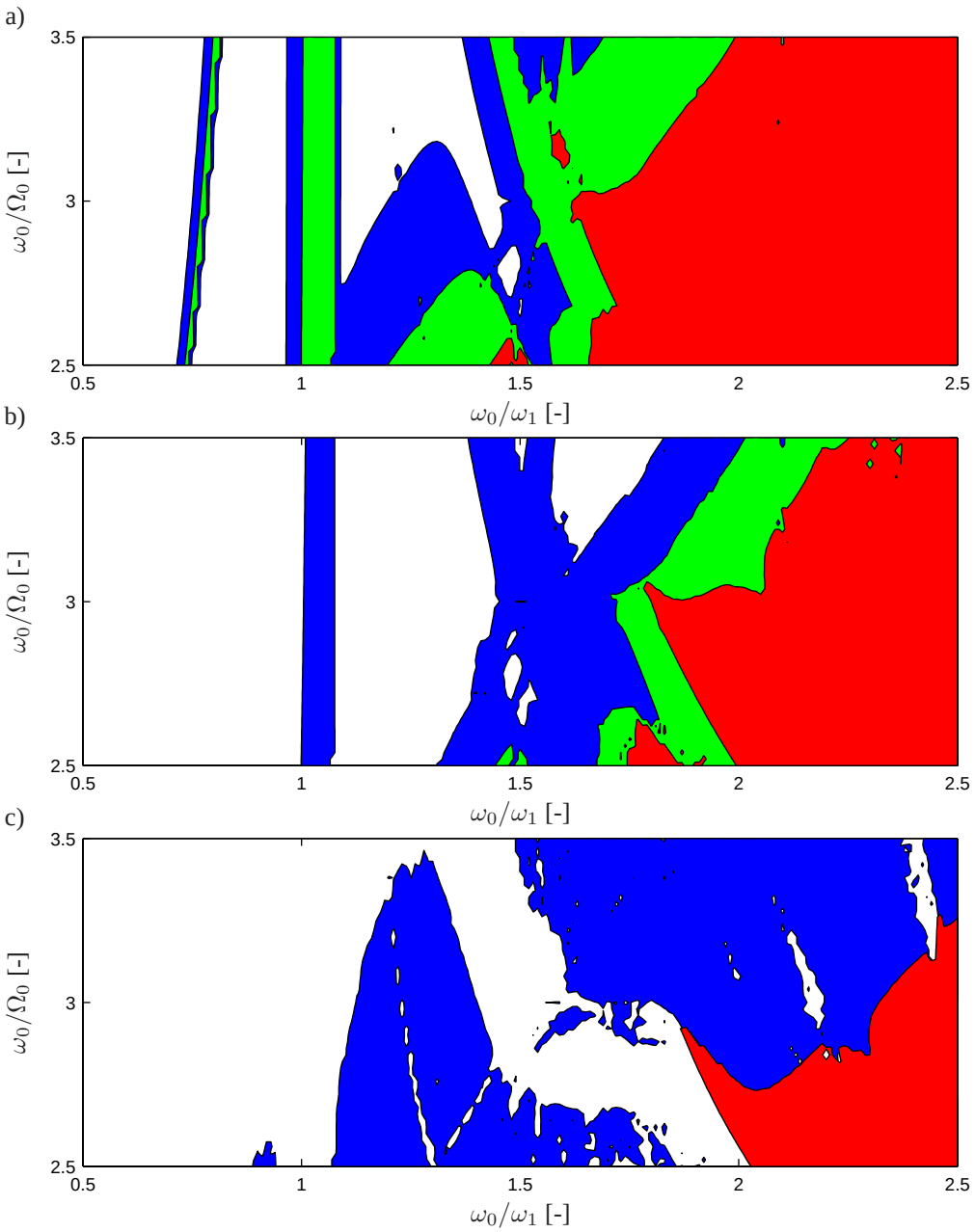

Figure 2.19 Contour curves for analysis made with constant eigenfrequency ratio $\omega_2/\omega_1 = 2.0$. $u_0 = 0.3$ m.
a) Q_1 [m]. (■) $Q_1 > 5$ m. (■) $Q_1 > 10$ m. (■) $Q_1 > 20$ m.
b) Q_2 [m]. (■) $Q_2 > 0.5$ m. (■) $Q_2 > 2$ m. (■) $Q_2 > 4$ m.
c) Largest Lyapunov exponent λ [-]. (■) $\lambda > 0$. (■) Infinite response.

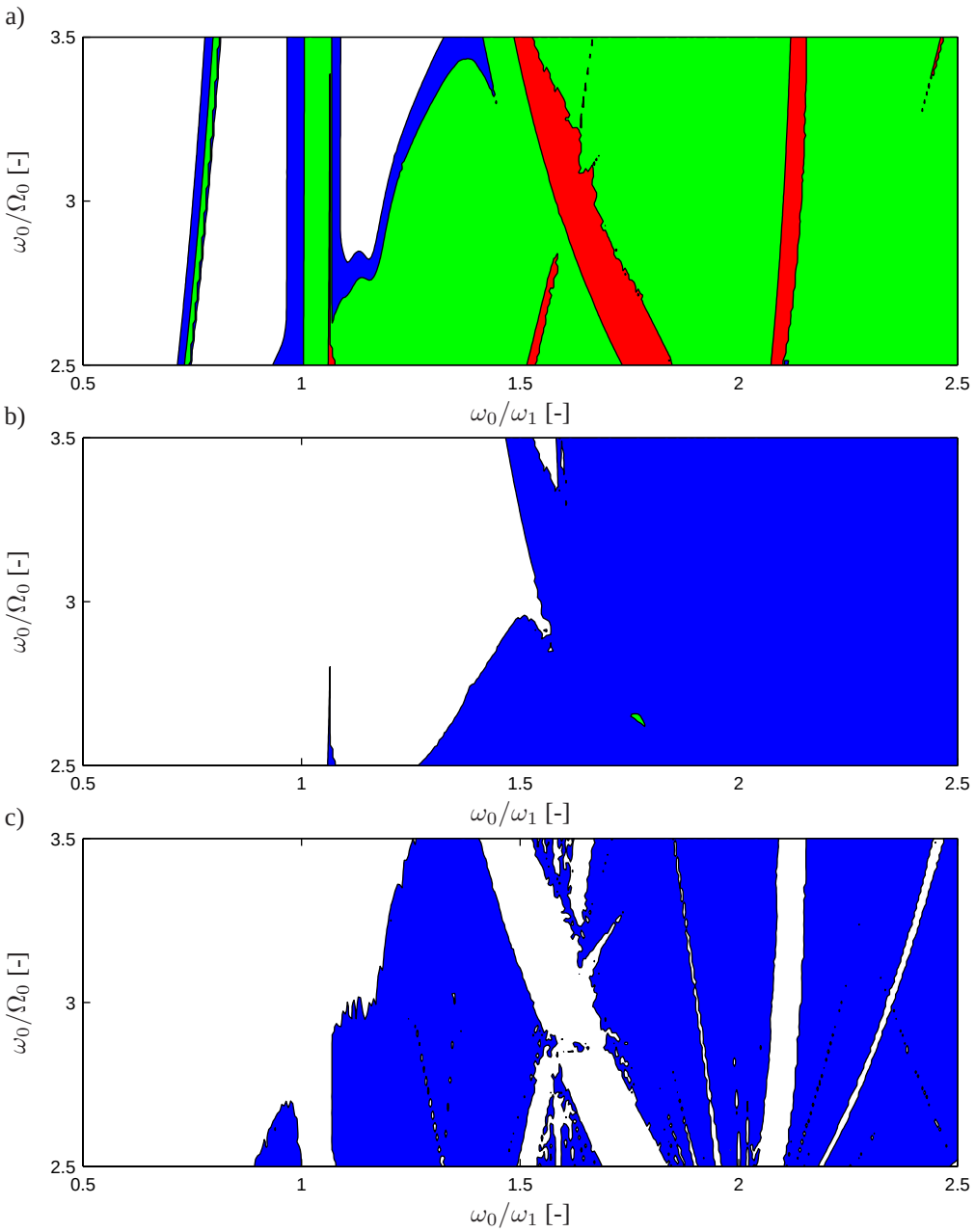

Figure 2.20 Contour curves for analysis made with constant eigenfrequency ratio $\omega_2/\omega_1 = 2.2$. $u_0 = 0.3$ m.
a) Q_1 [m]. (■) $Q_1 > 5$ m. (■) $Q_1 > 10$ m. (■) $Q_1 > 20$ m.
b) Q_2 [m]. (■) $Q_2 > 0.5$ m. (■) $Q_2 > 2$ m. (■) $Q_2 > 4$ m.
c) Largest Lyapunov exponent λ [-]. (■) $\lambda > 0$. (■) Infinite response.

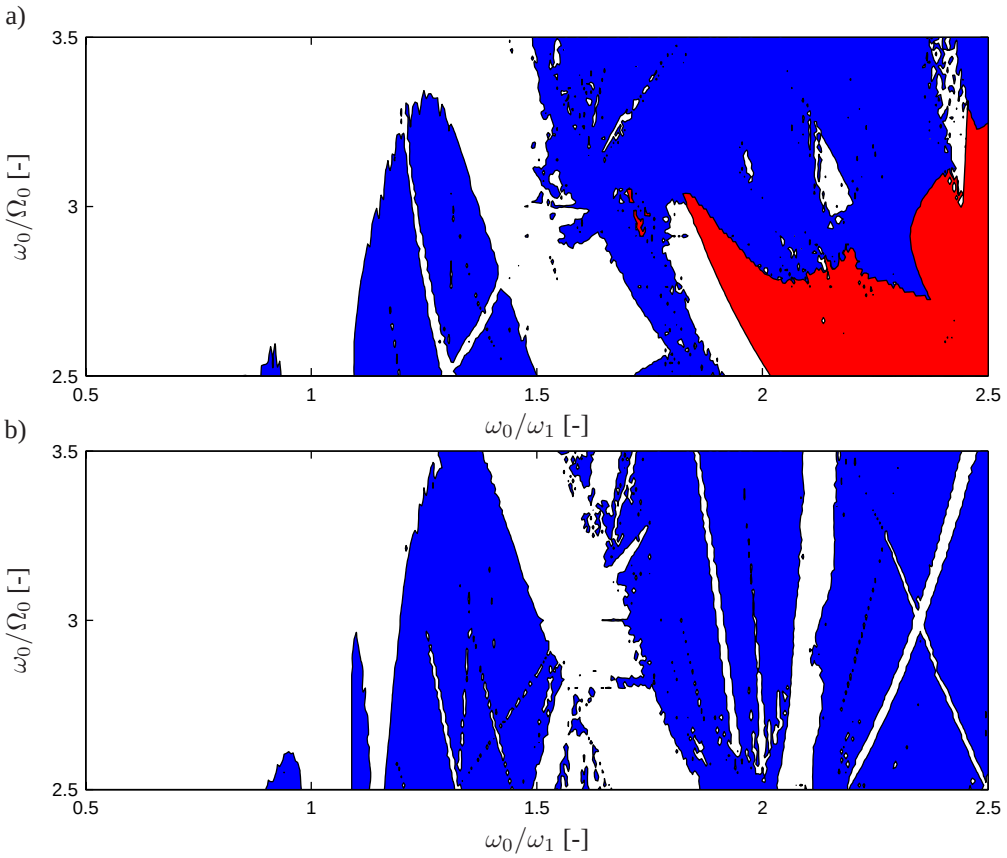

Figure 2.21 Contour curves for $\lambda = 0$ at various constant eigenfrequency ratio. $u_0 = 0.5$ m. (■) $\lambda > 0$. a) $\omega_2/\omega_1 = 2.0$. b) $\omega_2/\omega_1 = 2.2$.

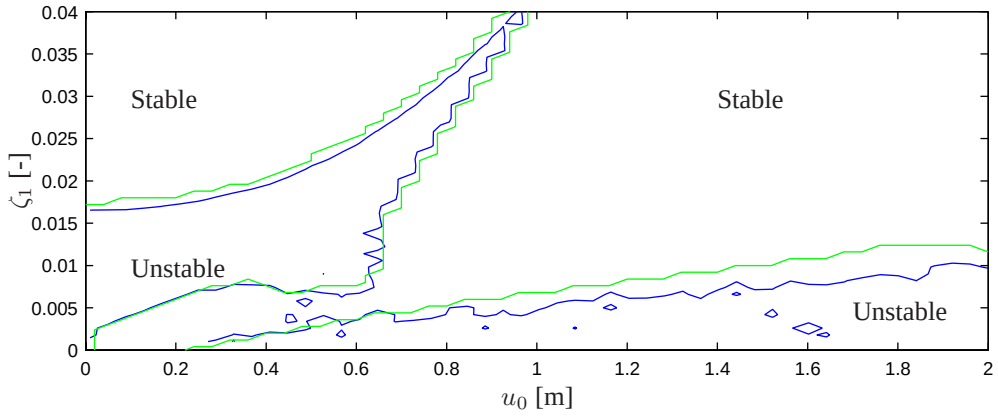

Figure 2.22 Contour curves for λ and r. $\omega_2/\omega_1 = 2.2$, $\omega_0/\Omega_0 = 3.0$, $\omega_0/\omega_1 = 1.7$. (———) contour line for $\lambda = 0$. (———) contour line for $r = 0.001$.

CHAPTER 3
Dynamic Stall Models of Wind Turbine Airfoils

In Chapter 2 a nonlinear structural model of a wind turbine wing is formulated. In the numerical analysis constant lift coefficients was assumed. In this chapter a model is presented for the aerodynamic lift of wind turbine profiles undergoing dynamic stall conditions. The model combines memory delay effects under attached flow with reduced lift due to flow separation under dynamic stall conditions. The lift coefficient of the separated flow is represented as a function of the degree of attachment. Non-stationary effects are included by three mechanisms: a memory integral representation of the lift coefficient of fully attached flow via a 2nd order filter, a delay of the development of separation represented via a first order filter, and a lift effect due to leading edge separation also represented via a first order filter. The presented model is fully described by 4 state variables. At present mainly three different dynamic stall models are used in the aeroelastic codes used by manufactures of wind turbines as described in chapter 1. A brief description of these models are given together with other models listed in the literature, which mainly have been used on helicopter wing profiles. All the presented models assume two dimensional flow and are one degree of freedom models in the angle of attack. The performance of the various models are compared with experimental data for fully attached flow conditions and dynamic stall conditions, respectively. Finally, a description is given on how to encompass elastic deformation of the wing and turbulence components into the model, i.e. how to include aeroelastic effects.

3.1 Introduction

Wind turbines are designed with increasingly slender blades and blade controls that can react rapidly to changing loading conditions. Thus it becomes increasingly important to account for load effects from dynamic stall. The basic mechanism is illustrated in Fig. 3.1, showing a typical airfoil profile with relative flow velocity V, angle of attack α, and lift force L per unit length. The lift force is represented via the non-dimensional lift coefficient c_L, defined by

$$L = c_L \tfrac{1}{2}\rho V^2 c \tag{3.1}$$

where c is the chord length. It is well established that under stationary attached flow conditions the lift force L acts approximately in the forward quarter-point named the aerodynamic centre and is approximately a linear function of the angle of attack α, when α is sufficiently small (Bisplinghoff 1996).

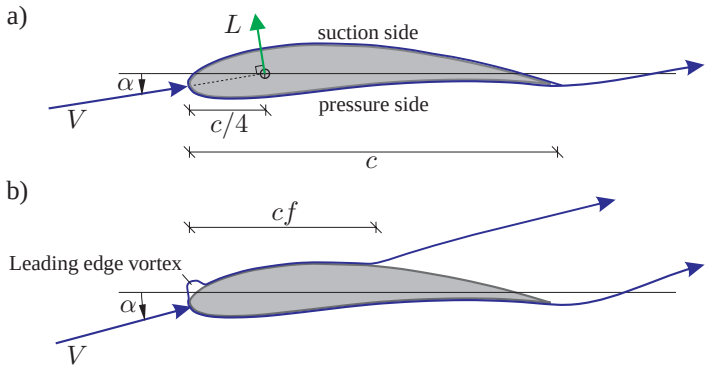

Figure 3.1 Principles of attached and separated flow.

At a limiting value of the angle of attack α_s the flow pattern changes, and the lift force passes through a maximum. This is the phenomenon of static stall. A typical curve of the static lift coefficient c_L is shown as (——) in Figure 3.2, (Leishman 2000, p. 385). Stall is associated with separation of the flow at the suction side of the profile as illustrated in Fig. 3.1b. The degree of separation can be represented in an approximate way by the distance cf from the leading edge to the separation point , where the non-dimensional parameter f is a measure of the degree of separation. For fully attached flow $f = 1$, and for separated flow f decreases towards zero with increasing separation.

Under non-stationary conditions it takes some time for the flow to approach the stationary flow pattern. For fully attached flow analytic solutions can be obtained for harmonic motion of the airfoil as well as for a step function change in position, (Fung 1993, p. 206 ff). In principle these solutions involve translation as well as rotation of the airfoil, but for the present purpose it is sufficient to combine the effect of the motion into an effective angle of attack. The analytical solutions indicate delayed lift during fully attached conditions with a lower lift at increasing α and higher lift at decreasing α compared to the quasi static solution. This effect is also seen on the dynamic lift in Fig. 3.2 at low angles of attack. When the flow is separated during the motion the degree of attachment, represented by the parameter f, also exhibits delay with respect to its stationary value. The delay in the flow and the degree of separation for harmonic motion influences the stall phenomenon. A typical dynamic stall curve is plotted as (——) in Figure 3.2. It is seen that for a harmonic variation of the angle of attack α between $0\,^\circ$ and 15° the occurrence of dynamic stall is delayed, and the lift during the phase of decreasing α is considerably lower than during the increasing phase. Thus, dynamic stall typically involves an increased range of attached flow and different branches for increasing and decreasing angle of attack.

Finally, in addition to trailing edge separation, a separation bubble may develop in the boundary layer at the suction side of the profile close to the leading edge, a phenomena characteristic for thin profiles. In front of the bubble the boundary layer is attached, whereas behind the bubble two situations can occur. In one case the boundary layer downstream of the bubble is turbulent, enhancing the tendency of attachment. This situation is illustrated in Fig. 3.1b. In the other case the boundary layer detaches fully, creating separation from the leading to the trailing edge. Under quasi-static conditions the situation is very unstable, and in fact both situations can occur at the same angle of attack. Hence, two different lift curves can occur. This phenomena is

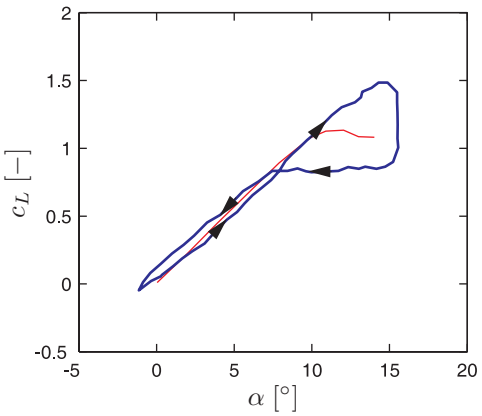

Figure 3.2 Lift coefficient under static and dynamic stall situations. ( ) Static lift. ( ) Dynamic lift.

called double stall. Under dynamic oscillations the flow will separate immediately to the separation bubble. Even though the flow is fully separated over the profile, experimental data shows an almost linearly increasing lift force (Leishman 2000). This increase in lift is generated by a rising pressure peak at the leading edge and a large vortex created in the turbulent wake as the trailing edge separation point moves abruptly to the leading edge. At low pitch velocities leading edge separation is usually no problem, but within recent years a wish for active control of tower and blade vibrations have lead to pitch control of large wind turbine wings with pitch velocities of up to $20^\circ/\text{s}$. Also, large deformations due to flexible wings, may produce high amplitude changes in the angle of attack. Under such conditions leading edge separation may contribute significantly to the lift. As the angle of attack is increased the vortex builds up in strength and finally detach from the leading edge travelling downstream. CFD calculations indicate the creation of a secondary vortex with opposite circulatory contribution at the trailing edge during dynamic stall conditions. The trailing edge vortex builds up during dynamic stall, and at some point it detaches and convects downstream similar to the leading edge vortex. A CFD calculation of a NACA-0015 profile in dynamic stall conditions is illustrated in Figure 3.3. The dynamic stall calculation have been performed by Risø National Laboratory, Wind Energy and Atmospheric Physics Department within the EC project VISCWIND (VISCWIND 1999). The red dots indicate particles added to the flow at the suction side of the profile, and the blue dots illustrate particles added at the pressure side. Figure 3.3a illustrates the onset of leading edge separation with the entire boundary layer starting to detach. Figure 3.3b shows the buildup of the leading edge vortex, which in Figure 3.3c detaches and moves downstream, while a trailing edge vortex starts building up. Finally, Figure 3.3d shows the detachment of the trailing edge vortex and breakdown of the leading edge travelling vortex. Both experimental data and CFD calculations indicate that the flow changes, caused by the leading edge separation vortex, generates an increased suction contribution, leading to increased lift.

At low frequency changes of the angle of attack, flow situations including trailing edge separation occur. As the frequency increases leading edge flow condition are likely to happen, especially for thin profiles. Flow reattachment mainly happens with the separation point moves from the leading to the trailing edge.

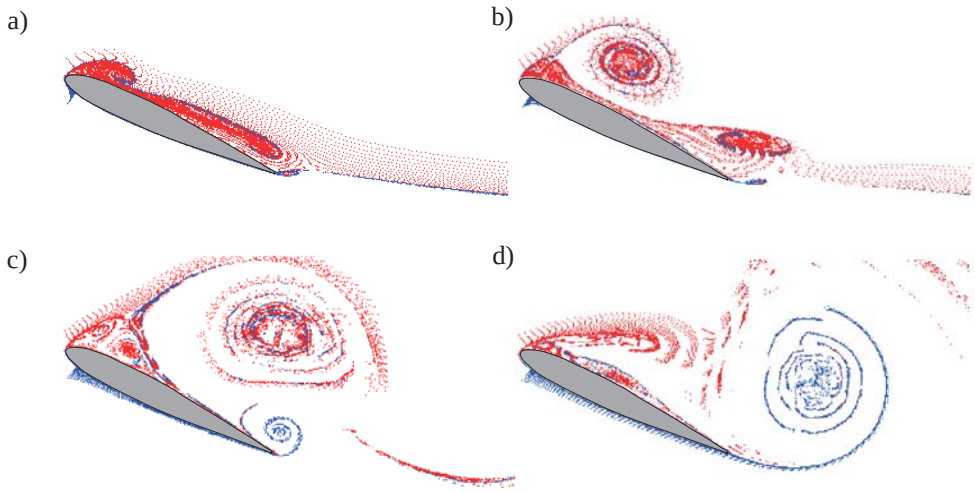

Figure 3.3 CFD calculation of a NACA-0015 wing section during dynamic stall conditions. a) Leading edge separation starts. b) Vortex buildup at the leading edge. c) Detachment of leading edge vortex and buildup of trailing edge vortex. d) Detachment of trailing edge vortex and breakdown of leading edge vortex.

The angle of attack α between the profile and the resulting wind may change due to rotations of the wing as a whole (pitch) or elastic torsional motions of the local cross-section. Additionally, the oscillation in the direction orthogonal to the chord c will introduce an apparent change of the angle of attack. Turbulent velocity components in the incoming wind field will cause a fluctuating change of the angle of attack. If the wavelength of the turbulence is large compared to the chord length these effects may be treated by a simple quasi-static modification of the angle of attack from the mean wind and rotational speed. For a pitching airfoil the downwash over the profile is not uniform. To satisfy the stationary attached flow conditions that the fluid must leave the trailing edge smoothly, it can be shown that the downwash at the $\frac{3}{4}c$-point must follow the chamber line of the profile, (Fung 1993, p. 401 ff). This assumption motivates the use of so called one-dimensional load models, where the lift load is specified by an equivalent angle of attack determined from the downwash at the $\frac{3}{4}c$-point alone, which will also be used in this outline.

In summary, delay of lift during fully attached conditions and the motion of the separation point as well as leading edge separation and the dynamic interaction between leading and trailing edge vortices are constituent properties of a load model for which dynamic stall phenomena occur. A good model of dynamic stall should describe these phenomena for different frequencies and different amplitude ranges.

There exists a great variety of dynamic stall models in the literature. These models may be categorized into three main groups.

1. The effects of the different flow conditions described above is modelled, e.g. lift reduction due to separation, contribution from leading edge separation etc.

2. The characteristics of the lift curve is modelled, e.g. a linear growing curve at low angles of attack, a drop in lift at a given stall angle etc.

3 A modification of the angle of attack is made introducing a so-called dynamic angle of attack

In a series of papers (Leishman and Beddoes 1986b; Leishman and Beddoes 1986a; Leishman 1988) Beddoes and Leishman have developed a model for dynamic stall combining the flow delay effects of attached flow with an approximate representation of the development and effect of separation. This model was developed with helicopter rotor dynamics in mind and therefore includes a fairly elaborate representation of the non-stationary attached flow depending on the Mach number and a rather complex structure of the equations representing the time delays. In contrast, a model proposed by Øye (1991) omits the transient effects of the attached flow, and represents the dynamic stall by introducing a first order filter on a static equivalent degree of attachment, obtained by a simple interpolation relation. Hansen *et al.* (Hansen *et al.* 2004) developed a reduced version of the Beddoes-Leishman model at Risø National Laboratories, Denmark, omitting the effects of compressible flow and leading edge separation. They introduced a interpolation relation similar to the one used by Øye to make the model valid in the entire range of the angle of attack. The Beddoes-Leishman model, Øye and Risø models may be categorized into the first group of models aiming to model the effects of the flow conditions. Tran and Petot (1981) developed a model, named ONERA, where the load coefficients are described by a 3rd order differential equation. The differential equation is split into a linear domain at low angles of attack determined by a first order differential equation, and a stall domain determined by a second order differential equation. The ONERA model may be categorized into the second group of models which seeks to describe the loads from the curve characteristics. Finally, Tarzanin (1972) developed a model also named the Boeing-Vertol model, based on a relation between the dynamic stall angle and static stall angle determined by Gross and Harris (1969). From this relationship a dynamic angle of attack is determined and the load coefficients is interpolated from the static data. Obviously this final model falls into the group of models which modifies the angle of attack.

In recent year also Navier-Stokes solver have been used to determine airfoil loads under dynamic stall situations. Due to the extensive cost of these calculation, practical applications doesn't seem within a near future, but solving the Navier-Stokes equations gives an insight into the flow and pressure changes occurring during a dynamic stall cycle. Srinivasan *et al.* (1995) used a Navier-Stokes solver to evaluate a variety of turbulence models. Du and Selig (1998, 2000) studied 3D effects on the boundary layer flow of a rotating wind turbine blade by solving the steady boundary layer equations. They found that the separation is slightly postponed due to rotation of the wing, which induces an increase in lift. They suggested a modification of the 2D static data to incorporated the rotational 3D effects. Akbari and Price (2003) studied the effects of several parameters including reduced frequency, mean angle of attack, location of the pitch axis and the Reynolds number. They found that the Reynolds number and position of the pitch axis have little effect on the characteristics of the lift cycle however the position of pitch axis have major effect on the pitching moment. Wernert *et al.* (1996) used Particle Image Velocimetry (PIV) and Laser Sheet Visualization to validate a numerical code based on Navier-Stokes equations, they found that the numerical and experimental results agreed but some discrepancies were observed. A completely different approach is suggested by Suresh *et al.* (Suresh *et al.* 2003) using neural network for identifying nonlinear unsteady lift. Comparing with experimental data, they show good agreement with their numerical model. They also argue, that the proposed method is easily implemented in available codes and should be less expensive than the ONERA model.

It should be noticed that larger discrepancies between numerical and experimental results seems to be accepted within the so-called semi-empirical models described above than for the Navier-Stokes solver. The goals of the semi-empirical models are not to capture every variation in the load, but to model the main characteristics in a fast and efficient way. The main drawback of the semi-empirical models is, that all of them are dependent on available static data and use interpolation into tabulated values or curve fitting techniques to determine quasi-static lift values. A semi-empirical model should be able to reproduce these static values for quasi-static rates of the angle of attack, i.e. $\dot{\alpha} \simeq 0$.

In the next section a semi-empirical dynamic stall model for the lift is formulated. The model is developed mainly with concern to realistic wind turbine flows, hence compressibility effects are omitted. An essential part is, that the model should fit into the first group of semi-empirical models, hence, the lift contributions introduced in the model should be explained by certain changes in flow and resulting changes in pressure. The model should be applicable both at high pitch rates during e.g. active control or large gust, and during normal operation conditions with low pitch rates.

Next, the numerical algorithms for the Beddoes-Leishman, Øye, Risø, ONERA and Boeing-Vertol models are shortly described. After that, numerical simulations are made and the performance of the presented models are studied and compared with existing experimental data. Finally, the inclusion of aeroelastic contributions and 3D-effects are discussed.

3.2 A Dynamic Stall Model for Wind Turbines

The model combines a simple two-term memory kernel for the transient behaviour of the attached flow with a lift reduction due to separation, represented via a first order filter, giving two state parameters to describe the flow delay under full attachment and one state parameter to describe the delayed placement of the separation point. The reason for using two timescales under attached flow conditions, is to model with sufficient accuracy both high pitch frequencies occurring e.g. during active control or normal operating conditions. Furthermore, an additional first order filter is used to model the increased lift under leading edge separation. The advantage of this compromise is that within a fairly simple model the transients of the flow are included in a manner that is sufficiently accurate for wind turbines, and the dynamic effect of trailing edge separation in essence only introduces one additional time-scale.

3.2.1 Stationary lift and separation

An essential part of a non-linear load model is the lift reduction due to separation. The lift coefficient of the profile under fully attached flow is denoted c_{L0} and is often linearized for small α in the following manner

$$c_{L0} = \frac{\partial c_L}{\partial \alpha}\bigg|_{\alpha_0} (\alpha - \alpha_0), \tag{3.2}$$

where α_0 is the angle of attack at zero lift. For a thin plate the coefficient $\partial c_L/\partial \alpha = 2\pi$ whereas the coefficient is somewhat smaller for a real profile. The lift coefficient c_L under separated flow can be found from Kirchhoff flow theory using complex mapping, see (Thwaites 1960, p. 170),

or more directly by a singular integral formulation of linearized airfoil flow theory (Krenk 2004a) as

$$c_L \simeq \left(\frac{1+\sqrt{f}}{2}\right)^2 c_{L0}. \tag{3.3}$$

According to (3.3), the total static lift coefficient is determined as a reduction of the linear lift according to the attachment degree f. At fully attached flow, where $f = 1$, c_L follows c_{L0}. As α increases the separation point moves towards the leading edge and f decreases. When the separation point reaches the leading edge $f = 0$ and $c_L \simeq \frac{1}{4}c_{L0}$ according to (3.3). A further increase in α will not change the location of the separation point, hence $f = 0$, but c_{L0} given by (3.2) increases linearly with α. As a consequence (3.3) predicts a linear increase with α of $c_L \simeq \frac{1}{4}c_{L0}$ for fully separated flow. However, according to measured values c_L remain constant or even decreases with increasing α in this regime. To remedy this inconsistency a modification is needed. Here the correction will be made on c_{L0}, which for $f > 0$ is determined as the linearized lift coefficient given in (3.2), and for $f = 0$ is set to $4c_L$ from measurements. This modification allows the use of (3.3) in the entire range of α.

The motion of the separation point may be modelled in the physical plane as done in the models of Beddoes and Leishman (1986b, 1986a) and Øye (1991). However, as follows from (3.3) changes of the lift coefficient are related to changes of the attachment degree as

$$dc_L = \tfrac{1}{4}\Big(1 + \frac{1}{\sqrt{f}}\Big)c_{L0}df. \tag{3.4}$$

Hence, at fully separated conditions ($f \simeq 0$) an increment of the separation degree results in a large increment of the lift coefficient. In order to circumvent this singularity the physical profile is mapped on a unit circle as traditionally performed in airfoil theory, see Figure 3.4, where the idea is to use the angle θ indicating the separation point in the complex map, rather than f. The functional relationship transforming f into θ is given by

$$2f = 1 + \cos\theta, \tag{3.5}$$

which inserted in (3.3) gives

$$c_L = \cos^4(\tfrac{1}{4}\theta)\, c_{L0}. \tag{3.6}$$

This formulation removes the square root singularity around $f = 0$, corresponding to $\theta = \pi$. $\theta(\alpha)$ is found from the inverse relation of (3.6). Hence, in the numerical algorithm a set of measured lift data $c_L(\alpha)$ is needed to determine the separation parameter $\theta(\alpha)$.

3.2.2 Dynamic lift and separation

Up to now only stationary conditions have been considered. In this section the non-stationary lift is modelled due to time dependent flow changes. Two main flow situations are considered.

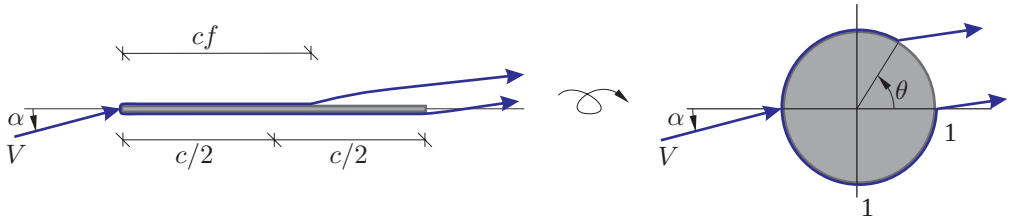

Figure 3.4 Transformation into the complex plane.

One at low angles of attack with fully attached flow, where the flow adjust so that the separation point is located at the trailing edge, and a situation with separated flow where the movement of the trailing edge separation point is delayed compared to the quasi static movement.

First consider the fully attached flow situation. For a change $d\alpha$ in the angle of attack a small separation occurs before the separation point is reestablished at the trailing edge by circulation built up around the profile. This change in circulation creates a corresponding change in lift.

The increment dc_{L0} of the linear lift due to an increment $d\alpha$ of the angle of attack is not achieved instantaneously. Given the linearized conditions (3.2) this delay can be modelled via the introduction of an impulse response function $\Phi(t)$, so the increment $dc_{L0,d}(t)$ at time t due to an increment $d\alpha(\tau)$ at an earlier time τ can be written

$$dc_{L0,d} = \Phi(t-\tau)dc_{L0}(\tau). \tag{3.7}$$

In (3.7) and below the dynamic lift is indicated by the lower index d. The impulse response function fulfills $\Phi(\infty) = 1$. For incompressible flow it can be shown for a thin profile that half the increment is felt instantaneously, so $\Phi(0) = \frac{1}{2}$, see (Fung 1993, p. 206 ff). Upon superposition of the effects of all previous increments, the linear dynamic lift, valid for attached flow conditions, is given as

$$c_{L0,d}(t) = \int_{-\infty}^{t} \Phi(t-\tau)\dot{c}_{L0}(\tau)d\tau. \tag{3.8}$$

The approach chosen here for the linear lift coefficient is similar to that of the Beddoes-Leishman model, described in section 3.3.1. However, the compressibility terms are neglected. The analytical solution of $\Phi(t)$ may be approximated by a first order filter with a single timescale with the initial condition $\Phi(0) = \frac{1}{2}$ and the limit $\Phi(\infty) = 1$, but as mentioned earlier, both high and low frequency components needs to be modelled accurately, hence, two timescales are needed. In what follows it is assumed that $\Phi(t)$ may be approximated with the expression

$$\Phi(t) = 1 - A_1 e^{-\omega_1 t} - A_2 e^{-\omega_2 t}, \tag{3.9}$$

where A_1, A_2, ω_1 and ω_2 are profile dependent variables describing the time delay. For a thin profile in incompressible flow $A_1 + A_2 \simeq \frac{1}{2}$, and ω_1 and ω_2 represents the timescale for low and high frequency rotations, respectively. Then a differential description of the convolution integral

(3.8) can be obtained as follows. Let $c_1(t)$ and $c_2(t)$ be state variables related to the filter, defined by the 1st order differential equations

$$\dot{c}_j(t) + \omega_j c_j(t) = A_j \dot{c}_{L0}(t) \quad , \quad j = 1, 2 \tag{3.10}$$

Then, $c_{L0,d}(t)$ as given by (3.8) can be represented by the following output equation

$$c_{L0,d}(t) = c_{L0}(\alpha) - c_1(t) - c_2(t) \tag{3.11}$$

Next consider a situation under separated flow conditions. According to (3.6) a step change in α is felt instantaneously through a direct change in θ. In a real flow situation a time interval is observed during which the separation angle moves to the new stationary value. Due to this delay the attachment angle is lower at increasing α and larger at decreasing α than the corresponding stationary value giving larger and lower lift forces, respectively.

Due to the relation between changes in separation and lift given in (3.4) the non-stationary effect on c_L from the delayed separation is modelled as a delay on the separation variable. The delayed motion of the separation point and hence the separation angle under dynamic conditions is described via a dynamic attachment angle θ_d obtained as the solution to the first order differential equation

$$\dot{\theta}_d(t) = -\omega_3(\theta_d(t) - \theta(\alpha)) \tag{3.12}$$

A similar approach has been used in the Beddoes-Leishman model (Leishman and Beddoes 1986b; Leishman and Beddoes 1986a) and by Øye (Øye 1991), where a dynamic attachment degree f_d is used, obtained from the differential equation

$$\dot{f}_d(t) = -\omega_3(f_d(t) - f(\alpha)) \tag{3.13}$$

Notice that the time constants ω_3 in (3.12) and (3.13) are identical. Although only valid for static conditions, the reduction of the dynamic linear lift coefficient $c_{L0,d}(t)$ due to the dynamic attachment angle is again calculated via (3.6) as follows

$$c_{L,d}(t) = \cos^4\left(\tfrac{1}{4}\theta_d\right) c_{L0,d}(t) \tag{3.14}$$

3.2.3 Leading edge separation

As mentioned earlier experimental data indicates that leading edge separation generates a linear increasing lift curve even at full separation due to a pressure peak forming at the leading edge and a large vortex forming in the wake of the profile at increasing α. Instead of modelling these contributions separately a combined lift correction is added to $c_{L,d}(t)$ to create this linear lift curve. This is possible because the total lift is assumed to follow the linear curve $c_{L0,d}(t)$ as long as the vortex is found on the profile, and the pressure peak is present. Assuming this, the additional lift contribution $\Delta c_L(t)$ becomes

$$\Delta c_L(t) = c_{L0,d}(t) - c_{L,d}(t) \tag{3.15}$$

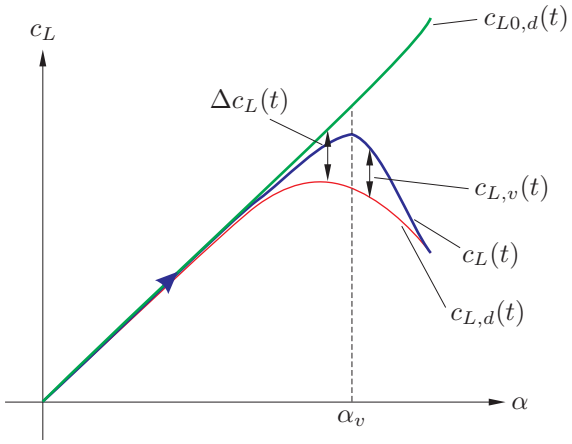

Figure 3.5 Illustration of lift components used to described leading edge separation.

At a certain angle α_v the leading edge vortex detaches from the leading edge and travels downstream over the profile with the velocity $\frac{V}{3}$. Green *et al.* (1992) came to approximately the same vortex convection velocity for a variety of profiles, hence showing that the vortex travelling velocity is independent of profile shape. The travelling vortex keeps building up strength as long as it is located somewhere on the profile. As it reaches the trailing edge the vortex contribution stops building up corresponding to $\Delta\dot{c}_L(t) = 0$, and a vortex with opposite circulation is formed at the trailing edge, see Figure 3.3. The trailing edge vortex counteracts the leading edge travelling vortex and the lift starts diminishing. This diminishing effect is assumed to be described by the following first order differential equation

$$\dot{c}_{L,v}(t) + \omega_4 c_{L,v}(t) = \begin{cases} \Delta\dot{c}_L(t) & \text{for} \quad \alpha \leq \alpha_v \\ 0 & \text{for} \quad \alpha \leq \alpha_v \end{cases} \tag{3.16}$$

where $c_{L,v}(t)$ is the actual value of the induced lift after the initiation of the diminishing effect. Hence, the total lift becomes

$$c_L(t) = c_{L,d}(t) + c_{L,v}(t) \tag{3.17}$$

This introduces one additional state variable $c_{L,v}(t)$ into the model. Furthermore, two profile dependent parameters are introduced, namely ω_4, which controls the diminishing rate of the vortex lift, and the critical angle α_v at which the leading edge vortex detaches from the leading edge. A variable τ should also be included to control the position of travelling vortex. However, assuming the travel velocity being given, this will not introduce additional parameters to be calibrated

3.2.4 State formulation

The present model includes four state variables for every wing section at which the lift is calculated. Two variables c_1 and c_2 to describe the delayed linear lift, one variable θ_d to describe

the dynamic movement of the separation angle and one variable $c_{L,v}$ to describe the induced lift from the pressure peak and vortex forming under leading edge separation. In matrix formulation the linear differential equations describing these state variables can be organized as follows

$$\dot{\mathbf{z}}(t) = \mathbf{A}\mathbf{z}(t) + \mathbf{b}_0(\alpha) + \mathbf{b}_1 \dot{c}_{L0}(t), \tag{3.18}$$

where

$$\mathbf{z}(t) = \begin{bmatrix} c_1(t) \\ c_2(t) \\ \theta_d(t) \\ c_{L,v}(t) \end{bmatrix}, \quad \mathbf{A} = \begin{bmatrix} -\omega_1 & 0 & 0 & 0 \\ 0 & -\omega_2 & 0 & 0 \\ 0 & 0 & -\omega_3 & 0 \\ 0 & 0 & 0 & -\omega_4 \end{bmatrix},$$
$$\mathbf{b}_0(\alpha) = \begin{bmatrix} 0 \\ 0 \\ \omega_3 \theta(\alpha) \\ \Delta \dot{c}_L(t) H(\alpha_v - \alpha) H(\dot{\alpha}) \end{bmatrix}, \quad \mathbf{b}_1 = \begin{bmatrix} A_1 \\ A_2 \\ 0 \\ 0 \end{bmatrix}, \tag{3.19}$$

where $H(x)$ is the unit step function. The total lift coefficient then follows from (3.11), (3.14) and (3.17) as

$$c_L(t) = \cos^4\left(\tfrac{1}{4}\theta_d(t)\right)\left[c_{L0}(\alpha) - c_1(t) - c_2(t)\right] + c_{L,v}(t). \tag{3.20}$$

The static coefficients to be determined are $c_{L0}(\alpha)$, $\dot{c}_{L0}(t)$ and $\theta(\alpha)$ which all can be found from experimental static lift coefficients. The first two are determined from the slope of $c_L(\alpha)$ at $\alpha = \alpha_0$, with the earlier mentioned modification at $f = 0$, where $c_{L0} = 4c_L$ at angles of attack larger than the angle of attack at which full separation occurs. $\theta(\alpha)$ is then found from (3.14). Furthermore a series of profile dependent constants are used in the model. A_1, A_2, ω_1 and ω_2 are determined from fully attached conditions, i.e. on the linear part of the lift curve. For a thin plate profile, these parameters may be determine by an appropriate 2nd order filter approximation to the Wagner function, see e.g. R. T. Jones (1940). For an actual profile the parameters may be determined from dynamic test data at low angles of attack. ω_3, ω_4 and α_v may all to be determined from dynamic test data at high angle of attack.

The delay flow conditions varies with the mean velocity V and the chord length of the profile c. It is often used, to introduce a reduced time variable depending on these quantities, see e.g. (Fung 1993, p. 207). However, a convenient way of introducing these effects is to adopt the variation of the timescale parameters ω_j, $j = 1, 2, 3, 4$. This approach is also used by the Risø model described in section 3.3.4. At low Mach numbers the following non-dimensional parameter $\hat{\omega}_j$ is, for a thin plated profile at fully attached flow conditions, constant during scaling of the chord length and incoming wind velocity

$$\hat{\omega}_j = \omega_j \frac{c}{2V}. \tag{3.21}$$

In the following various dynamic stall models are presented. In the referenced literature some of the models are presented in terms of reduced time. To avoid confusion, all the models are given in terms of dimensional time parameters ω_j, which vary according to (3.21), $\hat{\omega}_j$ being constant.

3.3 Other Dynamic Stall Models

3.3.1 Beddoes-Leishman model

The Beddoes-Leishman model presented in what follow has been developed with the main purpose of calculating lift loads on helicopter profiles.(Leishman 2000; Leishman and Beddoes 1986b; Leishman and Beddoes 1986b; Leishman 1988; Beddoes 1978) This semi-empirical model takes into account the effect of flow compressibility under high frequency movements. Additionally, the model includes time delays under attached flow, and the contribution to the load coefficient from a discrete vortex forming under leading edge separation.

Under fully attached flow conditions, where the load response is basically linear, the time delays of the lift coefficient is modelled by the following relations

$$c_{L0,d}(t) = c_{L0}(\alpha) - c_1(t) - c_2(t) + c_3(t) + c_4(t), \tag{3.22}$$

where $c_3(t)$ and $c_4(t)$ are impulsive contributions diminishing in time due to wave propagation. Beddoes and Leishman gives the following expression for finding the impulsive contributions

$$\dot{c}_3 + \omega_5 c_3 = \frac{4}{M} A_3 \dot{\alpha}, \quad \dot{c}_4 + \omega_6 c_4 = \frac{1}{M} A_4 \frac{c}{V} \ddot{\alpha}. \tag{3.23}$$

M is the Mach number given as $M = V/V_0$, with V_0 as the speed of sound. $c_1(t)$ and $c_2(t)$ is determined from (3.10) with $A_1 + A_2 = 1$. It should be noticed that while $c_1(t)$ and $c_2(t)$ are found using $\alpha_{eq}(t)$, $c_3(t)$ and $c_4(t)$ should be found using the actual pitch rate $\dot{\alpha}$ and pitch acceleration $\ddot{\alpha}$.

To determine the dynamic attachment degree f_d, two state variables are introduced in the following way. First a retarded linear lift $c'_{L0,d}(t)$ is introduced as a delayed state variable of the linear lift $c_{L0,d}(t)$, which should give a one-to-one correspondence between the pressure coefficient and the dynamic lift at changing pitch rates. The following differential equation is used for $c'_{L0,d}(t)$

$$\dot{c}'_{L0,d}(t) = -\omega_7 (c'_{L0,d}(t) - c_{L0,d}(t)) \tag{3.24}$$

An effective angle of attack $\alpha_f = c'_{L0,d}(t)/\frac{dc_L}{d\alpha}|_{\alpha_0} + \alpha_0$ is then used to find the actual static attachment degree by which f_d can be found from (3.13) substituting α with α_f. Inserting the dynamic linear lift coefficient $c_{L0,d}$ and attachment degree f_d into (3.3) gives the dynamic lift coefficient. Notice that the Beddoes-Leishman model uses the approach of a modified angle of attack, which falls into the third group of models.

The approach for finding the leading edge separation contribution to the lift is similar to that described in equation (3.15) and (3.16). Beddoes and Leishman relates this contribution to the discreet vortex forming as the flow separates. When a certain pressure level is reached at the leading edge the vortex is said to separate and start moving across the profile. Hence, when $c'_{L0,d}$ is increased above a critical value, here named $c'_{L0,v}$, the vortex starts to move at a velocity $\frac{V}{3}$. As it reaches the trailing edge it is released into the wake after which $\Delta \dot{c}_L(t) = 0$.

Thus, one extra profile dependent parameter is introduced to describe the leading edge contribution namely the critical retarded lift $c'_{L0,v}$ and the travel velocity of the vortex. Beddoes (1978) found that the travel velocity of the vortex at low Mach number is approximately $V/3$.

The Beddoes-Leishman model includes seven state variables for every wing section at which the lift is calculated. Four variables c_1, c_2, c_3 and c_4 to describe the delayed linear lift, two variables $c'_{L0,d}$ and f_d to describe the dynamic movement of the separation angle and one variable $c_{L,v}$ to describe the induced lift from vortex forming under leading edge separation. In matrix formulation the linear differential equations describing these state variables can be organized as follows

$$\dot{\mathbf{z}}(t) = \mathbf{A}\mathbf{z}(t) + \mathbf{b}_0(\alpha, \dot{\alpha}, \ddot{\alpha}) + \mathbf{b}_1 \dot{c}_{L0}(t), \tag{3.25}$$

where

$$\mathbf{z}(t) = \begin{bmatrix} c_1(t) \\ c_2(t) \\ c_3(t) \\ c_4(t) \\ c'_{L0,d}(t) \\ f_d(t) \\ c_{L,v}(t) \end{bmatrix}, \quad \mathbf{A} = \begin{bmatrix} -\omega_1 & 0 & 0 & 0 & 0 & 0 & 0 \\ 0 & -\omega_2 & 0 & 0 & 0 & 0 & 0 \\ 0 & 0 & -\omega_5 & 0 & 0 & 0 & 0 \\ 0 & 0 & 0 & -\omega_6 & 0 & 0 & 0 \\ -\omega_7 & -\omega_7 & \omega_7 & \omega_7 & -\omega_7 & 0 & 0 \\ 0 & 0 & 0 & 0 & 0 & -\omega_3 & 0 \\ 0 & 0 & 0 & 0 & 0 & 0 & -\omega_4 \end{bmatrix},$$

$$\mathbf{b}_1 = \begin{bmatrix} A_1 \\ A_2 \\ 0 \\ 0 \\ 0 \\ 0 \\ 0 \end{bmatrix}, \quad \mathbf{b}_0(\alpha, \dot{\alpha}, \ddot{\alpha}) = \begin{bmatrix} 0 \\ 0 \\ \frac{4}{M} A_3 \dot{\alpha} \\ \frac{1}{M} A_4 \frac{c}{V} \ddot{\alpha} \\ \omega_7 c_{L0}(\alpha) \\ \omega_3 f(\alpha_f) \\ \Delta \dot{c}_L(t) H(1-\tau) H(\dot{\alpha}) \end{bmatrix}, \tag{3.26}$$

where τ is a dimensionless variable describing the placement of the leading edge separation vortex. For the vortex placed at the leading and trailing edge $\tau = 0$ and $\tau = 1$, respectively. The timely change of τ can, for a travel velocity of the vortex at $V/3$, be found as

$$\dot{\tau} = \frac{V}{3c} H(c'_{L0,d} - c'_{L0,v}) \tag{3.27}$$

The total lift coefficient then follows from the state variables as

$$c_L(t) = \left(\frac{1 + \sqrt{f_d(t)}}{2} \right)^2 \left[c_{L0}(\alpha) - c_1(t) - c_2(t) + c_3(t) + c_4(t) \right] + c_{L,v}(t), \tag{3.28}$$

where $f_d(t)$ is a function of $c'_{L0,d}(t)$ through α_f.

3.3.2 ONERA model

The ONERA model is based on the characteristics of the lift curve. The same arguments and system of equations are used for dealing with the drag and moment curves. Here we first assume

that the lift is independent of the Mach number and that the difference between the unsteady and steady lift coefficient is small. A classical way, which is also adopted in the previous described models, is to introduce the history effects of the lift as a differential equation. A functional dependence between $c_{L,d}$ and α, and the time derivatives of up to order N of both is postulated, as follows

$$A\big(c_{L,d}, \alpha, \dot{c}_{L,d}, \dot{\alpha}, \ddot{c}_{L,d}, \ddot{\alpha}. \cdots\big) = 0, \tag{3.29}$$

The function A is nonlinear, since it is assumed to describe the dynamic stall behaviour. However, it is assumed that the dynamic lift may be linearized around the static lift $c_{L,s}$ at α, corresponding to the first order Taylor expansion

$$\frac{\partial A}{\partial c_{L,d}}(c_{L,d} - c_{L,s}) + \frac{\partial A}{\partial \dot{c}_{L,d}}\dot{c}_{L,d} + \frac{\partial A}{\partial \ddot{c}_{L,d}}\ddot{c}_{L,d} + \cdots + \frac{\partial A}{\partial \dot{\alpha}}\dot{\alpha} + \frac{\partial A}{\partial \ddot{\alpha}}\ddot{\alpha} + \cdots = 0, \tag{3.30}$$

where it has been used that $A(c_{L,d}, \alpha, 0, 0, \cdots) = 0$. This linearization is only valid for small changes of the angle of attack with small deviations between the dynamic and static lift. During a dynamic stall cycle these variation may become rather large, but comparison with experimental data seems to justify (3.30). Derivatives with respect to α of higher order than two may be neglected, and in terms of frequencies one real pole and two complex conjugated poles seems to capture the characteristics of the lift. Hence, derivatives of higher order than three with respect to $c_{L,d}$ may be neglected. This reduces (3.30) to

$$\frac{\partial A}{\partial c_{L,d}}c_{L,d} + \frac{\partial A}{\partial \dot{c}_{L,d}}\dot{c}_{L,d} + \frac{\partial A}{\partial \ddot{c}_{L,d}}\ddot{c}_{L,d} + \frac{\partial A}{\partial \dddot{c}_{L,d}}\dddot{c}_{L,d} = \frac{\partial A}{\partial c_{L,d}}c_{L,s} - \frac{\partial A}{\partial \dot{\alpha}}\dot{\alpha} - \frac{\partial A}{\partial \ddot{\alpha}}\ddot{\alpha} \tag{3.31}$$

Additionally, the following observations is made. At low angles of attack, in the linear regime, measured frequency response functions are smooth and continues. By contrast, in the stall regime rapid variation is registered. The first statement leads to the conclusion, that in the linear regime the lift may be modelled by a first order differential equation with one real negative pole. In the stall area the lift development may then be modelled as a second order differential equation with two complex conjugated poles with negative real part. The derivatives of A in (3.31) is further assumed to be time independent. This leads to the following set of equations

$$\dot{c}_1 + \omega_1 c_1 = \omega_1 c_{L0} + (\omega_1 B_1 + B_2)\dot{\alpha} + B_1\ddot{\alpha}, \tag{3.32}$$

$$\ddot{c}_2 + 2\zeta\omega_2\dot{c}_2 + \omega_2^2(1+\zeta^2)c_2 = -\omega_2^2(1+\zeta^2)\left(\Delta c_L + B_3\Delta\dot{c}_L\right), \tag{3.33}$$

$$c_{L,d} = c_1 + c_2. \tag{3.34}$$

where $\Delta c_L = c_{L0} - c_{L,s}$. (3.32) accounts for the negative real pole $-\omega_1$ and (3.33) accounts for the complex conjugated poles $-\zeta\omega_2 \pm \mathrm{i}\omega_2$. The right hand side of (3.33) ensures that the complex conjugated poles only affect the solution in the stall regime, where $\Delta c_L \neq 0$. In the static limit $c_1 = c_{L0}$ and $c_2 = -\Delta c_L$ giving $c_{L,d} = c_{L0} - (c_{L0} - c_{L,s}) = c_{L,s}$.

Assuming that the memory effect on the circulation built-up is modelled by a single first order filter, rather than the two first order filter used in the present model. It is then possible to

express the differential equation for $c_{L0,d}(t)$, using the first two terms of (3.9) inserted in (3.8) and differentiating with respect to time, giving

$$\dot{c}_{L0,d} + \omega_1 c_{L0,d} = \omega_1 c_{L0} + (1 - A_1)\frac{\partial c_L}{\partial \alpha}\dot{\alpha}. \tag{3.35}$$

Comparing (3.35) and (3.32) reveals that for a first order filter the dynamic lift is uninfluenced by $\ddot{\alpha}$. Hence, $B_1 = 0$ and $B_2 = (1 - A_1)\partial c_L/\partial\alpha$. It should be noticed that the ONERA model, as is the case for the proposed model and the Beddoes-Leishman model, includes a contribution from $\Delta\dot{c}_L$. The first two models relate this contribution to the leading edge vortex buildup.

Small amplitude oscillations in the linear regime makes it possible to determine the variables ω_1 and B_2. With these determined, small amplitude oscillations in the stall regime are used to determine the parameters ζ, ω_2 and B_3. The performance of the model should then be verified from large amplitude oscillations at various frequencies.

Finally, the state formulation of the ONERA model reads

$$\dot{\mathbf{z}} = \mathbf{A}\mathbf{z} + \mathbf{b} + \mathbf{B}\boldsymbol{\alpha},$$

$$\mathbf{z} = \begin{bmatrix} c_1 \\ c_2 \\ \dot{c}_2 \end{bmatrix}, \quad \mathbf{A} = \begin{bmatrix} -\omega_1 & 0 & 0 \\ 0 & 0 & 1 \\ 0 & -2\zeta\omega_2 & -\omega_d \end{bmatrix}, \quad \boldsymbol{\alpha} = \begin{bmatrix} \alpha \\ \dot{\alpha} \end{bmatrix}$$

$$\mathbf{b} = \begin{bmatrix} 0 \\ 0 \\ \omega_d c_L \end{bmatrix}, \quad \mathbf{B} = \begin{bmatrix} \omega_1 \frac{\partial c_L}{\partial \alpha}|_{\alpha_0} & (1 - A_1)\frac{\partial c_L}{\partial \alpha}|_{\alpha_0} \\ 0 & 0 \\ -\omega_d^2 \frac{\partial c_L}{\partial \alpha}|_{\alpha_0} & -\omega_d^2 A_2 \left(\frac{\partial c_L}{\partial \alpha}|_{\alpha_0} - \frac{\partial c_L}{\partial \alpha}|_{\alpha}\right) \end{bmatrix},$$

$$c_{L,d} = c_1 + c_2 \qquad , \tag{3.36}$$

where $\omega_d = \omega_2\sqrt{1 + \zeta^2}$ and B_3 is changed to A_2 for consistency in notation. It should be noticed, that the second term of row three, column two of $\mathbf{B}$ includes the slope of c_L at the present angle of attack. The ONERA model includes three state variables and 5 unknown parameters ω_1, ω_2, A_1, A_2 and ζ to be determined from experimental data

3.3.3 Øye model

As mentioned the nonlinearity in the aeroelastic load model is essentially due to the motion of the separation point on the back side of the profile. Øye (1991) has suggested a simple linear 1st order filter model, which is based on the same static data requirements as the Beddoes-Leishman model and the present model. The essence of the Øye model is that the relationship (3.3) for finding f is replaced by an interpolation between the lift coefficient at fully attached flow $c_{L0}(\alpha)$ determined from (3.2) and the static lift coefficient $c_{L1}(\alpha)$ at fully separated flow, corresponding to attachment degrees $f = 1$ and $f = 0$, respectively. The flow is defined to be fully separated at a given large angle of attack, α_{sep}, so $f = 0$ for $\alpha \geq \alpha_{\text{sep}}$. Øye assumes that the initial and final slopes of $c_{L1}(\alpha)$ may be chosen as $\partial c_{L1}/\partial\alpha|_{\alpha_0} = \frac{1}{2}dc_L/d\alpha|_{\alpha_0}$ and $\partial c_{L1}/\partial\alpha|_{\alpha_{\text{sep}}} = \frac{1}{12}dc_L/d\alpha|_{\alpha_0}$. Intermediate values of $c_{L1}(\alpha)$ are determined by Hermite interpolation. The interpolation curves c_{L0} and c_{L1} are shown in Fig. 3.6. Then, for $\alpha < \alpha_{\text{sep}}$ the static attachment degree f is determined by linear interpolation between the functional values c_{L0} and c_{L1}, i.e.

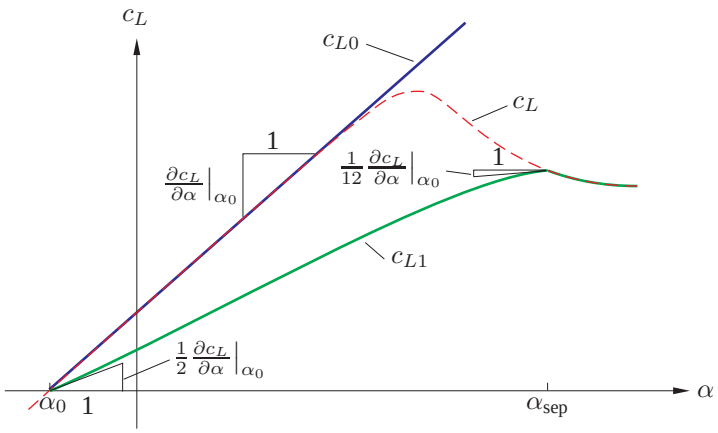

Figure 3.6 Interpolation curves in the Øye model.

$$f = \frac{c_L - c_{L1}}{c_{L0} - c_{L1}}. \tag{3.37}$$

Using f in (3.13) the dynamic attachment degree can be found. Øye proposed that a value of $\omega_3 = V/4c$ can be used (Øye 1991). Finally, the dynamic lift coefficient is determined from (3.37) by substituting f with f_d giving

$$c_L(t) = f_d(t)c_{L0} + (1 - f_d(t))c_{L1} \tag{3.38}$$

The Øye model is based on only one state variable $f_d(t)$, which introduces the dynamic effects under dynamic stall. However, no dynamic effects are introduced during attached flow conditions. Four parameters are introduced being the initial and final slopes of c_{L1}, the time scale parameter ω_3 and the angle of attack defining full separation α_{sep}. The first two are defined by Øye and are assumed to be profile independent. Hence, 2 profile dependent parameters needs calibration.

3.3.4 Risø model

The Risø model developed by Hansen *et al.* (2004) at Risø National Laboratory, Denmark, is a modified version of the Beddoes-Leishman model using only 4 state variable. Two to model the unsteady lift for attached flow conditions, and two to model the dynamics of trailing edge separation. Leading edge separation and the dynamics between the travelling and trailing edge vortices are disregarded in this model.

An approach similar to the Øye model is used to model the nonlinear quasi-static lift. Assuming knowledge of the separation point and the lift under fully attached flow and fully separated flow conditions, respectively, the lift is given by

$$c_L = f c_{L0} + (1 - f) c_{L1} \tag{3.39}$$

The linear lift c_{L0} is found from the lift slope at α_0, and the position of the separation point given by f is evaluated from (3.3). The restriction is that if f as determined from (3.3) is larger than 1.0, it is set equal to 1.0, and when full separation occur, f is set equal to 0. From a given set of measured c_L, f is found from (3.3) and c_{L1} may be determined from (3.39). Inverting (3.39) creates a singularity at $f = 1$, i.e. at fully attached flows. Under such conditions c_{L1} is set to half the linear lift, i.e. $c_{L1}(f = 1) = c_{L0}/2$.

To introduce dynamic effects f and c_{L0} is modified, as was the case for the proposed, Beddoes-Leishman and Øye models. Under fully attached flow conditions the Risø model works on a modified angle of attack instead of directly on the linear lift. The dynamic angle of attack α_d is given as

$$\alpha_d(t) = \alpha(1 - A_1 - A_2) + c_1(t) + c_2(t) \tag{3.40}$$

where

$$\dot{c}_i + \left(\omega_i + \frac{\dot{V}}{V}\right) c_i = \omega_i A_i \alpha \tag{3.41}$$

Now the dynamic linear lift is evaluated as

$$c_{L0,d} = c_{L0}(\alpha_d) + \frac{\pi c \dot{\alpha}}{2V} \tag{3.42}$$

The Risø model includes contribution from added mass. This term doesn't introduce additional state variables or parameters to be calibrated, hence it may easily be included in any of the other models. To introduce dynamic effects on the separation point motion the same approach as the Beddoes-Leishman model is used. A retarded linear lift $c'_{L0}(t)$ is found from (3.24), an effective angle of attack, not to be compared with the equivalent angle of attack described in section 3.5, is found as $\alpha_f = c'_{L0}/\frac{dc_L}{d\alpha}|_{\alpha_0} + \alpha_0$, and the delayed separation point f_d is determined from (3.13). This introduces additional 2 state variables c'_{L0} and f_d. In state space formulation the Risø may be written as follows

$$\dot{\mathbf{z}} = \mathbf{A}\mathbf{z} + \mathbf{b}, \tag{3.43}$$

$$\mathbf{z} = \begin{bmatrix} c_1 \\ c_2 \\ c'_{L0} \\ f_d \end{bmatrix}, \quad \mathbf{A} = \begin{bmatrix} -\left(\omega_1 + \frac{\dot{V}}{V}\right) & 0 & 0 & 0 \\ 0 & -\left(\omega_2 + \frac{\dot{V}}{V}\right) & 0 & 0 \\ 0 & 0 & -\omega_7 & 0 \\ 0 & 0 & 0 & -\omega_3 \end{bmatrix},$$

$$\mathbf{b} = \begin{bmatrix} \omega_1 A_1 \alpha \\ \omega_2 A_2 \alpha \\ \omega_7\left(c_{L0}(\alpha_d) + \frac{\pi c \dot{\alpha}}{2V}\right) \\ \omega_3 f(\alpha_f) \end{bmatrix} \tag{3.44}$$

$$c_{L,d}(t) = f_d(t) c_{L0}(\alpha_d) + (1 - f_d) c_{L1}(\alpha_d), \tag{3.45}$$

3.3.5 Boeing-Vertol model

The Boing-Vertol model presumes a relationship between the static and dynamic stall angle to determine a dynamic angle of attack α_d in the entire range of α. The relationship obtained by Liiva *et al.* (1969) is given as

$$\alpha_{ds} - \alpha_s = A_1 \sqrt{\frac{c|\dot{\alpha}|}{2V}}, \tag{3.46}$$

where α_{ds} is the dynamic stall angle as indicated in Figure 3.7. Hence, the dynamic angle of attack should in some way be delayed with the right hand side of (3.46) compared with the static angle of attack. This suggests the following setting

$$\alpha_d = \alpha - A_1 \sqrt{\frac{c|\dot{\alpha}|}{2V}} \frac{\dot{\alpha}}{|\dot{\alpha}|}, \tag{3.47}$$

where a sign factor has been included in the delay term in order to consider both positive and negative values of $\dot{\alpha}$. Now $c_{L,d}$ is determined as

$$c_{L,d} = c_L(0) + \frac{c_L(\alpha_d) - c_L(0)}{\alpha_d} \alpha. \tag{3.48}$$

The theory of the model is illustrated in Figure 3.7, where the static and dynamic lift curves are plotted as (– –) and (——), respectively. Firstly, consider an angle of attack α_1 in the linear domain during increasing α, hence $\dot{\alpha} > 0$. Using (3.47) gives a related dynamic angle of attack α_{d1} which is less than α_1. Now, $c_L(\alpha_{d1})$ is evaluated indicated by (○), the slope of the line going from $c_L(\alpha_d)$ is evaluated, giving the fraction in (3.48). Finally, $c_{L,d}$ illustrated by (○) is determined from (3.48). In the linear domain, the slope determined at α_d is equal to the slope of the static lift, thus, no distinction can be made between the static and dynamic lift curve. Now,

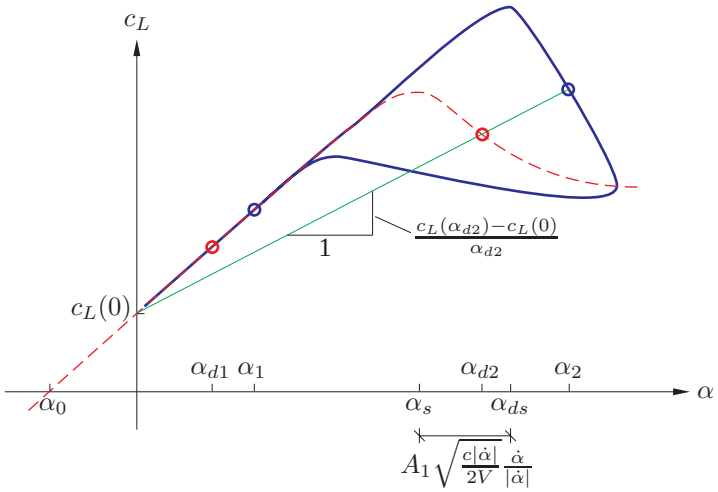

Figure 3.7 Illustration of the Boing-Vertol model. (— —) Static lift. (———) Dynamic lift. (○) Quasi-static angle of attack. (○) Dynamic angle of attack.

consider an angle of attack α_2 in the stall regime. Again, the corresponding dynamic angle of attack α_{d2} is found from (3.47). Then, the slope determined at α_d is less than that of the fully attached region, making $c_{L,d}(\alpha_2)$ less than that of a linear growing lift. This creates a dynamic stall cyclic behaviour as indicated in Figure 3.7.For $\dot\alpha = 0$ it is easily seen that the combination of (3.47) and (3.48) generates the static lift, i.e. the dynamic curve crosses the static curve for $\dot\alpha = 0$.

3.4 Comparison of Models

The main input to all the models are the quasi-static lift data. The dynamic stall models should be able to reproduce these in the entire range of α. At low reduced frequencies and at angles of attack below the point of full separation, all the models generate results close to the static lift curve. At angles of attack above this point the Beddoes-Leishman model is no longer capable of reproducing static data, whereas the proposed model follow the static curve nicely due to the modification C_{L0}. This is illustrated in Figure 3.8, where static data from a NACA 63-418 profile (Abbott and von Doenhoff 1959) is extrapolated linear from 20 ° into the deep stall regime to the point $c_L(90°) = 0$.

The Beddoes-Leishman model also seems to perform badly at angles of attack just below fully separated flow conditions (approximately 32 °), where the lift seems to curve away from the measured values. This is caused by the way the effective attachment degree is determined from the static data set, where linear interpolation is used in this simulation. The problem may be solved by using quadratic interpolation, which obviously is more time consuming.

In the following examples is the performance of the various models validated against experimental results from Wind-tunnel tests on a Vertol 23010-1.58 airfoil. The test results are presented by Liiva (1969), and are used to verify the Boing-Vertol model (Tarzanin 1972). The experimental data are produced for harmonic rotation of the airfoil at various mean angle of at-

Table 3.1 Profile dependent parameters for the various dynamic stall models determined from dynamic test data from Vertol 23010-1.58 profile. $\hat{\omega}_j = \omega_j 2V/c$.

	Presented	Beddoes-Leishman	ONERA	Øye	Risø	Boing-Vertol
$\hat{\omega}_1$	0.0455	0.125	0.125	-	0.0455	-
$\hat{\omega}_2$	0.3	0.375	0.1	-	0.3	-
$\hat{\omega}_3$	0.1	0.275	-	0.07	0.0875	-
$\hat{\omega}_4$	0.075	0.075	-	-	-	-
$\hat{\omega}_5$	-	2.5	-	-	-	-
$\hat{\omega}_6$	-	2.5	-	-	-	-
$\hat{\omega}_7$	-	0.4	-	-	0.4125	-
A_1	0.165	0.3	0.3	-	0.165	0.87
A_2	0.335	0.7	0.1	-	0.335	-
A_3	-	1.0	-	-	-	-
A_4	-	1.0	-	-	-	-
α_v	14.75°	-	-	-	-	-
$c'_{L0,v}$	-	1.6	-	-	-	-
α_{sep}	-	-	-	32°	-	-
ζ	-	-	0.7	-	-	-

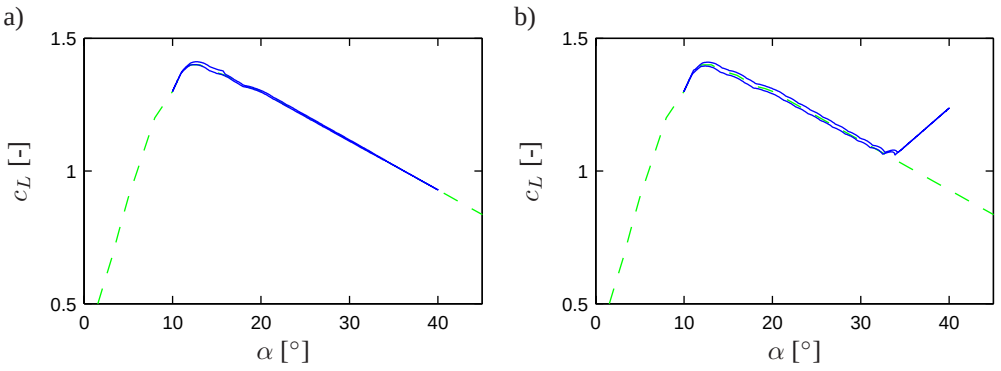

Figure 3.8 Lift coefficient for a NACA 63-418 at low reduced frequency. $k = 0.001$, $\alpha_{\text{mean}} = 25°$, $\Delta\alpha = 15°$, (– –) Static test data. a) (———) Presented model. b) (———) Beddoes-Leishman model

tack, the amplitude $\Delta\alpha$ is held constant at 4.85° and the reduced frequency $k = \frac{c\omega}{V}$ is kept constant at 0.124, where c is the chord length of the profile set equal to 1.5 m, V is the undisturbed incoming wind velocity equal to 60 m/s and ω is the rotational frequency of the oscillation. Ideally, to calibrate the various models a series of test data should be available at a range of reduced frequencies, amplitude and mean value of oscillation. The rather limited set of test data makes the calibration of the parameters very uncertain, but the performance of the models may to some extend be analysed. Under fully attached flow conditions the proposed, Beddoes-Leishman, ONERA and Risø models all perform well. For the presented and Risø models the incompressible parameters given by Jones (1940) are used. The parameters of the various models during stall

conditions are calibrated by least-square-error method between the model output and test data. The data point used in the least square method are evenly distributed, hence, all regions of the model are prioritized equally. The calibrated parameter values are listed in Table 3.1. It is obvious that the Boing-Vertol and the Øye models are relative easy to calibrate since only a few parameters needs to be identified. The presented model have 7 parameters, the ONERA model have 5 parameters and the Beddoes-Leishman model have 12 parameters that needs to be calibrated. The many parameters of the Beddoes-Leishman model makes optimal calibration virtual impossible. Tran and Petot (1981) devised a method of calibrating the ONERA model from small amplitude, low and high frequency test data below and above stall. Since no such variety of test data have been available, the calibration is also done by least square error method.

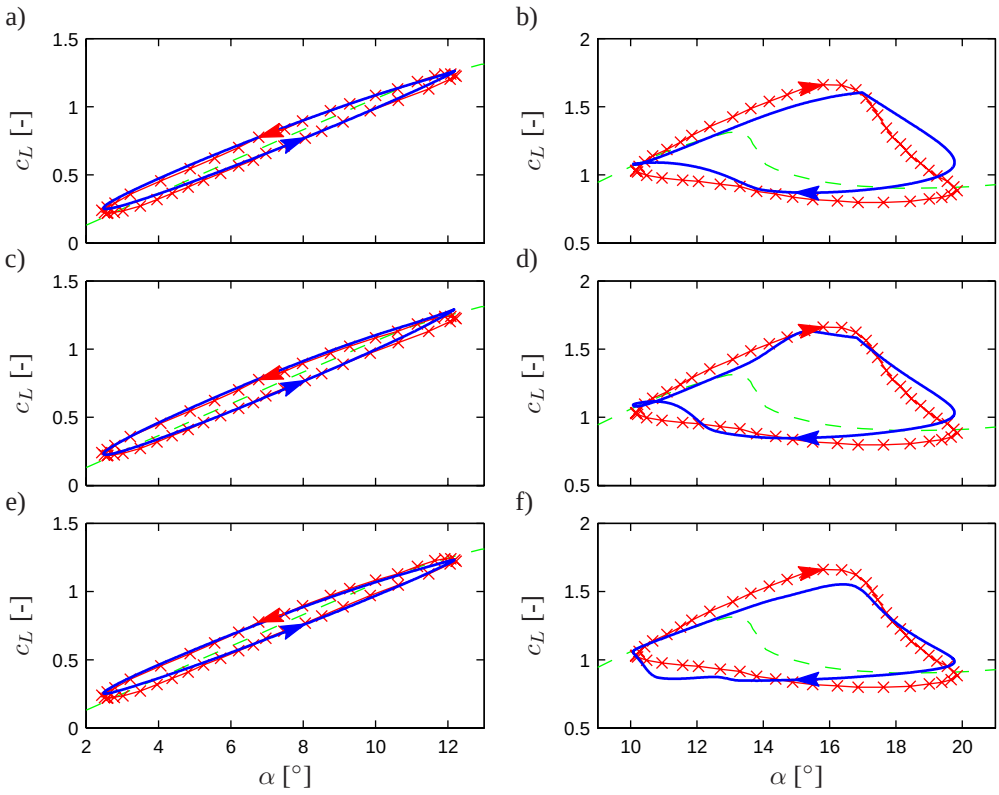

Figure 3.9 Comparison between dynamic stall models and lift coefficient for a Vertol 23010-1.58 profile at various mean angles of attack. $k = 0.124$ rad. (– –) Static test data. (×) Dynamic test data. a)-b) (——) Presented model. c)-d) (——) Beddoes-Leishman model. e)-f) (——) Risø model.

In Figure 3.9 and Figure 3.10 are the various models compared experimental data from the Vertol 23010-1.58 profile. Test data are indicated by (×), measured static data which serves as input are illustrated as (– –), and the results from the calibrated dynamic stall models using parameters given in table 3.1 are plotted as (——). From the top down in Figure 3.9 the numerical results are plotted obtained from the proposed, Beddoes-Leishman and Risø models, and in Figure 3.10 ONERA, Øye and Boing-Vertol models, respectively. The cyclic direction of the

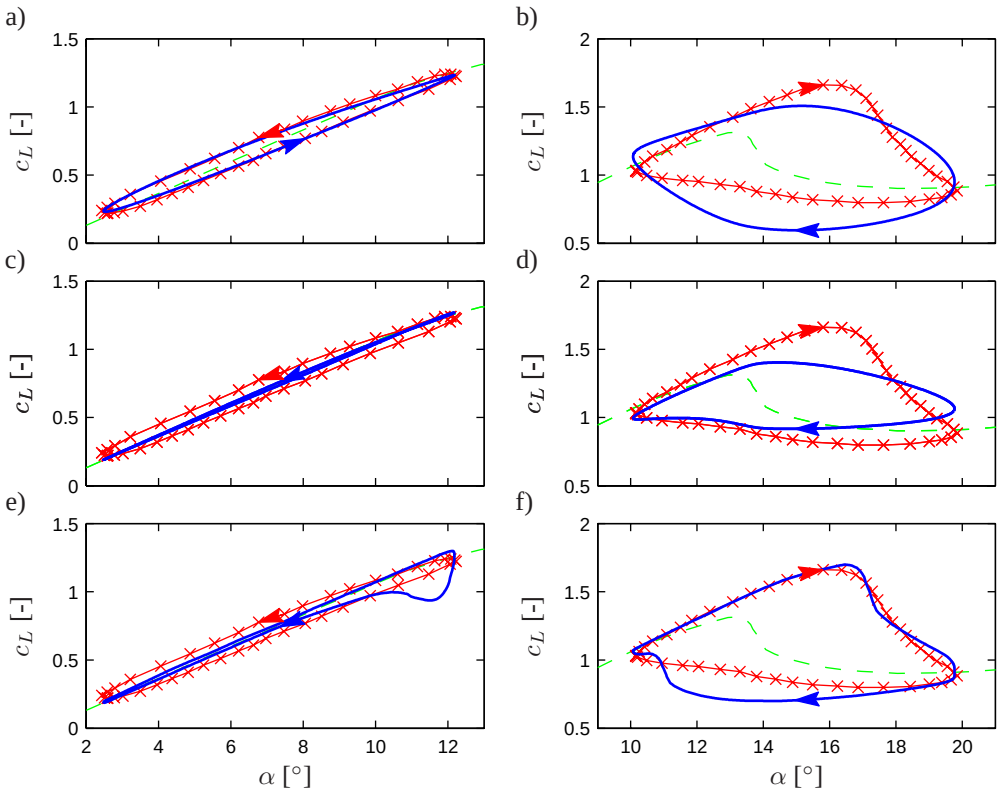

Figure 3.10 Comparison between dynamic stall models and lift coefficient for a Vertol 23010-1.58 profile at various mean angles of attack. $k = 0.124$ rad. (– –) Static test data. (×) Dynamic test data. a)-b) (——) ONERA model. c)-d) (——) Øye model. e)-f) (——) Boing-Vertol model.

experimental data are indicated by a red arrow, and are placed on the upper part of the cycle, whereas the cyclic direction of the numerical simulations are indicated by a blue arrow placed on the lower part of the cycle. Hence, the red and blue arrow should point in opposite directions for the cyclic behaviour to be alike. The subfigures to the left illustrate the results of a test situation under fully attached flow condition with a mean angle of attack of 7.33 °. As seen, the proposed, Beddoes-Leishman, Risø and ONERA models capture the cyclic behaviour, whereas both the Øye and Boing-Vertol models produce results, which travels in the opposite direction of the test data. To the right in Figures 3.9 and 3.10 the mean angle of attack is increased to 14.92 °, which is in the stall regime. All models capture the correct travel direction but especially the Øye and the ONERA models predict a maximum lift which is approximately 10-15% below the measured value. The Øye model fails mainly because of no travelling vortex contribution, which is significant at high reduced frequencies. Especially, the Boing-Vertol model captures the test data very effectively, but also the presented, Risø and Beddoes-Leishman models perform well. The presented and Beddoes-Leishman models predicts the declining lift after the dynamic stall peak too high. Beddoes and Leishman (1986a) suggest an increase of the vortex dissipation after the vortex leaves the profile, i.e. increasing ω_4. This modification will produce better results in

this particular case for both the present and Beddoes-Leishman models. The Risø model predicts a maximum lift, which is a little below that of the two other models but still within acceptable range. It should be noted that even though the state variable $c'_{L0,d}$ in the Beddoes-Leishman and the Risø model should describe the same effect the calibrated parameter ω_3 are very different. This is due to the fact that the Risø model does not include contributions from leading edge separation, why these contributions are absorbed into the first trailing edge separation state variable. As seen from Figure 3.9f, this work nicely for the presented case.

Next the performance of the presented model is analysed. Figure 3.11 shows the static values of c_{L0} and θ indicated by (– –) corresponding to the static lift coefficient from NACA 63-418. The reason for using the NACA 63-418 profile is to illustrate the variation of the static and dynamic variables also during fully separated flow conditions, which is not obtained within the angle of attack limits of the Vertol profile. A simulation of $c_{L0,d}$ and θ_d is shown as (——). As seen full separation occurs at approximately 32°, where $\theta = \pi$ and c_{L0} is changed from the linear approximation to $4c_L$.

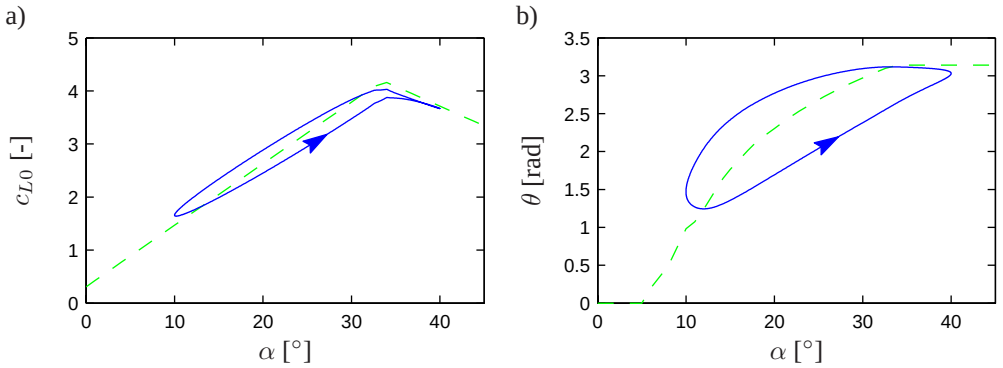

Figure 3.11 State variables of the present model during dynamic stall cycle of a NACA 63-418 profile, $k = 0.124$ rad, $\alpha_{\text{mean}} = 25°$, $\Delta\alpha = 15°$. (– –) Quasi-static component. a) (——) $c_{L0,d}$. b) (——) θ_d.

Figure 3.12 illustrate the performance of the present model at various variation of parameters. The static input indicated by (– –) is from the Vertol 23010-1.58 profile, and (——) indicate a reference case using the parameters given in 3.1 column 2. In Figure 3.12a the result of a simulation at low angles of attack in the fully attached flow domain is plotted. (——) illustrate a simulation with $A_1 = 0.3$ and $A_2 = 0.7$ which matches the compressible parameters of the Beddoes-Leishman model. The hysteretic loop becomes wider due to no initial change of the lift for a step change of angle of attack for compressible condition, i.e. when $A_1 + A_2 = 1$. Figure 3.12b-d illustrate numerical results during dynamic stall conditions with $\alpha_{\text{mean}} = 15°$ at variation of ω_3, ω_4 and α_v, respectively. As seen from Figure 3.12b, a change of ω_3 doesn't influence the maximum lift significantly. Also increasing ω_3 by 50% from the reference value indicated by (——) only introduces small deviations from the reference value. However, decreasing ω_3 by 50% indicated by (——) introduce significant changes to the lift both at flow reattachment at low angles of attack and also in the deep stall regime at high angles of attack. At low values of ω_3 small variations in the static lift is filtered out and the curve becomes more smooth. Variation of ω_4 and α_v illustrated in Figure 3.12c and 3.12d, basically moves the dynamic stall point up and down and sideways, respectively. In Figure 3.12c the dynamic lift without the vortex contribu-

tion $c_{L,d}$ is plotted as (– –), the vortex contribution at these relative high reduced frequencies is significant.

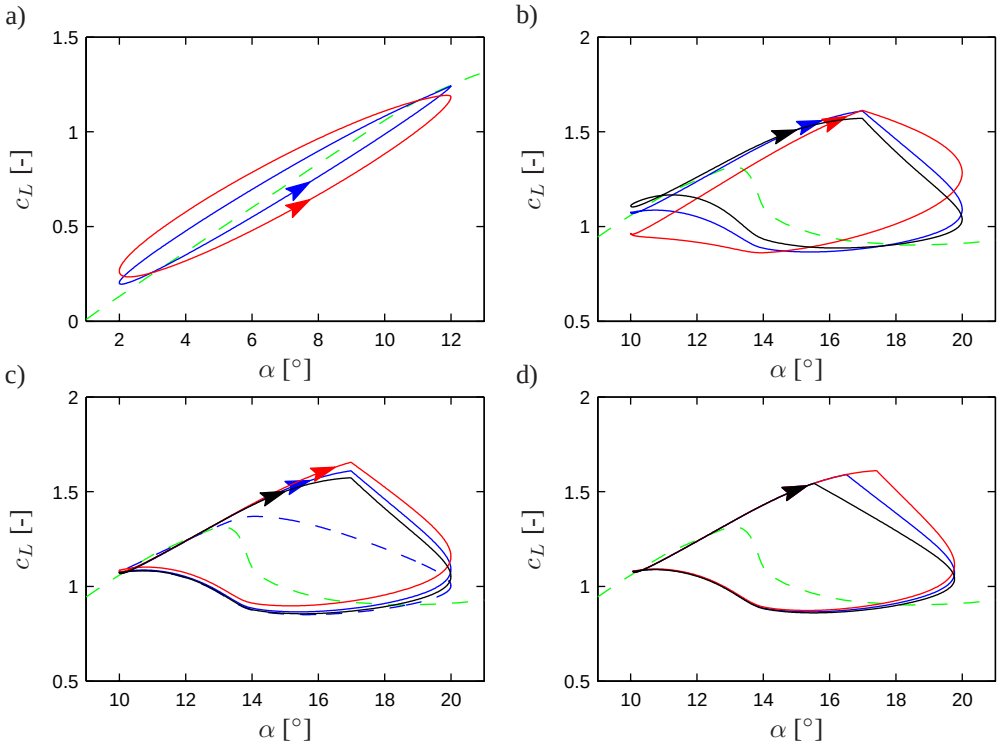

Figure 3.12 Lift curve of the Vertol 23010-1.58 profile at various parameter values. $k = 0.124$ rad, $\Delta\alpha = 10°$. (– –) Quasi-static component. (———) reference case using the parameters of table 3.1 column 2.
a) Variation of A_1 and A_2. $\alpha_{\text{mean}} = 7°$. (———) $A_1 = 0.3$, $A_2 = 0.7$.
b) Variation of ω_3. $\alpha_{\text{mean}} = 15°$. (———) $\omega_3 = 4$. (———) $\omega_3 = 12$.
c) Variation of ω_4. $\alpha_{\text{mean}} = 15°$. (———) $\omega_4 = 4$. (———) $\omega_4 = 8$.
d) Variation of α_v. $\alpha_{\text{mean}} = 15°$. (———) $\alpha_v = 13.75°$. (———) $\alpha_v = 15.75°$.

3.5 Other aspects of dynamic stall models

3.5.1 Aeroelastic Modelling

All the dynamic stall models are one-degree-of-freedom models in $\alpha(t)$. Assume that the profile has the translation velocity $\dot{u}_1'(t)$ and $\dot{u}_2'(t)$ in the blade and edgewise direction, respectively, the pitch velocity $\dot{\alpha}(t)$ around the aerodynamic centre A, and exposed to turbulence components $v_1'(t)$ and $v_2'(t)$. Assuming the wavelength of the turbulence is significantly larger than the chord length of the profile, the structural deformation velocities and turbulence components will introduce a uniform flow change over the entire profile. Whereas, the pitch motion introduces a linear flow variation over the section. These effects are included through the introduction of an equivalent angle of attack $\alpha_{eq}(t)$. From the profile the deformation velocities and turbulence

components can be regarded as a variation of the incoming velocity field, however, due to the flow variation over the profile from the pitch velocity, this contribution cannot be included directly. Under fully attached flow conditions with a pitch motion $\dot{\alpha}(t)$ it can be shown that $\alpha_{eq}(t)$ should be found from the downwash velocity at the $\frac{3}{4}c$ point for the flow to follow the profile and separate at the trailing edge fulfilling the so-called Kutta condition, see Fung (1993, p. 401 ff). This is illustrated in Figure 3.13.

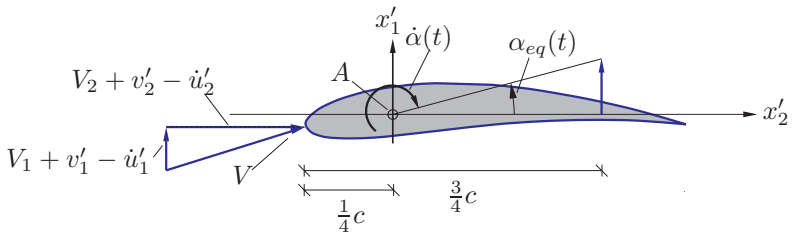

Figure 3.13 Definition of α_{eq}.

Including turbulence components and deformation velocities as variation of the mean wind gives the following expression for α_{eq}

$$\sin \alpha_{eq}(t) = \frac{V_1(t) + v_1'(t) - u_1'(t) + \frac{c}{2}\dot{\alpha}(t)}{V(t)} \tag{3.49}$$

where $V(t)$ is the resulting wind speed including contributions from both turbulence components and deformations velocities. This gives the following linearized expression for $\alpha_{eq}(t)$

$$\alpha_{eq}(t) \simeq \alpha(t) + \frac{c}{2V}\dot{\alpha}(t) + \frac{v_1'(t) - \dot{u}_1'(t)}{V(t)} \tag{3.50}$$

where $\alpha(t)$ is the mean wind contributions to the angle of attack. In (3.50) it is presumed that $\dot{u}_1'(t)$, $v_1'(t)$, $\alpha(t)$ and $\dot{\alpha}(t)$ are sufficiently small, so that linearization is possible. Even though, only valid under fully attached flow, it is common practise to determine $\alpha_{eq}(t)$ from the downwash at the $\frac{3}{4}c$-point under separated flow conditions. Now, $\alpha(t)$ in (3.19) is simply replaced with $\alpha_{eq}(t)$ to introduce aeroelastic contributions.

3.5.2 3-D effects

The presented models all assume 2D flow conditions, but the rotating blade will experience an outwards axial wind component generating so-called 3D effects on the load components. A widely adopted approach for including 3D effects is to modify the 2D quasi-static input to the models. Chaviaropoulos and Hansen (2000) proposed a correction law of lift drag and moment coefficients including the influence of twist angle throughout the wing. Harris (1966) came up with a simple correction used in the Boeing-Vertol model where the static 2D lift simply is divided by $\cos\Lambda$ where Λ is the yawed flow angle. This approach indicates that 3D effects tend to delay the static stall and hereby increase the maximum lift.

3.6 Concluding Remarks

In the present work a model for determining the dynamic lift coefficient of a wind turbine wing profile has been developed, based on the effects of various flow conditions. In the model three basic features have been included. Firstly, a time delay is introduced under fully attached flow situations using two filter equations. Secondly, the time delay in the motion of the separation point is described by one filter equation. And last, a contribution from leading edge separation vortex and pressure peak is included by one filter equation.

The characteristics of the present model are a simplified description of attached flow, calculating lift by analytical linearized flow theory in the entire range of the angle of attack and inclusion of a contribution from leading edge separation. Additionally, a modified model for the delay on the attachment degree has been suggested, which operates on a mapping of the profile onto a circle in the complex plane.

The model has been validated against dynamic test data of the Vertol 23010-1.58 profile. It has been demonstrated that the present model is capable of producing the correct cyclic behaviour of the lift under fully attached conditions. Also under dynamic stall cycle is the present model capable of modelling the maximum lift and reproducing lift data to a satisfactory degree. A variety of different approaches of modelling dynamic stall has been described including the Beddoes-Leishman, Risø, ONERA, Øye and Boing-Vertol methods. Only the present model, Risø and Beddoes-Leishman models are capable of reproducing the experimental data both at fully attached flow conditions and in the stall regime. 7 parameters are introduced in the present model compared to 12 in the Beddoes-Leishman model making calibration considerable less complicated. The Risø model introduces an arbitrary interpolation comparable to that devised of the Øye model, to introduce the effects of trailing edge separation. Further, it includes an extra state variable to model trailing edge separation. However, the present model perform equally well using only one state variable for trailing edge separation and introducing an extra state variable to account for leading edge separation, making the present model capable of reproducing effects under a greater variety of flow conditions.

CHAPTER 4
Coupling of Two-Degrees-of-Freedom Structural Model and Dynamic Stall Model

In this chapter a combined formulation is made of the nonlinear structural equations of motion given in chapter 2 and the dynamic stall model presented in chapter 3. To analyse the behaviour of the combined system various numerical examples are carried out. At first, the wing is assumed to rotate in a constant incoming wind field while the entire wing is pitch harmonically below and above stall. Then, the wing is subject to support point motion in a constant wind field at various constant pitch settings. Next, the wing is assumed to rotate in a boundary layer flow with effect of tower passage. Finally, the performance of the wing is illustrated under active vibration control using pitch actuation of the wing.

4.1 Formulation of the Combined Problem

The combined numerical analysis may be divided into three sub problems. First, the wind components at a given section of the wing should be determined, giving an effective angle of attack of that particular section. Then, the aeroelastic forces throughout the wing is determined using the dynamic stall model. Finally, the structural deformation of the wing subjected to the aeroelastic loading and support point motion is determined.

4.1.1 Wind profile

Two different wind profiles are considered.

1. Constant wind field used to analyse the effect of harmonic pitching of the wing and support point motion at different constant pitch settings.

2. Logarithmic boundary layer profile including tower passage modelled as potential flow around a cylinder, in order to analyse the effects of periodic variation of the wind profile and rotational effects.

In this chapter the qualitatively behaviour of the combined models is sought. To simplify matters the induced velocities, often determined by the BEM method, see e.g. (Hansen 2000), are disregarded. However, for a quantitatively analysis the induced velocity may in some cases contribute significantly and they should be incorporated into the model if more accurate results are needed.

The mean wind velocity in the undisturbed flow is modelled as

$$V = -V_0, \tag{4.1}$$

$$V(x_3) = -V_0 k_t \ln\left(\frac{x_3}{z_0}\right), \tag{4.2}$$

where V_0 is the basic wind velocity, k_t is the terrain factor, and z_0 is the roughness length. According to the Danish standard (1998) k_t and z_0 are chosen as 0.17 and 0.01, respectively, for open land or sea. The effect of tower passage is included as a potential flow over a cylinder composed of the sum of a uniform flow and a doublet. The flow velocities V_1 and V_2 in the local x_1- and x_2-directions indicated in Figure 2.2 are found to be, see e.g. (Anderson 2001)

$$\begin{aligned} V_1'(x_1,x_2,x_3) &= \left(1 + R^2(x_3)\frac{x_2^2 - x_1^2}{(x_1^2+x_2^2)^2}\right)V(x_3), \\ V_2'(x_1,x_2,x_3) &= x_3'\Omega_0 - R^2(x_3)\frac{2x_1x_2}{(x_1^2+x_2^2)^2}\cos(\Phi(t))V(x_3). \end{aligned} \tag{4.3}$$

where $R(x_3)$ is the radius of the cylinder, i.e. the tower radius at a given height. It should be noticed that V_1' is positive according to the transformation (2.3) between the global and local coordinate systems. Further, in addition to the initiated V_2' component from the tower passage, the rotational velocity $x_3'\Omega_0$ is added to V_2'. In Figure 4.1 is the reduction factor of V_1' indicated by the colour map for a given tower diameter, also the flow lines at discrete points are shown as black lines. (4.3) is used when the considered wing section is below the tower height, and (4.2) is used when the section is above the tower height. To avoid a discontinuity in the flow velocity when the section moves from below to above the tower height, the diameter of the tower is reduced linearly with height from the actual diameter to zero over a given length.

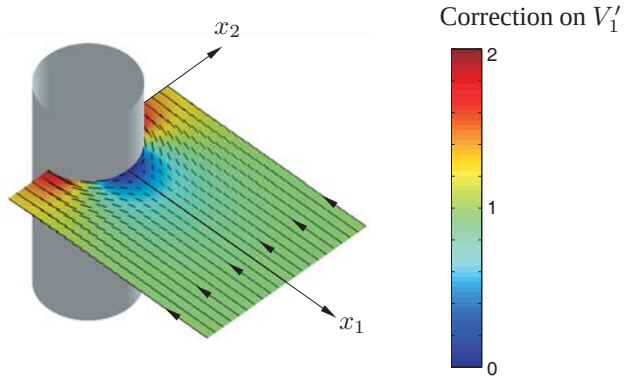

Figure 4.1 Potential flow around tower. The colours indicate the correction factor on V_1'.

4.1.2 Aeroelastic forces

From the mean wind velocities, an angle of attack is evaluated at given two dimensional wing sections throughout the wing. The dynamic stall state variables are determined from (3.18) for N sections as indicated in Figure 4.2, giving a lift force at discrete values of x'_3. The lift is then projected onto the local x'_1- and x'_2-directions to evaluate the aerodynamic forces $p'_{1,A}(x'_3,t)$ and $p'_{2,A}(x'_3,t)$.

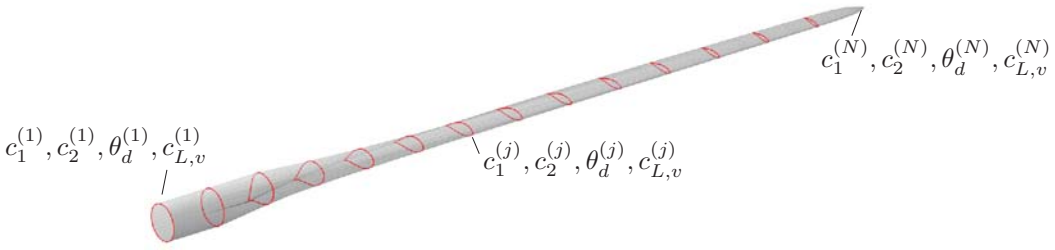

Figure 4.2 Dynamic stall state variables evaluated at discreet sections throughout the wing. Upper index indicate section number.

4.1.3 Structural system

The structural equations of motion (2.79) can now be integrated using e.g. a fourth order Runge Kutta algorithm. Only the coefficients $a_{ijk,0}$ and $f_{i,0}$ given in (2.70) are affected by the dynamic variation of the lift. The integral expressions for $a_{ijk,0}$ and $f_{i,0}$ are evaluated numerically. Differentiating (2.59) with respect to time and only including contributions from the first two modes, the modal coordinate velocities determined from solving (2.79) are used to determine the velocity components $\dot{u}'_1(t)$ and $\dot{u}'_2(t)$ throughout the wing. These velocities are finally introduced in the expression of the equivalent angle of attack α_{eq} from (3.50), making it possible to iterate forward in time. In short the numerical procedure is as follows

1. Give initial conditions at $t_i = t_0$ of: $\Phi(t_0)$, $q_1(t_0)$, $q_2(t_0)$, $\dot{q}_1(t_0)$, $\dot{q}_2(t_0)$, $c_1^{(j)}(t_0)$, $c_2^{(j)}(t_0)$, $\theta_d^{(j)}(t_0)$ and $c_{L,v}^{(j)}(t_0)$, $j = 1,2,\ldots,N$.
2. Use (2.59) to determine the velocities $\dot{u}_1'^{(j)}(t_i)$ and $\dot{u}_2'^{(j)}(t_i)$.
3. Determine global coordinates of N wing sections from $\Phi(t_i)$ and transformation matrix (2.3).
4. Calculate local wind velocities from (4.1) or (4.2) and (4.3), depending on the chosen profile.
5. Calculate $\alpha_{eq}^{(j)}(t_i)$ from (3.50) using $\dot{u}_1'^{(j)}(t_i)$ and $\dot{u}_2'^{(j)}(t_i)$.
6. Solve (3.18) for N wing sections, calculate the aerodynamic lift and project onto the local x'_1- and x'_2-directions in order to determine $p_{\alpha,A}'^{(j)}(x'_3,t_i)$.

7 Evaluate $a_{ijk,0}(t_i)$ and $f_{i,0}(t_i)$ from (2.70), using the distribution of $p''_{\alpha,A}((x'_3,t_i)$.

8 Solve the structural equations of motion (2.79) for $q'_1(t_{i+1})$, $q'_2(t_{i+1})$, $\dot{q}'_1(t_{i+1})$ and $\dot{q}'_2(t_{i+1})$.

9 Increment time and repeat step 2 to 8.

4.2 Numerical Examples

4.2.1 Data used in numerical simulations

The data used in the numerical examples are divided into three groups: wind field, structural system and dynamic stall parameters. Due to insufficient experimental data for the actual wing sections of the wing, the parameters calibrated for the Vertol 23010-1.58 profile in chapter 3 are used for all sections throughout the wing. The static lift data, used as input, is extrapolated lift data from the NACA 63-418 profile (Abbott and von Doenhoff 1959). The extrapolation is carried out from 20° to 90° as a linear variation to $c_L(90°) = 0$. The static data is illustrated in Figure 4.3a with (——) being measured data and (– –) being extrapolated values. To create an overview of the parameters needed within the model, the calibrated values for the dynamic stall model from Table 3.1 are repeated in Table 4.1 column 1. In order not to confuse the dynamic stall timescale parameters with the eigenfrequencies of the wing, the notation of the timescale parameters is changed from ω_i to ν_i. The parameters ν_1, ν_2, ν_3 and ν_4 are determined from a wind velocity of 60 m/s and a chord length of 1.5 m, which matches a section at approximately $x'_3 = 37$ m. These values are used as constants throughout the wing. In Table 4.1 column 2 and 3, the parameters used to define the wind field and the structural system are listed. The parameter values for ω_2, Ω_0 and u_0 are varied within the different numerical simulations to analyse the behaviour of the system. The wing properties: twist, moment of inertia mass per unit length and chord length, are those illustrated in Figure 2.11, and the components of the eigenmodes are illustrated in Figure 2.9. Then, the time independent coefficients of the structural system match those given in (2.78).

Table 4.1 Parameters used within the numerical simulations. T_h is the tower height, $T_{d,\text{bottom}}$ is the tower diameter at ground level, and $T_{d,\text{top}}$ is the tower diameter at top level. N_L is the distance from the tower centre to the rotor plane.

Dynamic stall		Wind field		Structural system	
ν_1	3.64 rad/s	k_t	0.17	ζ_1	0.01
ν_2	24 rad/s	z_0	0.01 m	ζ_2	0.01
ν_3	8 rad/s	V_0	12 m/s	ω_1	5.14 rad/s
ν_4	6 rad/s			ω_2	variable
A_1	0.165			Ω_0	variable
A_2	0.335			u_0	variable
α_v	14.75°			ω_0	$3\Omega_0$
				T_h	90 m
				$T_{d,\text{bottom}}$	4 m
				$T_{d,\text{top}}$	2 m
				N_L	5 m

4.2.2 Pitch of wing in constant wind field

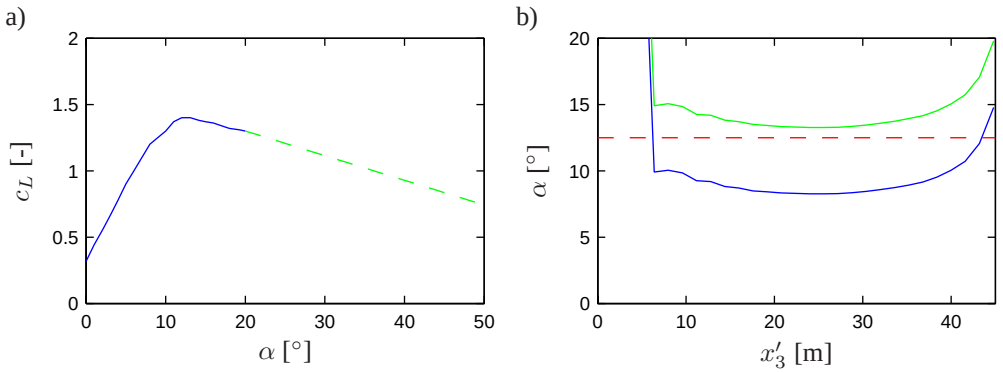

Figure 4.3 a) Static data for a NACA 63-418 profile. (——) Measured values. (– –) Extrapolated values. b) Variation of angle of attack throughout the wing. (——) $\alpha_p = 0°$. (——) $\alpha_p = 10°$. (– –) Static stall angle.

This example is created to investigated the effect of pitching the wing. The incoming flow field is constant 12 m/s, and no support point motion is applied. Hence, changes in excitation of the wing only occur due to change in pitch setting α_p.

In Figure 4.3a the static lift data is plotted for the NACA 63-418 profile used throughout the wing. It is seen that the static stall angle is approximately 12.5°. Figure 4.3b illustrates the angle of attack at $\Omega_0 = 1.6$ rad/s with $\alpha_p = 0°$ and $\alpha_p = 10°$ indicated by (——) and (——), respectively. The static stall angle at 12.5° is plotted as (– –). The angle of attack is approximately constant from $x_3' = 8$ m to $x_3' = 40$ m with a slight increase at the tip because of the twist of the wing sections throughout the wing. At the root of the wing the meeting wind velocity is close to zero, which produces angles of attack close to 90°. However, the lift from the root sections contributes insignificantly to the deformation of the wing and will be disregarded in the following analyses. For $\alpha_p = 0°$ most sections of the wing are below stall. When the pitch is increased to $10°$, all sections are in the stall region.

The pitch is varied harmonically as $\alpha_p = \alpha_{p,0} + 5° \cos(\Omega_0 t)$ with variable mean values $\alpha_{p,0}$. The simulation is performed with $\Omega_0 = 1.6$ rad/s and $u_0 = 0$ m. The results for the mean pitch equal to -5° and 10° are plotted to the left and right in Figure 4.4, respectively. In Figure 4.4a-b the static lift is indicated by (– –) and the dynamic lift is plotted as (——) for a section located at $x_3' = 32$ m. As illustrated, the pitch setting -5° produces attached flow conditions for this particular section, whereas the pitch setting 10° creates stalled flow conditions. Figure 4.4c-j show time series of $q_1(t)$ and $q_2(t)$ and the corresponding one-sided autospectral density function obtained through FFT. It is seen that both a change in amplitude and frequency occur when changing the pitch setting. At attached flow conditions the main frequency component of both q_1 and q_2 is equal to the pitch frequency 1.6 rad/s. When the wing is pitched into the stall region, the amplitude of q_1 decreases since the variation in lift decreases, but a significant high frequency contribution close to the first eigenfrequency is present in the response. The amplitude of q_2 increases, and the primary frequency is close to the eigenfrequency of the second mode. This indicates that aerodynamic damping is lost as the pitch is increased to 10°.

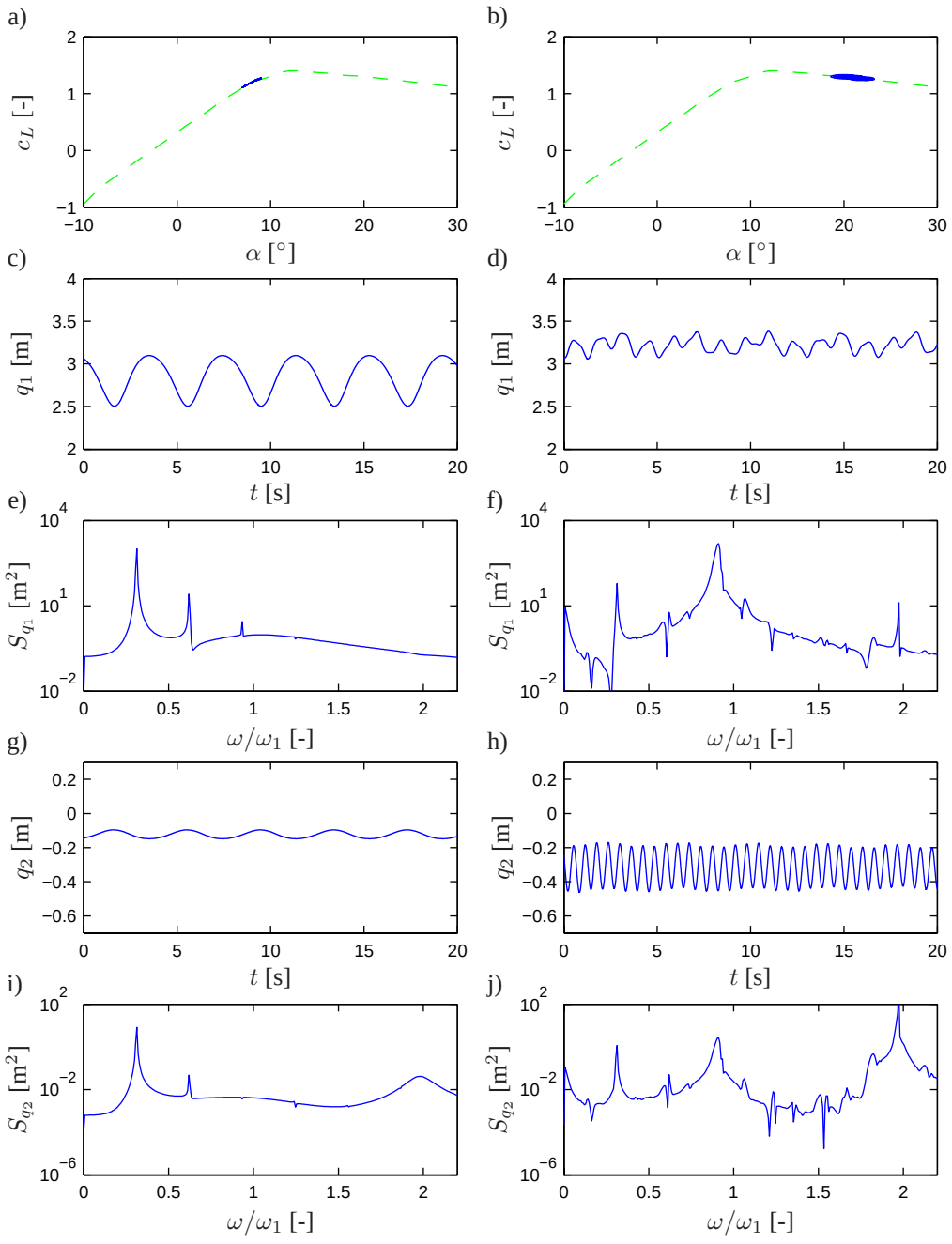

Figure 4.4 Numerical results at various pitch settings. $\Omega_0 = 1.6$ rad/s, $\omega_2/\omega_1 = 2.0$, $u_0 = 0$ m. Left: $\alpha_{p,0} = -5°$. Right: $\alpha_{p,0} = 10°$. a)-b) Lift coefficient. (– –) Static lift. (——) Dynamic lift $c_L(\alpha_{eq}(t))$. c)-d) $q_1(t)$. e)-f) $S_{q_1}(\omega)$ obtained through FFT. g)-h) $q_2(t)$. i)-j) $S_{q_2}(\omega)$ obtained through FFT.

4.2.3 Support point motion in constant wind field

The behaviour of the wing is analysed when excited by support point motion. The support point motion is varied harmonically at various constant pitch settings and eigenfrequency ratios. The frequency of the support point motion is $\omega_0/\omega_1 = 1.0$, the amplitude is kept constant $u_0 = 0.3$ m, and the excitation frequency ratio is $\omega_0/\Omega_0 = 3.0$. Comparing with the analyses performed in section 2.2 the system is stable for $\omega_2/\omega_1 = 2.0$ and unstable for $\omega_2/\omega_1 = 1.8$. Figure 4.5 shows results from a simulation with $\omega_2/\omega_1 = 1.8$. First the pitch setting is set to -5° with the results illustrated to the left of Figure 4.5. From the top down, Figure 4.5 shows results from $c_L(\alpha_{eq})$ of section $x_3' = 32$ m, $q_1(t)$, $q_2(t)$, Poincaré map of $q_1(t)$ and $\dot{q}_1(t)$ for 500 excitation periods T_0, and the one-sided autospectral density function of $q_1(t)$ corresponding to the illustrated time series. For the harmonic case with constant lift, these conditions creates chaotic response. At fully attached flow conditions, the response becomes periodic with the period $T = 3T_0$, indicated by three distinct circles in the Poincaré map. Also, the amplitude of $q_2(t)$ is relative limited, and three main components are observed in the response located at $\frac{2}{3}\omega_1$, ω_1 and $\frac{4}{3}\omega_1$. It should be noticed from Figure 4.5a that the equivalent angle of attack varies with an amplitude of approximately 3°. Now, the pitch is increased to 10° and the results are plotted to the right in Figure 4.5. As seen, the amplitude of both $q_1(t)$ and $q_2(t)$ increases significantly. From the Poincaré map it is seen that $q_1(t)$ seems chaotic to the extend of the simulated time series. The one-sided autospectral density function reveals the presence of several new peaks, especially a significant component is present at $1.8\omega_1$, which is due to the nonlinear coupling terms. Finally, the amplitude of α_{eq} is increased dramatically due to the aeroelastic contributions, creating large variation in c_L. From Figure 4.5b it is seen that the hysteretic loop of c_L seems chaotic. Hence, the loading on the profile resembles that of a broadbanded stationary process. Furthermore, the system is lightly dampened under dynamic stall conditions. Basic stochastic vibration theory suggests that the response at the undamped circular eigenfrequency will be amplified relatively to other frequencies, see e.g. Nielsen (2000), which, by comparing Figure 4.5i and Figure 4.5j, is also the case here.

Next, the eigenfrequency ratio is changed to $\omega_2/\omega_1 = 2.0$. The results are plotted in Figure 4.6. For the constant lift analysis, this situation is stable with a response period of $T = 3T_0$. This is also the case when introducing dynamic variation of the lift at attached flow condition illustrated to the left in Figure 4.6. The response is virtual identical to the results at $\omega_2/\omega_1 = 1.8$ illustrated in Figure 4.5. However, when the pitch setting is equal to 10° the solution becomes unstable due to loss of aerodynamic damping. The Poincaré map in Figure 4.6h illustrates a non-periodic response. The strange attractor seems to be located around a three period motion with three distinct areas of the Poincaré points, but within the simulation limits the response does not become periodic. Comparing Figure 4.6i and Figure 4.6j reveals some changes in the relative importance of the various frequency components. Especially, the resonance peak at $\omega/\omega_1 = 1.0$ is more marked, as also is clear from the time series in Figure 4.6d. Again this is a result of the broadbanded chaotic excitation.

To illustrate the behaviour of the dynamic stall state variables, the support point motion is varied harmonically with $u_0 = 0.3$ m and $\omega_0/\omega_1 = 1.0$, $\omega_2/\omega_1 = 2.0$ and $\omega_0/\Omega_0 = 3$, while α_p is changed slowly from -5° to 5° and back again. The variation of the pitch is illustrated in Figure 4.7a. The corresponding time series of $q_1(t)$ and $q_2(t)$ are plotted as (——) in Figure 4.7b-c, and the mean values $\mu_{q_1}(t)$ and $\mu_{q_2}(t)$ are indicated by (——). A significant increase in oscillation amplitude is registered in both $q_1(t)$ and $q_2(t)$ as the pitch is increased into the

stall regime, due to the loss of aerodynamic damping. The mean level of $q_1(t)$ increases due to increase in lift, while the mean level of $q_2(t)$ decreases as a result of the increased lift component in the negative x_2'-direction.

Time series of the dynamic stall state variables $c_1(t)$, $c_2(t)$, $\theta_d(t)$ and $c_{L,v}(t)$ are plotted in Figure 4.8 for various wing sections corresponding to the pitch variation illustrated in Figure 4.7a. Variation of the state variables for three sections located at $x_3' = 24$ m, $x_3' = 32$ m and $x_3' = 40$ m are plotted as (——), (——) and (——), respectively. The amplitude of the variations decreases clearly as the section is taken closer to the root, due to a decrease in deformation velocities. The twist makes the mean angle of attack almost constant throughout the considered sections, see Figure 4.3b, which causes the behaviour of the state variables to be similar, i.e. all sections enters the dynamic stall region with increasing mean value of θ_d and $c_{L,v}$. The mean value increase of θ_d and $c_{L,v}$ is a direct consequence of the section entering stall. The increase in amplitudes of c_1, c_2, θ_d and $c_{L,v}$ are caused by the loss of damping resulting in large oscillations. This introduces high amplitude oscillations of α_{eq}, which results in an amplitude increase of the state variables.

4.2.4 Rotation of wing in boundary layer flow with tower passage

The variation of the wind field is now included in the numerical simulation. The incoming flow is assumed to be described by (4.2) and (4.3) including variation both from the logarithmic wind field and the tower passage. The support point motion is assumed to vary harmonically with an amplitude $u_0 = -0.1$ m. The minus sign is to ensure that the support point motion is in phase with the variation in the wind field. When $\Phi(t) = 0^\circ$ the wing is in downwards position located in the tower shadow, see Figure 2.2. Then, two wings are positioned at the upper part of the flow field, introducing a high load situation with a resulting movement of the tower in the negative x_1-direction. The support point circular frequency is given as $\omega_0 = 3\Omega_0$, corresponding to a three bladed rotor. A primary resonance case is considered with $\omega_0/\omega_1 = 1.0$. First, a simulation is performed with a pitch setting of -5°. In Figure 4.9 results from two simulations are illustrated. The first simulation, indicated by (——), includes contributions from elastic deformation velocities $\dot{q}_1(t)$ and $\dot{q}_2(t)$ in the angle of attack, thus, aeroelastic contributions are considered. Results from a simulation where the aeroelastic contributions are disregarded are indicated by (——). Time series of $q_1(t)$, $q_2(t)$, and $V_1'(t)+\dot{u}_1'(t)$ and $\alpha_{eq}(t)$ of section $x_3' = 32$ m are plotted in Figure 4.9. A significant increase in deformation amplitude is registered, when the aeroelastic contributions are disregarded, which occur since the aerodynamic dampening is introduced via these terms. Also, from Figures 4.9c-d a clear support point frequency component is seen in both $V_1'+\dot{u}_1'$ and α_{eq} when including aeroelastic effects. This introduces high frequency components in the loading together with an increased maximum wind component. An increase of both wind velocity and angle of attack produces higher lift, but the aerodynamic damping keeps the oscillations low compared with the situation where the aeroelastic effects are disregarded.

Next, $q_1(t)$ and $q_2(t)$ are plotted in Figure 4.10 with corresponding one-sided autospectral densities at various pitch settings. Simulations with pitch settings -5°, 5° and 9° are indicated by (——), (——) and (——), respectively. As the pitch setting is changed from -5° to 5° the mean level of $q_1(t)$ increases, because attached flow conditions produces increasing lift with increasing angle of attack. However, the mean level of $q_2(t)$ decreases, because the lift component in the negative x_2'-direction increases with increasing angle of attack. As the pitch setting is changed to 9°, the system becomes unstable, and especially the amplitude of $q_2(t)$ increases,

introducing a frequency component at $\omega = 2\omega_1$ in $q_1(t)$.

4.2.5 Active Vibration Control of Wind Turbine Wings under Dynamic Stall

The final numerical example introduces an active vibration algorithm using pitch actuation. A closed loop control algorithm is used. Hence, the control law is determined from observable state variables. In recent years most wind turbines are manufactured with pitch control systems, with actuation systems which can induce pitch velocities close to $20^\circ/s$. This limit will be used as a cut-off limit for the control. To investigate the qualitative behaviour of the wing during active control, a simple linear closed loop control law is used with a side condition of $\dot{\alpha}_p(t) \leq \dot{\alpha}_{p,\max}$. As mentioned in Chapter 2, two modal coordinates can at most be observed during operating conditions. Correspondingly, the control law may be written as

$$\begin{aligned}
\alpha_p(t) &= \alpha_{p,0} - k_1\big(\dot{q}_1(t) + \kappa_1\omega_1 q_1(t)\big) + k_2\big(\dot{q}_2(t) + \kappa_2\omega_2 q_2(t)\big),\\
\dot{\alpha}_p(t) &= -k_1\big(\ddot{q}_1(t) + \kappa_1\omega_1 \dot{q}_1(t)\big) + k_2\big(\ddot{q}_2(t) + \kappa_2\omega_2 \dot{q}_2(t)\big),
\end{aligned} \tag{4.4}$$

where $\alpha_p(t)$ is the control angle of attack, $\alpha_{p,0}$ is the initial pitch setting, k_1, k_2, κ_1 and κ_2 are control gains. (4.4) is valid as long as $|\dot{\alpha}_p(t)| \leq \dot{\alpha}_{p,max}$, where $\dot{\alpha}_{p,max}$ indicates the maximal pitch rate of the actuator system. When $\dot{\alpha}_p$ crosses out of the barriers $\pm\dot{\alpha}_{p,max}$, α_p is determined from

$$\alpha_p(t) = \pm(t - \hat{t})\dot{\alpha}_{p,\max}, \quad \dot{\alpha}_p(t) = \pm\dot{\alpha}_{p,\max}, \tag{4.5}$$

where $\hat{t}$ is the time, when $\dot{\alpha}_p$ crosses out of the barrier.

To monitor the performance of the controlled system, the time variation of three variables are used, being the mean deformation level $\mu_{q_1}(t)$ of $q_1(t)$, the standard deviation $\sigma_{q_1}(t)$ of $q_1(t)$, and the mean level $\mu_W(t)$ of the produced effect. To monitor the change of these variable, a time average is taken over 6 support point excitation periods backwards in time. The selection of 6 periods for averaging interval seems to provide a fair tradeoff between localization in time and accuracy. The average operator $< \cdot >_t$ is introduced, defined as

$$< \cdot >_t = \frac{1}{6T_0}\int_{t-6T_0}^{t} (\cdot)d\tau. \tag{4.6}$$

Then, $\mu_{q_1}(t)$, $\sigma_{q_1}(t)$, and $\mu_W(t)$ are defined from

$$\begin{aligned}
\mu_{q_1}(t) &= < q_1(t) >_t,\\
\sigma_{q_1}(t) &= \sqrt{< q_1^2(t) >_t - \mu_{q_1}^2},\\
\mu_W(t) &= < W(t) >_t,
\end{aligned} \tag{4.7}$$

where $W(t)$ is determined as

$$W(t) = \Omega_0 \int_0^L p'_{2,A}(x'_3, t) x'_3 dx'_3. \tag{4.8}$$

In the following a series of simulations are performed with constant incoming wind field and harmonic varying support point motion. The following parameters are used, $u_0 = 0.5$ m, $\omega_2/\omega_1 = 2.0$, $\omega_0/\omega_1 = 1.0$ and $\omega_0/\Omega_0 = 3.0$. The initial pitch setting $\alpha_{p,0}$ is kept constant through the various simulations, however, after approximately 25 s, the gain factors are changed from 0 to $k_1 = 0.007$ s/m, $k_2 = 0.014$ s/m and $\kappa_1 = 0.7$, i.e. the active control is initialized. The term defined by κ_2 turns out to introduce very little effect on the response, and κ_2 is set to 0 in the subsequent analyses.

At first a simulation is carried out with $\alpha_{p,0} = -1°$. The results are illustrated in Figure 4.11 to the left, where, from the top down, $c_L(\alpha_{eq})$ of section $x'_3 = 32$ m, $\dot{\alpha}_p(t)$, $q_1(t)$, μ_W and $\sigma_{q_1}(t)$ are plotted. In Figure 4.11c it is seen that the pitch velocity does not reach the maximum of 20°/s for this particular choice of gains. Figure 4.11i and Figure 4.11g shows a decrease of approximately 37% in standard deviation and no significant change in produced effect, after initialization of the control. Next, $\alpha_{p,0}$ is increased to 5°. The results are illustrated to the right in Figure 4.11. At this pitch setting the section operate under separated flow conditions during the entire cycle. Here the pitch rate reaches the limit of $20\,°/s$. The efficiency of the controller is approximately the same as before. The efficiency in the stall region is kept due to the dynamic stall effect. No significant changes in the mean power level is observed, but the level increases with increasing $\alpha_{p,0}$, since a larger portion of the lift component works in the negative x'_2 direction. In these simulations the drag coefficient is kept constant, but at angles of attack close to the static stall angle a significant increase in drag is found keeping the power level constant or even decreasing with increasing angle of attack.

Figure 4.12 shows the dynamic lift coefficient at various sections throughout the wing. Section $x'_3 = 32$ m, corresponding to Figures 4.11a-b, are indicated by (——), while results from section $x'_3 = 24$ m and $x'_3 = 40$ m are plotted as (——) and (——), respectively. To the left the dynamic lift is plotted before initialization of the control, the right illustrates the corresponding results after the control is started. Figure 4.12a-b shows results from a simulation with $\alpha_{p,0} = -1°$, and Figure 4.12c-d illustrate results with $\alpha_{p,0} = 5°$. The static lift is plotted as (– –). For the low initial pitch case, illustrated in Figures 4.12a-b, no significant change in the qualitatively behaviour is registered in the angle of attack and lift after the controller is started. However, an increase in the amplitude of the effective angle of attack is noticed, especially for the inner part of the wing. This is due to the active pitching motion. Whereas, for the outer part of the wing, the effect is partly counteracted by the decrease in deformation velocities. For the high initial pitch conditions the same effect is noted. Before the initialization of the control the system exhibited chaotic behaviour, whereas after initialization of the control the motions seems to stabilize and the loading becomes periodic.

The optimal choices of control gains are dependent on the pitch setting. A limit in efficiency exists, when the pitch rate barrier is reached. By the method of trial and error the optimal gains are found to be $k_1 = 0.02$, $k_2 = 0.019$ and $\kappa_1 = 0.6$. A simulation with these gains is made and the results are illustrated in Figure 4.13. This choice of gains induce a decrease in standard deviation of approximately 45%, however, the strain on the pitch actuation system is severe with

the pitch rate being equal to the maximum most of the time. Also, the variation of angle of attack is relatively large, making calibration of the dynamic stall model essential.

4.3 Concluding Remarks

In this chapter the qualitative behaviour of the combine nonlinear two-degrees-of-freedom structural model and the 4 state variable dynamic stall model is analysed. The performance is illustrated through four different numerical examples. Firstly, the support point motion is disregarded and the wing is pitched harmonically around a mean level in the attached flow region and in the stall region. It is shown that a considerable damping is present in the attached flow region. Consequently, the pitch frequency becomes the main component in both $q_1(t)$ and $q_2(t)$. In the stall region the aerodynamic damping is lost and significant eigenfrequency components are present in both $q_1(t)$ and $q_2(t)$. Next, the support point motion is assumed to vary harmonically at various constant pitch settings and at various values of the eigenfrequency ratio ω_2/ω_1. At eigenfrequency ratio equal to 1.8 the response is chaotic under constant lift. During attached flow conditions all eigenfrequency ratios produces periodic response due to the significant aerodynamic damping. In the stall region non-periodic response exists for all eigenfrequency ratios, but at $\omega_2/\omega_1 = 2.0$ the strange attractor of the system is close to a period three motion, while for $\omega_2/\omega_1 = 1.8$ dynamic instability occur with large amplitudes of the state variables.

The significance of aeroelastic contributions is illustrated by simulations using a logarithmic wind field including effects from tower passage. Considerable aeroelastic damping is introduced via the aeroelastic contributions keeping low levels of oscillations at attached flow conditions. Also, a clear rotational frequency component and a support point frequency is present in the angle of attack when including aeroelastic effects. Under attached flow conditions the rotational frequency component is also present in the response, but as the pitch is increased into the stall region, this component becomes less significant.

Finally, a simple linear active control algorithm using the pitch system is devised with a side condition for maximum pitch velocity. The performance is evaluated with respect to standard deviation of $q_1(t)$ and mean level of power output. The intend is to decrease the standard deviation while keeping the mean power level approximately constant. The controller is shown to work well with a possible decrease in standard deviation of 37%, when the pitch setting is set for the wing to be in the stall region. If the pitch setting is increased a drop in efficiency is observed due to decrease of aerodynamic damping. The efficiency may be further increased, however, this would induce unrealistic strains on the pitch system. At high pitch settings the system may exhibit chaotic behaviour, which is shown to be stabilized by introducing the controller. In both cases no observable change of the power output is registered by introducing the controller. Using the observable state variable the control algorithm is easily implemented into the system. The qualitatively behaviour of the controlled system has been illustrated by numerical examples, but no stability issues of the controller has been addressed. In Larsen and Nielsen (2005a), which is under preparation, these issues are to be investigated.

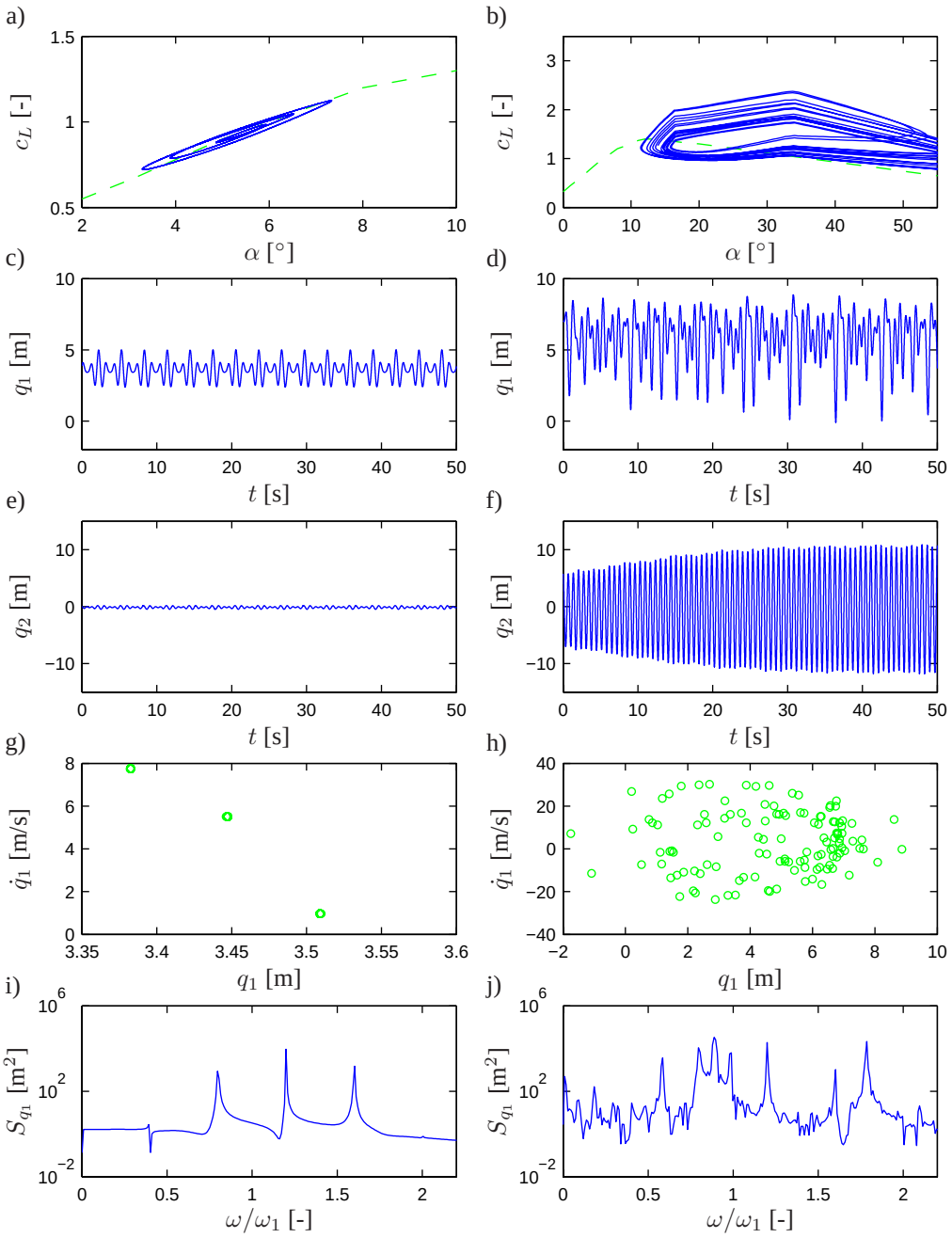

Figure 4.5 Numerical results during unstable conditions at various pitch settings. $\omega_0/\Omega_0 = 3.0$, $\omega_2/\omega_1 = 1.8$, $u_0 = 0.3$, $\omega_0/\omega_1 = 1.2$. Left: $\alpha_p = -5°$. Right: $\alpha_p = 10°$. a)-b) Lift coefficient. (— —) Static lift. (———) Dynamic lift $c_L(\alpha_{eq}(t))$. c)-d) $q_1(t)$. e)-f) $q_2(t)$. g)-h) Poincaré map of $q_1(t)$ and $\dot{q}_1(t)$. i)-j) $S_{q_1}(\omega)$ obtained through FFT.

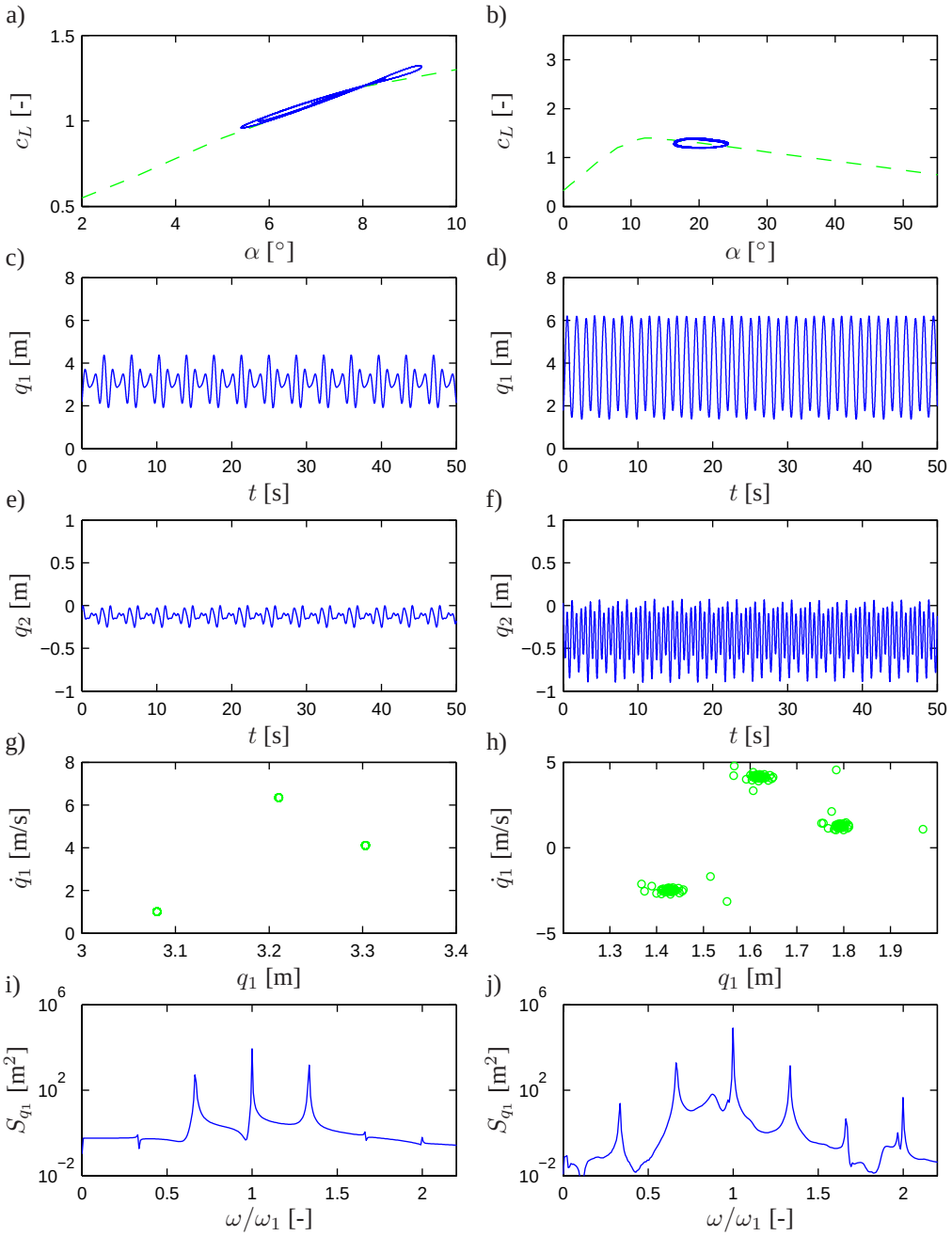

Figure 4.6 Numerical results during stable conditions at various pitch settings. $\omega_0/\Omega_0 = 3.0, \omega_2/\omega_1 = 2.0, \omega_0/\omega_1 = 1.0$, $u_0 = 0.3$. Left: $\alpha_p = -5°$. Right: $\alpha_p = 10°$. a)-b) Lift coefficient. (— —) Static lift. (——) Dynamic lift $c_L(\alpha_{eq}(t))$. c)-d) $q_1(t)$. e)-f) $q_2(t)$. g)-h) Poincaré map of $q_1(t)$ and $\dot{q}_1(t)$. i)-j) $S_{q_1}(\omega)$ obtained through FFT.

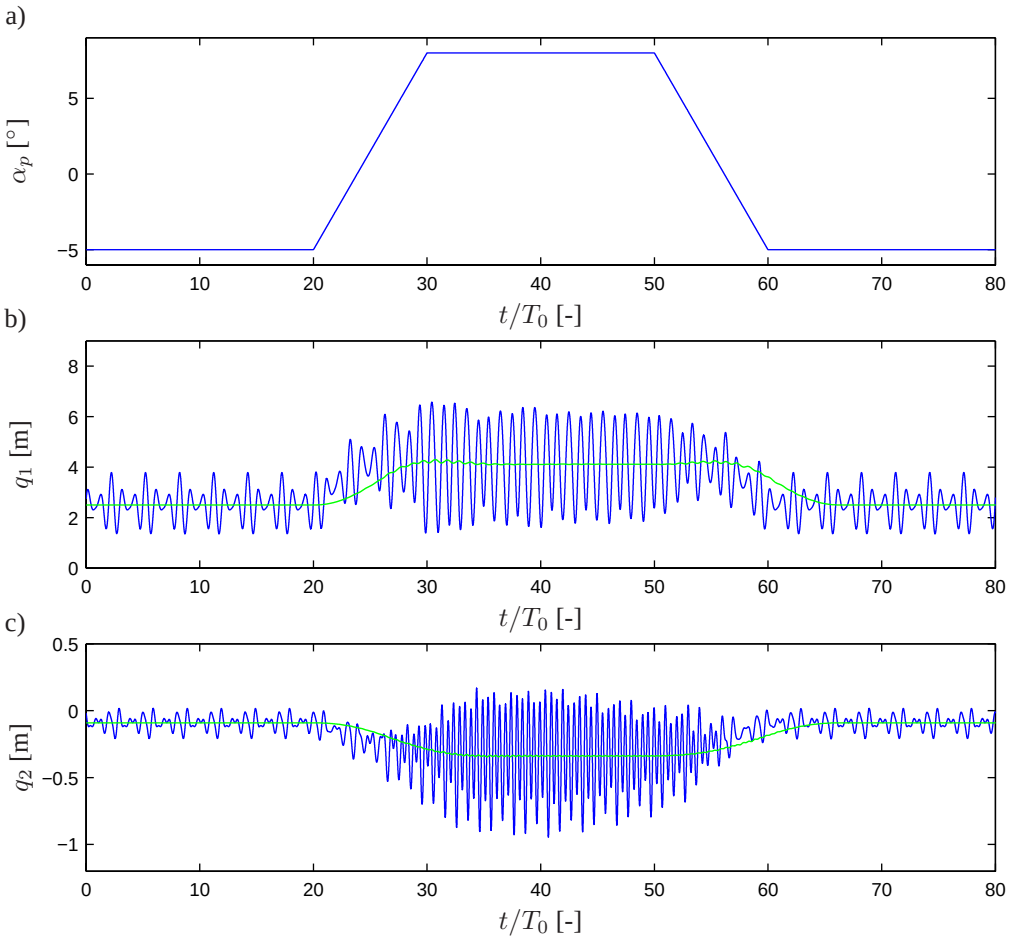

Figure 4.7 Results from a slowly variation of pitch setting with harmonic varying support point motion. $\omega_0/\Omega_0 = 3.0$, $\omega_0/\omega_1 = 1.0$, $\omega_2/\omega_1 = 2.0$, $u_0 = 0.3$ m. a) Variation of pitch setting. b) (——) $q_1(t)$. (——) $\mu_{q_1}(t)$. c) (——) $q_2(t)$. (——) $\mu_{q_2}(t)$.

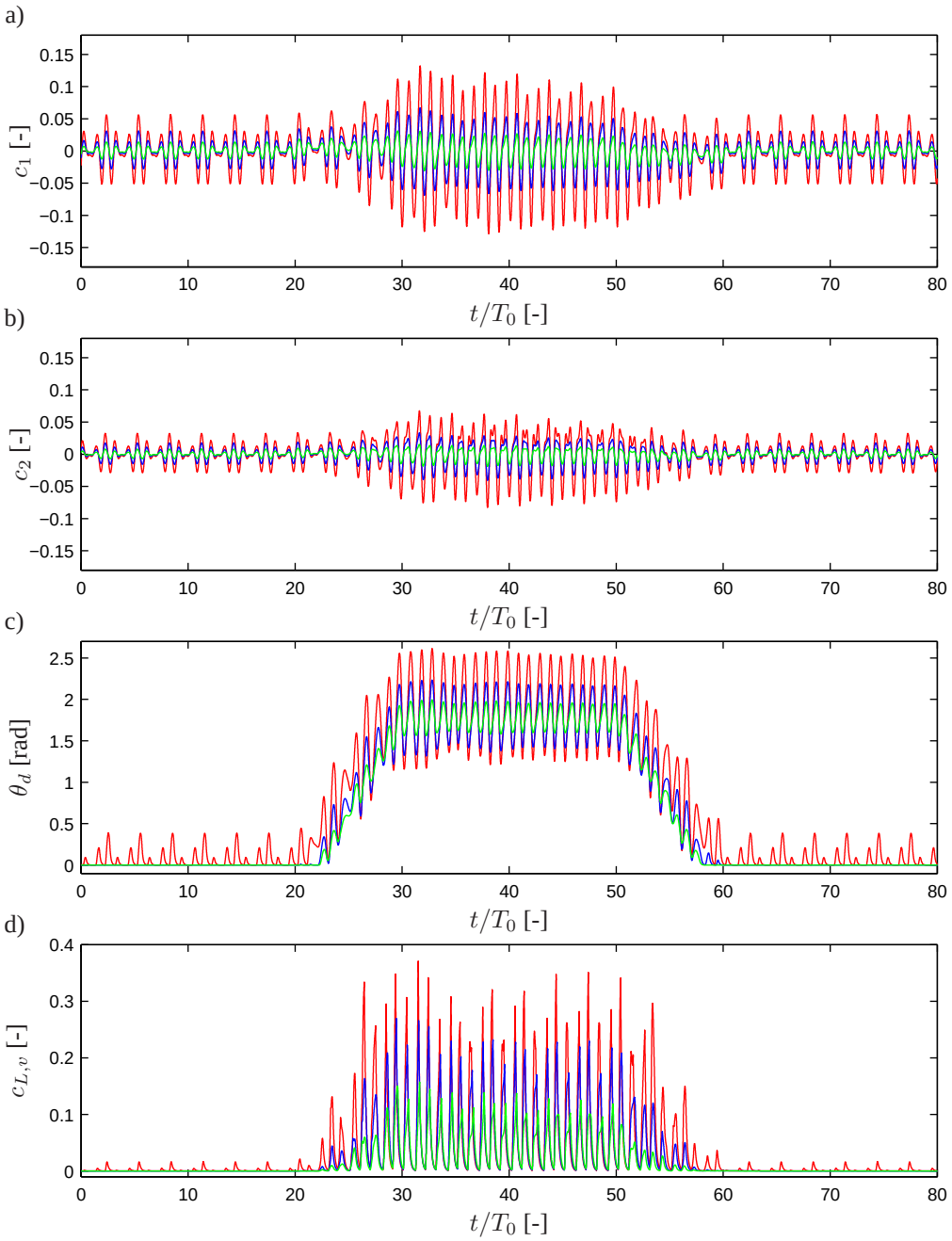

Figure 4.8 Dynamic stall state variables at various wing sections during simulation corresponding to that of Figure 4.7. (———) Section $x_3' = 24$ m. (———) Section $x_3' = 32$ m. (———) Section $x_3' = 40$ m. a) $c_1(t)$. b) $c_2(t)$. c) $\theta_d(t)$. d) $c_{L,v}(t)$.

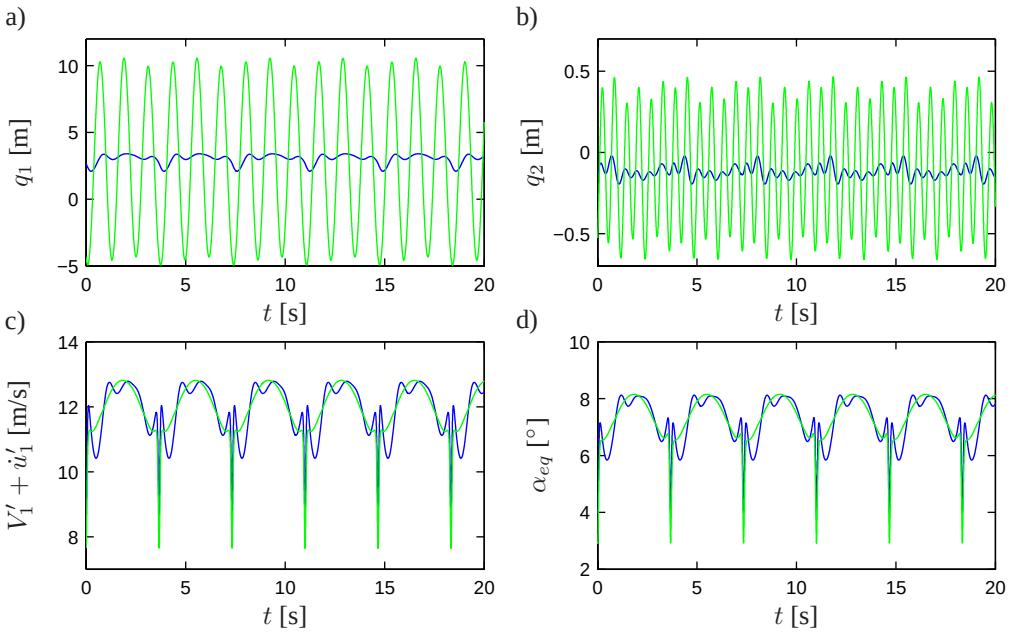

Figure 4.9 Results from simulation with logarithmic varying wind field including effects from tower passage. $\omega_0/\omega_1 = 1.0$, $\omega_0/\Omega_0 = 3.0$, $u_0 = -0.1$ m, pitch setting $-5°$. (———) Including aeroelastic effects. (———) Disregarding aeroelastic effects. a) $q_1(t)$. b) $q_2(t)$. c) $V_1'(t) + \dot{u}_1'(t)$ of section $x_3' = 32$ m. d) $\alpha_{eq}(t)$ of section $x_3' = 32$ m.

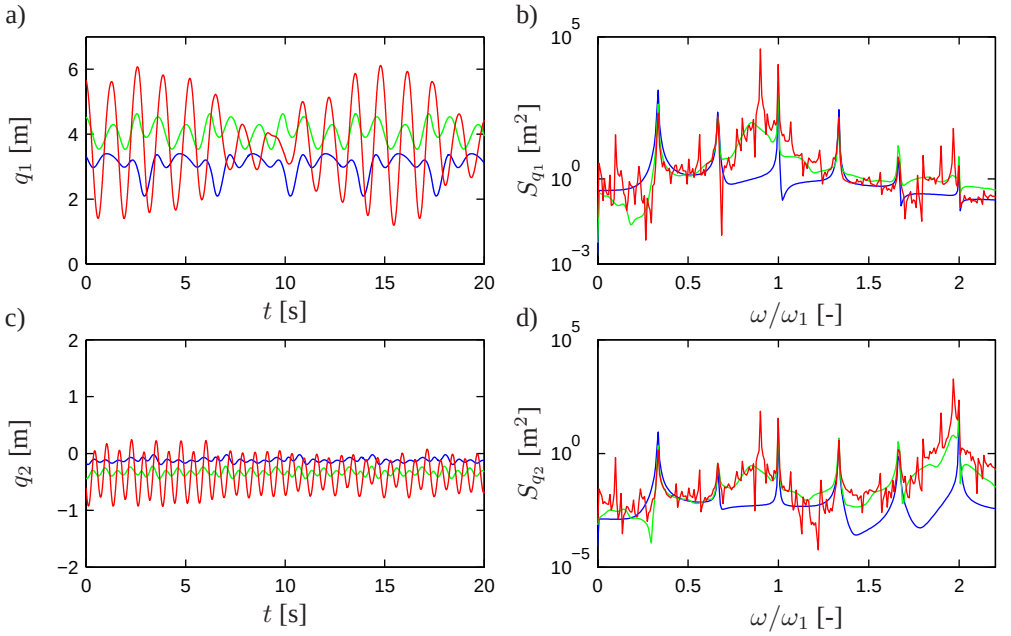

Figure 4.10 Logarithmic varying wind field with tower passage. $\omega_0/\omega_1 = 1.0$, $\omega_0/\Omega_0 = 3.0$, $\omega_2/\omega_1 = 2.0$, $u_0 = -0.1$ m. (———) $\alpha_p = -5°$. (———) $\alpha_p = 5°$. (———) $\alpha_p = 9°$. a) $q_1(t)$. b) $S_{q_1}(\omega)$. c) $q_2(t)$. d) $S_{q_2}(\omega)$.

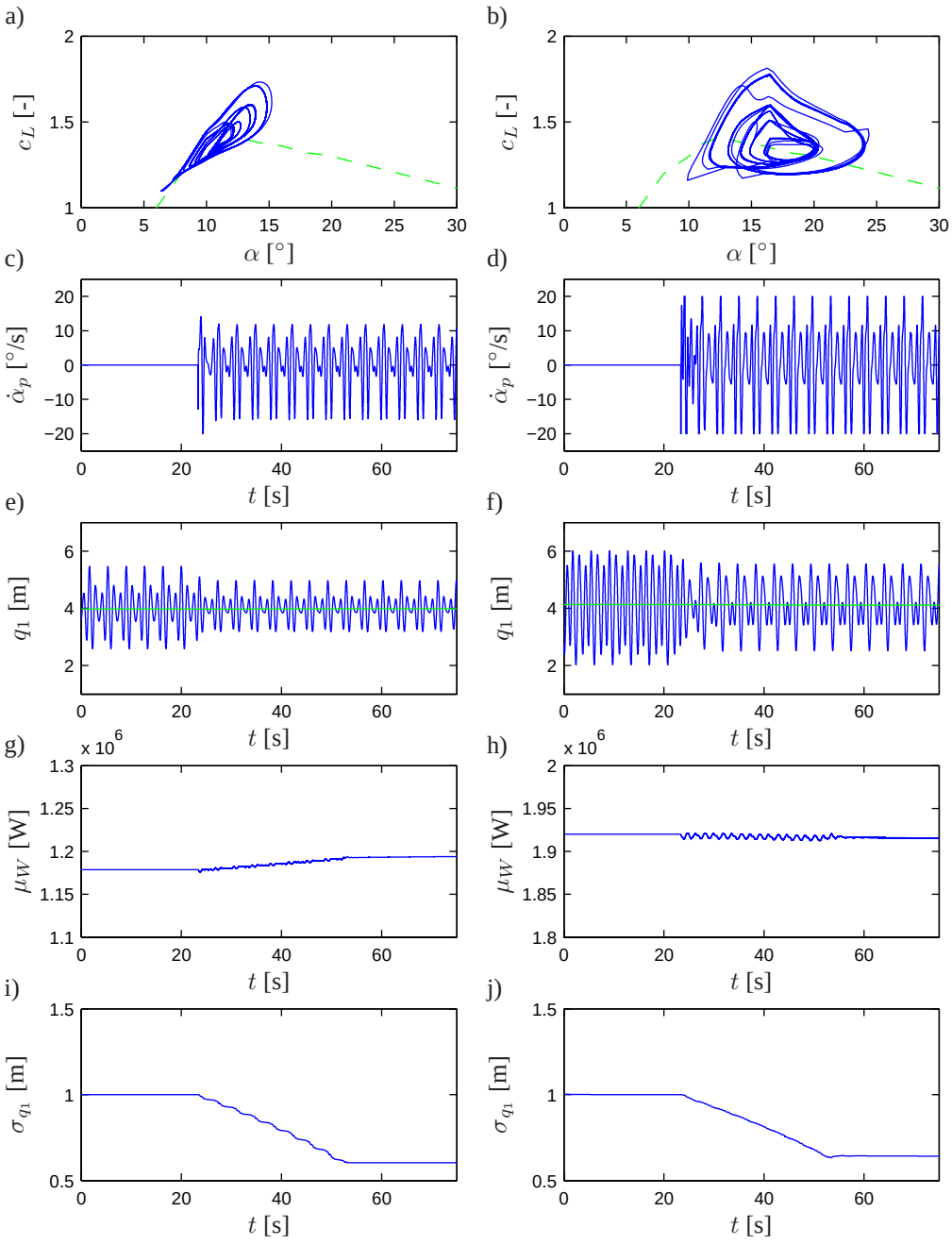

Figure 4.11 Results from simulation with constant wind field during active control at various mean pitch settings. The control is started after approximately 25 s. $\omega_0/\omega_1 = 1.0$, $\omega_0/\Omega_0 = 3.0$, $u_0 = 0.3$ m, $k_1 = 0.007$ s/m, $k_2 = 0.014$ s/m, $\kappa_1 = 0.7$. Left: $\alpha_{p,0} = -1°$. Right: $\alpha_{p,0} = 5°$.
a)-b) Lift coefficient. (– –) Static lift.(——) Dynamic lift $c_L(\alpha_{eq}(t))$.
c)-d) $\dot{\alpha}_p(t)$. e)-f) $q_1(t)$. g)-h) $\mu_w(t)$. i)-j) $\sigma_{q_1}(t)$. normalized with $\sigma_{q_1}(0)$ before initiation of pitch control.

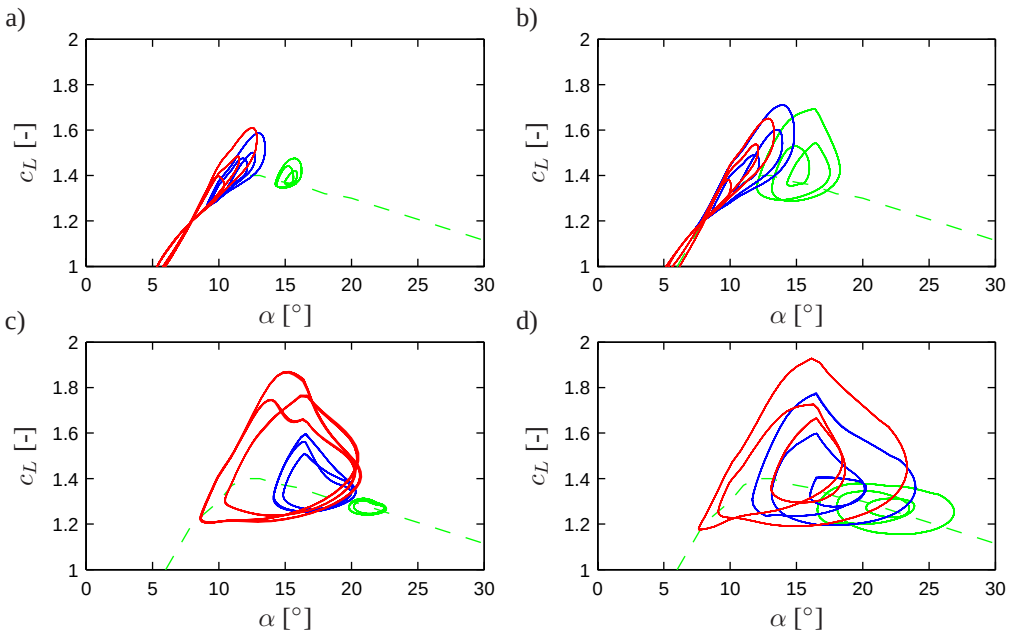

Figure 4.12 Lift variation before and after initialization of active control at various sections throughout the wing. (——) Section $x_3' = 24$ m. (——) Section $x_3' = 32$ m. (——) Section $x_3' = 40$ m. Left: Before start of pitch control. Right: After start of pitch control. a)-b) $\alpha_{p,0} = 5°$. c)-d) $\alpha_{p,0} = 8°$.

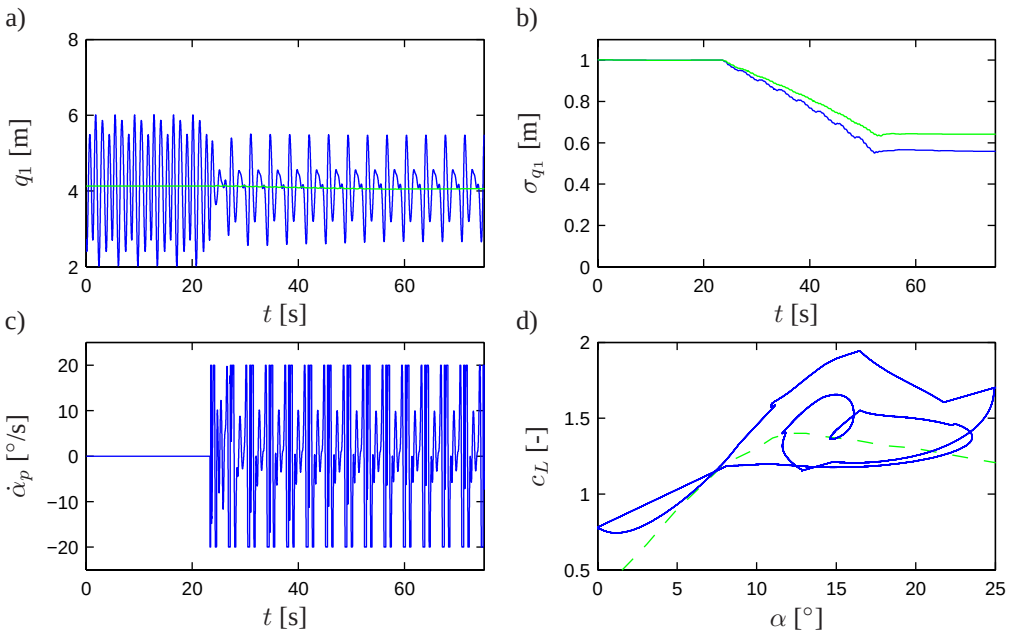

Figure 4.13 Results when using optimal values of the gains, $k_1 = 0.02$ s/m, $k_2 = 0.019$ s/m and $\kappa_1 = 0.6$. a) (——) $q_1(t)$. (——) $\mu_{q_1}(t)$. b) $\sigma_{q_1}(t)$. c) $\dot{\alpha}_p(t)$. d) $c_L(\alpha)$.

CHAPTER 5
Stochastic Stability of Linear and Nonlinear Parametrically Excited Systems

In this chapter work is presented on the stochastic stability of three different mechanical systems. Firstly, the stability of a linear mechanical system under stochastic parametric excitation is analysed using Lyapunov exponents. The stochastic excitation is modelled as a renewal jump process. Secondly, a two-degrees-of-freedom system of a support point excited cable is analysed under both harmonic and stochastic support point motion. The first two analyses are made as preliminary studies to the stability analysis of the nonlinear wind turbine wing under stochastic variation of the support point motion, where parametric excitation play a significant role. The work presented in section 5.1 and section 5.2 is based on the work of (Iwankiewicz *et al.* 2005) and (Larsen and Nielsen 2004b), respectively.

5.1 Stochastic Stability of Mechanical Systems Under Renewal Jump Process Parametric Excitation using Lyapunov Exponents

Dynamic stability of elastic systems under parametric stochastic excitation has been a subject of research for several decades. Most of the papers on stochastic stability which have appeared, deal with the systems under Gaussian white noise or wide-band parametric excitations. Ariaratnam (1966) was among the first to deal with the problem of dynamic stability of a beam-column under a Gaussian white noise parametric stochastic loading. Ariaratnam *et al.* (1991), Griesbaum (1999) and Simon and Wedig (2001) considered problems concerning stochastic stability of problems including more than two state variables. Griesbaum (1999) and Simon and Wedig (2001) considered problem governed by two coupled, white-noise driven, equations. For the four state variables they used a hyperspherical transformation and under the ergodicity assumption they investigated the Lyapunov exponents with the aid of ensemble averaging rather than time averaging.

Much less attention has been given to non-Gaussian stochastic parametric excitations for example to random pulse trains. Samuels (1963) was one of the first authors to deal with parametric excitation in form of a random train of impulses. Kotulski and Sobczyk (1988) dealt

with the moment stability of a system under a stochastic jump process excitation in form of the random telegraph process $X(t) = (-1)^{N(t)}$, where $N(t)$ is a Poisson counting process.

The stochastic parametric excitation considered here is a random train of non-overlapping rectangular pulses with equal, deterministic heights. The excitation, or dynamic loading, of this kind may occur in some control systems where the controlling device switches the clutch on and off. Thereby different parts of the system are coupled or decoupled, thus giving rise to sudden dynamic loading or unloading. The dynamic loading may act both as an external or as a parametric excitation. The duration of pulses are assumed to be negative exponential-distributed random variables, and the time gaps between two consecutive pulses are also negative exponential-distributed random variables. The parameters of the interval distributions are different. The pulse arrival times of the described load process define a specific renewal counting process, which is termed a generalized Erlang process (Iwankiewicz and Nielsen 1999, pp. 85). The excitation process is shown to allow for a reformulation of the original non-Markovian stochastic differential equation into a nonlinear generalized Itô differential equation driven by 2 independent Poisson counting processes at the expense of the introduction of an extra state variable. Moreover, if two state variables are introduced the problem may be recasted into an equivalent linear generalized Itô differential equation. The response in a single mode is investigated. Hence, the original problem is governed by the state vector made up of the velocity and displacement.

The objective is to investigate the asymptotic moment stability and Lyapunov asymptotic (sample curve) stability with probability 1. Asymptotic stability of first- and second-order ordinary moments is investigated analytically, by evaluating the largest of the real parts of all the eigenvalues. In order to investigate the asymptotic sample stability via Lyapunov exponents the transformation of the four state variables of the equivalent linear formulation to hyperspherical coordinates is made and two methods are used. One is the direct simulation of the stochastic equation governing the natural logarithm of the hyperspherical amplitude process and of the stochastic equations governing the angular processes. The other one is based on the ergodicity assumption where the time averaging of the pertinent expressions is replaced by ensemble averaging. A modification of the approach used in (Griesbaum 1999) and (Simon and Wedig 2001) has been developed. The numerical results show good qualitative agreement between the two methods of evaluating the Lyapunov exponents. However, direct simulation is found to be more robust and less time consuming and therefore more suitable for the problem. The asymptotic mean-square stability condition is more conservative than Lyapunov asymptotic (sample) stability with probability 1 (Arnold 1984; Kozin and Sugimoto 1977). It is however not overly conservative and may provide a good estimate of the asymptotic stochastic stability. The outline is based on (Iwankiewicz *et al.* 2005).

5.1.1 Statement of the problem

Consider a beam-column under an axial compressive force, or a plate under in-plane compressive forces. Using a single mode approximation we obtain the differential equation for the modal coordinate $Y(t)$

$$\ddot{Y}(t) + 2\zeta\omega\dot{Y}(t) + \omega^2 Y(t) - \beta\omega^2 Z(t)Y(t) = 0, \tag{5.1}$$

where the parametric load $Z(t)$ specify the time variation of the dynamic compressive force, or a parametric excitation. The values $\beta = 1$ and $Z(t) = \text{const.} = 1$ correspond to the classical,

Euler critical force for the static buckling problem.

The stochastic excitation $Z(t)$ is modelled as a jump process, in the form of a random train of step forces of equal deterministic magnitude, with random force pulses T_p and random time gaps T_g between two consecutive forces. A sample of the excitation is shown in Figure 5.1.

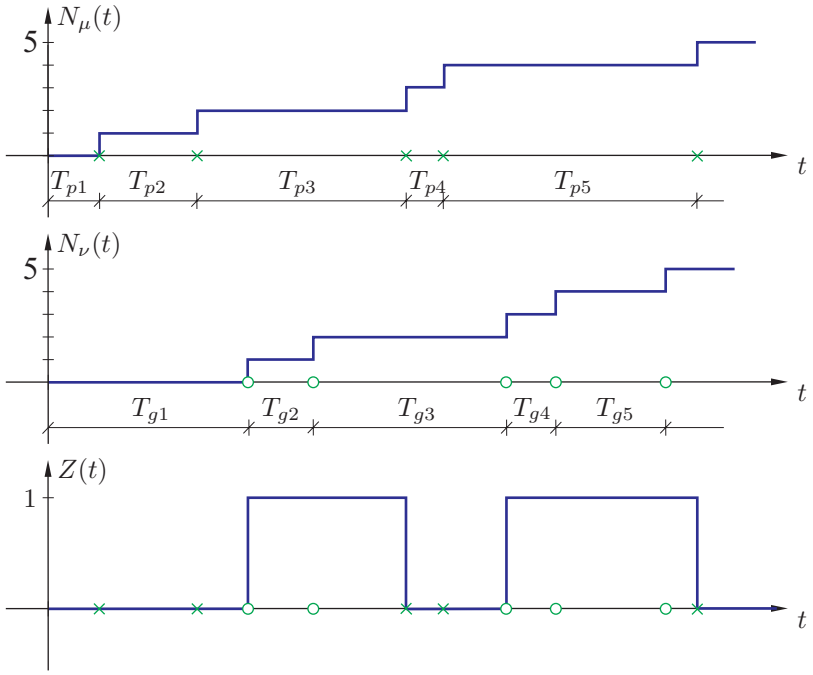

Figure 5.1 A sample path of the stochastic processes $N_\mu(t)$, $N_\nu(t)$ and $Z(t)$. ($\times$) indicate N_μ-driven points and ($\circ$) indicate N_ν-driven points.

The height of the pulses may be absorbed in the parameter β, so the amplitude of $Z(t)$ can be chosen as 1. It is assumed that the durations of all pulses are identically, negative-exponential distributed random variables T_p with the parameter μ corresponding to the probability density function

$$f_{T_p}(t) = \mu \mathrm{e}^{-\mu t} \quad , \quad t > 0. \tag{5.2}$$

Likewise, all time gaps are assumed to be identical, negative exponential-distributed random variables T_g with the parameter ν, so

$$f_{T_g}(t) = \nu \mathrm{e}^{-\nu t} \quad , \quad t > 0. \tag{5.3}$$

The arrival times of the force pulses make up a renewal counting process with the inter-arrival times $T_a = T_g + T_p$. The excitation $Z(t)$ is governed by the stochastic equation, (Iwankiewicz 2002; Iwankiewicz 2003)

$$dZ(t) = (1 - Z)dN_\nu(t) - ZdN_\mu(t), \tag{5.4}$$

where $N_\nu(t)$ and $N_\mu(t)$ are mutually independent homogeneous Poisson counting processes with parameters ν and μ, respectively. The differentials in (5.4) are $dZ(t) = Z(t + dt) - Z(t)$, $dN_\alpha(t) = N_\alpha(t + dt) - N_\alpha(t)$, $\alpha = \mu, \nu$. Hence, the increments are interpreted in the Itô sense as related to the succeeding differential time interval to present time t. Assume that the initial condition for the $Z(t)$ variable is $Z(0) = 0$. Then according to the equation (5.4) at the first $N_\nu(t)$-driven point the variable $Z(t)$ jumps from 0 to 1, at the first subsequent $N_\mu(t)$-driven point it jumps back to 0, at the first subsequent $N_\nu(t)$-driven point it jumps again to 1 and so forth. Due to memorylessness property of the Poisson counting processes $N_\mu(t)$ and $N_\nu(t)$, this situation implies that the time-intervals T_p and T_g become negative-exponential distributed (Iwankiewicz 2003).

Every sample function of $Z(t)$ as governed by the equation (5.4) is a discontinuous function of time of bounded variation. Consequently the sample function of $\ddot{Y}(t)$ is discontinues as follows from (5.1). In turn this means that $\dot{Y}(t)$ is continues, and the sample function of $Y(t)$ is differentiable. Then, the existence and uniqueness of solutions of (5.1) is ensured, see e.g. (Kreyszig 1999). Combining (5.1) and (5.4) the following state space formulation of the dynamic system is achieved.

$$d\mathbf{Y}(t) = \mathbf{c}(\mathbf{Y}(t))dt + \mathbf{b}_\nu(\mathbf{Y}(t))dN_\nu(t) + \mathbf{b}_\mu(\mathbf{Y}(t))dN_\mu(t), \tag{5.5}$$

where

$$\mathbf{Y}(t) = \begin{bmatrix} Y \\ \dot{Y} \\ Z \end{bmatrix}, \quad \mathbf{c}(\mathbf{Y}(t)) = \begin{bmatrix} \dot{Y} \\ -\omega^2 Y - 2\zeta\omega\dot{Y} + \beta\omega^2 YZ \\ 0 \end{bmatrix},$$
$$\mathbf{b}_\nu(\mathbf{Y}(t)) = \begin{bmatrix} 0 \\ 0 \\ 1 - Z \end{bmatrix}, \quad \mathbf{b}_\mu(\mathbf{Y}(t)) = \begin{bmatrix} 0 \\ 0 \\ -Z \end{bmatrix}. \tag{5.6}$$

(5.5) appears as a generalized Itô-differential equation driven by the Poisson counting processes $N_\mu(t)$ and $N_\nu(t)$. Due to the Markov property of the Poisson counting processes, the state vector $\mathbf{Y}(t)$ becomes a Markov vector. The drift vector $\mathbf{c}(\mathbf{Y}(\mathbf{t}))$ is quadratic nonlinear due to the term YZ. However, an equivalent linear system may be introduced at the expense of the introduction of 2 new state variables $Y_3 = YZ$ and $Y_4 = \dot{Y}Z$ as follows

$$dY_3 = \dot{Y}Zdt + YdZ = \dot{Y}Zdt + Y(1 - Z)dN_\nu - ZdN_\mu,$$
$$dY_4 = \ddot{Y}Zdt + \dot{Y}dZ = (-2\zeta\omega\dot{Y} - \omega^2 Y + \beta\omega^2 ZY)Zdt + \dot{Y}(1 - Z)dN_\nu + \dot{Y}ZdN_\mu\,. \tag{5.7}$$

Since, $Z(t)$ is evaluated to either 0 or 1, $Z^2(t)$ is also evaluated to 0 or 1. Hence, in the second equation of (5.7) $Z^2(t)$ may be replaced by $Z(t)$. Combining (5.1) and (5.7) the following generalized Itô differential equation may be formulated

$$d\mathbf{Z}(t) = \mathbf{A}\mathbf{Z}(t)dt + \mathbf{b}_\nu(\mathbf{Z}(t))dN_\nu(t) + \mathbf{b}_\mu(\mathbf{Z}(t))dN_\mu(t), \tag{5.8}$$

where

$$\mathbf{Z}(t) = \begin{bmatrix} Y \\ \dot{Y} \\ YZ \\ \dot{Y}Z \end{bmatrix} = \begin{bmatrix} Y_1 \\ Y_2 \\ Y_3 \\ Y_4 \end{bmatrix}, \quad \mathbf{A} = \begin{bmatrix} 0 & 1 & 0 & 0 \\ -\omega^2 & -2\zeta\omega & \beta\omega^2 & 0 \\ 0 & 0 & 0 & 1 \\ 0 & 0 & \omega^2(\beta-1) & -2\zeta\omega \end{bmatrix},$$

$$\mathbf{b}_\nu(\mathbf{Z}(t)) = \begin{bmatrix} 0 \\ 0 \\ Y_1 - Y_3 \\ Y_2 - Y_4 \end{bmatrix}, \quad \mathbf{b}_\mu(\mathbf{Z}(t)) = \begin{bmatrix} 0 \\ 0 \\ -Y_3 \\ -Y_4 \end{bmatrix}. \tag{5.9}$$

It is worthwhile to note that $Y_3 = YZ$ and $Y_4 = \dot{Y}Z$ are also jump processes. Both are equal to zero in the time intervals, where $Z(t) = 0$.

5.1.2 Moment stability

Performing the averaging of the stochastic equations (5.5) does not result in a closed set of equations for the mean values due to the presence of the term YZ. However, this is not the case for the linear stochastic equations (5.8). Taking the mean value of (5.8) provides

$$\begin{aligned} dE\big[Z_i(t)\big] &= A_{ij}E\big[Z_j(t)\big]dt \\ &+ E\big[B_{\nu,i}(Z)\big]E\big[dN_\nu(t)\big] + E\big[B_{\mu,i}(Z)\big]E\big[dN_\mu(t)\big], \quad i,j = 1,2,3,4 \end{aligned} \tag{5.10}$$

where index notation is used. In (5.10) it is utilized that $Z_i(t)$ and $dN_\mu(t)$ are mutual independent as a consequence of the Itô interpretation, as is the case of $Z_i(t)$ and $dN_\nu(t)$. Since $E\big[dN_\mu(t)\big] = \mu dt$ and $E\big[dN_\nu(t)\big] = \nu dt$ the following ordinary differential equations are obtained for the mean values $m_j(t) = E\big[Y_j(t)\big]$

$$\frac{d}{dt}\begin{bmatrix} m_1 \\ m_2 \\ m_3 \\ m_4 \end{bmatrix} = \begin{bmatrix} 0 & 1 & 0 & 0 \\ -\omega^2 & -2\zeta\omega & \beta\omega^2 & 0 \\ \nu & 0 & -(\nu+\mu) & 1 \\ 0 & \nu & \omega^2(\beta-1) & -(2\zeta\omega+\nu+\mu) \end{bmatrix}\begin{bmatrix} m_1 \\ m_2 \\ m_3 \\ m_4 \end{bmatrix} \tag{5.11}$$

In order to derive a closed set of differential equations for the second order moments, let $m_{ij}(t) = E\big[Z_i(t)Z_j(t)\big]$. Then

$$\begin{aligned} dm_{ij}(t) &= E\big[\dot{Z}_i(t)Z_j(t)\big]dt + E\big[Z_i(t)\dot{Z}_j(t)\big] \\ &= A_{ik}m_{kj}(t)dt + A_{jk}m_{ki}(t)dt + \Big(E\big[B_{\nu,i}Z_j(t)\big] + E\big[B_{\nu,j}Z_i(t)\big]\Big)E\big[dN_\nu(t)\big] \\ &+ \Big(E\big[B_{\mu,i}Z_j(t)\big] + E\big[B_{\mu,j}Z_i(t)\big]\Big)E\big[dN_\mu(t)\big]. \end{aligned} \tag{5.12}$$

By use of the symmetric property $m_{ij}(t) = m_{ji}(t)$, (5.12) produces 10 equations. Using the identities $E\left[\dot{Y}YZ\right] = E\left[Y\dot{Y}Z\right] \Rightarrow m_{23} = m_{14}$ and $E\left[YZ\dot{Y}Z\right] = E\left[Y\dot{Y}Z\right] \Rightarrow m_{34} = m_{14}$, the 6 equations specifying the development of $m_{11}, m_{12}, m_{22}, m_{13}, m_{14}$ and m_{24} form a closed set of equations listed as

$$\frac{d}{dt}\begin{bmatrix} m_{11} \\ m_{12} \\ m_{22} \\ m_{13} \\ m_{14} \\ m_{24} \end{bmatrix} = \begin{bmatrix} 0 & 2 & 0 & 0 & 0 & 0 \\ -\omega^2 & -2\zeta\omega & 1 & \beta\omega^2 & 0 & 0 \\ 0 & -2\omega^2 & -4\zeta\omega & 0 & 2\beta\omega^2 & 0 \\ \nu & 0 & 0 & -(\nu+\mu) & 2 & 0 \\ 0 & \nu & 0 & \omega^2(\beta-1) & -(2\zeta\omega+\nu+\mu) & 1 \\ 0 & 0 & \nu & 0 & 2\omega^2(\beta-1) & -(4\zeta\omega+\nu+\mu) \end{bmatrix} \begin{bmatrix} m_{11} \\ m_{12} \\ m_{22} \\ m_{13} \\ m_{14} \\ m_{24} \end{bmatrix}. \tag{5.13}$$

First- and second-order moments are asymptotically stable if all the eigenvalues of the coefficient matrices in (5.11) and (5.13) have negative real parts. The eigenvalues are evaluated numerically and the regions are determined where all the eigenvalues have negative real parts.

5.1.3 Transformation to hyperspherical coordinates

First the following change of variables is performed

$$X_1 = Y_1, \quad X_2 = Y_2/\omega, \quad X_3 = Y_3, \quad X_4 = Y_4/\omega, \tag{5.14}$$

The stochastic differential equations (5.8) are then written in the following form

$$d\mathbf{X}(t) = \mathbf{C}\mathbf{X}(t)dt + \mathbf{B}(\mathbf{X}(t))d\mathbf{N}(t),$$

$$\mathbf{X}(t) = \begin{bmatrix} X_1 \\ X_2 \\ X_3 \\ X_4 \end{bmatrix}, \quad \mathbf{C} = \begin{bmatrix} 0 & \omega & 0 & 0 \\ -\omega & -2\zeta\omega & \beta\omega & 0 \\ 0 & 0 & 0 & \omega \\ 0 & 0 & \omega(\beta-1) & -2\zeta\omega \end{bmatrix}, \quad \mathbf{N}(t) = \begin{bmatrix} N_\nu(t) \\ N_\mu(t) \end{bmatrix}$$

$$\mathbf{B}(\mathbf{X}(t)) = [\mathbf{B}_\mu(\mathbf{X}(t))\mathbf{B}_\nu(\mathbf{X}(t))], \quad \mathbf{B}_\mu(\mathbf{X}(t)) = \begin{bmatrix} 0 \\ 0 \\ X_1 - X_3 \\ X_2 - X_4 \end{bmatrix}, \quad \mathbf{B}_\nu = \begin{bmatrix} 0 \\ 0 \\ -X_3 \\ -X_4 \end{bmatrix}. \tag{5.15}$$

In Lyapunov exponents approach to stochastic stability problems it is convenient to transform the original coordinates to hyperspherical ones (Khasminskii 1967; Griesbaum 1999; Simon and

Wedig 2001), which are made up of the amplitude process $A(t)$ and the angular processes $\Psi(t)$, $\Phi_1(t)$ and $\Phi_2(t)$. The advantage of such a transformation is that the equations are easier to handle, as the introduced angular processes are always bounded and the equation for the logarithm of the amplitude process may be directly integrated with respect to time. The hypergeometrical transformation, which is a generalization of the van der Pol transformation for the 2D case, is defined as follows

$$\begin{aligned}
X_1(t) &= A(t)\cos\Psi(t)\cos\Phi_1(t)\cos\Phi_2(t),\\
X_2(t) &= A(t)\sin\Psi(t)\cos\Phi_1(t)\cos\Phi_2(t),\\
X_3(t) &= A(t)\sin\Phi_1(t)\cos\Phi_2(t),\\
X_4(t) &= A(t)\sin\Phi_2(t).
\end{aligned} \tag{5.16}$$

The hyperspherical coordinates are expressed by the inverse transformations as

$$\begin{aligned}
A(t) &= \sqrt{X_1^2(t)+X_2^2(t)+X_3^2(t)+X_4^2(t)}, && 0 \le A(t) < \infty,\\
\Psi(t) &= \begin{cases} \arctan\left(\dfrac{X_2(t)}{X_1(t)}\right), & X_1(t) \ge 0,\\ \arctan\left(\dfrac{X_2(t)}{X_1(t)}\right)+\pi, & X_1(t) < 0, \end{cases} && -\frac{\pi}{2} < \Psi(t) < \frac{3\pi}{2},\\
\Phi_1(t) &= \arctan\left(\frac{X_3(t)}{\sqrt{X_1^2(t)+X_2^2(t)}}\right), && -\frac{\pi}{2} < \Phi_1(t) < \frac{\pi}{2},\\
\Phi_2(t) &= \arctan\left(\frac{X_4(t)}{\sqrt{X_1^2(t)+X_2^2(t)+X_3^2(t)}}\right), && -\frac{\pi}{2} < \Phi_2(t) < \frac{\pi}{2}.
\end{aligned} \tag{5.17}$$

The generalized Itô's differential rule, see e.g. (Iwankiewicz and Nielsen 1999) reads

$$dV(\mathbf{X}(t)) = \frac{\partial V(\mathbf{X}(t))}{\partial X_i} C_{ij} X_j(t)dt + \sum_{\alpha=\mu,\nu}\Big(V(\mathbf{X}(t)+\mathbf{B}_\alpha(\mathbf{X}(t))) - V(\mathbf{X}(t))\Big)dN_\alpha(t), \tag{5.18}$$

where $V(\cdot)$ is an arbitrary differentiable function. The first term on the right hand side of (5.18) specifies the increment of V according to conventional differential theory, whereas the last term specifies the increment due to jumps of the Poisson processes. If a jump $dN_\alpha(t) = 1$ occurs, the state vector changes from $\mathbf{X}(t)$ to $\mathbf{X}(t) + \mathbf{B}_\alpha(t)$. Then, the increment of the function becomes $V(\mathbf{X}(t)+\mathbf{B}_\alpha(t))-V(\mathbf{X}(t))$ as indicated by (5.18). The stochastic equations for the transformed variables are obtained as

$$
\begin{aligned}
d\Big(\ln A(t)\Big) &= h_1\Big(\Psi(t),\Phi_1(t),\Phi_2(t)\Big)dt + g_{1\nu}\Big(\Psi(t),\Phi_1(t),\Phi_2(t)\Big)dN_\nu \\
&\quad + g_{1\mu}\Big(\Psi(t),\Phi_1(t),\Phi_2(t)\Big)dN_\mu \\
d\Big(\Psi(t)\Big) &= h_2\Big(\Psi(t),\Phi_1(t),\Phi_2(t)\Big)dt + g_{2\nu}\Big(\Psi(t),\Phi_1(t),\Phi_2(t)\Big)dN_\nu \\
&\quad + g_{2\mu}\Big(\Psi(t),\Phi_1(t),\Phi_2(t)\Big)dN_\mu, \\
d\Big(\Phi_1(t)\Big) &= h_3\Big(\Psi(t),\Phi_1(t),\Phi_2(t)\Big)dt + g_{3\nu}\Big(\Psi(t),\Phi_1(t),\Phi_2(t)\Big)dN_\nu \\
&\quad + g_{3\mu}\Big(\Psi(t),\Phi_1(t),\Phi_2(t)\Big)dN_\mu, \\
d\Big(\Phi_2(t)\Big) &= h_4\Big(\Psi(t),\Phi_1(t),\Phi_2(t)\Big)dt + g_{4\nu}\Big(\Psi(t),\Phi_1(t),\Phi_2(t)\Big)dN_\nu \\
&\quad + g_{4\mu}\Big(\Psi(t),\Phi_1(t),\Phi_2(t)\Big)dN_\mu,
\end{aligned}
\tag{5.19}
$$

where the drift terms are given by

$$
\begin{aligned}
h_1 &= \cos\Phi_2(t)\Big(-2\zeta\omega\sin^2\Psi(t)\cos^2\Phi_1(t)\cos\Phi_2(t) \\
&\quad + \beta\omega\sin\Psi(t)\sin\Phi_1(t)\cos\Phi_1(t)\cos\Phi_2(t) + \beta\omega\sin\Phi_1(t)\sin\Phi_2(t)\Big) - 2\zeta\omega\sin^2\Phi_2(t), \\
h_2 &= -\omega - 2\zeta\omega\sin\Psi(t)\cos\Psi(t) + \beta\omega\cos\Psi(t)\tan\Phi_1(t), \\
h_3 &= 2\zeta\omega\sin^2\Psi(t)\cos\Phi_1(t)\sin\Phi_1(t) - \beta\omega\sin\Psi(t)\sin^2\Phi_1(t) + \omega\cos\Phi_1(t)\tan\Phi_2(t), \\
h_4 &= 2\zeta\omega\sin^2\Psi(t)\cos^2\Phi_1(t)\cos\Phi_2(t)\sin\Phi_2(t) \\
&\quad - \beta\omega\sin\Psi(t)\cos\Phi_1(t)\sin\Phi_1(t)\cos\Phi_2(t)\sin\Phi_2(t) \\
&\quad - \omega\sin\Phi_1(t) + \beta\omega\sin\Phi_1(t)\cos^2\Phi_2(t) - 2\zeta\omega\cos\Phi_2(t)\sin\Phi_2(t),
\end{aligned}
\tag{5.20}
$$

and the diffusion terms are expressed as

$$
\begin{aligned}
g_{1\nu} &= \frac{1}{2}\ln 2 + \ln\Big(\cos\Phi_1(t)\cos\Phi_2(t)\Big),\\
g_{1\mu} &= \ln\Big(\cos\Phi_1(t)\cos\Phi_2(t)\Big),\\
g_{2\nu} &= 0,\\
g_{2\mu} &= 0,\\
g_{3\nu} &= \arctan\Big(\cos\Psi(t)\Big) - \Phi_1(t),\\
g_{3\mu} &= -\Phi_1(t),\\
g_{4\nu} &= \arctan\Big(\frac{\sin\Psi(t)}{\sqrt{1+\cos^2\Psi(t)}}\Big) - \Phi_2(t),\\
g_{4\mu} &= -\Phi_2(t).
\end{aligned}
\tag{5.21}
$$

The angular process $\Psi(t)$ is not a jump process driven by the Poisson processes, as it is seen in (5.19) and (5.21) ($g_{2\nu} = 0$ and $g_{2\mu} = 0$) this process develops only due to drift. However, it is a discontinuous, or a jump, process of another kind. As it follows from its definition (5.17) at the time instants when the displacement response $X_1(t)$ changes the sign, the process $\Psi(t)$ reveals jumps of magnitude 2π. Between these jumps the time evolution of $\Psi(t)$ is due to drift only. The angular processes $\Phi_1(t)$ and $\Phi_2(t)$ are exactly equal to zero in the time intervals where $Z(t) = 0$. This can be observed directly in (5.17), but it also follows from the coefficients h_3, h_4 as given by (5.20) and from $g_{3\nu}$, $g_{3\mu}$, $g_{4\nu}$, $g_{4\mu}$, as given by (5.17). If the processes $\Phi_1(t)$ and $\Phi_2(t)$ start, in some time interval, from zero values, then $h_3 = 0$ and $h_4 = 0$, hence there is no drift development and these processes continue to be zero. At the first N_ν-driven point there are jump changes in both $\Phi_1(t)$ and $\Phi_2(t)$ and at the first subsequent N_μ-driven point there is a jump back to zero. The drift development is only present when $Z(t) = 1$, hence $\Phi_1(t) \neq 0$ and $\Phi_2(t) \neq 0$.

5.1.4 Lyapunov exponents and stability with probability 1

The trivial solution $\mathbf{X}(t) \equiv 0$ of (5.15), is almost surely asymptotically stable, if the largest Lyapunov exponent is negative, hence if

$$
\lambda = \lim_{t\to\infty}\frac{1}{t}\ln\left(\frac{|\mathbf{X}(t)|}{|\mathbf{X}(0)|}\right) < 0, \tag{5.22}
$$

where $|\mathbf{X}(t)| = \sqrt{X_1^2(t) + X_2^2(t) + X_3^2(t) + X_4^2(t)}$. This definition of λ is used by Xie (2005), who devised a numerical approach for determining the pth moment Lyapunov exponents by the use of Monte carlo simulation. This approach is convenient when the noise excitation cannot be described in such a form it can be treated easily. Here the sample stability governed by (5.22) is of interest and the first and second moment stability is governed by the eigenvalues of the matrices of (5.11) and (5.13), respectively. The sample stability could be investigated numerically, by

simulating the stochastic equations (5.15). However when the sample curve is unstable, the values of the state variables become very large, which causes some numerical problems. It is more convenient to make use of the fact that $\sqrt{X_1^2(t)+X_2^2(t)+X_3^2(t)+X_4^2(t)} = A(t)$ and find the Lyapunov exponent as

$$\lambda = \lim_{t\to\infty} \frac{1}{t} \ln\left(\frac{A(t)}{A(0)}\right) < 0, \tag{5.23}$$

simulating directly the stochastic equation for $\ln A(t)$, as given by (5.19). The advantage of this kind of simulation is that the only functions involved at the right-hand sides of the equations (5.19) are the angular processes $\Psi(t)$, $\Phi_1(t)$ and $\Phi_2(t)$, which are bounded, see (5.17). As the amplitude process $A(t)$ is not involved at the right-hand side of (5.20) for $\ln A(t)$, *cf.* (Griesbaum 1999; Simon and Wedig 2001), this equation can be directly integrated with respect to time and substituted into (5.23) which results in a time-average integral

$$\lambda = \lim_{T\to\infty} \frac{1}{T} \int_0^T \Big(h_1\big(\Psi(t),\Phi_1(t),\Phi_2(t)\big)dt + g_{1\nu}\big(\Phi_1(t),\Phi_2(t)\big)dN_\nu + g_{1\mu}\big(\Phi_1(t),\Phi_2(t)\big)dN_\mu \Big) \tag{5.24}$$

Assuming ergodicity of $h_1\big(\Psi(t),\Phi_1(t),\Phi_2(t)\big)$, $g_{1\nu}\big(\Phi_1(t),\Phi_2(t)\big)$, and $g_{1\mu}\big(\Phi_1(t),\Phi_2(t)\big)$ we can make the following replacement

$$\begin{aligned}\lambda = \lim_{T\to\infty} \frac{1}{T} \int_0^T \Big(& E\big[h_1\big(\Psi(t),\Phi_1(t),\Phi_2(t)\big)\big]dt + E\big[g_{1\nu}\big(\Phi_1(t),\Phi_2(t)\big)dN_\nu\big] \\ & + E\big[g_{1\mu}\big(\Phi_1(t),\Phi_2(t)\big)dN_\mu\big] \Big)\end{aligned} \tag{5.25}$$

where $E\big[g_{1\nu}\big(\Phi_1(t),\Phi_2(t)\big)dN_\nu\big] = E\big[g_{1\nu}\big(\Phi_1(t),\Phi_2(t)\big)\big]\nu dt$ and $E\big[g_{1\mu}\big(\Phi_1(t),\Phi_2(t)\big)dN_\mu\big] = E\big[g_{1\mu}\big(\Phi_1(t),\Phi_2(t)\big)\big]\mu dt$. Further, it is assumed that the processes $\Phi_1(t)$, $\Phi_2(t)$ and $\Psi(t)$ are stationary, hence, there exist time-invariant marginal probability densities $p(\psi,\phi_1,\phi_2)$ and $p(\phi_1,\phi_2)$. Then the expectations in (5.25) are also time-invariant and we obtain

$$\begin{aligned}\lambda &= E\big[h_1\big(\Psi(t),\Phi_1(t),\Phi_2(t)\big)\big] + \nu E\big[g_{1\nu}\big(\Phi_1(t),\Phi_2(t)\big)\big] + \mu E\big[g_{1\mu}\big(\Phi_1(t),\Phi_2(t)\big)\big] \\ &= \int_{-\pi/2}^{3\pi/2}\int_{-\pi/2}^{\pi/2}\int_{-\pi/2}^{\pi/2} h_1(\psi,\phi_1,\phi_2)p(\psi,\phi_1,\phi_2)d\psi d\phi_1 d\phi_2 \\ &\quad + \int_{-\pi/2}^{\pi/2}\int_{-\pi/2}^{\pi/2} \big(\nu g_{1\nu}(\phi_1,\phi_2) + \mu g_{1\mu}(\phi_1,\phi_2)\big)p(\phi_1,\phi_2)d\phi_1 d\phi_2.\end{aligned} \tag{5.26}$$

The probability densities $p(\psi,\phi_1,\phi_2)$ and $p(\phi_1,\phi_2)$ are evaluated from Monte Carlo simulations of the hyperspherical angular coordinate processes $\Psi(t)$, $\Phi_1(t)$ and $\Phi_2(t)$ based on the equations (5.19). Due to the jump nature of the angular processes $\Phi_1(t)$ and $\Phi_2(t)$, and the fact that they are equal to zero during some significant time intervals, the marginal probability densities $p(\psi,\phi_1,\phi_2)$ and $p(\phi_1,\phi_2)$ are very spiky, the spikes being at $\phi_1=0$, $\phi_2=0$. This makes the numerical evaluation of the integrals (5.26) cumbersome. The evaluation is significantly improved if those spikes are represented in the probability densities in the following way

$$p(\psi,\phi_1,\phi_2)=P_0\delta(\phi_1)\delta(\phi_2)p(\psi)+(1-P_0)p^0(\psi,\phi_1,\phi_2), \tag{5.27}$$

$$p(\phi_1,\phi_2)=P_0\delta(\phi_1)\delta(\phi_2)+(1-P_0)p^0(\phi_1,\phi_2), \tag{5.28}$$

where $\delta(...)$ is the Dirac delta, $p(\psi)$ is the marginal probability density of $\Psi(t)$ and $p^0(\psi,\phi_1,\phi_2)$, $p^0(\phi_1,\phi_2)$ are conditional probability densities $p^0(\psi,\phi_1,\phi_2)=p(\psi,\phi_1,\phi_2|\phi_1\neq 0,\phi_2\neq 0)$, $p^0(\phi_1,\phi_2)=p(\phi_1,\phi_2|\phi_1\neq 0,\phi_2\neq 0)$, whose areas are normalized to one. The heights P_0 of the spikes are obtained by collecting the counts for which $\phi_1=0$, $\phi_2=0$. The integrals in (5.26) reduce to

$$\begin{aligned}\lambda=&-2\zeta\omega P_0\int_{-\pi/2}^{3\pi/2}\sin^2\psi p(\psi)d\psi\\&+(1-P_0)\int_{-\pi/2}^{3\pi/2}\int_{-\pi/2}^{\pi/2}\int_{-\pi/2}^{\pi/2}h_1(\psi,\phi_1,\phi_2)p^0(\psi,\phi_1,\phi_2)d\psi d\phi_1 d\phi_2\\&+\frac{1}{2}\nu P_0\ln 2+(1-P_0)\int_{-\pi/2}^{\pi/2}\int_{-\pi/2}^{\pi/2}\Big(\nu g_{1\nu}(\phi_1,\phi_2)+\mu g_{1\mu}(\phi_1,\phi_2)\Big)p^0(\phi_1,\phi_2)d\phi_1 d\phi_2.\end{aligned} \tag{5.29}$$

The simulation scheme for the hyperspherical angular processes governed by (5.19) is as follows. Between the Poisson points the Runge-Kutta scheme is used. At the first $N_\nu(t)$-driven point and at every first $N_\nu(t)$-driven point $t_{k\nu}$ subsequent to an $N_\mu(t)$-driven point there is an increment $dN_\nu=1$, hence according to (5.19) and (5.21) there is a jump change in $\Phi_i(t)$ of magnitude $g_{i\nu}\big(\Psi(t_{k\nu}^-),\Phi_1(t_{k\nu}^-),\Phi_2(t_{k\nu}^-)\big)$

$$\Phi_i(t_{k\nu}^+)=\Phi_i(t_{k\nu}^-)+g_{i\nu}\big(\Psi(t_{k\nu}^-),\Phi_1(t_{k\nu}^-),\Phi_2(t_{k\nu}^-)\big). \tag{5.30}$$

At the first $N_\mu(t)$-driven point $t_{k\mu}$ subsequent to an $N_\nu(t)$-driven point $dN_\mu=1$, hence according to (5.20) there is a jump change in $\Phi_i(t)$ of magnitude $g_{i\mu}\big(\Psi(t_{k\nu}^-),\Phi_1(t_{k\nu}^-),\Phi_2(t_{k\nu}^-)\big)=-\Phi_i(t_{k\nu}^-)$

$$\Phi_i(t_{k\mu}^+)=\Phi_i(t_{k\mu}^-)+g_{i\mu}\Big(\Psi(t_{k\mu}^-),\Phi_1(t_{k\mu}^-),\Phi_2(t_{k\mu}^-)\Big)=0. \tag{5.31}$$

Thus the initial conditions $\Phi_i(t_{k\nu}^+)$ or $\Phi_i(t_{k\mu}^+)$ for the subsequent time interval starting at $t_{k\nu}^+$ or $t_{k\mu}^+$ are determined.

5.1.5 Numerical results

As the pulses and time gaps are negative-exponential distributed the mean pulse is $E[T_p] = 1/\mu$ and the mean time gap is $E[T_g] = 1/\nu$. The mean inter-arrival time of the pulses equals $E[T_a] = E[T_p] + E[T_g] = \frac{\mu+\nu}{\mu\nu}$. Computations have been performed for pulses with parameters:

- $(\mu, \nu) = (0.1, 0.1)$; long pulses/long gaps.
- $(\mu, \nu) = (1, 1)$; moderate pulses/moderate gaps.
- $(\mu, \nu) = (10, 10)$; short pulses /short gaps.
- $(\mu, \nu) = (0.1, 10)$; long pulses/short gaps.

The respective mean inter-arrival times are $E[T_a] = 20; 2; 0.2; 10.1$ $[s]$. A non-dimensional parameter $\tau = \frac{(\mu+\nu)\omega}{\mu\nu\pi}$ is introduced, which is the ratio of the mean inter-arrival time $E[T_a]$ of the pulses to half of the natural period $T_n = 2\pi/\omega$ of the system. In other words, τ is a relative measure of the density of the pulse train or of its mean arrival rate. This setting is inspired by the fact that a corresponding harmonic parametric excitation with the circular frequency 2ω will cause instability for $\zeta = 0$. Example sample functions of the displacement response $Y(t)$ and of the velocity response $\dot{Y}(t)$ for the stable behaviour, obtained for the initial conditions $Y(0) = 1$ and $\dot{Y}(0) = 0$ are shown in Figures 5.2a and 5.2b, respectively. It is seen that the system is performing essentially the natural vibrations.

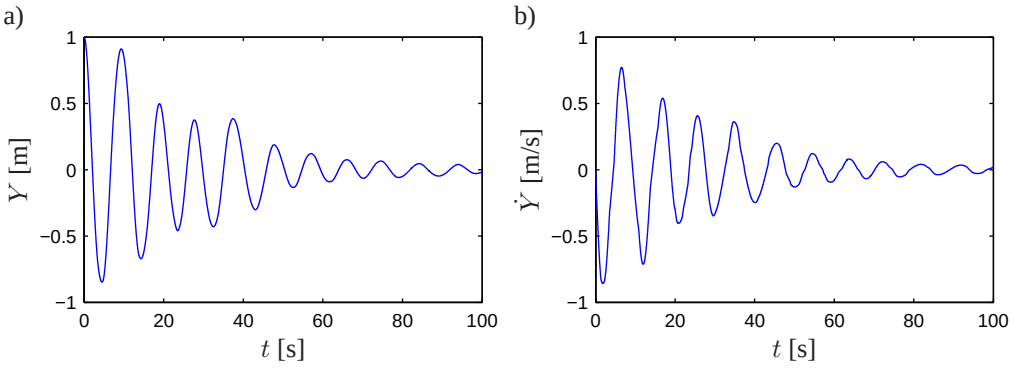

Figure 5.2 Sample function of the stable response. Moderate pulses/moderate gaps: $\mu = 1.0s^{-1}, \nu = 1.0s^{-1}$, $\zeta = 0.05$, $\beta = 0.5, \tau = 0.5$. a) Displacement $Y(t)$. b) Velocity $\dot{Y}(t)$.

Figure 5.3a shows an example phase plot of the stable response obtained for the initial conditions $Y(0) = 1$ and $\dot{Y}(0) = 0$. An example phase plot of the unstable response is shown in Figure 5.3b.

Simulated sample function of $Z(t)$ obtained for the initial condition $Z(0) = 0$ giving the stable response in Figures 5.2 and 5.3a is shown in Figure 5.4.

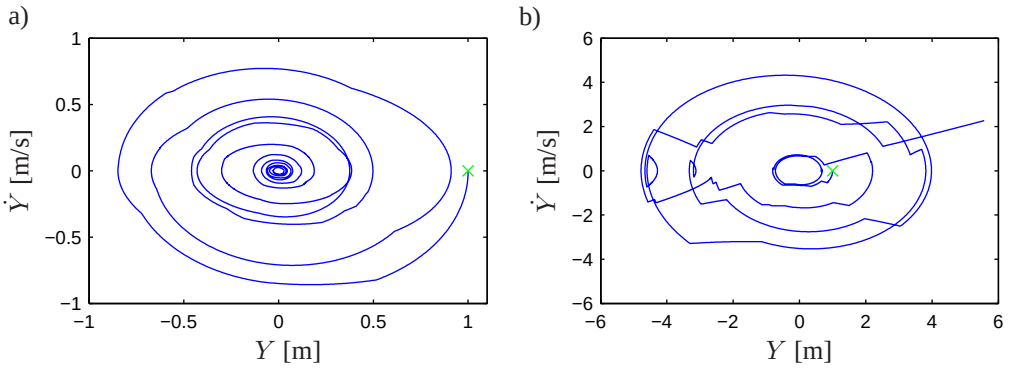

Figure 5.3 Phase plot of the response. $\zeta = 0.05, \mu = 1.0, \nu = 1.0, \tau = 0.5$. ($\times$) indicate start conditions. a) Stable condition $\beta = 0.5$. b) Unstable condition $\beta = 1.2$.

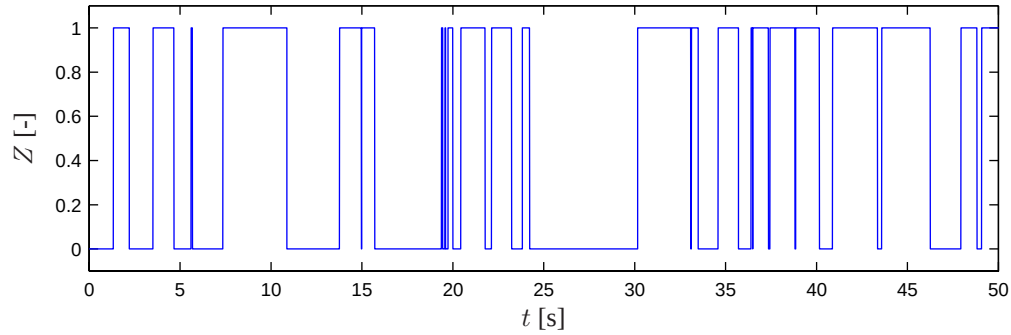

Figure 5.4 Simulated sample function of $Z(t)$ for $\mu = 1.0, \nu = 1.0$.

Figure 5.5a shows $\ln A(t)$ for the stable response behaviour illustrated in Figure 5.2 and 5.3a. The example sample functions of the angular processes $\Psi(t)$, $\Phi_1(t)$ and $\Phi_2(t)$ corresponding to the sample function of $Z(t)$ shown in the Figure 5.4 are shown in Figures 5.5b-d, respectively. The behaviour of $\Phi_1(t)$, $\Phi_2(t)$ is in agreement with the one predicted from the governing stochastic equations (5.19)-(5.21). The process $\Psi(t)$ reveals jumps of magnitude 2π at the time instants separated by the intervals equal to the natural periods. This is in agreement with the fact that the system is performing essentially the natural vibrations (*cf.* Figure 5.2), hence $X_1(t)$ changes the sign periodically.

The spectrum of the sample function of $\Psi(t)$, obtained by FFT, is plotted in Figure 5.6. Ω indicates the running frequency and the abscissae axis has been normalized with respect to the undamped circular eigenfrequency ω. The spectrum reveals the peak at the natural frequency $\Omega \simeq \omega$ and some finite value at $\Omega = 0$, which corresponds to the non-zero time average of the sample function.

Final, sample functions of the marginal probability densities $p^0(\Psi)$ and $p^0(\Phi_1, \Phi_2)$ used in (5.27) are illustrated in Figures 5.7a-b, respectively. The spiked behaviour of $p^0(\Phi_1, \Phi_2)$ is due to the numerical sorting of simulated Φ_1 and Φ_2, which is done in a cartesian grid with sides of

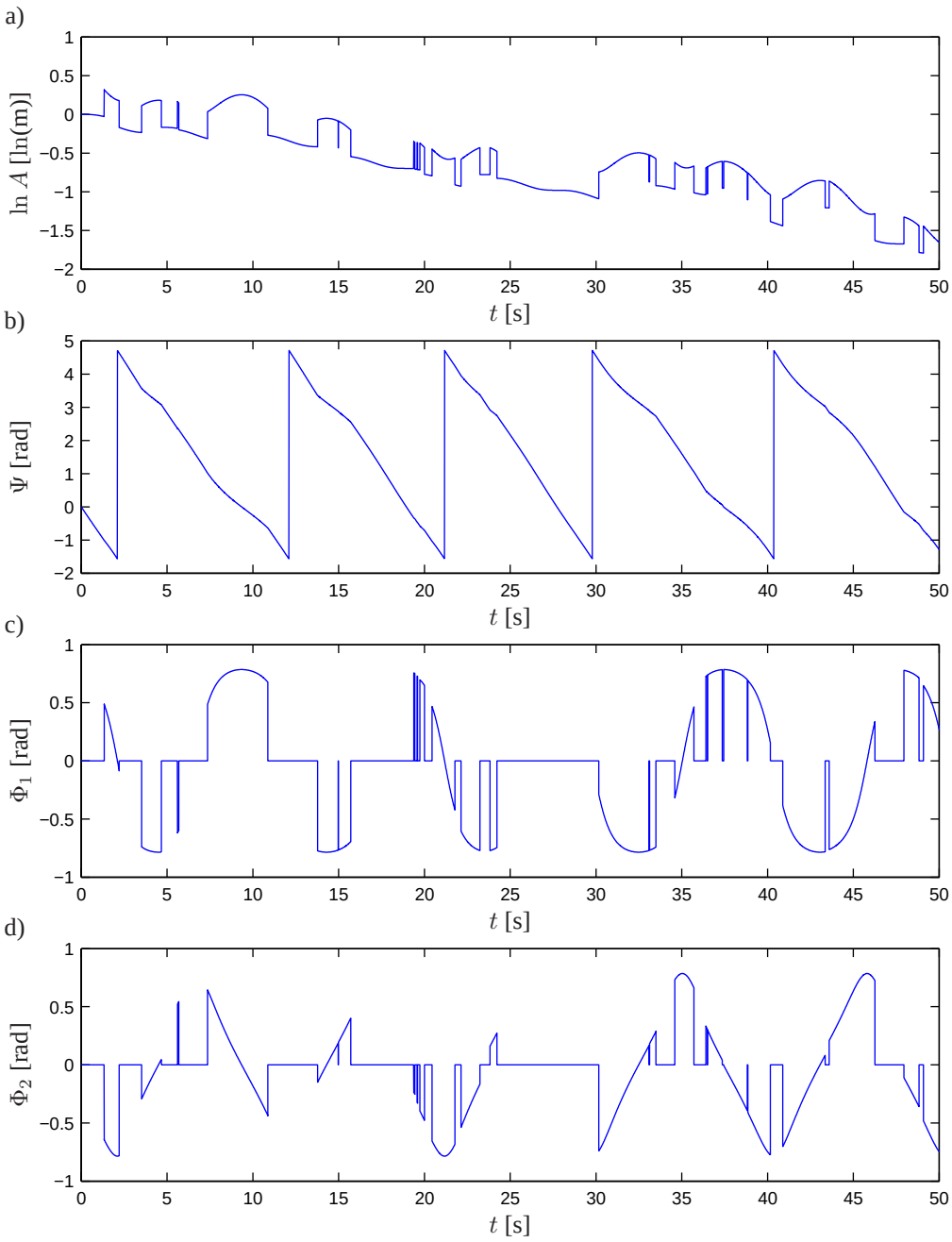

Figure 5.5 Sample function of hyperspherical coordinates for $\zeta = 0.05, \mu = 1.0, \nu = 1.0, \beta = 0.5, \tau = 0.5$. a) $\ln A(t)$. b) $\Psi(t)$. c) $\Phi_1(t)$. d) $\Phi_2(t)$

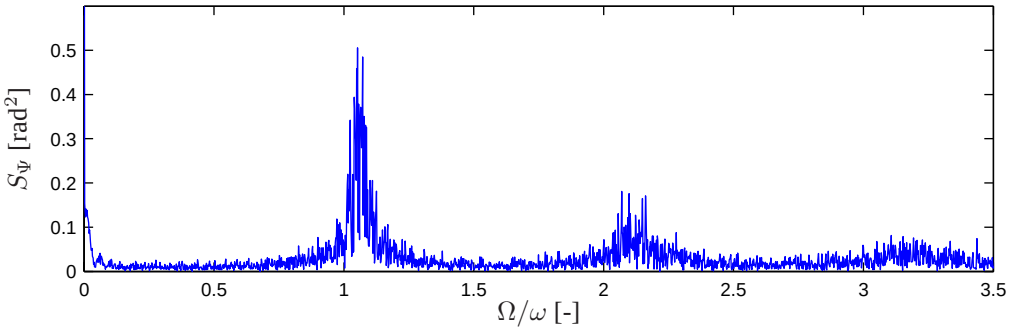

Figure 5.6 Spectrum of the sample function of $\Psi(t)$ for $\zeta = 0.05, \mu = 1.0, \nu = 1.0, \beta = 0.5, \tau = 0.5$.

length 0.01. As seen, a polar grid would be more convenient in this case.

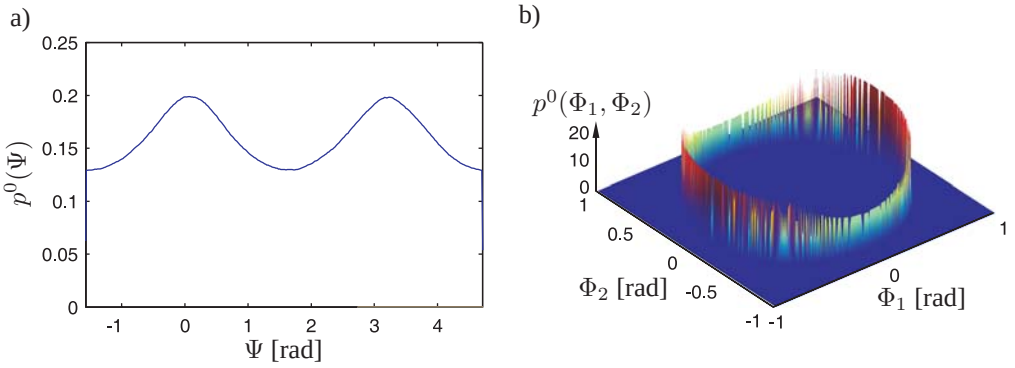

Figure 5.7 Marginal probability densities of the sample function for $\zeta = 0.05, \mu = 1.0, \nu = 1.0, \beta = 0.5, \tau = 0.5$. a) $p^0(\Psi)$. b) $p^0(\Phi_1, \Phi_2)$.

In Figure 5.8 the stability regions are plotted against the non-dimensional parameter τ. The curves in Figure 5.8 show the stability regions border lines. The stability region is below the curve. (— —) and (— —) indicate lines of zero real parts of the eigenvalue with the largest real part, for the mean and mean-square stability, respectively. (——) indicates the zero Lyapunov exponent as obtained by direct simulation of the equation for $\ln A(t)$, as given by (5.19). (——) corresponds to the zero Lyapunov exponent as evaluated by ensemble averaging, in terms of integrals (5.27). The results for Lyapunov exponents obtained from both methods are qualitatively the same. It is seen that the lines of zero Lyapunov exponents lie above the lines obtained from the mean-square stability.

If $\mu = \nu$, i.e. the mean duration of the pulses and mean time gaps are the same, the curves showing stability regions have very similar shape, see Figures 5.8a-c. As the natural frequency ω of the system decreases, so does the parameter τ and the stability region increases. The curves for the moment stability have identical shapes. However the stability regions are not the same, because the results are shown against the relative parameter τ. When μ and ν are large the same

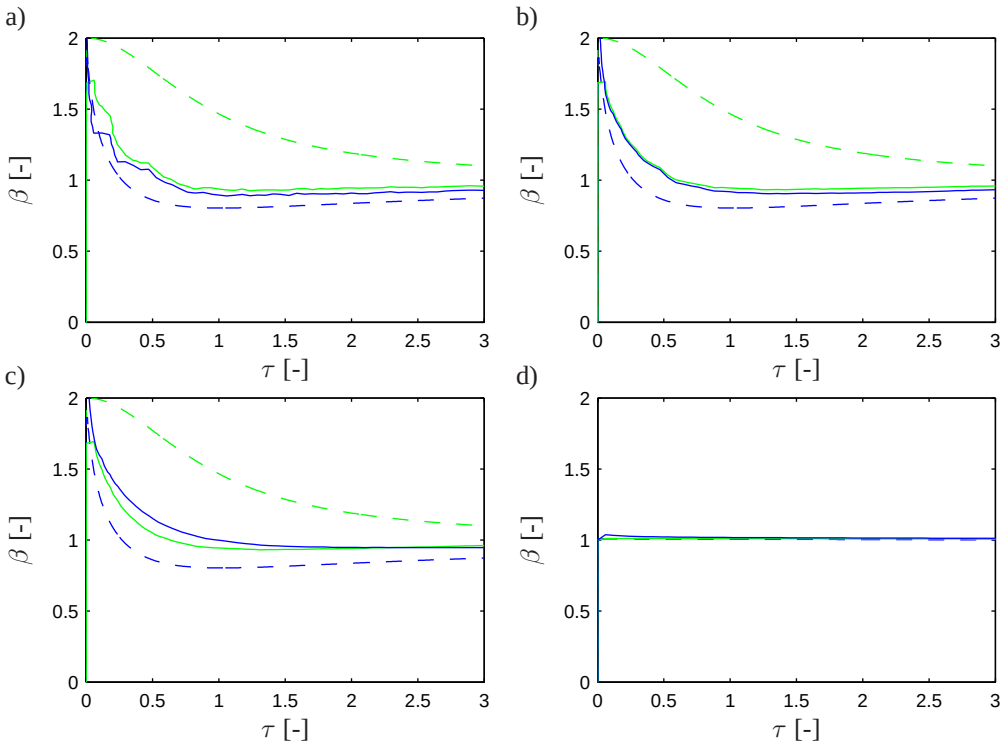

Figure 5.8 Stability curves as function of τ and β. $\zeta = 0.05$. (– –) mean stability. (– –) mean-square stability. (——) Lyapunov exponents by direct simulations. (——) Lyapunov exponents by ensemble averaging.
a) Long pulses/long gaps: $\mu = 0.1s^{-1}, \nu = 0.1s^{-1}$.
b) Moderate pulses/moderate gaps: $\mu = 1.0s^{-1}, \nu = 1.0s^{-1}$.
c) Short pulses /short gaps: $\mu = 10s^{-1}, \nu = 10s^{-1}$.
d) Long pulses /short gaps: $\mu = 0.1s^{-1}, \nu = 10s^{-1}$.

value τ as for small μ and ν corresponds to a higher natural frequency. For example for a pulse train with $(\mu, \nu) = (0.1, 0.1)$ and $E[T_a] = 20$ (Figure 5.8a) the natural frequency corresponding to a value $\tau = 1$ equals $\pi/20$, while for $(\mu, \nu) = (1, 1)$ with $E[T_a] = 2$ (Figure 5.8b) it is $\pi/2$. It is seen that a larger stability region corresponds to $\omega = \pi/20$ in Figure 5.8b than in Figure 5.8a. This means that as the mean inter-arrival time of the pulses decreases the stability region for the same oscillator increases. In other words, the stability region is larger for the pulse train with short pulses and short gaps then for long pulses and long gaps.

When the pulses have long mean pulses and short mean gaps (Figure 5.8d), it corresponds to the load which is almost constant and quasi-static. The lines for mean, mean-square and Lyapunov stability by the direct simulations coincide. The stability region is essentially the same as for the classical buckling problem, i.e. $\beta = 1$ is the critical value.

Regarding the computational effort, it should be commented that the direct simulation converges much faster than the time-averaging method, with a factor of 100. Further, the direct simulation is simpler to program. The main problem of the time-averaging method is to determine the probability density functions $p(\psi, \phi_1, \phi_2)$ and $p(\phi_1, \phi_2)$ which is very time consuming.

In all examined cases the asymptotic sample stability condition reveals larger regions of stability than the asymptotic mean square condition. This observation is in agreement with the general fact that the asymptotic moment stability is more conservative than Lyapunov asymptotic stability with probability one (asymptotic sample stability) (Arnold 1984; Kozin and Sugimoto 1977). In particular, the asymptotic mean square stability implies, for the linear systems, stability with probability 1 (Lin and Cai 1995).

5.1.6 Concluding remarks

Asymptotic stability of first- and second-order moments as well as Lyapunov asymptotic (sample) stability with probability 1 are investigated for the dynamic system under a renewal driven jump process parametric excitation. The original state vector of the system is a non-Markov process, however the excitation process is shown to be governed by the stochastic equation driven by two independent Poisson processes, with different parameters, which allows to convert the original non-Markov problem into a Markov one. The original state vector has been augmented by two additional equations. It has been shown that the set of equations for the mean values is closed by appending the equations for two extra second-order moments and the equations for second-order moments form a closed set if the equations for three extra third-order moments are added. In order to investigate the asymptotic sample stability the transformation of the four state variables to hyperspherical coordinates is made. The Lyapunov exponents have been evaluated with the aid of two methods. The first one is direct simulation of the stochastic equation governing the natural logarithm of the hyperspherical amplitude process. In the second approach, based on ergodicity assumption, time averaging of the pertinent expressions is replaced by ensemble averaging and the modification of the approach used in (Griesbaum 1999) and (Simon and Wedig 2001) has been developed. The numerical results show good qualitative agreement between two methods of evaluating the Lyapunov exponents. Direct simulation is however more robust and less time consuming, hence it is more suitable for the problem. The asymptotic mean-square stability condition is more conservative than Lyapunov asymptotic (sample) stability with probability 1. However, the asymptotic mean-square stability condition is shown not to be overly conservative and therefore provides a good estimate of the asymptotic stochastic stability.

5.2 Stochastic Stability of Whirling Motion of a Shallow Cable Using Floquet Theory

Cables used as structural support elements of masts, towers and cable-stayed bridges are characterised by a sag-to-chord-length ratio below of 0.01, which means that the natural frequencies for the vertical and the horizontal vibrations are pairwise close. The slenderness of the cables makes them prone to vibrations, either induced by direct loads on the cables from the wind or a combination of wind and rain (Cao *et al.* 2001; Geurts *et al.* 1998), or via motion of the supported structure. Typically, the supported structure is performing narrow-banded random vibrations, with the implication that the cables will be subjected to narrow-banded support-point motions. Especially, the component of the relative support-point motion along the chord is important for the cable dynamics. Primarily, the said displacement component is exciting the cable as an additive load term in the in-plane equation of motion. Additionally, the component appears as parametric load terms in both the in-plane and the out-of-plane equations of motion. If the centre frequency of this excitation is close to a pair of cable eigenfrequencies strong 1:1 internal resonance vibrations in the involved modes take place. Since the eigenfrequencies of the symmetric in-plane modes are increasing with the Irvine stiffness parameter, similar internal resonance couplings involving the first symmetric in-plane mode, the second antisymmetric in-plane and the second antisymmetric out-of-plane modes may occur at a somewhat higher sag-to-chord-length ratio corresponding to the so-called cross-over eigenfrequency of the cable. At a still higher sag-to-chord-length ratio nonlinear interactions between the first symmetric mode and the second symmetric out-of-plane modes may occur. Similar interaction patterns exist for the second and higher order symmetric in-plane modes.

For shallow cables additional internal resonances caused by nonlinear or parametric coupling terms occur, if the excitation frequency is a multiple of the eigenfrequencies of the considered pair of modes (super-harmonic response), or a fraction of these frequencies (subharmonic response). Normally, the subharmonic response is more pronounced. Also coupled or uncoupled harmonic responses with the frequency fraction 2/3 (combinatorial harmonic response) may occur.

Forced response with coupled vertical and horizontal responses has been analysed in a number of studies based on Galerkin based reduced two-degrees-of-freedom models. Tadjbakhsh and Wang (1990) investigated the response of wind induced cables modelled as a three-degrees-of-freedom system including quadratic nonlinearities with the internal resonant conditions $\omega_3 \simeq 2\omega_2$ and $\omega_2 \simeq 2\omega_1$ with the second mode excited ($\Omega \simeq \omega_2$). They found that the system exhibits both saturation and jump phenomena. It was demonstrated that the stable response to the vertical excitation at a certain vibration level was a whirling motion involving a phase lag of approximately $\pm\frac{\pi}{2}$ between the modal coordinates.

Multiple internal resonances in cables were also investigated by Lee and Perkins (1995), Benedettini *et al.* (1995a, 1995b), Rega *et al.* (1997), Benedettini and Rega (1994, 1997), Chang and Ibrahim (1997), and Rega *et al.* (1999). Alternatively, Pakdemirli *et al.* (1995) suggest direct attack on the partial differential equation since Galerkin reduced-order models of distributed-parameter systems with quadratic and cubic nonlinearities in some cases may lead to erroneously quantitative and even qualitative results.

Al-Noury and Ali (1985) considered the harmonic response due to a uniformly distributed load with harmonic time variation, using a two-degrees-of-freedom Galerkin approach with sine

functions used as functional basis, identical to the eigenmodes of the undamped taut cable. The same problem was dealt with by Rao and Iyengar (1991), who used the undamped eigenmodes of the parabolic equilibrium approximation as a functional basis at the reduction to a two-degrees-of-freedom system. The use of the parabolic approximation is restricted to relatively small sag-to-chord-length ratios. Vibrations caused by forced motions of the support points are especially important for supporting cables used in stay bridges and TV-towers. The main effect on the non-linear response is the introduction of significant parametric terms, which may cause significant sub-, super- and combinatorial harmonic responses either in-plane or coupled with the out-of-plane component, (Nielsen and Kirkegaard 2002). Nielsen and Krenk (2003) investigated the nonlinear response of a shallow cable with linear viscous dampers placed close to the lower support point, loaded in the static equilibrium state. The analysis focused on the whirling motion of the considered system under resonance using the complex eigenmode functions as a functional basis.

Chang *et al.* (1996), Chang and Ibrahim (1997) and Ibrahim and Chang (1999) considered the nonlinear stochastic response of a cable with a sag corresponding to the cross-over point with the intention to study nonlinear interaction in a 4-degrees-of-freedom system including the lowest two in-plane and the lowest two out-of-plane modes. Only the fundamental in-plane mode was loaded in terms of a distributed Gaussian white noise. The variance of the response was analysed by both a Gaussian closure scheme and a fourth order cumulant neglect closure scheme. Close to the bifurcation of the out-of-plane solution a so-called "on-off intermittence" was observed in which Monte Carlo simulation unveiled that multipeaked pdfs of all state variables occurred. Both the Gaussian closure and the fourth order cumulative closure scheme failed to give accurate predictions in this region. Moment methods such as Gaussian closure (equivalent linearization) and cumulant neglect closure works well in cases of a monomodal state variables, and fails to work satisfactory for multi-modal problems (Langley 1988; Sun and Hsu 1987).

Tagata (1978, 1989) studied the vibrations of a single-degree-of-freedom in-plane model of a nonlinear string with a van der Pol type of damping mechanism and a Duffing type of stiffness term. The excitation was a narrow-banded Gaussian excitation, obtained by filtering Gaussian white noise through a second order filter. The numerical results were obtained by Monte Carlo simulations.

Richard and Anand (1983) considered a two-degrees-of-freedom nonlinear string excited by a distributed in-plane weakly stationary narrow-banded Gaussian random process. They studied the existence of an upper bound on the bandwidth and a lower bound on the excitation intensity for the occurrence of multiple response states. A method for determining necessary and sufficient conditions for almost sure asymptotic stability is also presented.

The aim is to give an explanation of the mentioned "on-off intermittence" region reported by Ibrahim and co-workers. It is demonstrated that the multipeaked pdfs in the intermittence region is caused by random jumps between various periodic motions, which are stable under harmonic excitation, but become unstable with probability 1 under stochastic excitation. Especially, it is demonstrated that the jumps between vibration states in case of narrow-banded excitation are related to out-crossings of the envelope of the non-dimensional chord elongation at barrier levels.

Here a Galerkin based reduction of the nonlinear shallow cable equations to a two-degrees-of-freedom system is carried out using the fundamental in-plane and out-of-plane linear modal modes as a functional basis. At first possible stable periodic motions are identified under 1:1 internal resonance between the considered modes due to harmonically varying support points. These turn out to be a whirling and two in-plane modes of vibration. The in-plane modes are

characterized with large and small amplitudes, respectively. Next, the support point motion is changed to a narrow banded excitation with centre frequency Ω and envelope process comparable to the frequency and amplitude of the harmonic excitation. During the stochastic excitation the modal coordinates perform stochastic vibrations around the identified stable periodic motions, which form a kind of mean value response. Although stochastic, these motions are distinguishable by qualitatively different levels of amplitudes and phases, for which reason they will be referred to as "states". During narrow banded stochastic excitation it turns out that the motion in all states are unstable with probability 1 with the implication that jumps take place to one of the two other possible states. Correspondingly, the response of the cable is modelled as a three states homogeneous continuous time Markov chain, (Papoulis 1984). The transitional probability rate for jumps from state i to state j is denoted ν_{ij}, where the index values $i = 1, 2, 3$ denote the plane mode with small amplitude, the plane mode with large amplitude and the whirling mode, respectively. Hence, ν_{13} represent the probability rate of jumping from the plane mode with small amplitude to the whirling mode.

5.2.1 Modal equations of motion

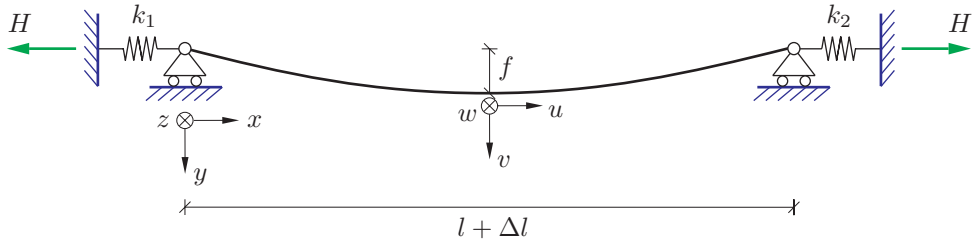

Figure 5.9 Cable in equilibrium configuration.

Figure 5.9 shows a cable with the chord placed along the horizontal x-axis and the static equilibrium state $y(x)$ in the (x, y)-plane. The cable is supported by springs k_1 and k_2 modelling the flexibility of the support point. The material point of the initial cable configuration with the coordinates $(x, y, 0)$ undergoes the displacement vector $[u(x,t), v(x,t), w(x,t)]^T$ in the three coordinate directions. The cable is elastic with the modulus of elasticity E and cross-sectional area A. The sag, the chord length, the total weight of the cable and the horizontal cable force in the equilibrium state are denoted as f, l, W and H, respectively.

The vibrations of the cable are caused by elongations $\Delta l(t)$ of the chord due to forced motions of the support point. Assuming a parabolic approximation to the equilibrium suspension, and retaining up to cubic geometric nonlinear terms, the following derivation of the equation of motion is based on conventional approximations in shallow cable theory, (Irvine 1992).

Within the shallow cable approximation the static curve of the cable is the parabola

$$y = 4f\Big(1 - \frac{x}{l}\Big)\frac{x}{l}, \tag{5.32}$$

where f and l are related to the chord force H as

$$Hf = \frac{1}{8}Wl. \tag{5.33}$$

The unit tangential vector at a certain point of the initial cable configuration with the coordinates $(x, y, 0)$ is given as

$$\mathbf{t}(x) = \frac{d}{ds}\begin{bmatrix} x \\ y \\ 0 \end{bmatrix}, \tag{5.34}$$

where ds denotes an infinitesimal cable element at the considered position. The unit tangential vector at the considered point in the new configuration becomes

$$\mathbf{t}_1(x,t) = \frac{\partial}{\partial s_1}\begin{bmatrix} x+u \\ y+v \\ w \end{bmatrix} = \left(\mathbf{t}(x) + \frac{\partial}{\partial s}\begin{bmatrix} u \\ v \\ w \end{bmatrix}\right)\frac{ds}{ds_1}. \tag{5.35}$$

It follows from (5.35) that the initial and deformed length of the considered cable element are related as

$$\Big(\frac{ds_1}{ds}\Big)^2 = 1 + 2\Big(\frac{dx}{ds}\frac{\partial u}{\partial s} + \frac{dy}{ds}\frac{\partial v}{\partial s}\Big) + \Big(\frac{\partial u}{\partial s}\Big)^2 + \Big(\frac{\partial v}{\partial s}\Big)^2 + \Big(\frac{\partial w}{\partial s}\Big)^2. \tag{5.36}$$

The axial strain ε then follows from (5.36) as

$$\varepsilon = \frac{ds_1 - ds}{ds} \simeq \frac{dx}{ds}\frac{\partial u}{\partial s} + \frac{dy}{ds}\frac{\partial v}{\partial s} + \frac{1}{2}\Big(\frac{\partial v}{\partial s}\Big)^2 + \frac{1}{2}\Big(\frac{\partial w}{\partial s}\Big)^2. \tag{5.37}$$

The term $\frac{1}{2}(\partial u/\partial s)^2$ is of magnitude ε^2, and has been omitted in comparison to the remaining terms on the right hand side of (5.36), which are all of the magnitude ε. To the same order of approximation

$$\frac{d(x+u)}{ds_1} = \Big(1 + \frac{\partial u}{\partial x}\Big)\frac{dx}{ds_1} \simeq \frac{dx}{ds}. \tag{5.38}$$

The increment of the component of the cable force in the x-direction must balance ΔH,

$$\Delta H = \big(F + \Delta F\big)\frac{d(x+u)}{ds_1} - F\frac{dx}{ds} \simeq \Delta F\frac{dx}{ds}, \tag{5.39}$$

where (5.38) has been used. The elasticity equation of the cable may then be written as

$$\Delta H\frac{ds}{dx} = EA\varepsilon. \tag{5.40}$$

Insertion of (5.37) and the introduction of x as independent parameter then provides

$$\Delta H\Big(\frac{ds}{dx}\Big)^3 = EA\bigg(\frac{\partial u}{\partial x} + \frac{dy}{dx}\frac{\partial v}{\partial x} + \frac{1}{2}\Big(\frac{\partial v}{\partial x}\Big)^2 + \frac{1}{2}\Big(\frac{\partial w}{\partial x}\Big)^2\bigg). \tag{5.41}$$

Due to the springs the chord length will change by

$$\Delta L(t) = -\Delta H(t)\left(\frac{1}{k_1} + \frac{1}{k_2}\right) + \Delta l(t). \tag{5.42}$$

Next, integration over l is performed in (5.41), and $\Delta L(t) = u(l,t) - u(0,t)$ is eliminated by means of (5.42), leading to

$$\Delta H(t) L_0 = EA\bigg(\Delta l(t) + 8\frac{f}{l^2}\int_0^l v dx + \frac{1}{2}\int_0^1 \bigg(\Big(\frac{\partial v}{\partial x}\Big)^2 + \Big(\frac{\partial w}{\partial x}\Big)^2\bigg) dx\bigg), \tag{5.43}$$

where

$$L_0 = L_{\mathrm{e}} + EA\left(\frac{1}{k_1} + \frac{1}{k_2}\right), \tag{5.44}$$

and L_{e} denotes the so-called effective cable length,

$$L_{\mathrm{e}} = \int_0^l \Big(\frac{ds}{dx}\Big)^3 dx \simeq \int_0^l \left(1 + \frac{3}{2}\Big(\frac{dy}{dx}\Big)^2\right) dx = l + 8\frac{f^2}{l}. \tag{5.45}$$

The approximation in the derivation of (5.45) introduces an error of the magnitude $f^{\,4}/l^4$.

Since no external dynamic loads are acting the equations of motion for nonlinear vibrations become

$$\begin{aligned} &\big(H + \Delta H\big)\frac{\partial^2 v}{\partial x^2} - m\frac{\partial^2 v}{\partial t^2} - 8\frac{f}{l^2}\Delta H = 0, \\ &\big(H + \Delta H\big)\frac{\partial^2 w}{\partial x^2} - m\frac{\partial^2 w}{\partial t^2} = 0, \end{aligned} \tag{5.46}$$

where m denotes the mass per unit length of the cable. Insertion of (5.43) into (5.46) provides the following coupled nonlinear integro-differential equations

$$
\begin{aligned}
8fe(t) &= \big(1+e(t)\big)\frac{\partial^2 v}{\partial \xi^2} - \frac{1}{\omega_0^2}\frac{\partial^2 v}{\partial t^2} - \lambda^2 \int_0^1 v d\xi \\
&+ \frac{\lambda^2}{8f}\left(\frac{\partial^2 v}{\partial \xi^2}\int_0^1 v d\xi - \frac{1}{2}\int_0^1 \left(\Big(\frac{\partial v}{\partial \xi}\Big)^2 + \Big(\frac{\partial w}{\partial \xi}\Big)^2\right) d\xi\right) \\
&+ \frac{\lambda^2}{128 f^2}\frac{\partial^2 v}{\partial \xi^2}\int_0^1 \left(\Big(\frac{\partial v}{\partial \xi}\Big)^2 + \Big(\frac{\partial w}{\partial \xi}\Big)^2\right) d\xi, \\
0 &= \big(1+e(t)\big)\frac{\partial^2 w}{\partial \xi^2} - \frac{1}{\omega_0^2}\frac{\partial^2 w}{\partial t^2} + \frac{\lambda^2}{8f}\frac{\partial^2 w}{\partial \xi^2}\int_0^1 v d\xi + \frac{\lambda^2}{128 f^2}\frac{\partial^2 w}{\partial \xi^2}\int_0^1 \left(\Big(\frac{\partial v}{\partial \xi}\Big)^2 + \Big(\frac{\partial w}{\partial \xi}\Big)^2\right) d\xi,
\end{aligned}
\tag{5.47}
$$

where the non-dimensional coordinate $\xi = x/l$ and the following parameters have been introduced

$$
e(t) = \frac{EA}{H}\frac{\Delta l(t)}{L_0}, \quad \lambda^2 = 64\frac{EA}{H}\frac{f^2}{L_0 l}, \quad \omega_0 = \frac{1}{l}\sqrt{\frac{H}{m}}. \tag{5.48}
$$

$e(t)$ is a non-dimensional representation of the chord-length elongation $\Delta l(t)$ of the order of magnitude 1, and λ^2 denotes the stiffness parameter defined by Irvine and Caughey (1974), which controls the linear as well as the nonlinear parts of the dynamics. ω_0 denotes the fundamental frequency for the taut wire. As seen, the differential equation for the in-plane displacement $v(\xi,t)$ is exposed to both parametric and additive excitation from the load term $e(t)$. By contrast, the differential equation for the out-of-plane displacement field $w(\xi,t)$ is only parametrically excited by $e(t)$.

Due to the shallowness of the cable the eigenfrequencies will be pairwise closely spaced. Further, the static equilibrium plane forms a symmetry plane for which reason the eigenvibrations decouple in the in-plane modes, only affecting the displacement component $v(x,t)$, and out-of-plane vibrations affecting the displacement component $w(x,t)$. Then, the following modal expansions for the displacements in the y- and z-directions are valid

$$
v(x,t) = \sum_{j=1}^{\infty} \Phi_{2j}(x) q_{2j}(t), \quad w(x,t) = \sum_{j=1}^{\infty} \Phi_{2j-1}(x) q_{2j-1}(t). \tag{5.49}
$$

Based on the parabolic approximation for the static equilibrium state the following solutions for the in-plane modes $\Phi_{2j}(x)$ and out-of-plane modes $\Phi_{2j-1}(x)$, as well as the related circular eigenfrequencies ω_{2j} and ω_{2j-1}, may be derived for the jth eigenmode pair, cf. Irvine and Caughey (1974)

$$
\begin{aligned}
\Phi_{2j}(x) &= \frac{\cos\left(\frac{\Omega_j}{2}\big(1-2\frac{x}{l}\big)\right) - \cos\frac{\Omega_j}{2}}{1-\cos\frac{\Omega_j}{2}}, \quad && \omega_{2j} = \Omega_j \omega_0, \\
\Phi_{2j-1}(x) &= \sin(j\pi\frac{x}{l}), && \omega_{2j-1} = j\pi\omega_0.
\end{aligned}
\tag{5.50}
$$

Odd and even numbers of j denote symmetric and antisymmetric modes, respectively. ω_0 denotes the fundamental eigenfrequency of the taut wire, (5.48). As seen the eigenmodes have been normalized to one at the midpoint of the cable. Ω_j are non-zero solutions to the equation

$$\tan\frac{\Omega_j}{2} = \frac{\Omega_j}{2} - \frac{4}{\lambda^2}\Big(\frac{\Omega_j}{2}\Big)^3. \tag{5.51}$$

λ^2 as defined by (5.48) is the non-dimensional parameter for the cable stiffness introduced by Irvine and Caughey (1974).

In what follows emphasize will be on the case where the chordwise elongation causes simultaneous resonance in the lowest in-plane and out-of-plane modes. This means that all other modes may be considered small, and consequently interaction from these modes on the directly loaded modes may be disregarded. Then only the first terms in the expansion (5.49) are considered in what follows. Upon insertion into the nonlinear field equations (5.47), and use of the relevant orthogonality properties, provides the following coupled ordinary differential equations for the pertinent modal coordinates $q_1(t)$ and $q_2(t)$

$$\begin{aligned}
&-\frac{1}{\omega_0^2}b_1\ddot{q}_1 - \big(1+e(t)\big)c_1q_1 - \frac{\lambda^2}{8f}a_2c_1q_1q_2 - \frac{\lambda^2}{128f^2}c_1\big(c_1q_1^2+c_2q_2^2\big)q_1 = 0,\\
&-\frac{1}{\omega_0^2}b_2\ddot{q}_2 - \big(1+e(t)\big)c_2q_2 - \lambda^2a_2^2q_2 - \frac{\lambda^2}{16f}a_2\big(c_1q_1^2+3c_2q_2^2\big)\\
&\quad-\frac{\lambda^2}{128f^2}c_2\big(c_1q_1^2+c_2q_2^2\big)q_2 = 8a_2fe(t).
\end{aligned} \tag{5.52}$$

where $e(t)$ is a non-dimensional chord elongation of the magnitude $\mathrm{O}(1)$ as given by (5.48). The remaining parameters are defined from

$$\begin{aligned}
a_1 &= \int_0^1 \Phi_1 d\xi = \frac{2}{\pi}, \quad b_1 = \int_0^1 \Phi_1^2 d\xi = \frac{1}{2}, \quad c_1 = \int_0^1 \Big(\frac{d\Phi_1}{d\xi}\Big)^2 d\xi = \frac{\pi^2}{2},\\
a_2 &= \int_0^1 \Phi_2 d\xi = \frac{2\sin\frac{\Omega_1}{2} - \Omega_1\cos\frac{\Omega_1}{2}}{\Omega_1\big(1-\cos\frac{\Omega_1}{2}\big)} \simeq \frac{2}{\pi}\Big(1 - \frac{4+2\pi-\pi^2}{4\pi}\Delta\Omega\Big),\\
b_2 &= \int_0^1 \Phi_2^2 d\xi = \frac{-3\sin\Omega_1 + \Omega_1\big(2+\cos\Omega_1\big)}{2\Omega_1\big(1-\cos\frac{\Omega_1}{2}\big)^2} \simeq \frac{1}{2}\Big(1 - \frac{\pi-3}{\pi}\Delta\Omega\Big),\\
c_2 &= \int_0^1 \Big(\frac{d\Phi_2}{d\xi}\Big)^2 d\xi = \frac{\Omega_1^2 - \Omega_1\sin\Omega_1}{2\big(1-\cos\frac{\Omega_1}{2}\big)^2} \simeq \frac{\pi^2}{2}\Big(1 - \frac{\pi-3}{\pi}\Delta\Omega\Big).
\end{aligned} \tag{5.53}$$

$\xi = x/l$ denotes a non-dimensional abscissa, and $\Delta\Omega = \Omega_1 - \pi$. $\Delta\Omega$ is a non-dimensional measure of the difference $\omega_2 - \omega_1$ between the in-plane and out-of-plane frequencies. (5.52) may be written in the following slightly simpler form

$$\ddot{q}_1 + 2\zeta_1\omega_1\dot{q}_1 + \omega_1^2\big(1+e(t)\big)q_1 + \beta_1 q_1 q_2 + q_1\big(\gamma_1 q_1^2 + \gamma_2 q_2^2\big) = 0,$$
$$\ddot{q}_2 + 2\zeta_2\omega_2\dot{q}_2 + \omega_2^2\big(1+\alpha e(t)\big)q_2 + \beta_2 q_1^2 + \beta_3 q_2^2 + q_2\big(\gamma_3 q_1^2 + \gamma_4 q_2^2\big) = -\delta e(t), \tag{5.54}$$

where

$$\alpha = \frac{c_2}{c_2+\lambda^2 a_2} \simeq \frac{\pi^3}{\pi^3+4\lambda^2},$$
$$\beta_1 = \frac{1}{8}\omega_0^2\frac{\lambda^2}{f}a_2\frac{c_1}{b_1} \simeq \frac{\pi}{4}\omega_0^2\frac{\lambda^2}{f}\Big(1-\frac{4+2\pi-\pi^2}{4\pi}\Delta\Omega\Big),$$
$$\beta_2 = \frac{1}{16}\omega_0^2\frac{\lambda^2}{f}a_2\frac{c_1}{b_2} \simeq \frac{\pi}{8}\omega_0^2\frac{\lambda^2}{f}\Big(1-\frac{16-2\pi-\pi^2}{4\pi}\Delta\Omega\Big),$$
$$\beta_3 = \frac{3}{16}\omega_0^2\frac{\lambda^2}{f}a_2\frac{c_2}{b_2} \simeq \frac{3\pi}{8}\omega_0^2\frac{\lambda^2}{f}\Big(1-\frac{4+2\pi-\pi^2}{4\pi}\Delta\Omega\Big),$$
$$\gamma_1 = \frac{1}{128}\omega_0^2\frac{\lambda^2}{f^2}\frac{c_1}{b_1}c_1 = \frac{\pi^4}{256}\omega_0^2\frac{\lambda^2}{f^2},$$
$$\gamma_2 = \frac{1}{128}\omega_0^2\frac{\lambda^2}{f^2}\frac{c_1}{b_1}c_2 \simeq \frac{\pi^4}{256}\omega_0^2\frac{\lambda^2}{f^2}\Big(1-\frac{\pi-3}{\pi}\Delta\Omega\Big),$$
$$\gamma_3 = \frac{1}{128}\omega_0^2\frac{\lambda^2}{f^2}\frac{c_2}{b_2}c_1 \simeq \frac{\pi^4}{256}\omega_0^2\frac{\lambda^2}{f^2},$$
$$\gamma_4 = \frac{1}{128}\omega_0^2\frac{\lambda^2}{f^2}\frac{c_2}{b_2}c_2 \simeq \frac{\pi^4}{256}\omega_0^2\frac{\lambda^2}{f^2}\Big(1-\frac{\pi-3}{\pi}\Delta\Omega\Big),$$
$$\delta = 8\omega_0^2 f\frac{a_2}{b_2} \simeq \frac{32}{\pi}\omega_0^2 f\Big(1-\frac{16-2\pi-\pi^2}{4\pi}\Delta\Omega\Big). \tag{5.55}$$

Additionally, linear viscous damping terms with the modal damping ratios ζ_1 and ζ_2 have been included in the equations of motion. Since $\lambda^2 a_2 \ll c_2$ it follows from (5.55) that $\alpha \simeq 1$, which means that the parametric excitation is equally strong in both modes. Further, within an error of the magnitude $\mathrm{O}\big((\Delta\Omega)^2\big)$ it follows that $\beta_3 = \frac{3}{2}\beta_1$, $\gamma_3 = \gamma_1$ and $\gamma_4 = \gamma_2$. The latter approximate relations will be used in the following, which means that the problem is defined merely by the parameters α, β_1, β_2, γ_1, γ_2, δ and $e(t)$.

5.2.2 Harmonic analysis

The data of the considered cable refer to the longest stay in the cable-stayed bridge across the Øresund between Denmark and Sweden. The supports are assumed fixed, corresponding to $k_1 = k_2 = \infty$. The stiffness of the cable is $EA = 2.17\cdot 10^9$ N, and the equilibrium force $H = 5.5\cdot 10^6$ N. The chord length is 260 m, and the cable mass per unit length is $m = 81.05$ kg/m, corresponding to a total weight of $W = 2.038\cdot 10^5$ N. The referential amplitude of the chord elongation is $\Delta l_0 = 0.5$ m corresponding to $e_0 = 0.76$.

First a deterministic harmonic excitation with the circular frequency $\Omega \simeq \omega_1 \simeq \omega_2$ is considered, which means that

$$e(t) = e_0 \cos\left(\Omega t + a\right). \tag{5.56}$$

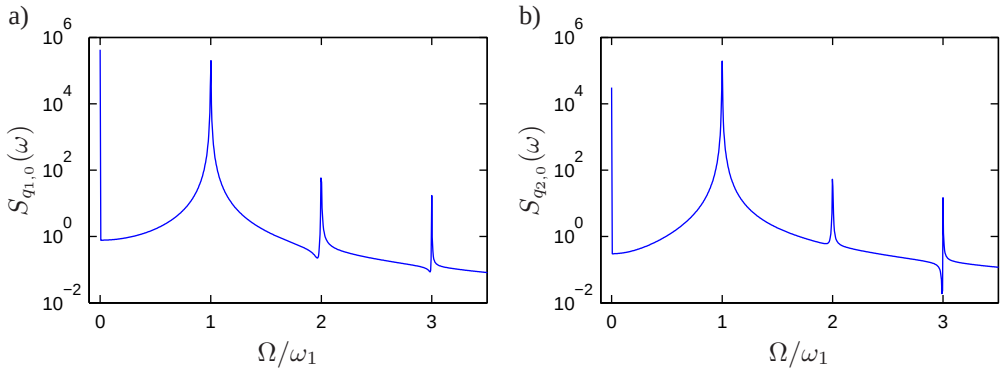

Figure 5.10 One-sided auto-spectral densities of whirling motion. $\zeta_1 = \zeta_2 = 0.01$, $e_0 = 0.76$, $\Omega/\omega_1 = 1.2$.

The phase a will influence the attraction to various stable motions, when (5.54) is integrated with given initial values.

The stationary periodic response from the harmonic excitation is denoted as $q_{i,0}(t)$. On Figure 5.10 the one-sided auto-spectral densities of $q_{1,0}(t)$ and $q_{2,0}(t)$ under whirling motion have been shown at the excitation frequency $\Omega/\omega_1 = 1.2$. From the figure the amplitudes of the second and third harmonics may be estimated to 6-8% and 0.3-0.6% of those of the first harmonics, respectively. Additionally, significant non-zero mean values are present.

As a consequence the following truncated Fourier expansions of the periodic motion are presumed

$$q_{i,0}(t) \simeq A_i + B_i \cos\left(\Omega t + b_i\right) + C_i \cos\left(2\Omega t + c_i\right) \quad , \quad i = 1, 2. \tag{5.57}$$

The amplitudes A_i, B_i and C_i are independent of the phase a of the excitation (5.56), whereas the phases b_i and c_i depend on this quantity. However, if $b_{2,0}$ and $c_{i,0}$ indicate the phases corresponding to $a = 0$, the corresponding quantities at the phase a are determined from

$$b_i = b_{i,0} - a, \quad c_i = c_{i,0} - 2a. \tag{5.58}$$

In Appendix A the equations for the 6 unknown amplitudes A_i, B_i, C_i and the 4 phases b_i and c_i are listed. The root-mean-square (RMS) equivalent amplitudes of (5.57) are defined as

$$Q_i = \sqrt{2A_i^2 + B_i^2 + C_1^2}. \tag{5.59}$$

Figure 5.12 shows possible solution of (5.52) solved with various start conditions at a fixed excitation amplitude $e_0 = 0.76$ and frequency $\Omega = 1.2$. At these conditions three different

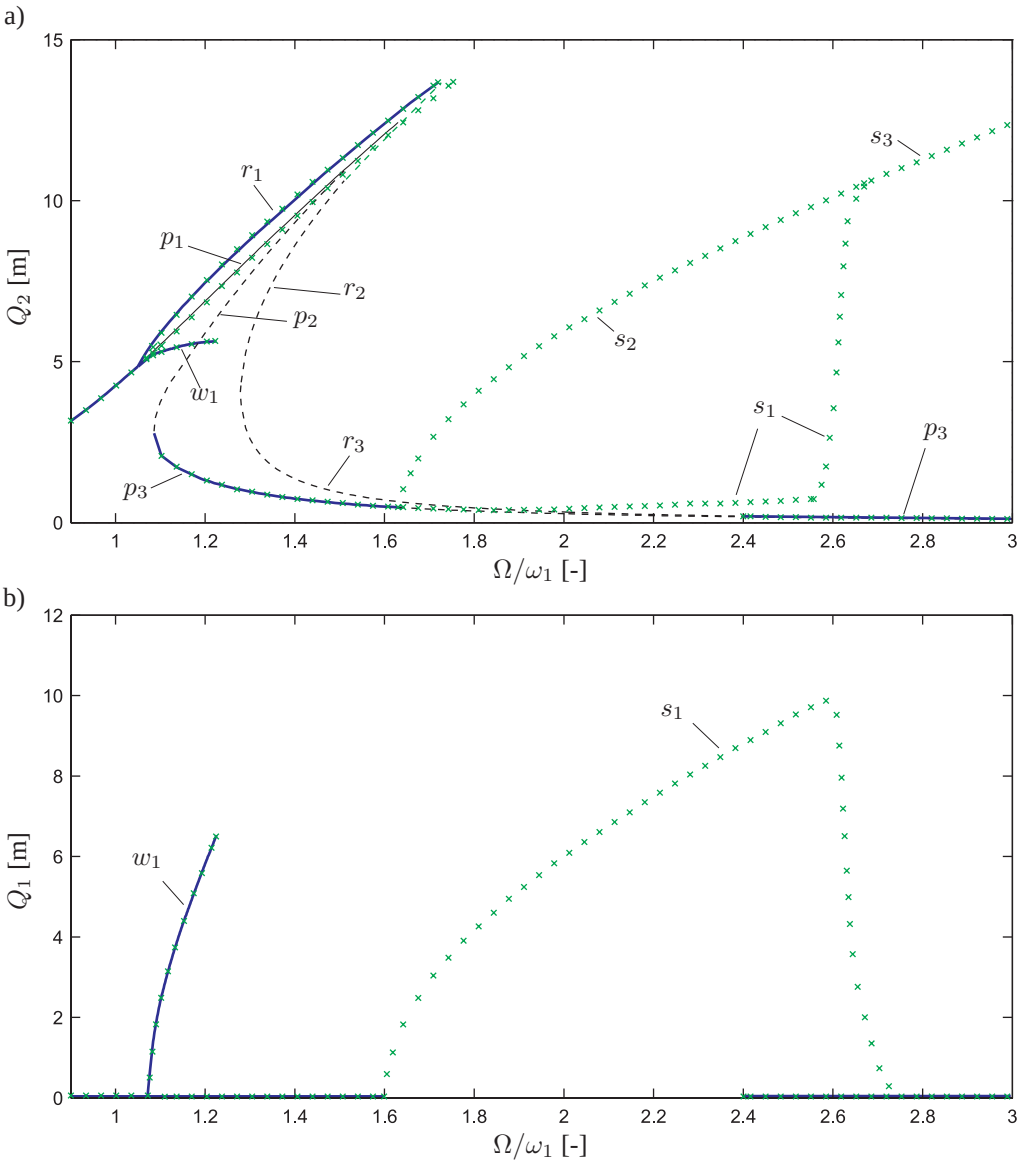

Figure 5.11 Response during harmonic excitation as a function of excitation frequency Ω, $\epsilon_0 = 0.76$. (——) Stable solutions in 3D. (——) Stable solutions in 2D. (– –) Unstable solutions. ($\times$) Numerical solutions.a) Q_2. b) Q_2.

solutions are obtainable. A so-called whirling motion, a plane motion with low amplitude and a plane motion with large amplitude.

Figure 5.11 shows possible solutions of the equivalent amplitudes Q_1 and Q_2 as function of the excitation frequency Ω. Analytical solutions, which are stable in 3D, i.e. where the out-of-plane component $q_1(t)$ is free to move, have been indicated by (——), whereas stable analytical

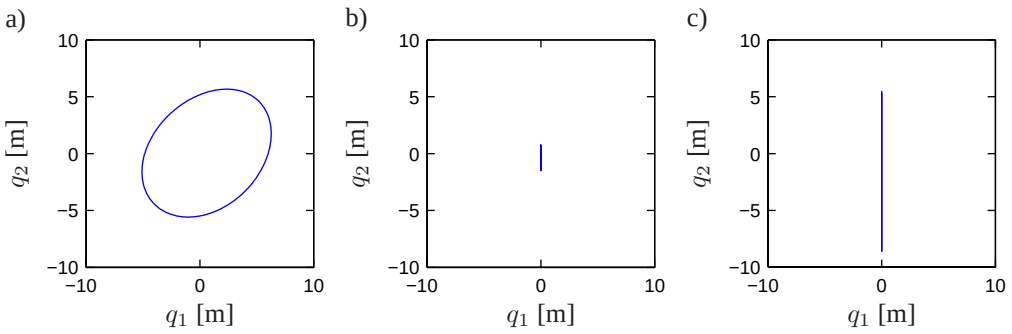

Figure 5.12 Phase plane of possible solutions at $\Omega = 1.2\omega_1$ and $e_0 = 1.2$. $\zeta_1 = \zeta_2 = 0.01$. a) Whirling motion w_1 obtained with $q_1(0) = q_2(0) = 6$ m. b) Plane motion p_3 obtained with $q_1(0) = q_2(0) = 1$ m. c) Plane motion r_1 obtained with $q_1(0) = q_2(0) = 3$ m

solutions in 2D, where the out-of-plane component is suppressed so $q_1(t) \equiv 0$, are marked as (——). Finally, unstable solutions are indicated by (– –). The quality of the analytic solutions has been checked by numerical integration of (5.54) for the stable branches, and has been indicated by a $(\times)$ on the plot. In this case Q_1 and Q_2 have been obtained from RMS values obtained as time average over one period $T = 2\pi/\Omega$. The stability analysis of the various solutions has been carried out by means of Floquet theory as explained in Appendix B.

The branches indicated by p_1, p_2 and p_3 indicate the harmonic response in 2D. p_1 is stable up to a certain maximum excitation frequency Ω, where a fold instability takes place. p_3 is stable in certain disjoint sub intervals of the Ω-axis.

In 3D the stable plane motion (i.e. $q_1(t) = 0$, but is free to move) is indicated by r_1, whereas r_2 and r_3 signify corresponding unstable solutions. r_1 is formed by bifurcation from p_1 at a critical frequency and remain stable up to a certain maximum excitation frequency Ω, where a fold instability takes place. Attraction to r_1 takes place if the system is started with very small initial values $q_1(0) \neq 0$ or $\dot{q}_1(0) \neq 0$ along with relatively large values of $q_2(0)$ and $\dot{q}_2(0)$. If $q_1(0) = \dot{q}_1(0) \equiv 0$ the system is attracted to p_1. The amplitudes of the mode of vibration p_1 and r_1 are comparable, whereas the phases are completely different.

w_1 indicates a whirling motion. This motion is also formed by bifurcation from r_1 which takes place at a slightly larger frequency than the bifurcation into the branch p_1. The whirling motion remains stable up to a certain maximum frequency.

At the frequency in the vicinity of $\Omega \sim 2\omega_1$, where p_3 is unstable, a stable branch s_2 exists. In this mode $q_2(t)$ is harmonic with the frequency $\Omega \simeq 2\omega_1$, whereas $q_1(t)$ is subharmonic of the order $n = 2$, resulting in an eight-shaped trajectory. s_1 indicates the corresponding plane subharmonic in 2D. No analytic solutions have been indicated for the subharmonic responses.

5.2.3 Stability analysis of harmonic solutions

The stability of the solutions obtained in Appendix A can be determined by Floquet theory (Nayfeh and Mook 1995). Let $\Delta q_i(t)$ be a perturbation to the periodic solution $q_{i,0}(t)$

$$q_i(t) = q_{i,0}(t) + \Delta q_i(t). \tag{5.60}$$

Both the perturbed solution $q_i(t)$ and the periodic solution $q_{i,0}$ are assumed to fulfil (5.54). Insertion of (5.60) in (5.54) and disregarding quadratic and cubic terms of $\Delta q_i(t)$ then give the following equations of motion for the perturbation $\Delta q_i(t)$

$$\begin{aligned}
&\Delta\ddot{q}_1 + 2\zeta_1\omega_1\Delta\dot{q}_1 + \omega_1^2\big(1+e(t)\big)\Delta q_1 + \beta_1\big(q_{1,0}\Delta q_2 + q_{2,0}\Delta q_1\big) + 3\gamma_1 q_{1,0}^2\Delta q_1 \\
&\quad + \gamma_2\big(q_{2,0}^2\Delta q_1 + 2q_{1,0}q_{2,0}\Delta q_2\big) = 0, \\
&\Delta\ddot{q}_2 + 2\zeta_2\omega_2\Delta\dot{q}_2 + \omega_2^2\big(1+\alpha e(t)\big)\Delta q_2 + 2\beta_2 q_{1,0}\Delta q_1 + 2\beta_3 q_{3,0}\Delta q_3 + 3\gamma_4 q_{2,0}^2\Delta q_2 \\
&\quad + \gamma_3\big(q_{1,0}^2\Delta q_2 + 2q_{1,0}q_{2,0}\Delta q_1\big) = 0.
\end{aligned} \tag{5.61}$$

(5.61) may be rewritten into the following state vector formulation

$$\dot{\mathbf{X}}(t) = \mathbf{A}(t)\mathbf{X}(t), \quad \mathbf{X}(t) = [\Delta q_1(t)\ \Delta q_2(t)\ \Delta\dot{q}_1(t)\ \Delta\dot{q}_2(t)]^T, \quad \mathbf{A}(t) = \begin{bmatrix} \mathbf{0} & \mathbf{I} \\ -\mathbf{k}(t) & -\mathbf{c} \end{bmatrix}, \tag{5.62}$$

where the components of $\mathbf{k}(t)$ and $\mathbf{c}$ are given as

$$\begin{aligned}
&k_{11} = \omega_1^2\big(1+e(t)\big) + \beta_1 q_{2,0} + 3\gamma_1 q_{1,0}^2 + \gamma_2 q_{2,0}^2, \quad k_{12} = \beta_1 q_{1,0} + 2\gamma_2 q_{1,0}q_{2,0}, \\
&k_{21} = 2\beta_2 q_{1,0} + 2\gamma_3 q_{1,0}q_{2,0}, \quad k_{22} = \omega_2^2\big(1+\alpha e(t)\big) + 2\beta_3 q_{2,0} + 3\gamma_4 q_{2,0}^2 + \gamma_3 q_{1,0}^2, \\
&c_{11} = 2\zeta_1\omega_1, \quad c_{12} = c_{21} = 0, \quad c_{22} = 2\zeta_2\omega_2.
\end{aligned} \tag{5.63}$$

For a certain periodic solution $q_{i,0}(t)$, $i = 1, 2$, characterized by the amplitudes A_i, B_i, C_i, the phases b_i, c_i and the circular frequency Ω, the fundamental set of solutions $\mathbf{\Phi}(T)$ are determined by numerical integration of (5.62) over the interval $[0\ T]$, see Appendix B. Then, the stability is determined from the eigenvalues ν_i of $\mathbf{\Phi}(T)$. If $|\nu_i| < 1$ are fulfilled the solution is found to be stable according to the Floquet theory. Notice that the stability criteria is independent of the phase a of the excitation as given by (5.56). Figure 5.13 shows the four eigenvalues of $\mathbf{\Phi}(T)$ for the four solution branches r_1, p_1, w_1 and p_3.

As seen from figure 5.13 solution branches r_1 and w_1 are stable while solution branch p_1 becomes unstable at the bifurcation point at $\Omega/\omega_1 = 1.08$. Solution branch p_3 is stable up to the point at $\Omega/\omega_1 = 1.6$ then becomes unstable up to $\Omega/\omega_1 = 2.4$ where stable solutions again are possible.

5.2.4 Narrow-banded excitation

The stochastic model for the non-dimensional elongation of the chord-length $e(t)$ is obtained as a second order filtration of Gaussian white noise

$$\ddot{e}(t) + 2\mu\Omega\dot{e}(t) + \Omega^2 e(t) = \sqrt{2\mu\Omega^3}e_0 W(t), \tag{5.64}$$

where μ is a bandwidth parameter, Ω is a circular centre frequency, and $W(t)$ is a unit Gaussian white noise process defined by the auto-covariance function

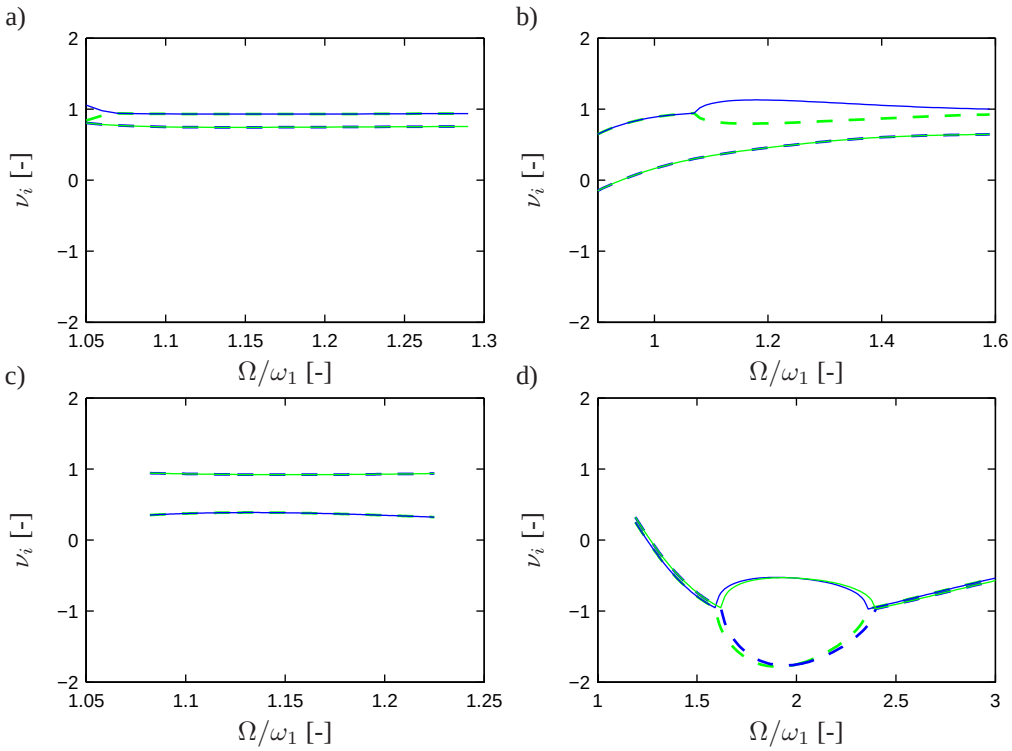

Figure 5.13 Eigenvalues λ_i for various solution branches, $e_0 = 0.759$. (———) λ_1. (– – –) λ_2. (———) λ_3 . (– – –) λ_4. a) r_1. b) p_1. c) w_1. d) p_3.

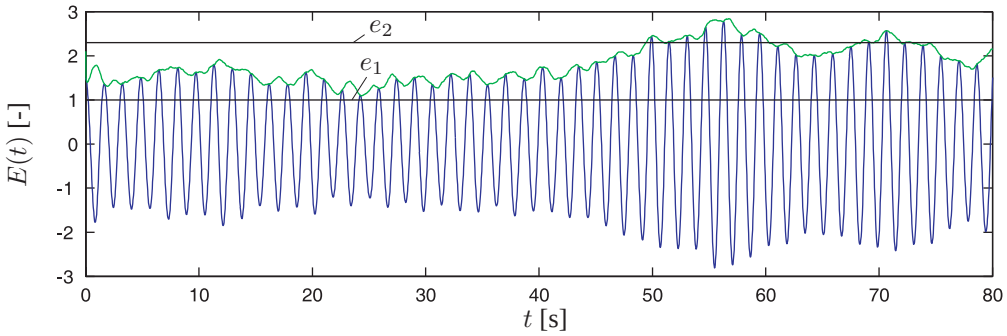

Figure 5.14 Narrow banded chord elongation process, $\mu = 0.003$, $e_0 = 1.5$, $\Omega = 1.2\omega_1$. (———) Underlying process $e(t)$. (———) Envelope process $E(t)$.

$$\kappa_{WW}(\tau) = E\big[W(t)W(t+\tau)\big] = \delta(\tau). \tag{5.65}$$

$\delta(\tau)$ signifies the Dirac Delta function. The normalization (5.65) insures that the standard deviation σ_e of $e(t)$ becomes

$$\sigma_e = \frac{\sqrt{2}}{2} e_0. \tag{5.66}$$

Hence, e_0 is a characteristic amplitude, and Ω is a characteristic frequency of the excitation which should be related to the amplitude and frequency of the harmonic excitation (5.56).

A realization of $e(t)$ and the related envelope process $E(t)$ are shown on Figure 5.14. e_1 and e_2 represent the minimum and maximum value of the amplitude e_0 where a certain periodic motion may exist under harmonic excitation with the circular frequency Ω. As seen at $t \simeq 50$ s the upper envelope process performs a first passage out of the interval $[e_1, e_2]$ at the upper boundary e_2. We shall later see that such an out-crossing causes a transition from one periodic motion to another. The energy envelope $E(t) = \sqrt{e^2(t) + \dot{e}^2(t)/\Omega^2}$ is not differentiable. In order to have a more smooth envelope in relation to Monte Carlo simulation the Cramér-Leadbetter envelope (Cramér and Leadbetter 1967), will alternatively be considered, defined as

$$E(t) = \sqrt{e^2(t) + \hat{e}^2(t)}, \tag{5.67}$$

where $\hat{e}(t)$ denotes the Hilbert transform of $e(t)$

$$\hat{e}(t) = \frac{1}{\pi} \int_{-\infty}^{\infty} \frac{e(t)}{t-\tau} d\tau. \tag{5.68}$$

Under narrow banded conditions the envelope process may be shown to be a one-dimensional Markov process. The corresponding distribution function for the first passage time can then be determined analytically by integration of the backwards Kolmogorov equation, (Helstrom 1959). Instead, this distribution will be determined by Monte Carlo simulation along with other first passage time distributions to be considered.

5.2.5 Homogeneous continuous time Markov chain

Let T_{ij} be the first passage time interval until transition to state j takes place on condition that the system starts in state i. Similarly, T_i denotes the first passage time interval of occupancy in state i until transition to any of the other states.

It is assumed that the transition from one state to another may be described by a three state homogeneous continuous time Markov chain. Let $P_i(t)$ describe the probability of being in the ith state. Then $P_i(t+\Delta t)$ may be written as

$$\begin{aligned}
P_1(t+\Delta t) &= P_1(t)\big(1 - \nu_{12}\Delta t - \nu_{13}\Delta t\big) + P_2(t)\nu_{21}\Delta t + P_3(t)\nu_{31}\Delta t,\\
P_2(t+\Delta t) &= P_2(t)\big(1 - \nu_{21}\Delta t - \nu_{23}\Delta t\big) + P_1\nu_{12}\Delta t + P_3\nu_{32}\Delta t,\\
P_3(t+\Delta t) &= P_3(t)\big(1 - \nu_{31}\Delta t - \nu_{32}\Delta t\big) + P_1(t)\nu_{13}\Delta t + P_2\nu_{23}\Delta t.
\end{aligned} \tag{5.69}$$

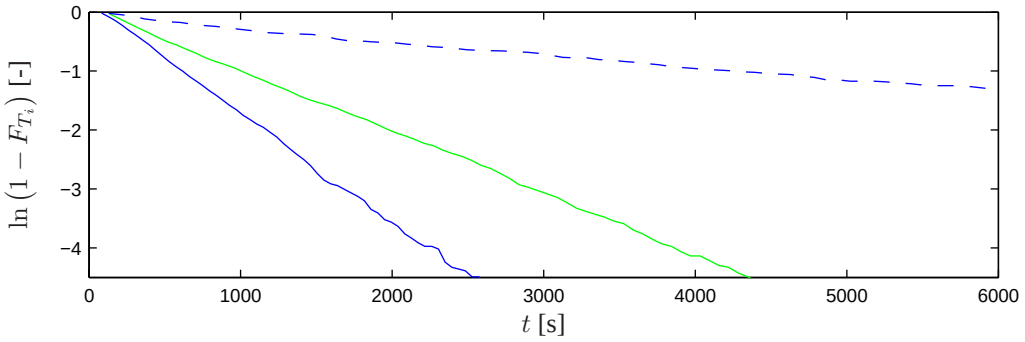

Figure 5.15 Monte Carlo simulation of distribution function for the time interval in a given state, $\Omega = 1.25\omega_1$, $\mu = 0.0003$, $e_0 = 1.5$. (– –) Low-amplitude in-plane mode p_3. (——) High-amplitude in-plane mode r_1. (——) Whirling mode w_1.

Rearranging and letting $\Delta t \to 0$ gives the following differential equations for determining $P_i(t)$

$$\dot{\mathbf{P}}(t) = \boldsymbol{\nu}\mathbf{P}(t), \quad \mathbf{P}(t) = [P_1(t)\ P_2(t)\ P_3(t)],$$
$$\boldsymbol{\nu} = \begin{bmatrix} -(\nu_{12}+\nu_{13}) & \nu_{21} & \nu_{31} \\ \nu_{12} & -(\nu_{21}+\nu_{23}) & \nu_{32} \\ \nu_{13} & \nu_{23} & -(\nu_{31}+\nu_{32}) \end{bmatrix}. \tag{5.70}$$

Under the conditions stated the distribution function of T_{ij} becomes

$$F_{T_{ij}}(t) = 1 - \mathrm{e}^{(-\nu_{ij}t)}. \tag{5.71}$$

Let j_1 and j_2 denote the possible transition states from state i. Then the distribution function of T_i follows from

$$P\big(T_i > t\big) = P\big(T_{ij_1} > t \wedge T_{ij_2} > t\big) = \mathrm{e}^{(-\nu_{ij_1}t)}\mathrm{e}^{(-\nu_{ij_2}t)} \quad \Rightarrow$$
$$F_{T_1}(t) = 1 - \mathrm{e}^{\left(-(\nu_{12}+\nu_{13})t\right)},$$
$$F_{T_2}(t) = 1 - \mathrm{e}^{\left(-(\nu_{21}+\nu_{23})t\right)},$$
$$F_{T_3}(t) = 1 - \mathrm{e}^{\left(-(\nu_{31}+\nu_{32})t\right)}. \tag{5.72}$$

The transition rates are then found from

$$\nu_{ij} = \frac{1}{E[T_{ij}]}, \tag{5.73}$$

where $E[T_{ij}]$ denotes the expected first passage time interval until transition. The results (5.72) have been verified by Monte Carlo simulation using the following procedure. At first the system

(5.54) is integrated with an equivalent harmonic excitation until stationarity is achieved in state i. Next, the excitation is changed to a stochastic excitation by integrating (5.64) with initial values $e(0)$ and $\dot{e}(0)$ determined by the terminal values of the harmonic excitation. In the numerical procedure the unit white noise process is replaced by an equivalent broad-banded Gaussian process (broken-line process). Figure 5.15 shows plots of the resulting histograms based on 2500 sample values. $\ln\left(1 - F_{T_i}(t)\right)$ should map into a straight line as a function of time for an exponentially distributed random variable.

5.2.6 Triggering mechanisms for transition between states

Figure 5.11 shows the harmonic amplitude response in the resonance area as a function of the excitation frequency Ω at a fixed amplitude $e_0 = 0.76$. In Figure 5.16 the corresponding amplitude plots of Q_2 have been shown, when the amplitude e_0 is varied, and the frequency Ω is fixed at the indicated values.

The response branch r_1 (state $i = 2$) only exists for excitation amplitudes e_0 in the interval $[e_{21}, e_{23}]$. As e_0 is decreased towards the limit e_{21} the maximum point (fold instability point) in Figure 5.11 is achieved at smaller and smaller frequencies. For $e_0 = e_{21}$ the maximum value takes place at a frequency equal to the excitation frequency Ω. If e_0 is decreased below e_{21} the branch r_1 cannot be achieved at harmonic excitation with the frequency Ω, for which reason a jump to another state must take place, which is to the state p_3 ($i = 1$) as shown in the figures. In the same way, as e_0 is increasing towards the limit e_{23} the bifurcation of the branch r_1 from p_3 will take place at increasingly larger frequencies. For $e_0 = e_{23}$ the bifurcation takes place at the excitation frequency Ω. If e_0 is increased above e_{23} no bifurcation to r_1 takes place at harmonic excitation with the frequency Ω, which means that r_1 does not exist at the frequency Ω for $e_0 > e_{23}$. Instead, a jump to another state takes place, which in the present case is to the whirling mode w_1 ($i = 3$).

As seen, the whirling mode w_1 ceases to exist at sufficient large values of e_0, where the curve is continued into p_1. The limit point, noticeable as a bend on the w_1-p_1 curve, represents the highest value of e_0, where bifurcation of w_1 from p_1 is possible. Due to the continued extension of the branches w_1 and p_1 we shall consider the combination of w_1 and p_1 as a single branch, which exists for e_0 in the interval $[e_{32}, \infty[$. As e_0 is decreased towards e_{32} the instability point of w_1 (the right-most point on Figure 5.11) is achieved at smaller and smaller frequencies. For $e_0 = e_{32}$ the instability point is achieved at a frequency equal to the excitation frequency Ω. Consequently, if e_0 is decreased below e_{32} the branch w_1 cannot be achieved under harmonic excitation with the frequency Ω, for which reason a jump to another state takes place, which happens to the state r_1 if this exists at the amplitude e_{32}, see Figures 5.16a-b. Else the jump takes place to p_3, see Figure 5.16c.

Similarly, the branch p_3 exists for excitation amplitudes e_0 in the interval $[0, e_2]$. As e_0 is increased towards the limit e_2 the instability point of p_3 (the left-most point with a vertical tangent on Figure 5.11) is achieved at larger and larger frequencies. For $e_0 = e_2$ the instability point is achieved at the excitation frequency. Consequently, if e_0 is increased above e_2 the branch p_3 cannot be achieved under harmonic excitation with the frequency Ω, for which reason a jump to another state takes place. In the present case the jump takes place to r_1 if this exists at the amplitude $e_2 = e_{12}$ (Figure 5.16c), else the jump takes place to w_1 (Figure 5.16a and 5.16b) with $e_2 = e_{13}$. As e_0 is increased the bifurcation point between p_3 and the subharmonic solution s_1 moves towards the left on Figure 5.11. At sufficiently large values of the excitation frequency Ω

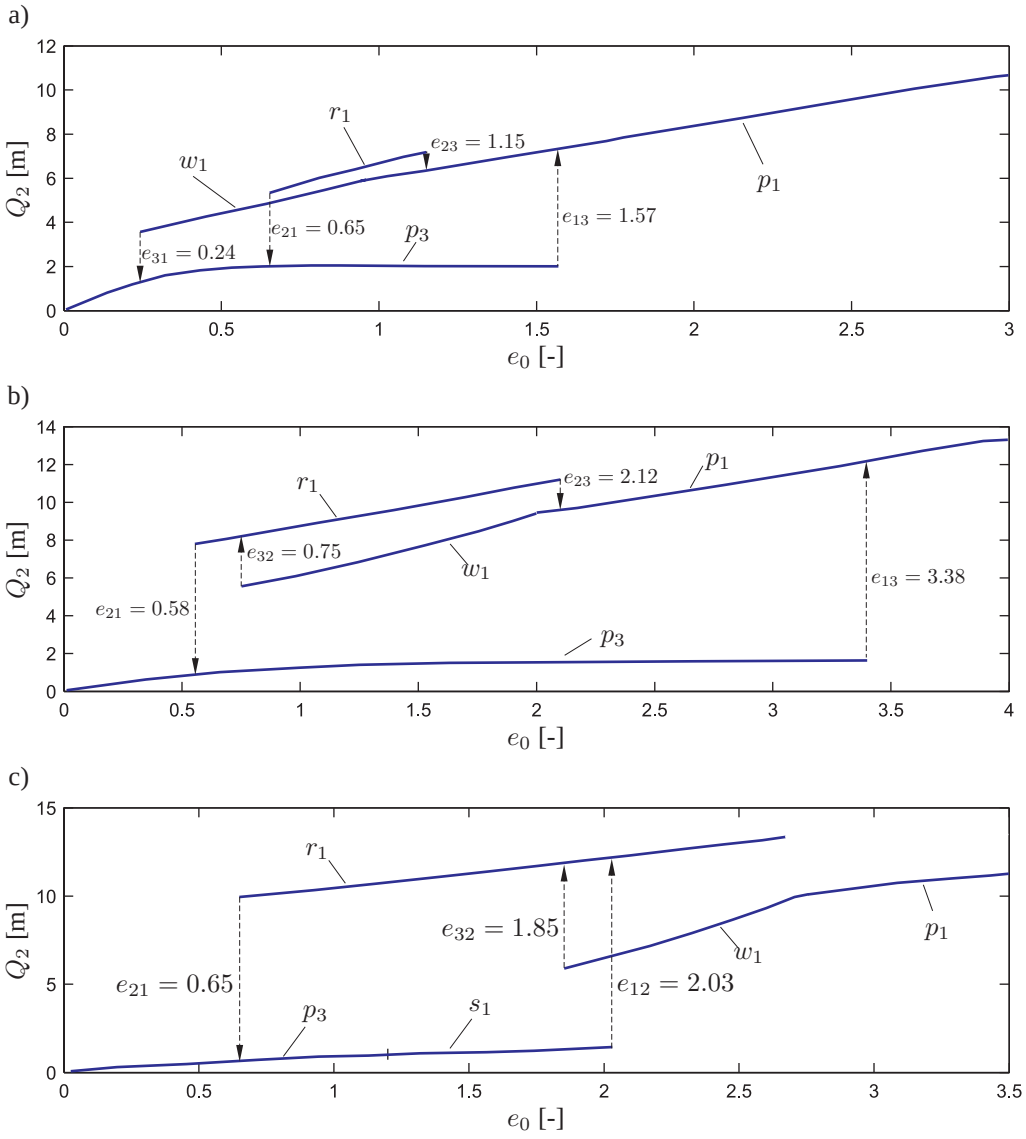

Figure 5.16 Q_2 during harmonic excitation as a function of amplitude e_0. a) $\Omega = 1.1\omega_1$. b) $\Omega = 1.25\omega_1$. c) $\Omega = 1.4\omega_1$.

and at increasing e_0 the bifurcation point between p_3 and s_1 passes the present frequency before the instability point of p_3. Hence, at large values of Ω the p_3 branch continues into the s_1 branch (Figure 5.16c) before p_3 becomes unstable.

In Figure 5.18 the transition of the equivalent amplitude $Q_2(t)$ is plotted during transition between the in-plane states r_1 and p_3 at $\Omega = 1.25\omega_1$. The excitation is harmonic with the amplitude $e_0 = 1.5$ and response in state r_1 up to the time $t = 100$ s, where the stochastic excitation is switched on. Succeedingly, the envelope process decreases to 0.55 at $t = 200$ s,

which also caused a continued decrease of the equivalent amplitude $Q_2(t)$. At $t = 180$ s the envelope process $E(t)$ crosses the critical barrier level $e_{21} = 0.58$ for existence of the state r_1, which causes a state transition to p_3 to take place, noticeable by the oscillations in response. The figure also shows a rather lengthy transition phase approximately of length 150 s before a steady vibration is achieved in vibration mode p_3. The transition mode to a whirling state turns out to be even longer.

Under the assumption of narrow banded excitation, the results show that the main triggering mechanism of transition from one state to another is the outcrossing of the envelope process of the non-dimensional chord elongations. If broad banded excitation is considered other triggering mechanisms may arise. One is the phase lag between the excitation and the response which also may trig jumps between vibration modes.

5.2.7 Numerical example

First the modal expansion into two modes is validated against a difference scheme solving the equations of motion (5.46) devised by Zhou *et al.* (2005). The numerical analysis uses 30 elements across the cable. In Figure 5.17 the results from solving the modal equations of motion (5.54) are plotted as (——), compared with results from the difference model indicated by (——). The exitation is stochastic with various values of μ and e_0. The Figure shows good agreement between the reduced and difference model, but some discrepancies occur at high bandwidth and high mean amplitude values. Figure 5.17d shows an initial match between the models, but after approximately 20 s a transition occur of the reduced model to r_1, whereas the difference model stays in w_1. This indicates that the transition boundaries changes slightly due to the reduction of the model, hence, transition to new states occur at different times. However, the qualitatively behaviour, and at low bandwidths and mean amplitudes also the quantitatively behaviour, is retained in the reduced model. Only the harmonic solutions are considered within this work, however, Zhou *et al.* (2005) also showed good agreement between the reduced and the difference model during subharmonic response under harmonic excitation. But, as was the case for harmonic response, the reduced model fails under stochastic excitation with large amplitude and bandwidth parameter.

In this example the mean first-passage time $E[T_{ij}]$ until transition to state j, given the process starts in states i is evaluated by two methods. In one case the transition is defined to take place, when the envelope makes a first-passage at the barrier e_{ij}. In the other case transition is determined from the qualitative behaviour of the responses $q_1(t)$ and $q_2(t)$. Because the transition of states is only visible in the responses after rather long transition intervals the latter method will predict larger mean values than the former. In the numerical simulation based on the response the following procedure for identification of state transitions was used. A transition from w_1 to p_3 is registered when Q_1 and Q_2 are decreased below $Q_1 < 1.0$ and $Q_2 < 2.2$ for $\Omega = 1.1\omega_1$. A transition from w_1 to r_1 is registered, either when $Q_1 < 1.0$ and $E(t) < 1.8$ for $\Omega = 1.25\omega_1$, or $Q_1 < 1.0$ and $E(t) < 2.5$ for $\Omega = 1.4\omega_1$. The reason for using the envelope levels in the criteria is to exclude transitions from w_1 to p_1 in the sample, since these states are grouped as explained above. Correspondingly, a transition from r_1 to p_3 is registered when $Q_2 < 2.2$ and a transition from r_1 to w_1 is registered when $Q_1 > 1.0$. Finally, a transition from p_3 to w_1 is registered when $Q_2 > 3.5$. In all cases at least 500 sample values are used in the estimate of $E[T_{ij}]$. Based on this estimate ν_{ij} is next determined from (5.73).

The transition rates are listed in Table 5.1. The results of the two numerical methods

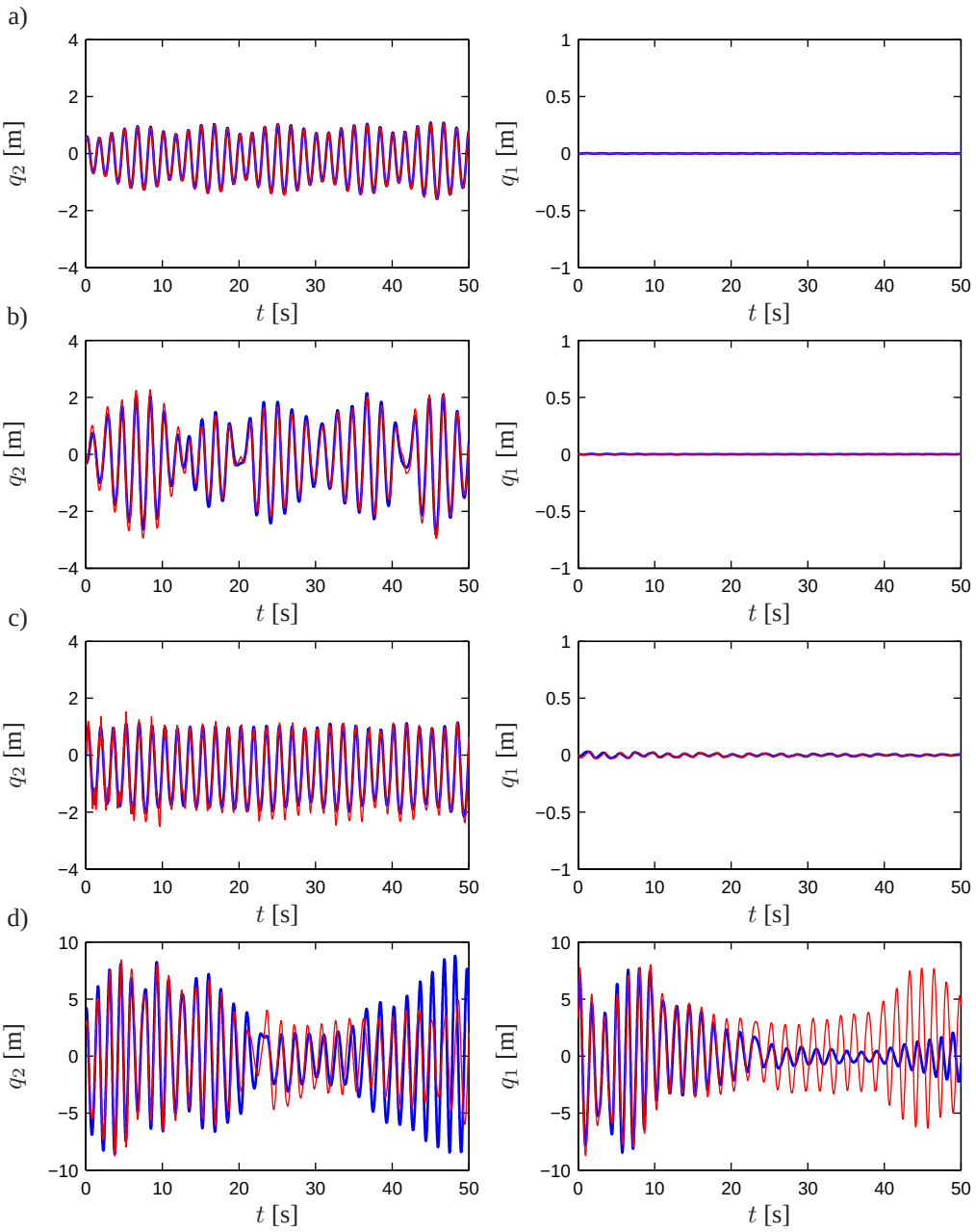

Figure 5.17 Response comparison between difference model and reduced model at various values of μ and e_0. (———) Reduced model solving (5.54). (———) Solving (5.46) using difference scheme. a) $\mu = 0.0003, e_0 = 0.2$ m. b) $\mu = 0.0003, e_0 = 0.5$ m. c) $\mu = 0.03, e_0 = 0.2$ m. d) $\mu = 0.03, e_0 = 0.5$ m.

agree qualitatively, but the transition rates determined from the response are 100%-300% smaller than those determined from the expected first passage time of the envelope process of the non-dimensional chord elongation. The reason for this discrepancy is the difficulty in observing the state transition from the response due to the long transition interval. Since it has been demonstrated that the triggering mechanism unambiguously is related to the crossing of the envelope process, it is concluded that state observations based on the response may be erroneously.

Table 5.1 Transition rates found from the envelope process of the chord elongation and from the response using Monte Carlo simulation.

	$e_0 = 1.0\ ,\ \mu = 0.0003$ $\Omega = 1.10\omega_1$		$e_0 = 1.5\ ,\ \mu = 0.0003$ $\Omega = 1.25\omega_1$		$e_0 = 1.9\ ,\ \mu = 0.0003$ $\Omega = 1.40\omega_1$	
	Envelope	Response	Envelope	Response	Envelope	Response
ν_{12}	0	0	0	0	0.0699	0.0210
ν_{13}	0.000707	0.000481	0.000495	0.000491	0	0
ν_{21}	0.0130	0.00457	0.00298	0.00189	0.00174	0.00134
ν_{23}	0.0126	0.00309	0.00408	0.00134	0	0
ν_{31}	0.000801	0.000498	0	0	0	0
ν_{32}	0	0	0.00235	0.00121	0.0230	0.00412

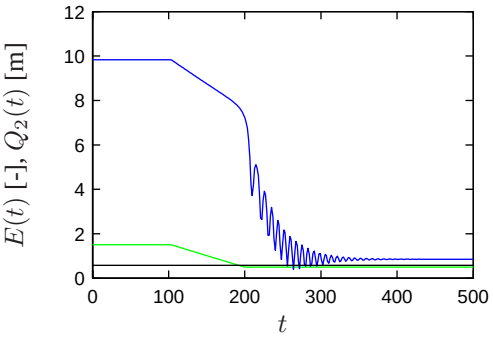

Figure 5.18 $Q_2(t)$ and $E(t)$ during transition from state r_1 to state p_3, $\Omega = 1.25\omega_1$. (——) $E_0(t)$. (——) $Q_2(t)$. (——) $e_{12} = 0.58$

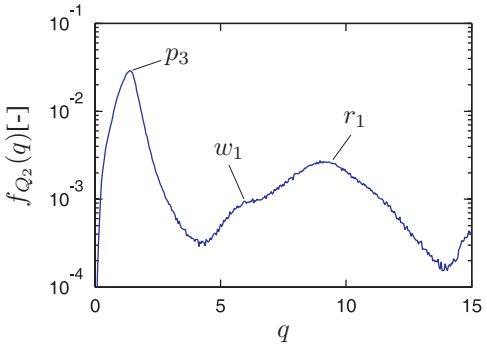

Figure 5.19 Probability density function for Q_2. The system is started in state r_1. $\Omega = 1.25\omega_1$, $E_0 = 1.5$, $\mu = 0.0006$.

Finally, Figure 5.19 shows a plot of the marginal stationary probability density function of Q_2 obtained by ergodic sampling with 1,000,000 periods. As seen, the pdf is multi-peaked corresponding to the temporary occupancy in the various states. The multi-peaked pdfs registered by Chang et al. (Chang *et al.* 1996; Chang and Ibrahim 1997; Ibrahim and Chang 1999) in the so-called intermittence area are believed to be caused by similar transitions between stable attractors.

5.2.8 Concluding remarks

In order to analyse nonlinear resonance phenomena in the lowest modes of vibration of a shallow cable a reduced two-degrees-of-freedom model has been formulated involving a mode representing motion in the static equilibrium plane, and a mode representing out-of-plane motion. Due to the shallowness of the cable the retained modes have closely separated eigenfrequencies. At first possible periodic solutions to the reduced equations of motion under harmonically varying support point motion have been identified based on truncated Fourier series, and the stability has been checked by the Floquet theory.

It is shown that up to three stable periodic motions may co-exist: An in-plane low amplitude motion, an in-plane large amplitude motion, and a whirling motion involving the in-plane and out-of-plane modal coordinates. Above a certain frequency the in-plane large amplitude motion has a slightly different amplitude and a completely different phase from the corresponding motion with the out-of-plane component suppressed, which turns out to be unstable.

Next, the excitation is changed to a narrow-banded Gaussian process with centner frequency and mean envelope equal to the frequency and amplitude of the harmonic excitation. It turns out that vibrations in any of the three states sooner or later become unstable, followed by a jump to another state. Based on Monte Carlo simulations it is demonstrated that the transition between the states may be described by a homogeneous, continuous time three states Markov chain. Additionally, it is demonstrated that the jump is related to critical values of the envelope process of the non-dimensional chord elongation, which represent limit values for excitation of the harmonic motions at the frequency Ω. A unique correspondence exists between outcrossings of the envelope process and the initiation of state transitions. Hence, the transitional probability rates of the Markov chain may be calculated from the mean first-passage times of the envelope process relative to the indicated limit values. Finally, due to relatively long transition time intervals between the states, it is demonstrated that estimates of the transitional probability rates from the response may lead to significant errors.

It is demonstrated that the jumps between the various states result in multi-peaked probability density functions which have previous been registered by Chang *et al.* (Chang *et al.* 1996; Chang and Ibrahim 1997; Ibrahim and Chang 1999).

5.3 Stochastic Stability of a Nonlinear Parametrically Excited Wind Turbine Wing

The studies made in section 5.1 and 5.2 have been made as preliminary studies of the stability of nonlinear stochastically parametrically excited systems. In this section, the two-degrees-of-freedom system described in Chapter 2 is studied. In Chapter 2 the movement of the tower-nacelle system was assumed to vary harmonically with the frequency ω_0 and the amplitude u_0. For wind turbines as is the case for all structural systems under natural loading, a harmonic variation is only an unobtainable approximation to a more or less narrow-banded variation. In this section stability of the nonlinear wing system excited by a narrow-banded variation of the support point motion is analysed. The aerodynamic loading is modelled as described in Chapter 2.

5.3.1 Narrow-banded support point motion

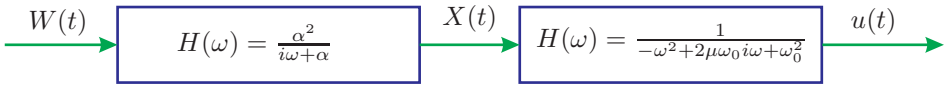

Figure 5.20 Block diagram illustrating the used filtration of white noise $W(t)$.

The nonlinear wing model assumes knowledge of $u(t)$, $\dot{u}(t)$ and $\ddot{u}(t)$, see the coefficients listed in (2.69). Hence, the stochastic model of the support point motion should be twice differentiable. The second order filtration of white noise described in section 5.2.4 is only once differentiable. To solve this, the white noise process is first filtered through a first order filter with the timescale parameter α. The output process $X(t)$, a so-called Ornstein-Uhlenbeck process, is continues and non-differentiable. Next, $X(t)$ is filtered through a second order filter with centre frequency ω_0 and bandwidth μ. $u(t)$ forms the output process, which is Gaussian and twice differentiable. The frequency response functions of the filters are illustrated in Figure 5.20. The state vector formulation of this procedure is

$$\dot{\mathbf{Z}}(t) = \mathbf{A}\mathbf{Z}(t) + \mathbf{b}W(t), \tag{5.74}$$

where

$$\mathbf{Z}(t) = \begin{bmatrix} X(t) \\ u(t) \\ \dot{u}(t) \end{bmatrix}, \quad \mathbf{A} = \begin{bmatrix} \alpha & 0 & 0 \\ 0 & 0 & 1 \\ 1 & -\omega_0^2 & -2\mu\omega_0 \end{bmatrix}, \quad \mathbf{b} = \begin{bmatrix} \alpha^2 \\ 0 \\ 0 \end{bmatrix}. \tag{5.75}$$

$W(t)$ is a unit white noise with the auto-covariance function

$$\kappa_{ww}(\tau) = E\big[W(t)W(t+\tau)\big] = \delta(\tau). \tag{5.76}$$

The standard deviation σ_u of $u(t)$ is written as

$$\sigma_u = \frac{\sqrt{2}}{2} u_0. \tag{5.77}$$

This is ensured if the filter variable α is chosen as

$$\alpha = \omega_0 \left(-\mu + \sqrt{\mu^2 + \frac{2\mu\omega_0^3 u_0^2}{1 - 2\mu\omega_0^3 u_0^2}} \right). \tag{5.78}$$

(5.78) can be derived by means of residual calculus, see e.g. (Nielsen 2000). Hence, the characteristic amplitude u_0 and frequency ω_0 may be related to the harmonic case. μ is the bandwidth parameter for the stochastic support point motion $u(t)$. To ensure α being real the following restriction exists

$$2\mu\omega_0^3 u_0^2 < 1. \tag{5.79}$$

A typical realization of the driving equivalent white noise process $W(t)$, the corresponding Ornstein-Uhlenbeck process $X(t)$, the displacement $u(t)$ and acceleration $\ddot{u}(t)$ as given in (5.74) is shown in Figure 5.21. As seen, the acceleration $\ddot{u}(t)$ becomes "fuzzy", but continuous.

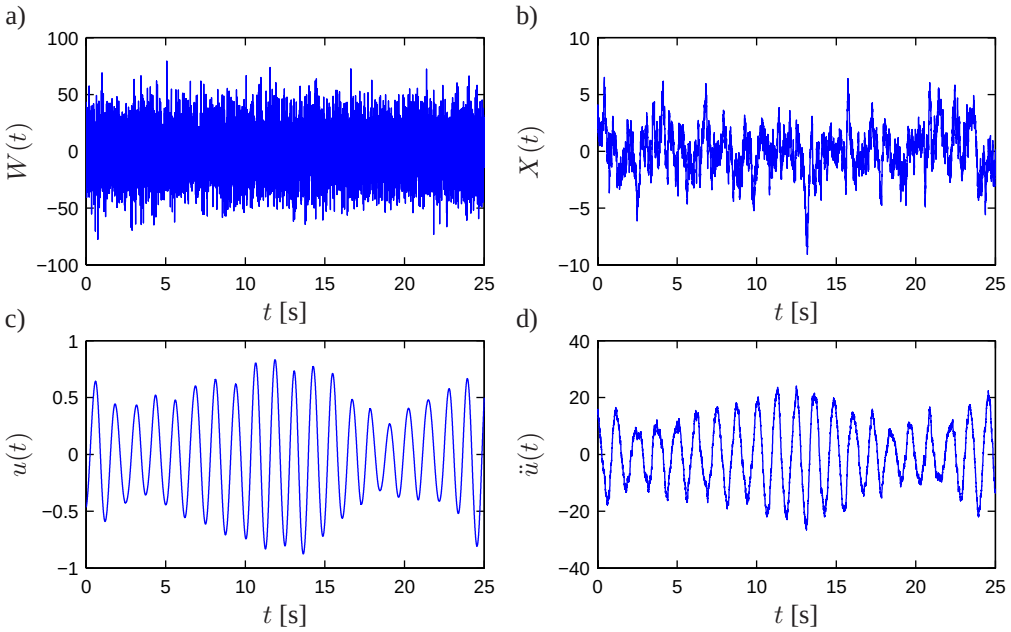

Figure 5.21 Typical realization of $W(t)$, $X(t)$, $u(t)$ and $\ddot{u}(t)$. $\omega_0/\omega_1 = 1.0$, $\mu = 0.01$, $u_0 = 0.5$ m. a) Equivalent white noise process $W(t)$. b) Ornstein-Uhlenbeck process $X(t)$. c) Displacement process $u(t)$. d) Acceleration process $\ddot{u}(t)$.

5.3.2 Numerical analysis

In the following stability of the nonlinear wing is evaluated for situations corresponding to the ones made in Chapter 2 for harmonic variation of the support point motion.

In Figure 5.22 contour regions for the largest Lyapunov exponent indicating stability boundaries are shown as function of u_0 and ζ_1. The numerical simulation is done with $\omega_2/\omega_1 = 2.2$, $\omega_0/\Omega_0 = 3.0$ and $\omega_0/\omega_1 = 1.7$. (——) indicate the stability boundaries for the harmonic case also shown in Figure 2.22. (■) indicate unstable regions for bandwidth parameters $\mu = 0.0001$. The analysis shows that the stable region increases as the excitation becomes stochastic. The stability regions become more distorted as the bandwidth increases, which is due to the limitation in the length of the simulated time series and the fact that the convergence rate of λ decreases with increase of bandwidth.

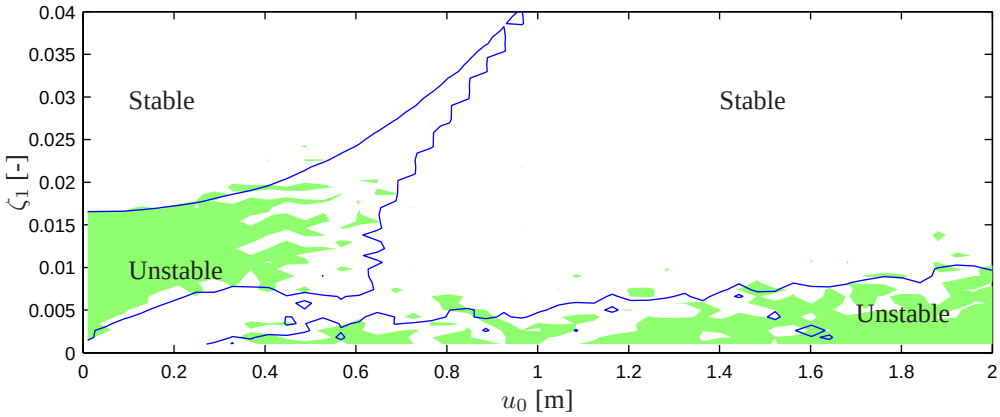

Figure 5.22 Contour curves for $\lambda = 0$ at harmonic and stochastic variation of the support point motion at varying u_0 and ζ_1. $\omega_2/\omega_1 = 2.2$, $\omega_0/\Omega_0 = 3.0$ and $\omega_0/\omega_1 = 1.7$. (——) Harmonic support point motion, $\mu = 0$. (■) Stochastic support point motion, $\mu = 0.0001$.

In Figure 5.23 time variations of λ are shown during unstable and stable conditions together with the corresponding realization of $q_1(t)$. As seen, the convergence of λ is very close to 0 for the unstable solution. Close to the stability boundary convergence may not be obtained since the solution may cross in and out of the unstable region, which will make λ oscillate around 0. This is partly the reason why the boundaries in Figure 5.22 become not well defined. However, it is seen that the stable region expands as the support point motion becomes stochastic, hence, the system becomes increasingly stable with increasing bandwidth. It should be noted that increased stability with increasing bandwidth is not the case for all frequency regions.

Next, the analysis is made for variation of ω_2/ω_1 at various values of μ with $\omega_0/\Omega_0 = 3.0$ and $u_0 = 0.3$ m. The result for $\mu = 0.0001$ is shown in Figure 5.24 with (——) indicating stability boundary for the harmonic case matching that of Figure 2.18, and (■) signifies the stability boundaries for a simulation with $\mu = 0.0001$. As seen, the stability boundaries with respect to variation of ω_2/ω_1 are fairly insensitive to variations in μ.

Now, the stability is evaluated with respect to variation of ω_0/Ω_0 at various values of ω_2/ω_1. Results of the corresponding harmonic analyses are plotted in Figures 2.19-2.21. Figures 5.25a-b show the contour lines of $\lambda = 0$ of simulations with $u_0 = 0.3$ m for $\omega_2/\omega_1 = 2.0$, and with

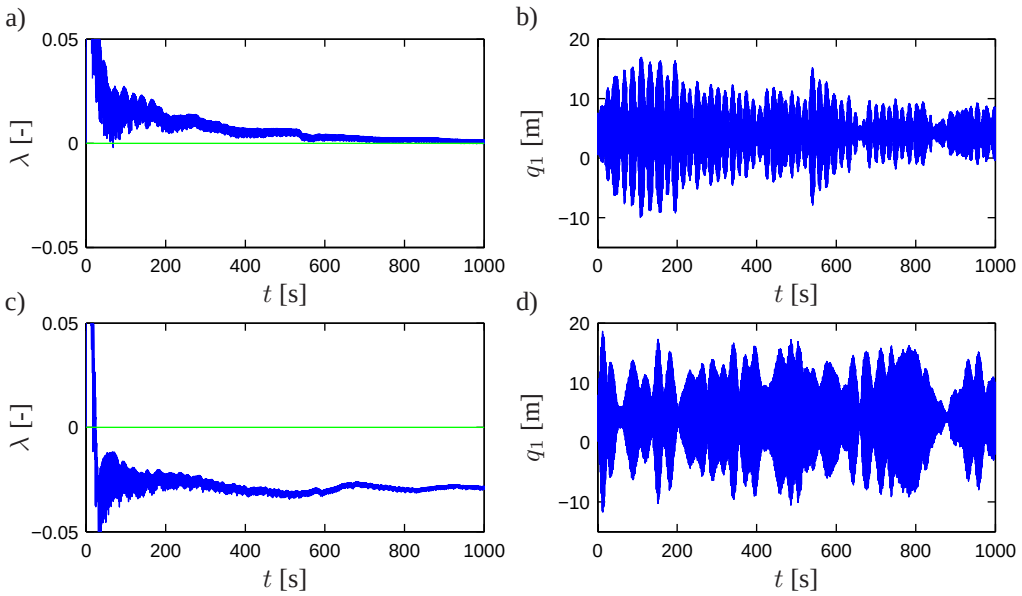

Figure 5.23 Time variation of λ and the corresponding time series. $u_0 = 0.3$, $\zeta_1 = 0.01$, $\mu = 0.001$, $\omega_2/\omega_1 = 2.0$ and $\omega_0/\Omega_0 = 3.0$. a) and b) $\lambda(t)$ and $q_1(t)$, respectively, during unstable situation with $\omega_0/\omega_1 = 1.15$ c) and d) $\lambda(t)$ and $q_1(t)$, respectively, during stable situation with $\omega_0/\omega_1 = 1.0$

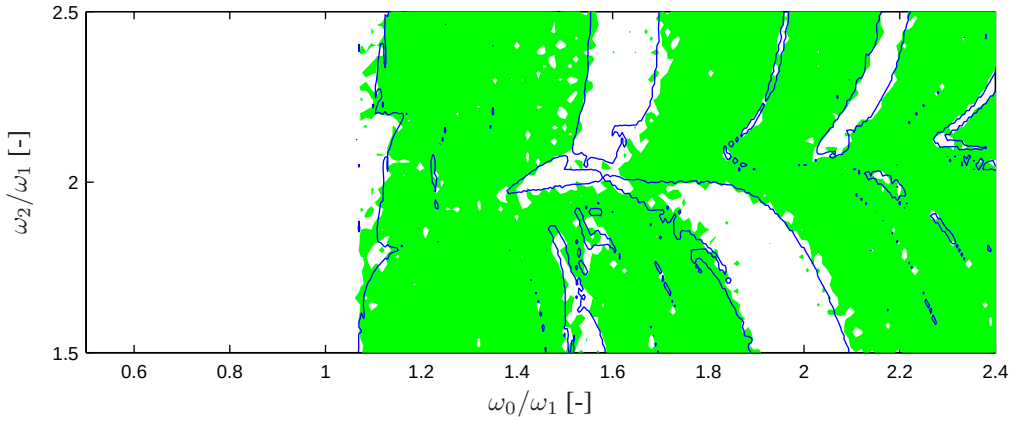

Figure 5.24 Contour curves for $\lambda = 0$ at stochastic variation of the support point motion. $\zeta_1 = 0.01$, $u_0 = 0.3$ and $\omega_0/\Omega_0 = 3.0$. (——) Harmonic support point motion, $\mu = 0$. (■) Stochastic support point motion, $\mu = 0.0001$.

$\mu = 0.0001$ and 0.001, respectively. In Figures 5.26a-b the corresponding analyses are made with $\omega_2/\omega_1 = 2.2$. The stability boundaries for the harmonic cases are indicated by (——) and simulations with stochastic variation of the support point motions are plotted as (■). The stability boundaries with respect to variation of ω_0/Ω_0 are in many cases relatively insensitive to variation of the bandwidth. Most regions become slightly more stable with increasing μ.

However the region defined by $1.6 < \omega_0/\omega_1 < 1.8$ and $2.6 < \omega_0/\Omega_0 < 2.8$ tends to become increasingly unstable with increasing bandwidth.

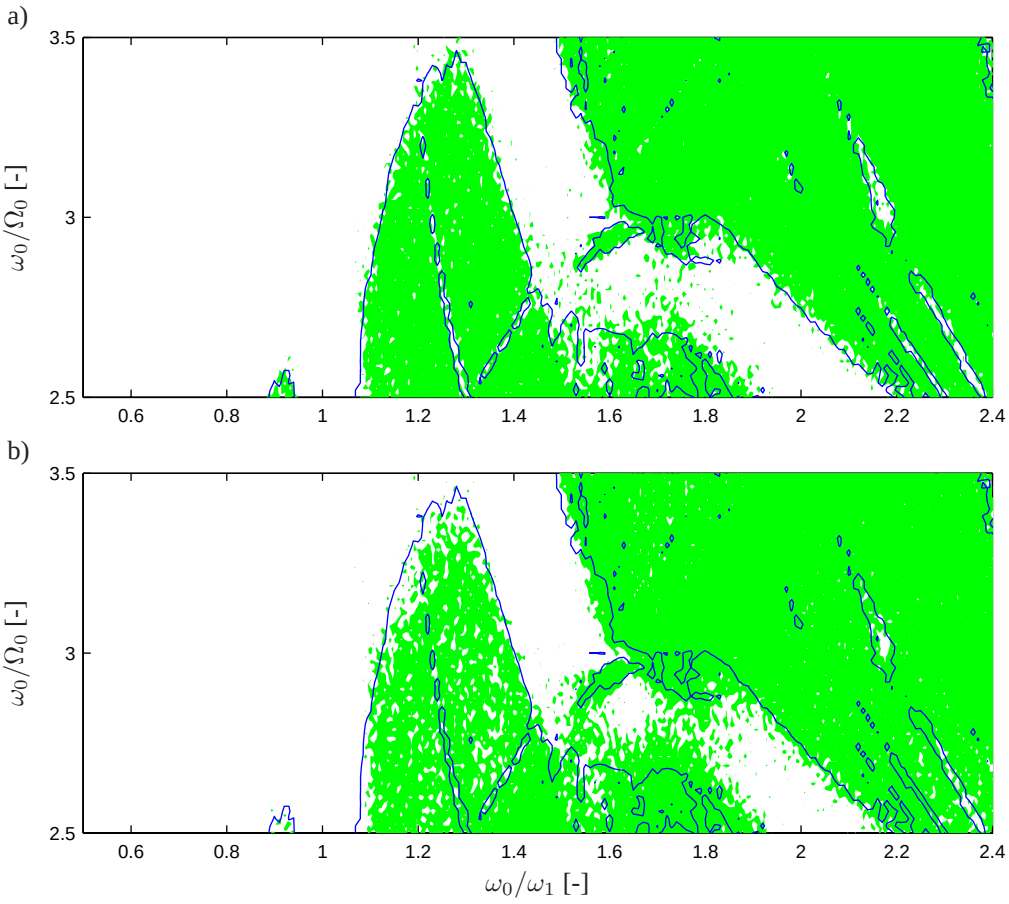

Figure 5.25 Contour curves for $\lambda = 0$ at harmonic and stochastic variation of the support point motion. $\zeta_1 = 0.01$, $u_0 = 0.3$ m, $\omega_2/\omega_1 = 2.0$. (——) Harmonic support point motion, $\mu = 0$. (■) Stochastic support point motion. a) $\mu = 0.0001$. b) , $\mu = 0.001$.

Figure 5.27 shows a variation of u_0 from 0.3 m to 0.6 m over 100 excitation periods keeping $u_0 = 0.6$ m for 900 periods and finally changing u_0 from 0.6 m to 0.3 m over 100 periods. The analysis is made with constant $\zeta_1 = 0.01$, $\omega_0/\Omega_0 = 3.0$, $\omega_2/\omega_1 = 2.2$ and $\omega_0/\omega_1 = 1.7$. Comparing with Figure 5.22 for the harmonic variation of $u(t)$, this corresponds to moving from the stable region into the unstable region and back to the stable region. The response changes character, as the envelope process crosses into the unstable region. The same behaviour was observed for the whirling motion of a shallow cable analysed in section 5.2. However, for this particular case the response becomes unstable as u_0 changes back to unstable conditions.

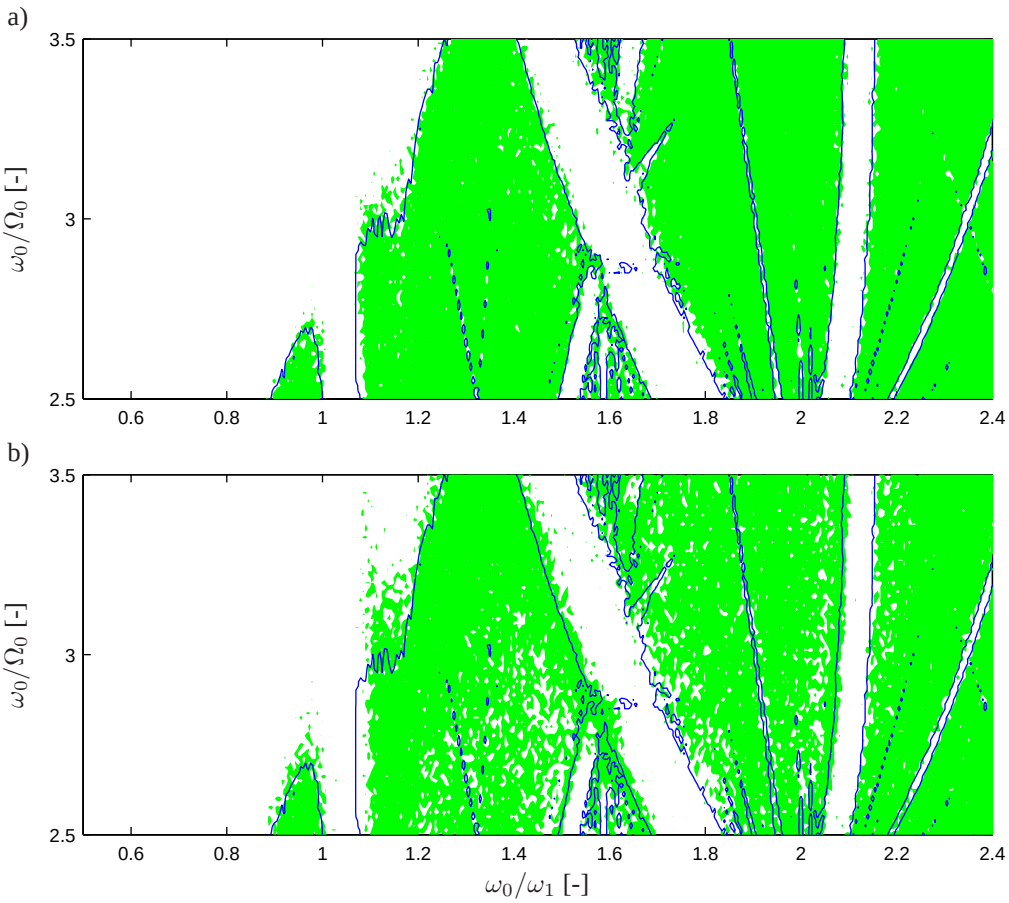

Figure 5.26 Contour curves for $\lambda = 0$ at harmonic and stochastic variation of the support point motion. $\zeta = 0.01$, $u_0 = 0.3$ m, $\omega_2/\omega_1 = 2.2$. (——) Harmonic support point motion, $\mu = 0$. (■) Stochastic support point motion. a) $\mu = 0.0001$. b) , $\mu = 0.001$.

5.3.3 Concluding remarks

The stability of the nonlinear wing model, formulated in chapter 2, has been analysed by Monte-Carlo simulations, when the wing is excited by stochastic support point motion. Due to the demand of a twice differentiable support point motion, the stochastic variation is modelled by a filtration of a unit Gaussian white noise through a first order filter followed by a filtration through a second order filter. The stability boundaries are found by means of the largest Lyapunov exponent as described in Appendix B. With respect to variation of the frequency ratios ω_2/ω_1, ω_0/Ω_0 and ω_0/ω_1 the stability boundaries are found to be relative uninfluenced by variation of the bandwidth of the stochastic excitation. However, significant changes are registered with changes of bandwidth for the stability boundaries plotted as function of the characteristic amplitude of the excitation. This indicates that for a given eigenfrequency ratio and excitation frequency ratio stability may be determined as an outcrossing problem of the excitation envelope process. The

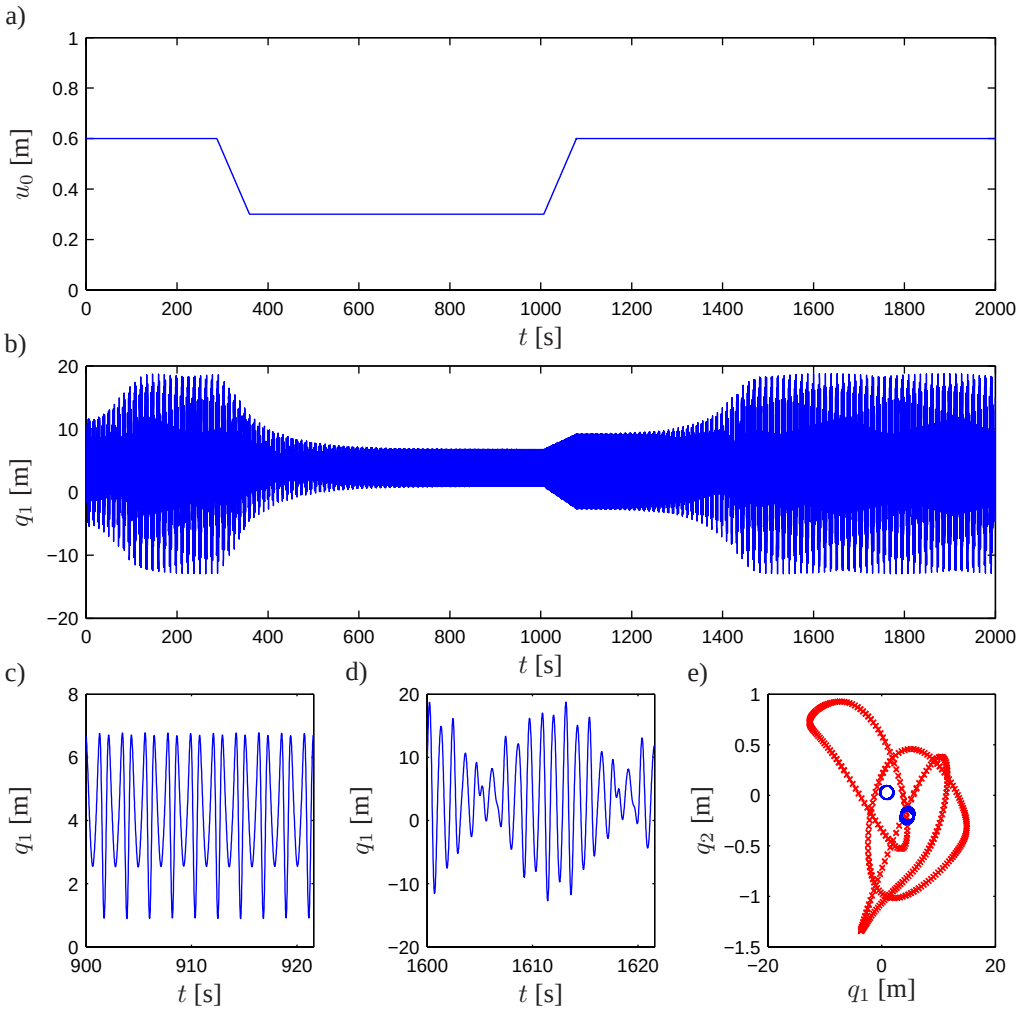

Figure 5.27 $u_0(t)$ and $q_1(t)$ during transition from stable to unstable region. $\zeta_1 = 0.02, \omega_0/\Omega_0 = 3.0, \omega_2/\omega_1 = 2.2$ and $\omega_0/\omega_1 = 1.7$. a) Variation of u_0. b) Variation of $q_1(t)$. c) Variation of $q_1(t)$ during stable conditions. d) Variation of $q_1(t)$ during unstable conditions. e) Poincaré map of response during ($\circ$) stable conditions, ($\times$) chaotic conditions

same behaviour was observed for the nonlinear cable system described in section 5.2. The behaviour of the strange attractor under chaotic response is to be analysed within the paper (Larsen *et al.* 2005), which is under preparation.

CHAPTER 6
Conclusion

In the present thesis a number of analyses have been carried out regarding nonlinear dynamics of wind turbine wings. This final chapter gives an overview of the results achieved throughout the project, and the main conclusions are summarized.

6.1 Overall Conclusions

In the previous chapters a nonlinear structural beam model excited by aerodynamic loading and support point motion is formulated together with a nonlinear dynamic stall model. The models are analysed independently as well as in combination. Finally, the nonlinear wing model is subjected to a narrow banded support point motion and the stability behaviour is analysed. Previous to the stochastic stability analysis of the wing, stability analyses are carried out for two simpler systems stochastically excited by parametric terms in a similar manner as the wing.

Chapter 2 A nonlinear two-degrees-of-freedom model including the nonlinear interactions between the fundamental blade and edgewise modes is formulated retaining nonlinear terms up to cubic order. The model includes inertial nonlinearities from support point motions and geometrical nonlinearities from a nonlinear description of the curvature, and rotation of the aerodynamic loads caused by deflection of the beam. Assuming a harmonic variation of the support point, the important nonlinear couplings are identified and a reduced system is indicated retaining all terms of importance for the quantitative and qualitative behaviour of the system.

Four different frequencies influence the response of the two-degrees-of-freedom system, these are the rotational frequency of the rotor, the frequency of the support point motion and the eigenfrequencies of the fundamental eigenmodes. Keeping the rotational frequency constant, it is demonstrated that significant resonances may occur due to nonlinear parametric excitation.

Next, the nonlinear parametric instability of the system is analysed at various excitation ratios between the support point excitation frequency and the rotational frequency of the rotor and at various eigenfrequency ratios.

It is shown that the parametric instability mainly is influenced by quadratic parametric terms and cubic terms. In combination these terms may produce large regions of chaotic response for fixed excitation ratios. On the other hand the cubic terms at low excitation frequencies tend to stabilize the resonance peaks.

At rational excitation ratios the response becomes periodic, but only certain ratios produces relative short response periods. At irrational excitation ratios the response is shown to be almost periodic with infinitely long response periods. Furthermore, the quadratic parametric terms may

induce chaotic response. In order to determine the stability of the periodic, almost periodic or chaotic response, the theory of Lyapunov exponents is used.

By means of numerical simulations it is shown that within a relative small frequency band around $\omega_2/\omega_1 = 2.1$ the resonance peaks of the first mode remain stable even at large excitation frequencies, whereas large unstable chaotic regions appear when $\omega_2/\omega_1 > 2.1$, and infinite response occur when $\omega_2/\omega_1 < 2.1$ at high excitation frequencies. At $\omega_2/\omega_1 = 2.0$ it is shown that the unstable regions produce large amplitude oscillations, while the amplitude is significantly reduced by increasing the eigenfrequency ratio to 2.2, especially the response second of the second mode is significantly reduced.

Chapter 3 In the present chapter a model for determining the dynamic lift coefficient of a wind turbine wing profile is developed based on the effects of variation in flow conditions. The model includes three basic features . The first is a time delay introduced under fully attached flow situations using two filter equations. The second is a time delay in the motion of the separation point described by one filter equation. Finally, a contribution from leading edge separation vortex is included by one filter equation.

The model uses a simplified description of attached flow, calculating lift by analytical linearized flow theory in the entire range of the angle of attack, and include a contribution from leading edge separation. Additionally, a modified model for the delay on the attachment degree has been suggested, which operates on a mapping of the profile onto a circle in the complex plane. This removes a singularity problem in the lift description when the flow is close to full separation conditions.

The model is validated against dynamic test data of the Vertol 23010-1.58 profile. It is demonstrated that the present model is capable of producing the correct cyclic behaviour of the lift under fully attached conditions. Also under dynamic stall cycle the present model is capable of modelling the maximum lift and reproducing lift data to a satisfactory degree. The performance of the present model is compared with a variety of different models. Only two others are capable of reproducing experimental data, which are the so-called Risø model and Beddoes-Leishman model. 7 parameters are introduced in the present model compared to 12 in the Beddoes-Leishman model making calibration considerable less complicated. The Risø model introduces a linear interpolation, to introduce the effects of trailing edge separation, comparable to that devised within the Øye model. Further, the Risø model includes two state variables to model trailing edge separation. The present model perform equally well using only one state variable for trailing edge separation and introducing an extra state variable to account for leading edge separation, making the present model capable of reproducing effects under a greater variety of flow conditions.

Chapter 4 In this chapter the qualitative behaviour of the combine nonlinear structural model and the dynamic stall model is analysed by means of numerical simulations. To investigate the effect of changing the mean pitch angle the support point motion is set equal to zero, while the pitch is varied harmonically around various mean values. A considerable damping exists in the attached flow region, whereas the aerodynamic damping is lost when the pitch is set in the stall region. Under attached flow conditions the pitch frequency component is the main component in the response, while the eigenfrequency component is significant when the main part of the wing is in the stall region. Next, the support point motion is assumed to vary harmonically at various constant pitch settings and at various values of the eigenfrequency ratio. At the eigenfrequency

ratio equal to 1.8. The response for the chosen frequency ratios is chaotic when using constant lift coefficients. During attached flow conditions all eigenfrequency ratios produces periodic response due to the significant aerodynamic damping. In the stall region non-periodic response exists for all eigenfrequency ratios, but at $\omega_2/\omega_1 = 2.0$ the strange attractor of the system is close to a period three motion, while for $\omega_2/\omega_1 = 1.8$ dynamic instability occur with large amplitudes of the state variables. Hence, a qualitative difference exists in the response between simulations with an eigenfrequency ratio of 2.0 and 1.8.

The significance of aeroelastic contributions are illustrated by simulations using a logarithmic wind field including effects from tower passage. Considerable aeroelastic damping is introduced via the aeroelastic contributions keeping low levels of oscillations at attached flow conditions. Also, a rotational frequency component and a support point frequency are present in the angle of attack when including aeroelastic effects. Under attached flow conditions the rotational frequency component is also present in the response, but as the pitch is increased into the stall region this component becomes less significant.

Finally, a simple linear active control algorithm using the pitch system is devised. The intend of the controller is to decrease the standard deviation while keeping the power output approximately constant. The controller is shown to work well with a decrease of 37% in standard deviation of the blade modal coordinate, when the pitch setting is set for the wing to be in the stall region. If the pitch setting is increased a drop in efficiency is observed due to decrease of aerodynamic damping. At high pitch settings the system may exhibit chaotic behaviour, which is shown to be stabilized by introducing the controller. In both cases no observable change of the power output is registered by introducing the controller. By a more optimal choice of control gains, the efficiency may be increased, but this will introduce severe strains on the pitch system.

Chapter 5 In this chapter three different systems are analysed with respect to stochastic stability. The nonlinear wing system includes several nonlinear parametric terms. In order to understand the behaviour of systems subjected to such terms two simpler systems including nonlinear parametric excitation are analysed.

The first investigation is of the asymptotic stability of first- and second-order moments as well as Lyapunov asymptotic (sample) stability with probability 1 for a dynamic system under a renewal driven jump process parametric excitation. It is shown that the original non-Markov problem can be converted into a Markov one by augmenting two additional equations. Closed sets of equations for the mean values and second-order moments are given.

In order to investigate the asymptotic sample stability a transformation of the four state variables to hyperspherical coordinates is made. The Lyapunov exponents have been evaluated by two methods. The first one is direct simulation of the stochastic equation governing the natural logarithm of the hyperspherical amplitude process. In the second approach, based on ergodicity assumption, time averaging of the pertinent expressions is replaced by ensemble averaging. The numerical results show good qualitative agreement between the two methods of evaluating the Lyapunov exponents. However, direct simulation turns out to be more suitable for the problem. The asymptotic mean-square stability condition is shown to be more conservative than Lyapunov asymptotic (sample) stability with probability 1. However, the asymptotic mean-square stability condition is shown not to be overly conservative and therefore provides a good estimate of the asymptotic stochastic stability.

The second system, which has been analysed, is a reduced two-degrees-of-freedom modal model of a shallow cable. Due to the shallowness of the cable the retained modes have closely

separated eigenfrequencies. At first possible periodic solutions to the reduced equations of motion under harmonically varying support point motion has been identified based on truncated Fourier series, and the stability has been checked by Floquet theory.

It is shown that up to three stable periodic motions may co-exist: an in-plane low amplitude motion, an in-plane large amplitude motion and a whirling motion involving the in-plane and out-of-plane modal coordinates.

Now, the excitation is changed to narrow-banded Gaussian process with centre frequency and mean envelope process equal to the frequency and amplitude of the harmonic excitation. It turns out that vibrations in any of the three states sooner or later become unstable followed by a jump to another state. Based on Monte Carlo simulations it is demonstrated that transition between states may be described by a homogeneous, continues time three state Markov chain. Additionally, it is demonstrated that jumps are related to critical values of the envelope process of the non-dimensional chord elongation, which represent limit values for excitation of the harmonic motions. A unique correspondence exists between out-crossings of the envelope process and the initiation of state transitions. Hence, the transitional probability rates of the Markov chain may be calculated from the mean first-passage times of the envelope process relative to the indicated limit values. Finally, due to very long transition time intervals between the states, it is demonstrated that estimates of the transitional probability rates from the response may lead to significant errors.

The stability of the nonlinear wing model, is analysed by Monte-Carlo simulations, when the wing is excited by stochastic support point motion. Due to the demand of a twice differentiable support point motion, the stochastic variation is modelled by a filtration of a unit Gaussian white noise through a first order filter followed by a filtration through a second order filter. The stability boundaries are found by means of the largest Lyapunov exponent. With respect to variation of the same frequency ratios as for the harmonic case, the stability boundaries are found to be relatively uninfluenced by variation of the bandwidth of the stochastic excitation. However, significant changes are registered with changes of bandwidth for the stability boundaries determined as function of the characteristic amplitude of the excitation. This indicates that for a given eigenfrequency ratio and excitation frequency ratio the stability may be determined as an outcrossing problem of the excitation envelope process.

The stability of the harmonic solutions of the shallow cable is analysed using the Floquet theory. However, the nonlinear wing only produces one stable response solution for each excitation frequency. Also, the shallow cable exhibits periodic response at all excitation frequencies, whereas the wing may produce close to periodic or chaotic response. This renders the Floquet theory impractical with regards to stability analysis of the wing. Instead the Lyapunov exponents are used. Within the stability analysis of the mechanical system subjected to a renewal jump process, two different methods of determining the Lyapunov exponents are given. A third method is used for the wing model, however, the three methods essential describe the same measure. The third method is introduced to be able to classify response with limited amplitude as unstable, i.e. chaotic response.

The main conclusions with regards to the nonlinear wing system and dynamic stall model may be summarized in the following points:

- The behaviour and stability of the nonlinear wing system are mainly influenced by quadratic parametric terms originating from rotation of the aeroelastic loading and support point mo-

tion, and cubic terms originating from the nonlinear description of curvature and displacement of mass due to bending.

- Under certain eigenfrequency ratios and excitation frequencies the nonlinear system exhibits chaotic behaviour. At irrational ratios between the frequency of the support point motion and the rotational frequency of the rotor the response period becomes infinite. Even at rational ratios the response period may become relatively long.
- Due to the above characteristics, the Floquet theory is impractical for analysing the stability behaviour. Instead the Lyapunov exponent is used for stability analysis, which turns out to be very efficient.
- Three main flow conditions describe a dynamic stall cycle, which are fully attached flow conditions, trailing edge separation and leading edge separation.
- The main characteristics mentioned above can be modelled with sufficient accuracy by four state variables.
- Elastic deformation velocities of the wing should be introduced into the load model, i.e. aeroelastic contributions should be included in order to model the correct behaviour of the aerodynamic damping.
- With the intent to keep the mean power output at a relatively constant level, an effective control law can be formulated from the observable state variables when the main part of the wing is under dynamic stall conditions.
- The efficiency of the control can be significant when the wing is within the stall region. Chaotic behaviour, occurring in the deep stall region, may be effectively stabilized by the control system.
- The stability of the nonlinear wing model subjected to stochastic support point motion may be evaluated by the Lyapunov exponent.
- The stochastic stability with regards to excitation frequency ratio and eigenfrequency ratio turns out to be relative uninfluenced by the bandwidth parameter of the stochastic excitation.
- The stochastic stability with fixed excitation frequency ratio and eigenfrequency ratio is related to a one-dimensional outcrossing problem of the excitation envelope process.

The presented models have been used to determine the behaviour of a single wing system. Within a multi-body-dynamic system the combined structural and dynamic stall models may be included without further problems. However, the accuracy of the two-degrees-of-freedom reduction should be further investigated. The stochastic excitation is to be introduced as either a turbulence perturbation in the wind field or as a tower support excitation.

Bibliography

Abbott, I. H. and von Doenhoff, A. E. (1959). *Theory of Wing Sections*. Dover Publications, Inc.

Akbari, M. H. and Price, S. J. (2003). Simulation of dynamic stall for a NACA 0012 airfoil using a vortex method. *Journal of Fluids and Structures* **7**, 855–874.

Al-Noury, S. I. and Ali, S. A. (1985). Large amplitude vibrations of parabolic cables. *Journal of Sound and Vibration* **101**, 451–462.

Anderson, J. D. (2001). *Fundamentals of Aerodynamics* (3 ed.). McGraw-Hill.

Ariaratnam, S. T. (1966). *Dynamic stability of a column under random loading, In: Dynamic stability of structures*. Pergamon Press. 255-265.

Ariaratnam, S. T., Tam, D. S. F., and Xie, Wei-Chau (1991). Lyapunov exponents and stochastic stability of coupled linear systems under white noise excitation. *Probabilistic Engineering Mechanics* **6**(2), 51–56.

Arnold, L. (1984). A formula connecting sample and moment stability of linear stochastic systems. *SIAM Journal of Applied Mathematics* **44**(4), 793–802.

Beddoes, T. S. (1978). Onset of leading edge separation effects under dynamic conditions and low mach numbers. *Proceedings of the 34th Annual Forum of the American Helicopter Society*.

Benedettini, F. and Rega, G. (1994). Analysis of finite oscillations of elastic cables under internal/external resonance conditions. *Nonlinear Stochastic Dynamics* **192**, 39–46.

Benedettini, F. and Rega, G. (1997). Experimental investigation of the nonlinear response of a hanging cable .part II global analysis. *Nonlinear Dynamics* **14**, 119–138.

Benedettini, F., Rega, G., and Alaggio, R. (1995a). Experimental analysis of the finite dynamics of a suspended cable. In *Proceedings of the Design Engineering Technical Conferences - The 15th Biennial Conference on Mechanical Vibration and Noise*, Volume ASME DE 84-1, Boston, MA, pp. 543–552.

Benedettini, F., Rega, G., and Alaggio, R. (1995b). Non-linear oscillations of a four-degree-of-freedom model of a suspended cable under multiple internal resonance conditions. *Journal of sound and Vibration* **182**, 775–798.

Bisplinghoff, R. L. (1996). *Aeroelasticity*. Dover Publications Inc., New York.

Cao, D. Q., Tucker, R. W., and Wang, C. (2001). A stochastic approach to cable dynamics with moving rivulets. www.lancs.ac.uk/depts/mgg/cable.

Castanier, M.P. and Pierre, C. (1995). Lyapunov exponents and localization phenomena in multi-coupled nearly periodic systems. *Journal of Sound and Vibration* **183**(3), 493–515.

Chang, W. K. and Ibrahim, R. A. (1997). Multiple internal resonance in suspended cables under random in-plane loading. *Nonlinear Dynamics* **12**, 275–303.

Chang, W. K., Ibrahim, R. A., and Afaneh, A. A. (1996). Planar and non-planar non-linear dynamics of suspended cables under random in-plane loading - i. single internal resonance. *International Journal of Non-linear Mechanics* **31**(6), 837–859.

Chaviaropoulos, P. K. and Hansen, M. O. L. (2000). Investigating three-dimensional and rotational effects on wind turbine blades by means of a quasi-3d navier-stokes solver. *Journal of Fluids Engineering* **122**, 330–336.

Cramér, H. and Leadbetter, M. R. (1967). *Stationary and related stochastic processes*. John Wiley & Sons, Inc., New York.

Danish Energy Authority (1996). Energi 21, regeringens energihandlingsplan 1996. In Danish.

Danish Energy Authority (2005, June). www.ens.dk.

Danish Standard (1998). *Norm for last på konstruktioner DS410* (4 ed.). Dansk Standard.

Danish Wind Industry Association (2005, June). www.windpower.org.

Du, Z. and Selig, M. S. (1998). A 3-d stall-delay model for horizontal axis wind turbine performance prediction. *AIAA-98-0021*, 9–19.

Du, Z. and Selig, M. S. (2000). The effect of rotation on the boundary layer of a wind turbine blade. *Renewable Energy* **20**, 167–181.

Dwivedy, S. and Kar, R. (1999a). Dynamics of a slender beam with an attached mass under combination parametric and internal resonances part I: Steady state response. *Journal of Sound and Vibration* **221**(5), 823–848.

Dwivedy, S. and Kar, R. (1999b). Dynamics of a slender beam with an attached mass under combination parametric and internal resonances part II: Periodic and chaotic response. *Journal of Sound and Vibration* **222**(2), 281–305.

Dwivedy, S. K. and Kar, R. C. (1999c). Nonlinear response of a parametrically excited system using higher-order method of multiple scales. *Nonlinear Dynamics* **20**, 115–130.

Dwivedy, S. K. and Kar, R. C. (2001). Simultaneous combination, principal parametric and internal resonances in a slender beam with a lumped mass: Three-mode interactions. *Journal of Sound and Vibration* **242**(1), 27–46.

Dwivedy, S. K. and Kar, R. C. (2003). Nonlinear dynamics of a cantilever beam carrying an attached mass with 1:3:9 internal resonance. *Nonlinear Dynamics* **31**, 49–72.

Esmailzadeh, E. and Jalili, N. (1998). Parametric response of cantilever Timoshenko beams with tip mass under harmonic support motion. *International Journal of Non-Linear Mechanics* **33**(5), 765–781.

Fung, Y. C. (1993). *An Introduction to the Theory of Aeroelasticity*. Dover Publications Inc., New York.

Ge, Z. M. and Shiue, J. S. (2002). Non-linear dynamic and control of chaos for a tachometer. *Journal of Sound and Vibration* **253**(4), 773–793.

Ge, Z. M. and Tsen, P. C. (2001). Non-linear dynamic analysis and control of chaos for a two-degrees-of-freeedom rigid body with vibrating support. *Journal of Sound and Vibration* **240**(2), 323–349.

Geurts, C., Vouwenvelder, T., and Reusink, J. (1998). Numerical modelling of rain-wind-induced vibration: Erasmus Bridge Rotterdam. *Structural Engineering International* **8**(4), 129.

Green, R. B., Galbraith, R. A. McD., and Niven, A. J. (1992). Measurements of the dynamic stall vortex convection speed. *Aeronautical Journal*, 319–325.

Griesbaum, R. (1999). *On the stability of dynamic systems with stochastic parametric excitations*. Ph. D. thesis, University of Karlsruhe.

Gross, D. and Harris, F. (1969, May). Prediction of inflight stalled airloads from oscillating airfoil data. *Proceedings of the 25th Annual National Forum of the American Helicopter Society*.

Hanagud, S. and Sarkar, S. (1989). Problem of the dynamics of a cantilever beam attached to a moving base. *Journal of Guidance, Control, and Dynamics* **13**(3), 438–441.

Hansen, M. H., Gaunaa, M., and Madsen, H. Aa. (2004). A Beddoes-Leishman type dynamic stall model in state-space and indicial formulations. Risø-r-1354(en), Risø National Laboratory, Roskilde, Denmark.

Hansen, M. O. L. (2000). *Aerodynamics of Wind Turbines*. James & James.

Harris, F. D. (1966). Preliminary study of radial flow effects on rotor blades. *The Journal of American Helicopter Society* **11**(3), 1–21.

Helstrom, C. W. (1959). Two notes on a markoff envelope process. IRE Transactions on Information Theory. IT-5, pp. 139–140.

Hodges, D. H. and Dowell, E. H. (1974). Nonlinear equations of motion for the elastic bending and torsion of twisted nonuniform rotor blades. Technical Report NASA TN D-7818, NASA.

Holm-Jørgensen, K., Larsen, J. W., and Nielsen, S. R. K. (2005). Nonlinear structural analysis of wind turbine wings using reduced degree-of-freedom models. In preparation.

Ibrahim, R. A. and Chang, W. K. (1999). Stochastic excitation of suspended cables involving three simultaneous internal resonances using Monte Carlo simulation. *Computer Methods in Applied Mechanics and Engineering* **168**, 285–304.

Irvine, H. M. (1992). *Cable Structures*. New York: Dover.

Irvine, H. M. and Caughey, T. K. (1974). The linear theory of free vibrations of a suspended cable. In *Proceedings of the Royal Socity of London*, Volume 341, pp. 299–315.

Iwankiewicz, R. (2002). Dynamic response of non-linear systems to random trains of non-overlapping pulses, (presented at euromech 413 “stochastic dynamics of non-linear mechanical systems", 12-14 june 2000, palermo, italy). *Meccanica* **37**(1), 1–12.

Iwankiewicz, R. (2003). Dynamic systems under random impulses driven by a generalized erlang renewal process. In H.Furuta, M.Dogaki and M.Sakano, (Eds.), *Proceedings of 10th IFIP WG 7.5 Working Conference on Reliability and Optimization of Structural Systems, 25-27.III.2002*, Kansai University, Osaka, Japan, pp. 103–110.

Iwankiewicz, R. and Nielsen, S. R. K. (1999). *Advanced methods in stochastic dynamics of non-linear systems*, Volume 4. Aalborg University Press, Denmark. ISSN 1395-8232.

Iwankiewicz, R., Nielsen, S. R. K., and Larsen, J. W. (2005). Stochastic stability of mechanical systems under renewal jump process parametric excitation using Lyapunov exponents. *Journal of Applied Mechanics* **72**, 213–221.

Jones, R. T. (1940). The unsteady lift of a wing of finite aspect ratio. NACA Report 681, NACA.

Kane, T., Ryan, R., and Bannerjee, A. (1987). Dynamics of a cantilever beam attached to a moving base. *Journal of Guidance Control and Dynamics* **10**, 139–151.

Khasminskii, R. Z. (1967). Necessary and sufficient conditions for the asymptotic stability of linear stochastic systems. *Theory of probability* **12**(1), 144–147. English translation of the Soviet journal.

Kotulski, Z. and Sobczyk, K. (1988). On the moment stability of vibratory systems with random impulsive excitation. *Archives of Mechanics* **40**, 465–476.

Kozin, F. and Sugimoto, S. (1977). Relation between sample and moment stability for linear stochastic differential equations. In Mason, D. (Ed.), *Proceedings of the conference on stochastic differential equations*, pp. 145–162. Academic Press, New York.

Krenk, S. (1983a). A linear theory for pretwisted elastic beams. *Journal of Applied Mechanics* **105**, 137–142.

Krenk, S. (1983b). The torsion-extension coupling in pretwisted elastic beams. *International Journal of Solids and Structures* **19**(1), 67–72.

Krenk, S. (2004a). Airfoil theory for separated flow. Mechanical Engineering, Technical University of Denmark, 2004. (to be published).

Krenk, S. (2004b). Non-linear modelling and analysis of structures and solids. Lecture Notes.

Krenk, S. and Gunnerskov, O. (1986). A triangulation procedure for elastic cross sections with moderate wall thickness. *Computers and Structures* **24**(1), 1–12.

Kreyszig, Erwin (1999). *Advanced Engineering Mathematics* (8 ed.). John Wiley & Sons, Inc.

Langley, R. S. (1988). An investigation of multiple solutions yielded by the equivalent linearization method. *Journal of Sound and Vibration* **127**, 271–281.

Larsen, J. W., Iwankiewicz, R., and Nielsen, S. R. K. (2005). Stochastic analysis of wind turbine wings. In preparation.

Larsen, J. W., Krenk, S., and Nielsen, S. R. K. (2005). Dynamic stall model of wind turbine airfoils. In preparation.

Larsen, J. W. and Nielsen, S. R. K. (2004a). Nonlinear dynamics of wind turbine wings. *International Journal of Non-Linear Mechanics*. In Press.

Larsen, J. W. and Nielsen, S. R. K. (2004b). Nonlinear stochastic response of a shallow cable. *International Journal of Nonlinear Mechanics*. In Press.

Larsen, J. W. and Nielsen, S. R. K. (2005a). Adaptive control of dynamic stall induced vibrations of wind turbine wings. In preparation.

Larsen, J. W. and Nielsen, S. R. K. (2005b). Nonlinear parametric instability of wind turbine wings. *Journal of Sound and Vibration*. In review.

Lee, C. L. and Perkins, N. C. (1995). Three-dimensional oscillations of suspended cables involving simultaneous internal resonances. *International Journal of Nonlinear Dynamics* **8**, 45–63.

Leishman, J. G. (1988). Validation of approximate indicial aerodynamic functions for two-dimensional subsonic flow. *Journal of Aircraft* **25**, 917–922.

Leishman, J. G. (2000). *Principles of Helicopter Aerodynamics*. Cambridge University Press, Cambridge.

Leishman, J. G. and Beddoes, T. S. (1986a). A generalised model for airfoil unsteady aerodynamic behaviour and dynamic stall using the indicial method. *Proceedings of the 42nd Annual Forum of the American Helicopter Society*.

Leishman, J. G. and Beddoes, T. S. (1986b). A semi-empirical model for dynamic stall. *Journal of the American Helicopter Society* **34**, 3–17.

Liiva, J. (1969). Unsteady aerodynamic and stall effects on helicopter rotor blade airfoil sections. *Journal of Aircraft* **6**(1), 46–51.

Lin, Y. K. and Cai, G. Q. (1995). *Probabilistic structural dynamics. Advanced theory and applications*. McGraw-Hill, New York.

LM (2005, June). www.lm.dk.

Mann, J. and Krenk, S. (1993, August). Fourier simulation of non-isotropic wind field model. In Schueller, Shinozuka & Yao (Ed.), *Proceedings of the 6th International Conference on Structural Safety and Reliability, ICOSSAR'93*, Volume 3, Innsbruck, Austria, pp. 1669–1674.

Moon, F. C. (1987). *Chaotic Vibrations. An Introduction for Applied Scientists and Engineers*. John Wiley & Sons.

Nayfeh, A.H. (2000). *Nonlinear Interactions, Analytical, Computational, and Experimental Methods*. John Wiley & Sons, Inc.

Nayfeh, A. H. (1983a). The response of multidegree-of-freedom systems with quadratic non-linearities to a harmonic parametric resonance. *Journal of Sound and Vibration* **90**, 237–244.

Nayfeh, A. H. (1983b). The response of multidegree-of-freedom systems with quadratic non-linearities to a parametric excitation. *Journal of Sound and Vibration* **88**, 547–557.

Nayfeh, A. H. and Mook, D. T. (1995). *Nonlinear Oscillations*. New York: John Wiley & Sons, Inc.

Nayfeh, A. H., Nayfeh, S. A., and Pakdemirli, M. (1995). On the discretization of weakly nonlinear spatially continous systems. In Kliemann, W. and Namachchivaya, N. Sri (Eds.), *Nonlinear Dynamics and Stochastic Mechanics*, Florida, pp. 175–200. CRC Press.

Nielsen, S. R. K. (2000). *Vibration Theory, Vol. 3. Linear Stochastic Vibration Theory* (3 ed.). Aalborg Tekniske Universitetsforlag.

Nielsen, S. R. K. and Kirkegaard, P. H. (2002). Super and combinatorial harmonic response of flexible elastic cables with small sag. *Journal of Sound and Vibration* **251**(1), 79–102.

Nielsen, S. R. K. and Krenk, S. (2003). Whirling motion of a shallow cable with viscos dampers. *Journal of Sound and Vibration* **265**(2), 417–435.

Offshore Center Denmark (2005, June). www.offshorecenter.dk.

Oh, S. Y. and Librescu, L. (2003). Effects of pretwist and presetting on coupled bending vibrations of rotating thin-walled composite beams. *International Journal of Solids and Structures* **40**, 1203–1224.

Øye, S. (1991). Dynamic stall simulated as time lag of separation. Technical report, Department of Fluid Mechanics, Technical University of Denmark.

Papoulis, A. (1984). *Probability, Random Variables and Stochastic Processes* (2 ed.). Tokyo: McGraw-Hill.

Petersen, J. T. (1990). *Kinematically Nonlinear Finite Element Model of a Horizontal Axis Wind Turbine*. Ph. D. thesis, Department of Meteorology and Wind Energy, Risø National Laboratory, Denmark.

Preumont, A. (2002). *Vibration Control of Active Structures* (2 ed.). Kluwer Academic Publisers.

Rao, G. V. and Iyengar, R. (1991). Internal resonance and non-linear response of elastic cable under periodic excitation. *Journal of Sound and Vibration* **149**, 25–41.

Rega, G., Alaggio, R., and Benedettini, F. (1997). Experimental investigation of the non-linear response of a hanging cable. *International Journal of Nonlinear Dynamics* **14**, 89–114.

Rega, G., Lacarbonara, W., Nayfeh, A. H., and Chin, C. M. (1999). Experimental investigation of the nonlinear response of a hanging cable. *Nonlinear Dynamics* **14**, 89–117.

REpower systems (2005, June). www.repower.de.

Richard, K. and Anand, G. V. (1983). Non-linear resonance in strings under narrow band random excitation, part i: Planar response and stability. *Journal of Sound and Vibration* **86**(1), 85–98.

Samuels, J. C. (1963). The dynamics of impulsively and randomly varying systems. *Journal of Applied Mechanics* **30**(1).

Shin, K. and Hammond, J. K. (1998). The instantaneous Lyapunov exponent and its application to chaotic dynamical systems. *Journal of Sound and Vibration* **218**(3), 389–403.

Simon, M. and Wedig, W. (2001). Stochastic stability of elastic structures - quantification of uncertainties by lyapunov exponents, in structural safety and reliability. In Corotis *et al.* , (Ed.), *Structural Safety and Reliability*. Swets & Zeitlinger.

Srinivasan, G. R., Ekaterinaris, J. A., and McCroskey, W. J. (1995). Evaluation of turbulence models for unsteady flows of an oscillating airfoil. *Computers & Structures* **24**(7), 833–861.

Sun, J. Q. and Hsu, C. S. (1987). Cumulant neglegt closure method for nonlinear systems under random excitation. *Journal of Applied Mechanics* **54**, 649–655.

Suresh, S., Omkar, S. N., Mani, V., and Prakash, T. N. Guru (2003). Lift coefficient prediction at high angle of attack using recurrent neural network. *Aerospace Science and Technology* **7**, 595–602.

Svendsen, R. (2005, June 21). Personal communication. Vestas Wind Systems A/S.

Tadjbakhsh, I. G. and Wang, Y. (1990). Wind-driven nonlinear oscillations. *International Journal of Nonlinear Dynamics* **1**, 265–291.

Tagata, G. (1978). Analysis of a randomly excited non-linear stretched string. *Journal of Sound and Vibration* **58**(1), 95–107.

Tagata, G. (1989). Non-linear string random vibration. *Journal of Sound and Vibration* **129**(3), 361–384.

Tarzanin, F. J. (1972, April). Prediction of control loads. *Journal of the American Helicopter Society* **17**(2), 33–46.

Thomsen, J. J. (1997). *Vibrations and Stability*. McGraw-Hill.

Thwaites, B. (1960). *Incompressible Aerodynamics*. Clarndon Press, Oxford.

To, C. W. S. and Liu, M. L. (1996). Lyapunov exponents and information dimensions of multi-degree-of-freedom systems under deterministic and stationary random excitations. *IUTAM Symposium on Advances in Nonlinear Stochastic Mechanics*, 449–458.

Tran, C. T. and Petot, D. (1981). Semi-empirical model for the dynamic stall of airfoils in view of the application to the calculation of responses of a helicopter blade in forward flight. *Vertica* **5**, 35–53.

Veers, P. S. (1988). Three-dimensional wind simulation. Technical Report SAND88-0152, Sandia National Laboratories.

VISCWIND (1999). Viscous effects on wind turbine blades, final report on the JOR3-CT95-0007, Joule III project,. Technical report ET-AFM-9902, Technical University of Denmark.

Wernert, P., Geissler, W., Raffel, M., and Kompenhans, J. (1996). Experimental and numerical investigations of dynamic stall on a pitching airfoil. *AIAA Journal* **34**(5), 982–989.

Wolf, A., Swift, J. B., Swinney, H. L., and Vastano, J. A. (1984). Determining Lyapunov exponents from a time series. *Physica* **16D**, 285–317.

Xie, Wei-Chau (2005). Monte carlo simulation of moment lyapunov exponents. *Journal of Applied Mechanics* **72**(2), 269–275.

Yang, J. B., Jiang, L. J., and Chen, D. C. (2004). Dynamic modelling and control of a rotating Euler-Bernoulli beam. *Journal of Sound and Vibration* **274**, 863–875.

Zhou, Q., Nielsen, S. R. K., and Qu, W. L. (2005). Semi-active control of three-dimensional vibration of inclined sag cable with MR dampers. *Journal of Sound and Vibration*. In review.

APPENDIX A
Analytical Solution of Cable Equations Using a Truncated Fourier Expansion

In the following analytical solutions are listed to the equations of motion for the shallow cable given in (5.54). The Fourier expansion (5.57) is inserted and terms of $\sin(\Omega t + b_i)$, $\cos(\Omega t + b_i)$, $\sin(2\Omega t + c_i)$, $\cos(2\Omega t + c_i)$ and constant terms are collected giving 10 equations used to determine the 10 unknowns A_i, B_i, b_i, C_i and c_i. In the derivations the phase a of the excitation has been assumed equal 0. For ease the corresponding phases have been denoted b_i and c_i rather than $b_{i,0}$ and $c_{i,0}$. The equations should be solved iteratively. For the in-plane solutions the equations are solved with $A_1 = B_1 = C_1 = 0$.

$$
\begin{aligned}
0 = {} & \omega_1^2 A_1 + \frac{1}{2}\omega_1^2 e_0 B_1 \cos b_1 + \beta_1 \Big(A_1 A_2 + \frac{1}{2} B_1 B_2 \cos(b_1 - b_2) + \frac{1}{2} C_1 C_2 \cos(c_1 - c_2) \Big) \\
& + \gamma_1 \Big(A_1^3 + \frac{3}{2} A_1 (B_1^2 + C_1^2) + \frac{3}{4} B_1^2 C_1 \cos(2b_1 - c_1) \Big) + \gamma_2 \Big(A_1 \Big(A_2^2 + \frac{1}{2} B_2^2 + \frac{1}{2} C_2^2 \Big) \\
& + B_1 A_2 B_2 \cos(b_1 - b_2) + \frac{1}{2} B_1 B_2 C_2 \cos(b_1 + b_2 - c_2) + \frac{1}{4} C_1 B_2^2 \cos(c_1 - 2b_2) \\
& + C_1 A_2 C_2 \cos(c_1 - c_2) \Big),
\end{aligned} \tag{A.1}
$$

$$
\begin{aligned}
0 = {} & (\omega_1^2 - \Omega^2) B_1 + \frac{1}{2}\omega_1^2 e_0 \Big(2A_1 \cos b_1 + C_1 \cos(b_1 - c_1) \Big) \\
& + \beta_1 \Big(A_1 B_2 \cos(b_1 - b_2) + B_1 A_2 + \frac{1}{2} B_1 C_2 \cos(2b_1 - c_2) + \frac{1}{2} C_1 B_2 \cos(b_1 - c_1 + b_2) \Big) \\
& + \frac{3}{4}\gamma_1 \Big(4A_1^2 + B_1^2 + 2C_1^2 + 4A_1 C_1 \cos(2b_1 - c_1) \Big) B_1 + \gamma_2 \Big(B_1 \Big(A_2^2 + \frac{1}{2} B_2^2 + \frac{1}{2} C_2^2 \Big) \\
& + 2A_1 A_2 B_2 \cos(b_1 - b_2) + A_1 B_2 C_2 \cos(b_1 + b_2 - c_2) + \frac{1}{4} B_1 B_2^2 \cos(2b_1 - 2b_2) \\
& + B_1 A_2 C_2 \cos(2b_1 - c_2) + C_1 A_2 B_2 \cos(b_1 - c_1 + b_2) \\
& + \frac{1}{2} C_1 B_2 C_2 \Big(\cos(b_1 - c_1 - b_2 + c_2) + \cos(b_1 + c_1 - b_2 - c_2) \Big) \Big),
\end{aligned} \tag{A.2}
$$

$$
\begin{aligned}
0 = {} & 2\zeta_1\omega_1\Omega B_1 - \frac{1}{2}\omega_1^2 e_0\Big(2A_1\sin b_1 + C_1\sin(b_1 - c_1)\Big) \\
& - \beta_1\bigg(A_1B_2\sin(b_1 - b_2) + \frac{1}{2}B_1C_2\sin(2b_1 - c_2) + \frac{1}{2}C_1B_2\sin(b_1 - c_1 + b_2)\bigg) \\
& - 3\gamma_1A_1B_1C_1\sin(2b_1 - c_1) + \gamma_2\bigg(-2A_1A_2B_2\sin(b_1 - b_2) - A_1B_2C_2\sin(b_1 + b_2 - c_2) \\
& - \frac{1}{4}B_1B_2^2\sin(2b_1 - 2b_2) - B_1A_2C_2\sin(2b_1 - c_2) - C_1A_2B_2\sin(b_1 - c_1 + b_2) \\
& - \frac{1}{2}C_1B_2C_2\Big(\sin(b_1 - c_1 - b_2 + c_2) + \sin(b_1 + c_1 - b_2 - c_2)\Big)\bigg),
\end{aligned}
\tag{A.3}
$$

$$
\begin{aligned}
0 = {} & (\omega_1^2 - 4\Omega^2)C_1 + \frac{1}{2}\omega_1^2 e_0B_1\cos(b_1 - c_1) \\
& + \beta_1\bigg(A_1C_2\cos(c_1 - c_2) + C_1A_2 + \frac{1}{2}B_1B_2\cos(b_1 - c_1 + b_2)\bigg) \\
& + \frac{3}{4}\gamma_1\bigg((4A_1^2 + 2B_1^2 + C_1^2)C_1 + 2A_1B_1^2\cos(2b_1 - c_1)\bigg) + \gamma_2\bigg(C_1\Big(A_2^2 + \frac{1}{2}B_2^2 + \frac{1}{2}C_2^2\Big) \\
& + \frac{1}{2}A_1B_2^2\cos(c_1 - 2b_2) + 2A_1A_2C_2\cos(c_1 - c_2) + B_1A_2B_2\cos(b_1 - c_1 + b_2) \\
& + \frac{1}{2}B_1B_2C_2\Big(\cos(b_1 - c_1 - b_2 + c_2) + \cos(b_1 + c_1 - b_2 - c_2)\Big) + \frac{1}{4}C_1C_2^2\cos(2c_1 - 2c_2)\bigg),
\end{aligned}
\tag{A.4}
$$

$$
\begin{aligned}
0 = {} & 4\zeta_1\omega_1\Omega C_1 + \frac{1}{2}\omega_1^2 e_0B_1\sin(b_1 - c_1) - \beta_1\bigg(A_1C_2\sin(c_1 - c_2) - \frac{1}{2}B_1B_2\sin(b_1 - c_1 + b_2)\bigg) \\
& + \frac{3}{2}\gamma_1A_1B_1^2\sin(2b_1 - c_1) + \gamma_2\bigg(-\frac{1}{2}A_1B_2^2\sin(c_1 - 2b_2) - 2A_1A_2C_2\sin(c_1 - c_2) \\
& + B_1A_2B_2\sin(b_1 - c_1 + b_2) + \frac{1}{2}B_1B_2C_2\Big(\sin(b_1 - c_1 - b_2 + c_2) - \sin(b_1 + c_1 - b_2 - c_2)\Big) \\
& - \frac{1}{4}C_1C_2^2\sin(2c_1 - 2c_2)\bigg),
\end{aligned}
\tag{A.5}
$$

$$
\begin{aligned}
0 = {} & \omega_2^2A_2 + \frac{\alpha}{2}\omega_2^2e_0B_2\cos b_2 + \frac{3}{4}\beta_1\Big(2A_2^2 + B_2^2 + C_2^2\Big) + \frac{1}{2}\beta_2\Big(2A_1^2 + B_1^2 + C_1^2\Big) \\
& + \gamma_2\bigg(A_2^3 + \frac{3}{2}A_2(B_2^2 + C_2^2) + \frac{3}{4}B_2^2C_2\cos(2b_2 - c_2)\bigg) \\
& + \gamma_3\bigg(\Big(A_1^2 + \frac{1}{2}B_1^2 + \frac{1}{2}C_1^2\Big)A_2 + A_1B_1B_2\cos(b_1 - b_2) + \frac{1}{2}B_1C_1B_2\cos(b_1 - c_1 + b_2) \\
& + \frac{1}{4}B_1^2C_2\cos(2b_1 - c_2) + A_1C_1C_2\cos(c_1 - c_2)\bigg),
\end{aligned}
\tag{A.6}
$$

$$
\begin{aligned}
-\delta e_0 \cos b_2 &= (\omega_2^2 - \Omega^2)B_2 + \frac{\alpha}{2}\omega_2^2 e_0\Big(2A_2\cos b_2 + C_2\cos(b_2 - c_2)\Big) \\
&+ \frac{3}{2}\beta_1\Big(2A_2 + C_2\cos(2b_2 - c_2)\Big)B_2 + \beta_2\Big(2A_1\cos(b_1 - b_2) + C_1\cos(b_1 - c_1 + b_2)\Big)B_1 \\
&+ \frac{3}{4}\gamma_2\Big(4A_2^2 + B_2^2 + 2C_2^2 + 4A_2C_2\cos(2b_2 - c_2)\Big)B_2 + \gamma_3\Big(\Big(A_1^2 + \frac{1}{2}B_1^2 + \frac{1}{2}C_1^2\Big)B_2 \\
&+ 2A_1B_1A_2\cos(b_1 - b_2) + B_1C_1A_2\cos(b_1 - c_1 + b_2) + \frac{1}{4}B_1^2B_2\cos(2b_1 - 2b_2) \\
&+ A_1C_1B_2\cos(c_1 - 2b_2) + A_1B_1C_2\cos(b_1 + b_2 - c_2) \\
&+ \frac{1}{2}B_1C_1C_2\Big(\cos(b_1 - c_1 - b_2 + c_2) + \cos(b_1 + c_1 - b_2 - c_2)\Big)\Big),
\end{aligned} \tag{A.7}
$$

$$
\begin{aligned}
\delta e_0 \sin b_2 &= 2\zeta_2\omega_2\Omega B_2 - \frac{\alpha}{2}\omega_2^2 e_0(2A_2\sin b_2 + C_2\sin(b_2 - c_2)) - \frac{3}{2}\beta_1 B_2C_2\sin(2b_2 - c_2) \\
&+ \beta_2\Big(2A_1\sin(b_1 - b_2) - C_1\sin(b_1 - c_1 + b_2)\Big)B_1 - 3\gamma_2A_2B_2C_2\sin(2b_2 - c_2) \\
&+ \gamma_3\Big(2A_1B_1A_2\sin(b_1 - b_2) - B_1C_1A_2\sin(b_1 - c_1 + b_2) + \frac{1}{4}B_1^2B_2\sin(2b_1 - 2b_2) \\
&+ A_1C_1B_2\sin(c_1 - 2b_2) - A_1B_1C_2\sin(b_1 + b_2 - c_2) \\
&+ \frac{1}{2}B_1C_1C_2\Big(\sin(b_1 - c_1 - b_2 + c_2) + \sin(b_1 + c_1 - b_2 - c_2)\Big)\Big),
\end{aligned} \tag{A.8}
$$

$$
\begin{aligned}
0 &= (\omega_2^2 - 4\Omega^2)C_2 + \frac{\alpha}{2}\omega_2^2 e_0 B_2\cos(b_2 - c_2) + \frac{3}{4}\beta_1\Big(B_2^2\cos(2b_2 - c_2) + 4A_2C_2\Big) \\
&+ \frac{1}{2}\beta_2\Big(B_1^2\cos(2b_1 - c_2) + 4A_1C_1\cos(c_1 - c_2)\Big) \\
&+ \frac{3}{4}\gamma_2\Big((4A_2^2 + 2B_2^2 + C_2^2)C_2 + 2A_2B_2^2\cos(2b_2 - c_2)\Big) + \gamma_3\Big(\Big(A_1^2 + \frac{1}{2}B_1^2 + \frac{1}{2}C_1^2\Big)C_2 \\
&+ \frac{1}{2}B_1^2A_2\cos(2b_1 - c_2) + 2A_1C_1A_2\cos(c_1 - c_2) + A_1B_1B_2\cos(b_1 + b_2 - c_2) \\
&+ \frac{1}{2}B_1C_1B_2\Big(\cos(b_1 - c_1 - b_2 + c_2) + \cos(b_1 + c_1 - b_2 - c_2)\Big) + \frac{1}{4}C_1^2C_2\cos(2c_1 - 2c_2)\Big),
\end{aligned} \tag{A.9}
$$

$$
\begin{aligned}
0 = {} & 4\zeta_2\omega_2\Omega C_2 + \frac{\alpha}{2}\omega_2^2 e_0 B_2 \sin(b_2 - c_2) + \frac{3}{4}\beta_1 B_2^2 \sin(2b_2 - c_2) \\
& + \frac{1}{2}\beta_2\Big(B_1^2 \sin(2b_1 - c_2) + 4A_1 C_1 \sin(c_1 - c_2)\Big) \\
& + \frac{3}{2}\gamma_2 A_2 B_2^2 \sin(2b_2 - c_2) + \gamma_3\Bigg(\frac{1}{2}B_1^2 A_2 \sin(2b_1 - c_2) + 2A_1 C_1 A_2 \sin(c_1 - c_2) \\
& + A_1 B_1 B_2 \sin(b_1 + b_2 - c_2) - \frac{1}{2}B_1 C_1 B_2\Big(\sin(b_1 - c_1 - b_2 + c_2) - \sin(b_1 + c_1 - b_2 - c_2)\Big) \\
& + \frac{1}{4}C_1^2 C_2 \sin(2c_1 - 2c_2)\Bigg).
\end{aligned}
\tag{A.10}
$$

APPENDIX B
Stability Analysis Using Lyapunov Exponents and Floquet Theory

Two different stability theories are applied the various systems analysed throughout the present project. In this appendix the algorithm, due to Wolf *et al.* (1984), used for determining the entire spectrum of Lyapunov exponents from a given time series is described. For systems with periodic response the stability may be evaluated by the Floquet theory, see e.g. Nayfeh and Mook (1995). The algorithm for the Floquet theory is given in the final part of this appendix.

B.1 Lyapunov Exponents

Consider a dynamical system in an n-dimensional phase space. Then, an n-dimensional set of start conditions spanning a sphere will in time evolve into an n-dimensional set of vectors spanning an ellipsoid due to the time dependent deformation of the dynamical system. In this case the ith Lyapunov exponent is defined in terms of the length of the principal axis of the ellipsoid $p_i(t)$

$$\lambda_i = \lim_{t\to\infty} \frac{1}{t} \ln \frac{p_i(t)}{p_i(0)} \tag{B.1}$$

where λ_i are ordered as $\lambda_1 \geq \lambda_2 \geq ... \geq \lambda_n$. The linear length of the ellipsoid grows as $\mathrm{e}^{\lambda_1 t}$, the area defined by the first and second principal axis grows as $\mathrm{e}^{(\lambda_1+\lambda_2)t}$ and so on.

The centre of the n-dimensional sphere is defined from the evolution of the nonlinear equations of motion subjected to some initial conditions, whereas trajectories of points on the surface are defined from a set of linearized equations of motions. Hence, the principal axes of the ellipsoid can be found from the evolution of the linearized equations of motion of an initially orthonormal vector set attached to the trajectory of the nonlinear equations of motion.

The algorithm goes as follows. The reference trajectory of the centre of the sphere is determined from integration of the nonlinear equations of motion. Simultaneously, the linearized equations of motion are integrated for n different orthonormal initial conditions. The n set of orthonormal initial conditions are found by Gram-Schmidt reorthonormalization procedure given as

$$\tilde{\mathbf{v}}_k = \frac{\mathbf{v}_k - \sum_{i=1}^{k-1} \left(\mathbf{v}_k \tilde{\mathbf{v}}_i^T\right) \tilde{\mathbf{v}}_i}{\left| \mathbf{v}_k - \sum_{i=1}^{k-1} \left(\mathbf{v}_k \tilde{\mathbf{v}}_i^T\right) \tilde{\mathbf{v}}_i \right|} \tag{B.2}$$

where k is running from 1 to n, $|\cdot|$ indicate the vector norm, $\mathbf{v}_k$ is a given vector set spanning the n-dimensional space, and $\tilde{\mathbf{v}}_k$ is an orthonormal vector set spanning the same n-dimensional space as $\mathbf{v}_k$.

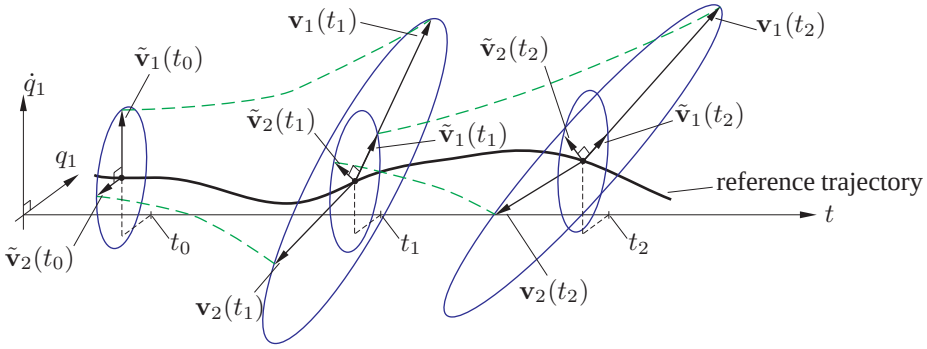

Figure B.1 Evolution and replacement procedure used to estimate the Lyapunov spectrum.

The algorithm is illustrated in Figure B.1 for a two state variable nonlinear system given from $q_1(t)$ and $\dot{q}_1(t)$. At a given initial time $t = t_0$, after the initial conditions on the reference trajectory has dissipated away, the linearized equations are started with an orthonormal set of initial conditions $\tilde{\mathbf{v}}_1(t_0)$ and $\tilde{\mathbf{v}}_2(t_0)$. The linearized equations are integrated until $t = t_1$ where the state vector $\tilde{\mathbf{v}}_1(t_0)$ and $\tilde{\mathbf{v}}_2(t_0)$ have evolved into $\mathbf{v}_1(t_1)$ and $\mathbf{v}_2(t_1)$. $\mathbf{v}_1(t_1)$ is normalized to $\tilde{\mathbf{v}}_1(t_1)$ while the direction is kept free, $\mathbf{v}_2(t_1)$ is then orthonormalized through (B.2) giving $\tilde{\mathbf{v}}_2(t_2)$, which is used in the linearized equation to continue the algorithm until $t = t_2$, when the orthonormalization is carried out again. Hence, the state vectors $\mathbf{v}_1(t)$ and $\mathbf{v}_2(t)$ stay limited as they are normalized at chosen intervals. $\mathbf{v}_1(t)$ is free to move in the most rapidly expanding direction, hence $|\mathbf{v}_1|$ is proportional to $\mathrm{e}^{\lambda_1 t}$, whereas, $\mathbf{v}_2(t)$ is prevented from moving in this direction due to the orthonormalization procedure. However, the span of $\mathbf{v}_1(t)$ and $\mathbf{v}_2(t)$ is proportional to the most rapidly growing two-dimensional subspace with the area $\mathrm{e}^{(\lambda_1+\lambda_2)t} = |\mathbf{v}_1(t)||\mathbf{v}_2(t)|$. Hence, the Lyapunov spectrum can be determined from

$$\lambda_i = \lim_{t\to\infty} \frac{1}{t} \ln |\mathbf{v}_i| \quad , \quad i = 1, 2. \tag{B.3}$$

The arguments presented here are easily expanded to n-dimensional space in which the full spectrum is found from (B.3) with $i = 1, ..., n$ using n orthonormal start conditions.

To determine the entire Lyapunov spectrum of a two-degrees-of-freedom system with 4 state variables, 20 equations of motions are solved simultaneously in time. Firstly, the four

nonlinear equations of motion for the four state variables. Then, the four linearized equations of motions determined from the solution of the nonlinear equation are solved with four different start conditions, $\mathbf{v}(0) = [1\ 0\ 0\ 0]^T$, $\mathbf{v}(0) = [0\ 1\ 0\ 0]^T$, $\mathbf{v}(0) = [0\ 0\ 1\ 0]^T$ and $\mathbf{v}(0) = [0\ 0\ 0\ 1]^T$, respectively. If $\lambda_i > 0$, then the trajectories will diverge exponentially and the system is unstable. Since the relation $\lambda_1 \leq \lambda_2 \leq \ldots \leq \lambda_n$ exists, it suffice to investigate the sign of λ_1 to evaluate the stability of the system.

B.2 Floquet Theory

Assuming periodic response of a nonlinear system Floquet theory may be used to evaluate the stability. Given the following state vector formulation of the linearized equations of motion

$$\dot{\mathbf{v}}(t) = \mathbf{A}(t)\mathbf{v}(t), \tag{B.4}$$

where $\mathbf{v}(t)$ is the state vector and $\mathbf{A}(t)$ is the time dependent coefficient matrix assumed to be periodic with the period T. Now, let $\mathbf{\Phi}(t)$ denote the fundamental set of solutions to (B.4) fulfilling the initial value $\mathbf{\Phi}(0) = \mathbf{I}$. Then at $t = T$

$$\mathbf{v}(T) = \mathbf{\Phi}(T)\mathbf{v}(0). \tag{B.5}$$

Further, since $\mathbf{A}(t+T) = \mathbf{A}(t)$, it follows that

$$\begin{aligned} \mathbf{v}(2T) &= \mathbf{\Phi}(T)\mathbf{v}(T) = \mathbf{\Phi}^2(T)\mathbf{v}(0), \\ &\vdots \\ \mathbf{v}(nT) &= \mathbf{\Phi}(T)\mathbf{v}((n-1)T) = \mathbf{\Phi}^n(T)\mathbf{v}(0). \end{aligned} \tag{B.6}$$

$\mathbf{\Phi}(T)$ may be written as

$$\mathbf{\Phi}(T) = \mathbf{P}\mathbf{N}\mathbf{P}^{-1}, \tag{B.7}$$

where $\mathbf{P}$ is a matrix storing the 4 eigenvectors of $\mathbf{\Phi}(T)$ column wise, and $\mathbf{N}$ is a diagonal matrix with the corresponding eigenvalues $\nu_1, \cdots, \nu_4$ in the main diagonal. Then

$$\mathbf{v}(nT) = \mathbf{P}\mathbf{N}^n\mathbf{P}^{-1}\mathbf{v}(0), \quad n = 1, 2, \ldots. \tag{B.8}$$

Hence, for arbitrary initial value $\mathbf{v}(0)$, $\mathbf{v}(nT) \to \mathbf{0}$ as $n \to \infty$, if $\mathbf{N}^n \to \mathbf{0}$. This is the case if all 4 eigenvalues fulfil

$$|\nu_i| < 1, \quad i = 1, \ldots, 4. \tag{B.9}$$

According to (B.5), $\mathbf{\Phi}(T)$ can be determined by numerical integration of the linearized equations of motion over the interval $[0\ T]$. Using initial conditions $\mathbf{v}(0) = [1\,0\,0\,0]$, $[0\,1\,0\,0]$, $[0\,0\,1\,0]$ and $[0\,0\,0\,1]$, respectively, $\mathbf{v}(T)$ will assume the form of the fundamental solutions $\mathbf{\Phi}(T)$. Solving for the eigenvalues of $\mathbf{\Phi}(T)$ provides ν_i, and (B.9) may then be evaluated to determine the stability.